SLAC-R-499
UC-408

X-RAY ABSORPTION SPECTROSCOPIC STUDIES OF MONONUCLEAR NON-HEME IRON ENZYMES

Tami E. Westre

Stanford Linear Accelerator Center
Stanford Synchrotron Radiation Laboratory
Stanford University, Stanford, California 94309

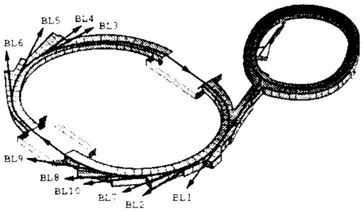

SLAC-Report-499
January 1996

Prepared for the Department of Energy under contract number DE-AC03-76SF00515
and the NIH, Biomedical Resource Technology Program,
Division of Research Resources

Printed in the United States of America. Available from the National Technical Information Service,
U.S. Department of Commerce, 5285 Port Royal Road, Springfield, VA 22161

*Ph.D. Thesis Stanford University, Stanford, CA 94309

X-RAY ABSORPTION SPECTROSCOPIC STUDIES OF MONONUCLEAR NON-HEME IRON ENZYMES

A DISSERTATION
SUBMITTED TO THE DEPARTMENT OF CHEMISTRY
AND THE COMMITTEE ON GRADUATE STUDIES
OF STANFORD UNIVERSITY
IN PARTIAL FULFILLMENT OF THE REQUIREMENTS
FOR THE DEGREE OF
DOCTOR OF PHILOSOPHY

By
Tami E. Westre
January 1996

Abstract

Fe K-edge X-ray absorption spectroscopy (XAS) has been used to investigate the electronic and geometric structure of the iron active site in non-heme iron enzymes. A new theoretical extended X-ray absorption fine structure (EXAFS) analysis approach, called GNXAS, has been tested on data for iron model complexes to evaluate the utility and reliability of this new technique, especially with respect to the effects of multiple-scattering. In addition, a detailed analysis of the 1s—>3d pre-edge feature has been developed as a tool for investigating the oxidation state, spin state, and geometry of iron sites. Edge and EXAFS analyses have then been applied to the study of non-heme iron enzyme active sites.

GNXAS and Its Application to Inorganic Iron Model Complexes. GNXAS, a recently developed integrated approach to the analysis of EXAFS data is presented in detail. Using the GNXAS approach, it is possible to calculate all the signals related to two-, three- and four-atom correlation functions with the proper treatment of correlated distances and Debye-Waller factors. The technique is particularly well-suited for the analysis of multiple-scattering effects and thus allows for accurate determination of bond distance and angular information of second and third neighbors. Herein the application of GNXAS to several chemical systems of known structure is reported. The reliability of GNXAS was evaluated on both a well-ordered inorganic complex, Fe(acac)$_3$, as well as a lower-symmetry coordination complex with mixed ligation, Na[Fe(OH$_2$)EDTA]. The total EXAFS signal generated by GNXAS matches closely the experimental data for both complexes, especially when all the multiple-scattering contributions were included in the theoretical signal. First neighbor distances obtained from refinement using GNXAS, as well as distances and angles for further neighbors, compared very well with crystallographic values. The angle dependence of the Fe-C-N multiple-scattering contribution in K$_3$Fe(CN)$_6$ was also examined. The results indicate that GNXAS can be used to determine angles relatively accurately for Fe-C-N configurations with angles greater than about 150°. These results establish the utility and reliability of the GNXAS approach and provide a reliable means to determine additional structural information from EXAFS analysis of structures of chemical interest.

Angle Determination Using GNXAS. The Fe-N-O bond angle in a series of $\{FeNO\}^7$ complexes has been probed by EXAFS, utilizing the new theoretical data analysis package, GNXAS. Since it is possible with GNXAS to calculate all the signals related to two-, three-, and four-atom correlation functions with the proper treatment of correlated distances and Debye-Waller factors, the methodology is particularly

well-suited for analysis of multiple-scattering effects and bond angle determination. EXAFS data were obtained on a series of crystallographically-characterized $\{FeNO\}^7$ inorganic complexes with varying Fe-N-O angles to examine the sensitivity of the GNXAS fit to this angle. The compounds studied were Fe(TMC)NO which has an Fe-N-O bond angle of 177.5(5)°, Fe(TACN)$(N_3)_2$NO which has an angle of 156(1)° and Fe(salen)NO which has a bond angle of 127(6)° at -175° C and 147(5)° at 23° C. EXAFS data for FeEDTA-NO (whose crystal structure has not been determined and thus the angle is unknown) were also obtained and analyzed using GNXAS to determine the Fe-N-O bond angle. Results are presented which indicate that it is possible to determine whether the Fe-N-O unit is bent or linear, with the GNXAS analysis being extremely sensitive when the angle is between 150° and 180°. Using this method the Fe-N-O angle in FeEDTA-NO is found to be 156(5)°. The results of this study establish that EXAFS analysis using GNXAS can provide reliable angular information for small molecules coordinated to transition metals with rather complex coordination environments. This study thus provides the basis for the determination of the coordination geometry of molecules like NO and O_2 to metalloprotein active sites.

A Multiplet Analysis of the 1s—>3d Pre-Edge Feature. In this study, XAS Fe K-edge data on high spin and low spin ferrous and ferric model complexes with varying geometries, as well as binuclear complexes with varying oxidation state, geometry, and bridging ligation, were collected in order establish a detailed understanding of the 1s—>3d pre-edge feature and its sensitivity to the electronic and geometric structure of the iron site. The energy splitting and intensity distribution of the pre-edge feature of these complexes varied with spin state, oxidation state, geometry, and bridging ligation (in the binuclear complexes). A methodology for interpreting the energy splitting and intensity distribution of the 1s—>3d pre-edge features was developed for high spin ferrous and ferric complexes in octahedral, tetrahedral and square pyramidal environments and low spin ferrous and ferric complexes in octahedral environments. In each case, the allowable many-electron excited states were determined using ligand field theory. The energies of the excited states were calculated and compared to the energy splitting in the 1s—>3d pre-edge features and the relative intensities of transitions into the many-electron excited states were obtained and compared to the intensity pattern of the pre-edge feature. The effect of distorting the iron site to tetrahedral and square-pyramidal geometries was analyzed. The contribution to the pre-edge intensity from both a quadrupole and a dipole (from 4p-3d mixing) intensity mechanism was determined for these distorted cases where the amount of 4p mixing was experimentally determined and compared to a theoretical estimate of the amount of 4p mixing determined from density functional calculations.

The results presented should further aid in the interpretation of the 1s—>3d pre-edge region for non-heme iron enzymes as the energy splitting and intensity pattern of the pre-edge features are directly related to the oxidation state, spin state and geometry of the iron site.

Characterization of the Active Sites in Non-Heme Iron Enzymes. Edge and EXAFS analyses have been used to characterize the active sites in several non-heme iron enzymes. A detailed analysis of the intensity and splitting of the 1s—>3d pre-edge feature allowed for determination of the oxidation state, spin state, and coordination geometry of the iron active site. In addition, an EXAFS analysis provided accurate first shell distances with information on the number and type of coordinating atoms. Not only were the resting enzymes studied, but stable substrate and oxygen bound intermediates were also investigated including the nitric oxide derivatives of the ferrous active sites which serve as reversible analogues of possible dioxygen intermediates.

As a probe of non-heme iron active sites, nitric oxide has been shown to react with the ferrous state of many mononuclear non-heme iron enzymes and model complexes to form an $\{FeNO\}^7$ complex which has a distinct S=3/2 ground state. An edge analysis of the XAS data for three $\{FeNO\}^7$ model complexes was used to determine the oxidation state of the iron site in these iron-nitrosyl systems. The edge results were used in combination with results from other spectroscopies and theoretical methods to produce a new bonding description of the $\{FeNO\}^7$ unit which involves high spin ferric iron (S=5/2) antiferromagnetically coupled to NO^- (S=1) to produce the S=3/2 ground state.

Bleomycin (BLM) is a glycopeptide antibiotic currently used in the treatment against a variety of carcinomas and lymphomas due to its ability to selectively cleave DNA. The geometric and electronic structure of high spin ferrous complexes of BLM and the structural analog PMAH have been investigated by XAS edge and EXAFS analyses. The XAS results have been used in combination with results from optical absorption (Abs), magnetic circular dichroism (MCD), and resonance Raman (rR) studies to define the electronic and geometric structure of the ferrous active site. The results indicate that there is a short Fe-N bond which increases along the series solid $[Fe(II)PMA]^+$ > solution $[Fe(II)PMA]^+$ > Fe(II)BLM. The short bond is attributed to the pyrimidine ligand which is involved in pyrimidine π-backbonding. This pyrimidine π-backbonding mediates the electron density localized on the Fe^{2+} center which contributes to the unique chemistry of Fe(II)BLM relative to other non-heme iron sites.

Activated BLM is the first mononuclear non-heme iron oxygen intermediate stable enough for detailed spectroscopic study. It has been postulated that activated BLM is an oxoferryl intermediate on the basis of its reactivity and analogy with cytochrome P-450 chemistry. Alternatively, spectroscopic and model studies have indicated activated BLM to have an Fe(III)-peroxide site. XAS has been used to *directly* probe the oxidation and spin states of the iron in activated BLM and to determine if a short iron-oxo bond is present, which would be characteristic of the oxo-ferryl species of heme iron. Both the pre-edge and edge regions of the Fe K-edge spectra indicate that activated BLM is a low spin ferric complex. The pre-edge intensity of activated BLM is also similar to that of low spin ferric BLM and does not show the intensity enhancement which would be present if there were a short Fe-O bond. Furthermore, bond distances obtained from EXAFS are similar to those in low spin Fe(III)BLM and show no evidence for a short iron-oxo bond. These data indicate that activated BLM is a peroxy-low spin ferric complex and suggest that such an intermediate may play an important role in activating O_2 for further chemistry in the catalytic cycles of mononuclear non-heme iron enzymes.

Lipoxygenases (LOs) are non-heme iron enzymes which catalyze the reaction of dioxygen with *cis,cis*-1,4-pentadiene containing fatty acids to form hydroperoxide products, which in mammals are the precursors to the inflammation and immunity mediating compounds lipoxins and leukotrienes. Recent X-ray crystal structures of ferrous soybean lipoxygenase-1 (SLO-1) offer two different descriptions of the active site: one four-coordinate and one five- or six-coordinate. Near infrared (NIR) circular and magnetic circular dichroism (CD/MCD) and variable temperature, variable field (VTVH) MCD have been used to study SLO-1 in solution which is found to exist as a 40/60% mixture of five- and six-coordinate forms, respectively. An XAS edge and pre-edge analysis also shows that the mammalian 15-LOs and SLO-1 in glycerol are six-coordinate. This is consistent with the EXAFS results of SLO-1 in glycerol which show the iron active site to have 5 ± 1 N/O at ~2.16 Å. VTVH MCD data on the six-coordinate sites show that the mammalian and soybean enzymes have very different ground state splittings, indicative of differences in π bonding interactions with the ligand set. These differences in ferrous site coordination in solution and ground state splittings are attributed to the substitution of a stronger histidine ligand in the mammalian 15-LOs for an asparagine in SLO-1.

Phenylalanine hydroxylase (PAH) is involved in the metabolism of phenylalanine and its dysfunction is responsible for the genetic disorder phenylketonuria which is characterized by irreversible, progressive brain damage. A transition between the resting low affinity state (the "T" state) and the high affinity state (the "R" state) is required for the enzyme to achieve catalytic competence where phenylalanine binds to an allosteric effector site (as distinguished from the active site phenylalanine binding site). XAS was used to define the geometric and electronic structure of the non-heme iron active site of Fe(II)PAH^R, Fe(II)PAH^T, Fe(III)PAH^R, and Fe(III)PAH^T. The edge and pre-edge features for the four forms of PAH studied indicate that the iron site is six-coordinate. The fits to the EXAFS data for all four forms of the protein give ligand distances typical of six-coordinate iron model complexes with oxygen and nitrogen ligation. There were subtle differences in the EXAFS fits to the data of Fe(II)PAH^R *vs.* Fe(II)PAH^T. The differences seen in the EXAFS data of Fe(II)PAH^R and Fe(II)PAH^T can either be attributed to changes caused by phenylalanine in the active site or by the activation process (*i.e.* phenylalanine in the allosteric site). Further studies need to be done to sort out the effects of phenylalanine in the active site *vs.* the allosteric site.

Protocatechuate 3,4-dioxygenase (PCD), one of the most well-studied intradiol dioxygenases, catalyzes the intradiol cleavage of protocatechuic acid to produce β-carboxy-*cis,cis*-muconic acid. It is clear from previous studies that the native intradiol dioxygenases have a high spin ferric active site and that the enzyme mechanism involves initial substrate binding followed by O_2 attack. Herein XAS studies on Fe(II)PCD, Fe(III)PCD, Fe(III)PCD + 3,4 dihydroxybenzoic acid (Fe(III)PCA), and FePCD-NO are reported. The XAS edge and pre-edge features of Fe(II)PCD indicate that the iron active site is six-coordinate with an EXAFS analysis showing those ligands to be oxygens and nitrogens. The iron active site of both Fe(III)PCD and Fe(III)PCA appear to be five-coordinate as the pre-edge and edge features are similar to those of five-coordinate ferric complexes. An analysis of the EXAFS data for Fe(III)PCD shows O/N ligands at 1.92 Å and 2.12 Å. The EXAFS of Fe(III)PCA could not be well simulated without a longer O/N contribution at 2.47 Å in addition to contributions at 1.97 and 2.10 Å. The edge and pre-edge results for FePCD-NO indicate that the iron atom is in the ferric oxidation state with the rising edge of FePCD-NO being at lower energy than that of Fe(III)PCD due to the highly covalent nature of the Fe(III)-NO$^-$ bond. An analysis of the pre-edge intensity for FePCD-NO predicts that the iron site is five-coordinate with a bent Fe-N-O unit. FePCD-NO having a bent Fe-N-O unit is also supported by a GNXAS analysis of the EXAFS data of FePCD-NO. In addition the EXAFS data of FePCD-NO were fit well with 1 O/N at 1.89 Å, 4 O/N at 2.11 Å, and 1 O/N at 2.45 Å. The shorter distance is attributed to the Fe-N(O) bond distance. An Fe-N(O) distance of 1.89 Å is much longer than previously observed Fe-N(O) distances for $\{FeNO\}^7$ model complexes. The nature of the longer Fe-N(O) bond in FePCD-NO needs to be further investigated keeping in mind that tyrosinate—>Fe(III) charge donation may limit the ability of NO$^-$ to donate electron density to the ferric site, thereby weakening the Fe-N(O) interaction.

Acknowledgments

I have been very fortunate in my graduate career to not only work on very interesting projects, but also to have worked as a joint student - reaping the benefits of two advisors and two research groups. My advisors Ed Solomon and Keith Hodgson have encouraged and guided me through my various projects over the past five and a half years. They have very different advising styles, but I feel as if I have benefited from working under both of them. Ed was always the motivator and Keith allowed for independent thinking, while the both provided unequaled insight into their respective fields of expertise. I appreciate their guidance and also the opportunities that they have given me to present the projects that I worked on at conferences locally and internationally.

Britt Hedman and Pat Frank are two remarkable people that have accurately been referred to as the "secret weapons" of the Hodgson group. Their many years of scientific experience have proven to be an invaluable resource and their many years of doing research in Keith's lab provided continuity to the group. I not only respect Pat and Britt as scientists, but they have both become friends and confidantes. I will miss working with them!

One of the benefits of working for two advisors is the opportunity to interact with so many different people. Numerous people have influenced my graduate career both directly and indirectly including all the past and present members of the Solomon and Hodgson groups: Heather Bufford, Jason Chen, Ling Ling Chen, Jane DeWittt, David Eliezer, Isaac Liu, Kent Nakagawa, Dan Segel, Susan Shadle (1/2), Chrisie Stanfel, Grace Tan, Trevor Tyson, Erik Wasinger (1/2), Kendra Williams (1/2), Holly Zhang, Mike Baldwin, Carl Brown, Cecelia Campochiaro, Pat Clark, Sabine (Pulver) Coates, Jim Cole, Mindy Davis, Daniel Gamelin, Jeff Guckert, Melissa Hanson, Brooke Hemming, Ted Holman, Paul Jones, Pierre Kennepohl, Marty Kirk, Lou LaCroix, Kelly Loeb, Mike Lowery, Tim Machonkin, Jennifer May, Jim McCormick, Amy Palmer, Elizabeth Pavel, Mark Pavlosky, Brad Reitz, Dave Root, Uma Sandaram, Susan Shadle (1/2), Woon Shin, Felix Tuczek, Erik Wasinger (1/2), Kendra Williams (1/2), Yi-Shan Yang, Mark Yeager, Jeff Zaleski, Yan Zhang, Jing Zhou. They are all terrific people and I grateful for the chance to work with them and get to know them. I have enjoyed interacting with my lab-mates both scientifically and socially (gambling for mooncakes, dining on authentic Swedish food, and the numerous barbecues and Christmas parties). I wish them all the best of luck in the future!

Collecting data at SSRL is a very tiring and stressful process. The success of our experiments can in part be attributed to the staff at SSRL who work hard to ensure that all the equipment is working properly and that there is "beam". I have really enjoyed the camaraderie that ensues during a beamtime experiment. Typically there are twice as many samples as we have time for and so everyone must work together to get the experiments done as efficiently as possible. Most of the time there are other obstacles placed in the way - no beam, faulty power supplies, mis-labelled gas cylinders, *etc.* that make beamtime experiments challenging. Such an intense, stressful time could bring out the worst in people, but that has not been my experience. I am grateful to all the people involved in these experiments for making beamtime fun and challenging instead of dreadful and challenging. I should also thank the people that actually provided the samples for me to run. Yan Zhang, Mark Pavlosky, Kelly Loeb and Jeff Zaleski have spent a lot of time preparing and characterizing protein samples for me to run. I appreciate the time that they spent ensuring the quality of the samples.

I worked closely with Rino Natoli, Andrea Di Cicco, and Adriano Filipponi on the GNXAS approach to data analysis. Not only did they develop the theory behind the approach and the software, but their guidance was crucial in implementing this new software in our lab. I really enjoyed working with Rino, Andrea, and Adriano on their numerous visits here and on my trip to Frascati, Italy. They were great hosts!

Sabine (Pulver) Coates, Jane DeWitt, and Susan Shadle have played very special roles in my graduate career. Being a year, three years, and two years ahead of me, respectively, they taught me the ropes and served as role models. They indoctrinated me into the world of X-ray absorption spectroscopy, non-heme iron enzymes, and ligand field theory, encouraged me throughout my years here, and bolstered my confidence in the my ability to do science. Not only were they great lab-mates, but they are AWESOME friends. I am extremely thankful for the opportunity to work with them and for their friendship.

I have also had the pleasure of working with 1/2 people, that is joint Hodgson/Solomon students. Susan Shadle, myself, Kendra Williams, and Erik Wasinger (the newest member) have had joint projects over the past few years. Susan, Kendra, and I have worked closely together building a vacuum chamber and running our first L-edge experiments, as well as discussing the intricacies of ligand field theory and how it relates to our X-ray absorption experiments. By being thrown in the same boat so to speak, we have developed close relationships. I wish Kendra and Erik success in their future experiments and speedy graduate careers!

I want to give a special thanks to my family and friends for supporting and encouraging me over the past 5 (or so) years and for providing the entertainment! Geoff and Sabine Coates, Jane DeWitt, Carl (OhNO) Brown and Susan Shadle, Tom and Lendy Vail, and Erik and Kim Westre have provided breaks away from lab to have a nice dinner, a weekend get-away, a challenging game of ravine ball, and camping trips (you can throw in a few good wedding celebrations too!) - which have been imperative to my sanity. Long live Gila Monsters and Vodka Collins!! My family, Chris and Faye Gansberg, Todd and Julie Gansberg, Wendy and Anthony Reis, Barb and Doug Westre (plus my grandparents, aunts and uncles and cousins), has also provided their share of both relaxing (and rejuvenating) and fun-filled get-aways. In addition, I should acknowledge Star, Belle, Beau, and Cassie, our horses which have had stints at a stable in Portola Valley. They were probably the first to know when I had a frustrating day and I am sure that Sjon was grateful for the stress relief that they provided for me before I got home to him. Lastly, I want to thank Sjon for putting up with me as I experienced the ups and downs of research over the past few years. Having gone through the graduate experience himself, he could rejoice and empathize with me as the situation warranted and he was always there to put things into perspective and encourage me to move forward. I should also thank him for not having me committed during beamtime!

This dissertation is dedicated to all the teachers in my life: first and foremost, my parents, who taught me that anything worth doing is worth doing right; my brother and sister, who encouraged me to have fun (even during the most monotonous tasks); my elementary and high school teachers, who gave me an interest science (especially Charlie Condron and Barb Gallagher); my undergraduate advisor, Peter Kelly, who gave me my first taste of research; my advisors, Ed Solomon and Keith Hodgson, who guided me through my graduate career; Britt Hedman and Pat Frank, who never tired (at least they never told me so) of my endless questions about experimental techniques, data analysis, and metalloprotein chemistry; past and present members of the Hodgson and Solomon labs, who taught me about these things called enzymes and X-ray absorption spectroscopy; and lastly and most importantly my husband, Sjon, who taught me to take research one step at a time, one day at a time and things will get done!

Contents

List of Tables

Chapter 1

Chapter 2

Chapter 3

Chapter 4

Chapter 5

List of Figures

Chapter 1

Chapter 2

Chapter 3

Chapter 4

Chapter 5

List of Abbreviations

1,2-DBD	2,3-dihydroxybiphenyl 1,2-dioxygenase
2,3-CTD	catechol 2,3-dioxygenase
13-HPOD	13(*S*)-hydroperoxy-9,11-(*E,Z*)-octadecadienoic acid
α-KG	α-ketoglutarate
Abs	optical absorption
Asn	asparagine
acac	acetylacetonate (2,4-pentanedionate)
$BIPhMe_2$	2,2'-bis(1-methylimidazolyl)phenylmethoxymethane
BLM	bleomycin
$BzPhMe_2N$	benzyldimethylphenylammonium
CD	circular dichroism
Chel	4-hydroxo-2,6-pyridinedicarboxylate
CS	clavaminate synthase
CT	charge transfer
CVPAH	phenylalanine hydroxylase from *Chromobacterium violaceum*
Dipic	2,6-pyridinedicarboxylate
DNA	deoxyribonucleic acid
DOE	Department of Energy
DW	Debye-Waller
EPR	electron paramagnetic resonance
EDTA	ethylenediaminetetraacetic acid
ENDOR	electron-nuclear double resonance
ESEEM	electron spin echo envelope modulation
EXAFS	extended X-ray absorption fine structure
FeSOD	iron superoxide dismutase
FT	Fourier transform
FWHM	full-width-at-half-maximum
GNXAS	EXAFS data analysis package where g_n stands for *n*-atom distribution function and XAS stands for X-ray absorption spectroscopy
H_4BP	tetrahydrobiopterin
$HB(pz)_3$	hydrotris-1-pyrazolylborate
$HB(3,5\text{-}i\text{Pr}_2\text{pz})_3$	hydrotris(3,5-diisopropyl-1-pyrazolyl)borate

His	histidine
HL	Hedin-Lundqvist
HLO	human lipoxygenase
HPTB	[*N*,*N*,*N*',*N*'-tetrakis(2-benzimidazoylmethyl)-2-hydroxy-1,3-diaminopropane]$^-$
Ile	isoleucine
IPNS	isopenicillin N synthase
LF	ligand field
LLD-ACV	δ-(L-α-aminoadipoyl)-L-cysteinyl-D-valine
LO	lipoxygenase
MCD	magnetic circular dichroism
MLCT	metal to ligand charge transfer
MOPS	3-(*N*-morpholino)propanesulfonic acid
MS	multiple-scattering
NADH	reduced nicotinamide-adenine dinucleotide
NIH	National Institutes of Health
NIR	near infrared
NMR	nuclear magnetic resonance
NSF	National Science Foundation
NSLS	National Synchrotron Light Source
PAH	phenylalanine hydroxylase
PCD	protocatechuate 3,4-dioxygenase
PDO	phthalate dioxygenase
PDR	phthalate dioxygenase reductase
PrpepH	*N*-(2-(4-imidazole)ethyl)pyrimidine-4-carboxamide
RLO	rabbit lipoxygenase
rR	resonance Raman
salen	*N*,*N*'-ethylenebis(salicylideneiminato)
salmp	[2-bis(salicylideneamino)methylphenolate]$^{3-}$
SCF-Xα-SW	self-consistent field-Xα-scattered wave
SLO	soybean lipoxygenase
SS	single-scattering
SSRL	Stanford Synchrotron Radiation Laboratory
TACN	*N*,*N*',*N*''-trimethyl-1,4,7-triazacyclononane
TH	tyrosine hydroxylase

TMC	1,4,8,11-tetramethyl-1,4,8,11-tetraazacyclotetradecane
TPA	tris(2-pyridylmethyl)amine
TPH	tryptophan hydroxylase
Tyr	tyrosine
VTVH	variable temperature, variable field
ωH	ω-Hydroxylase
XAS	X-ray absorption spectroscopy

Chapter 1

Introduction to Mononuclear Non-Heme Iron Enzymes and X-ray Absorption Spectroscopy

1.1. Scope and Organization of this Dissertation

This dissertation focuses on the use of Fe K-edge X-ray absorption spectroscopy (XAS) as a tool in defining the geometric and electronic structure of the iron active sites in mononuclear non-heme iron enzymes. Chapter 1 provides a general introduction to mononuclear non-heme iron enzymes, in particular putting these types of enzymes into functional context with classes of iron proteins. In addition, Chapter 1 contains a brief overview of X-ray absorption spectroscopy, including the information content of both the edge and extended X-ray absorption fine structure (EXAFS) regions. In the course of the last five years, several studies on inorganic iron model complexes have been completed in order to redefine the information content available in the edge and EXAFS regions. These studies are presented in Chapters 2, 3, and 4. Chapter 2 describes the methodology of a new multiple-scattering approach to EXAFS analysis, called GNXAS, and the application of this approach to iron model complexes. GNXAS was also used to obtain angular information for $\{FeNO\}^7$ model complexes (presented in Chapter 3). In Chapter 4, a multiplet analysis of Fe K-edge pre-edge features for iron model complexes of varying oxidation states, spin states, and geometries is presented.

Chapter 5 describes XAS edge and EXAFS studies of the active sites of mononuclear non-heme iron enzymes and $\{FeNO\}^7$ complexes. An overview of the reactions catalyzed by these enzymes, as well as a review of previous structural and mechanistic studies, is given in the first section. The following sections contain the results from individual studies of $\{FeNO\}^7$ complexes, ferrous bleomycin, activated bleomycin, lipoxygenase, phenylalanine hydroxylase, and protocatechuate 3,4-dioxygenase. Each of these sections are divided into parts with an introduction to the enzyme studied, results and analysis of the XAS edge and EXAFS, and a discussion relating the XAS results to those of previous studies. Complementary electron paramagnetic resonance, magnetic circular dichroism, resonance Raman, and optical absorption studies were frequently performed on these enzymes in conjunction with the XAS studies by members of Prof. Ed Solomon's research group. In such cases, the results of the other spectroscopies are discussed for each enzyme in order obtain a more detailed description of the iron active site.

1.2. Mononuclear Non-Heme Iron Enzymes

Metals are commonly found as natural constituents of proteins and nature has learned to use the special properties of metal ions to perform a wide variety of specific functions associated with life processes. Iron is the most abundant transition metal in the Earth's crust and is essential for all plants, animals, and bacteria (with the exception of *Lactobacillus* and some strains of *Bacillus*).[1] Iron can be found in several oxidation states with Fe^{2+} and Fe^{3+} being the most common. The iron can be high spin or low spin in each of these oxidation states depending on the ligand environment. Iron is usually complexed to four, five, or six ligands. Different iron coordination environments alter the reactivity of the iron allowing for a large diversity in protein function. Due to its abundance and versatility, iron is distributed into a variety of proteins with varying biological functions: iron transport, electron transfer, oxygen binding, oxygen activation, and multi-electron reduction. Iron-containing proteins can be classified, based upon the coordination of the iron active site, into heme, iron-sulfur, and non-heme sub-groups.

The most studied class of iron-containing enzymes are the heme proteins. These systems are responsible for oxygen binding, oxygen activation, and multi-electron reduction and include such examples as: hemoglobin, cytochrome P-450, prostaglandin synthase, cytochrome oxidase, and catalase.[2] Hemoglobin is involved in respiration by reversibly binding oxygen in the lungs and transporting it to cells throughout the body. Prostaglandin synthase is a dioxygenase that catalyzes the cyclooxygenase reaction where two dioxygen molecules are inserted into arachidonic acid.[3] Cytochrome P-450 activates dioxygen for monooxygenase chemistry and is thought to involve an oxo-ferryl intermediate, which is believed to be responsible for the oxygen transfer chemistry.[4] Cytochrome oxidase acts as a proton pump across cell membranes requiring four electron reduction from cytochrome *c* to reduce molecular oxygen to water.[5,6] Catalase catalyzes the dismutation of the toxic peroxide byproduct to oxygen and water in the cells of nearly all aerobic organisms. Interestingly enough, all these heme proteins involve the same kind of cofactor in their active site, an iron porphyrin, and a common iron axial imidazole from a histidine residue (except for cytochrome P-450). However, because of a very different structure of the protein and distal environment of the heme, they have clearly different roles and/or catalyze different reactions.

There is another class of proteins which contains iron-sulfur clusters that are involved in electron transfer and storage.[7] Rubredoxin is an electron transfer protein which contains one iron tetrahedrally coordinated to four cysteine sulfurs. Electron storage is accomplished by [2Fe-2S] plant ferredoxins, in which the two iron atoms are tetrahedrally coordinated to four sulfur atoms (two bridging sulfides and two cysteine sulfurs). Rieske centers also perform electron storage, however, they differ from the plant ferredoxins in that one of the two tetrahedrally coordinated irons is ligated to two histidine nitrogens. [4Fe-4S] ferredoxins are low molecular weight proteins which are also involved in oxidation/reduction reactions in substrate metabolism and have a distorted cubane geometry. Iron-sulfur clusters are also found in complex iron-sulfur proteins,[8] such as nitrogenases which are the enzymes responsible for the biological fixation of atmospheric dinitrogen to ammonia.[9] Whereas most iron-sulfur clusters, even when they are found in association with enzyme activities, play essentially the role of electron transport, at least one case is known where an iron-sulfur protein catalyzes a chemical reaction. This is aconitase, which transforms citrate to isocitrate in the Kreb's cycle, catalyzing successive reactions of dehydration and rehydration. When purified aerobically from beef heart mitochondria, aconitase is obtained in an inactive [3Fe-4S] form which can be activated with Fe^{2+} under reducing conditions to give a [4Fe-4S] cluster.[8]

It is important to realize that there are also large number of ***non-heme iron enzymes*** which perform reactions similar to those of the heme enzymes involving oxygen binding, oxygen activation, four-electron reduction, and disproportionation. The non-heme iron enzymes can be subdivided into binuclear and mononuclear classes. For the binuclear proteins, the nature of the oxo or hydroxy bridge appears to play a key role in the catalytic mechanisms.[10,11] Hemerythrin is an oxygen carrier protein analogous to hemoglobin, methane monooxygenase catalyzes the conversion of methane to methanol, and ribonucleotide reductase reduces ribonucleotides to deoxyribonucleotides in the first committed step in DNA synthesis. Finally, the mononuclear non-heme iron enzymes, which are the focus of this dissertation, are an extensive class of iron proteins which do not have the dominant structural features of the above proteins (the heme ligand, iron-sulfur bonds, or oxo bridges) and are thus the least well understood. Several recent reviews describe in detail the current understanding of the structure and mechanistic function of these non-heme iron enzymes.[12-15]

Mononuclear iron enzymes are involved in a variety of important biological functions requiring dioxygen. These enzymes are classified according to the types of reactions catalyzed: dismutation, oxidation, monooxygenation, dioxygenation, hydroperoxidation, and DNA cleavage. The dioxygenases may be further subdivided into extra- and intradiol dioxygenases, *cis*-dihydroxylases, and pterin- and α-ketoglutarate-dependent hydroxylases. The latter two systems incorporate one oxygen atom from dioxygen into substrate and one into the organic cofactor and are thus formally dioxygenases. Specific enzyme reactions from each class are given in Table 5.1 in Chapter 5. Briefly, iron superoxide dismutase is one of three superoxide dismutases that catalyze the dismutation of superoxide ions to oxygen and hydrogen peroxide.[16] Isopenicillin N synthase is an oxidase which is unusual in that it catalyzes the four-electron oxidative double ring closure of its substrate which is the key step in the biosynthesis of penicillins.[17] The hydroxylation of fatty acids and alkanes and the epoxidation of alkenes using molecular oxygen are catalyzed by ω-hydroxylase.[18] Several different types of dioxygenases are involved in the bacterial degradation of aromatic rings. The final ring cleavage in the degradation of aromatic rings (breakdown of a catechol) is catalyzed by the extra- and intradiol dioxygenases (*e.g.*, catechol 2,3-dioxygenase and protocatechuate 3,4-dioxygenase, respectively) which exhibit fundamental differences in structure and reactivity.[13,19] Prior to this reaction, conversion of an unactivated aromatic to the *cis*-dihydrodiol is required and is catalyzed by the *cis*-dihydroxylase phthalate dioxygenase and related enzymes.[20] Phenylalanine hydroxylase, one of the three pterin-dependent hydroxylases, catalyzes the hydroxylation of phenylalanine to tyrosine.[21] A deficiency in this enzyme is responsible for the genetic disorder phenylketonuria that is associated with severe mental retardation. Clavaminate synthase is an α-ketoglutarate-dependent hydroxylase which catalyzes the key biosynthetic ring closure step in the formation of clavulanic acid, a potent β-lactamase inhibitor.[22] This type of inhibitor is important since bacterial resistance to penicillin antibiotics is largely due to the hydrolytic activity of the β-lactamase enzymes. The lipoxygenases catalyze the hydroperoxidation of *cis,cis*-1,4-pentadiene-containing fatty acids. Mammalian lipoxygenases catalyze the conversion of arachidonic acid to leukotrienes, which mediate hypersensitiviy and inflammation, and lipoxins, which inhibit cellular immunity.[23] Bleomycin is a non-heme iron glycopeptide that reversibly binds and activates oxygen for hydrogen atom abstraction which is similar to heme chemistry (cytochrome P-450)[24,25] but involves a different oxygen intermediate. Bleomycin is used as an anti-cancer agent due to its ability to selectively cleave DNA. More detailed mechanistic and structural information for these enzymes is presented in Chapter 5.

Both ferrous and ferric oxidation states have been determined to be involved in catalysis for the different mononuclear non-heme iron enzymes, and substrate- and oxygen-bound intermediates have been observed for several of these enzymes. Much less is known about the active sites in these enzymes relative to heme systems as the non-heme iron centers are less spectroscopically accessible particularly in the ferrous oxidation state. This is due to the fact that non-heme ferrous active sites are generally high spin S=2 non-Kramers systems and, therefore, do not have an EPR signal. Also, these non-heme ferrous active sites do not have ligand-to-metal charge transfer transitions in a spectroscopically accessible region. For high spin ferric systems the d—>d transitions, which are powerful probes of active site geometric and electronic structure, are spin forbidden. Only ligand—>metal charge transfer transitions are observed. Fortunately, X-ray absorption spectroscopy is ideally suited for studying dilute metal proteins and the information obtainable from the iron active site is not dependent on the oxidation state or spin state of the iron as in other spectroscopies.

1.3. X-ray Absorption Spectroscopy

1.3.1. General Background

X-ray absorption spectroscopy (XAS) involves the measurement of the absorption coefficient, μ, as a function of energy.[26] A typical X-ray absorption spectrum (Figure 1.1) exhibits a decreasing absorption as the photon energy is increased with a sharp discontinuity, called an absorption edge, superimposed on the smooth background. An absorption edge occurs when the incident photon has sufficient energy to promote a core electron to unoccupied valence orbitals or to the continuum. Thus, the edge occurs at a characteristic threshold energy which is specific to the absorbing atom. Edges are named according to the Bohr atomic level from which the photoionized electron originates. Hence, a K-edge refers to the ionization of a 1s electron, a L_1 edge to the ionization of a 2s electron, *etc*. The data in this dissertation were measured at the Fe K-edge where the ionization of a 1s electron requires ~7130 eV.

XAS spectra can be divided into several regions (Figure 1.1). In the pre-edge and edge region the incident energy is below the ionization threshold. This region contains transitions from core levels to unoccupied or partially occupied atomic and molecular orbitals localized on the absorbing atom, as well as to localized and delocalized continuum levels.[27] These features occur below or are superimposed on the rising edge. Throughout this dissertation, features which are at energies well-separated from the onset of the edge will be referred to as pre-edge features, while those transitions which actually overlap the rising edge intensity will be called edge or rising-edge features. At X-ray energies above the threshold for ionization, electrons are promoted into the continuum. The oscillations in this region are known as extended X-ray absorption fine structure (EXAFS) and result from interference between the photoelectron wave propagating from the absorbing atom and the wave back scattered by neighboring atoms.[28] There is an

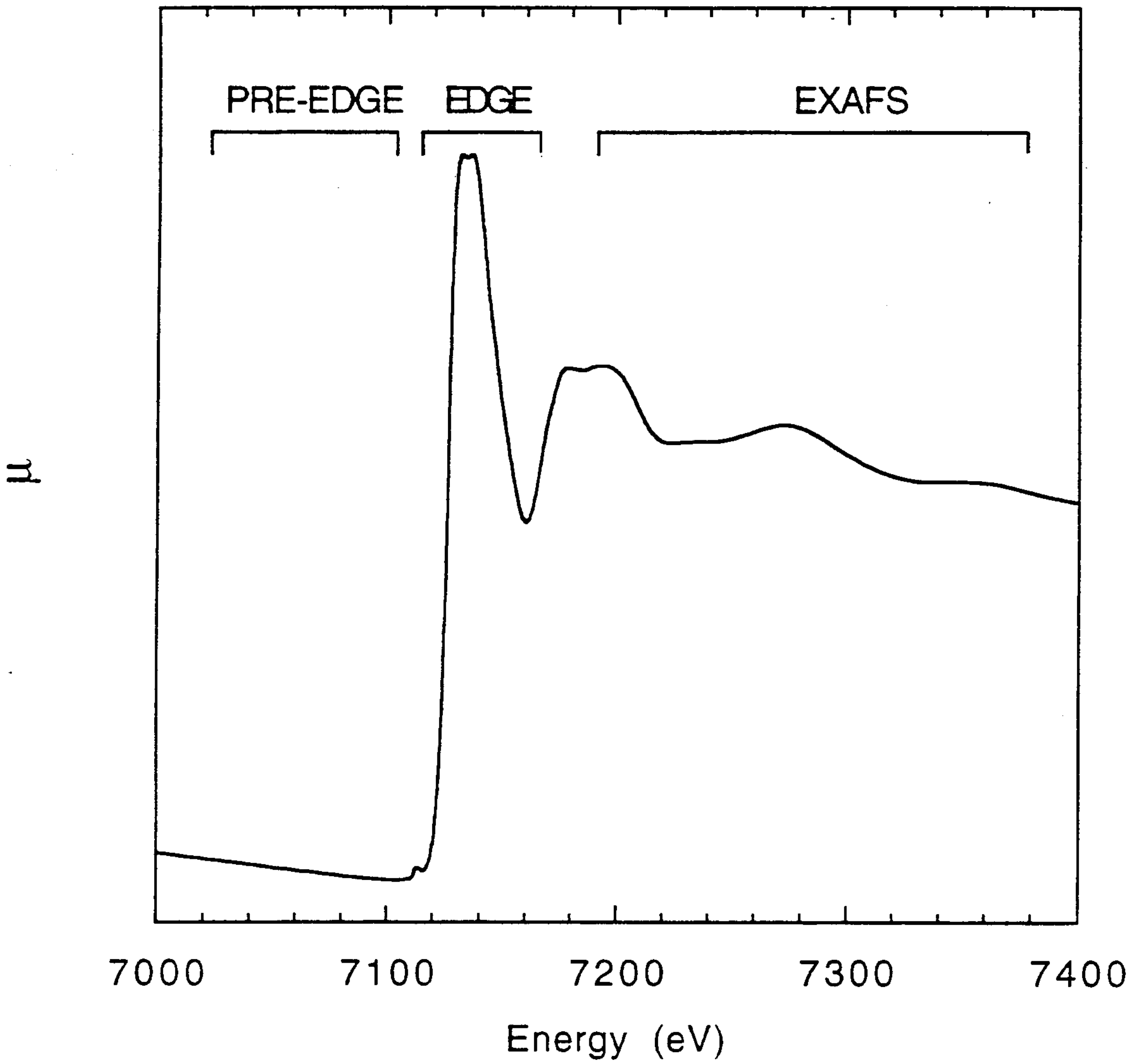

orbitals localized on the absorbing atom, as well as to localized and delocalized continuum levels.[27] These features occur below or are superimposed on the rising edge. Throughout this dissertation, features which are at energies well-separated from the onset of the edge will be referred to as pre-edge features, while those transitions which actually overlap the rising edge intensity will be called edge or rising-edge features. At X-ray energies above the threshold for ionization, electrons are promoted into the continuum. The oscillations in this region are known as extended X-ray absorption fine structure (EXAFS) and result from interference between the photoelectron wave propagating from the absorbing atom and the wave back scattered by neighboring atoms.[28] There is an increase in the absorption if the scattered wave is in phase with the outgoing photoelectron wave, or a decrease in the absorption if the scattered wave is out of phase with the outgoing photoelectron wave.

Although edge structure and EXAFS have different physical origins, they contain complementary information about the absorbing atom and its environment. Absorption features in the pre-edge and edge regions are sensitive to the local electronic and geometric environment of the absorbing atom. Analysis of the position and relative intensities of the absorption edge features can reveal details about the absorbing atom's site symmetry, oxidation state, and the nature of the surrounding ligands. Interpretation of the phase, amplitude, and frequency of the EXAFS oscillations can provide information about the type, number, and distances of the atoms in the vicinity of the absorber. XAS is ideally suited for studying the local electronic and geometric structure of metal active sites in metalloproteins. With the advent of synchrotron radiation sources, which provide X-ray fluxes many orders of magnitude higher than those previously obtainable with conventional X-ray tubes, XAS data can be collected on very dilute metalloproteins in a reasonable amount of time. Since XAS does not depend on long-range order, samples in any physical state can be studied. Even without long-range order, EXAFS provides very detailed metrical information about the local environment of the absorber (within ~4 Å of the absorber). Interatomic distances can be determined with an accuracy typically of ±0.02 Å or better with the accuracy in coordination numbers being about 25%.[29]

1.3.2. Experimental Considerations

The design of a basic X-ray absorption experiment is presented in Figure 1.2. Synchrotron radiation provides a polychromatic source of X-ray energies. The X-ray beam, which is highly vertically collimated, is further defined vertically and horizontally by a pair of slits and then energy resolved with a double-crystal monochromator. After passing through a set of tantalum slits that minimize scatter, the incident intensity is measured with a gas-filled ionization chamber (nitrogen is used at the Fe K-edge). There are two basic configurations for a standard XAS experiment: transmission and fluorescence. Transmission mode is used for concentrated samples, such as solid model complexes, where the absorption of the sample is determined by measuring the X-ray intensity before and after the sample using ionization chambers (I_0 and I_1 in Figure 1.2). Fluorescence mode is used for dilute samples, where the fluorescence signal emitted as the excited nucleus relaxes after photoionization is measured at 90° from the incident

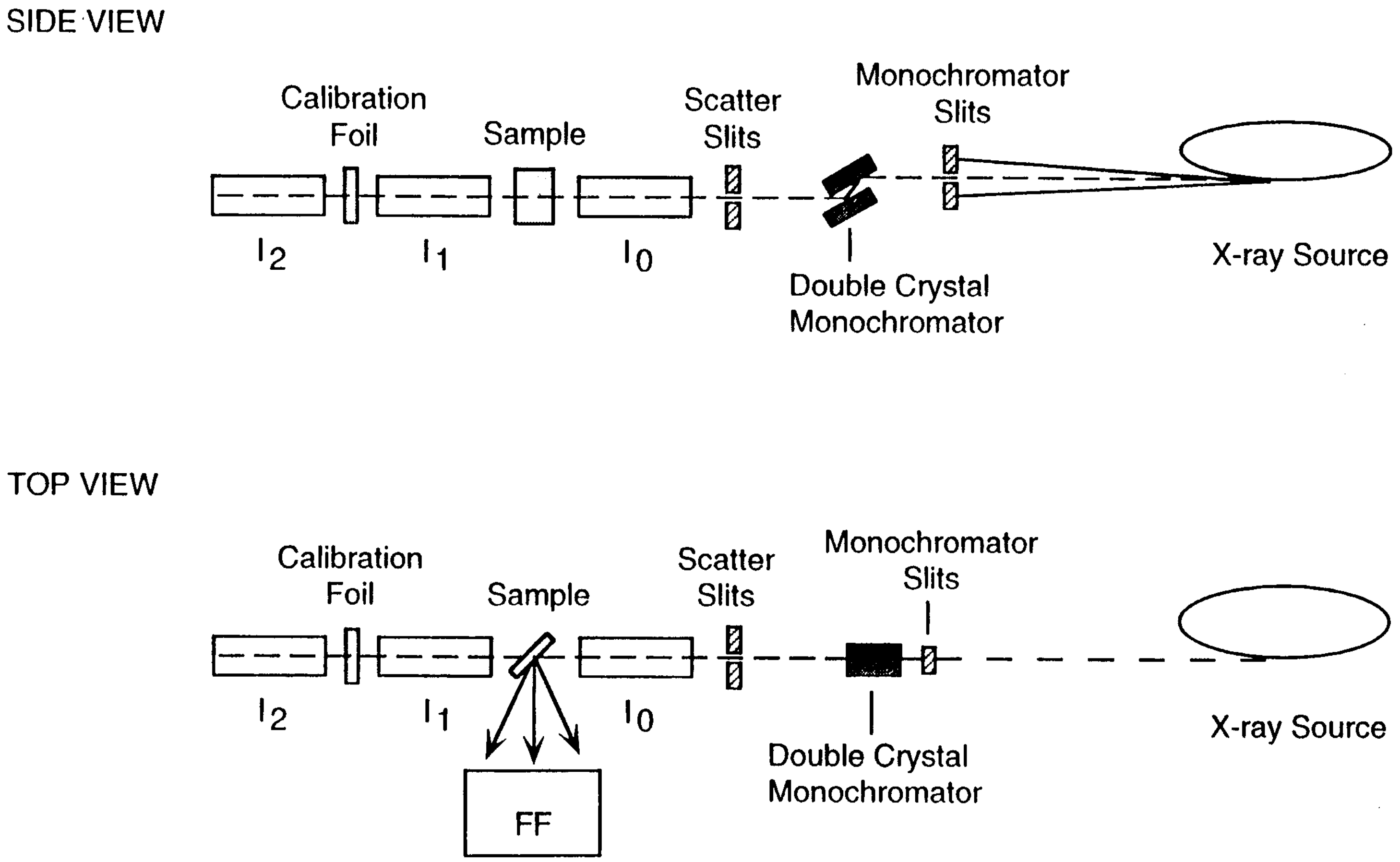

Figure 1.2. A typical hard X-ray experimental set-up (side and top views) for transmission and fluorescence measurements.

X-ray beam (FF in Figure 1.2). In both configurations, the transmitted or fluorescence intensity is ratioed by the incident intensity to correct for any X-ray beam instabilities and for the continuous decay of intensity with decreasing ring current. Internal energy calibration for each scan is achieved by placing an Fe foil after I_1 followed by a third ionization chamber, I_2. Thus, the transmitted intensity of the Fe foil is measured simultaneously with that of the sample.

A primary consideration in XAS data collection is the energy resolution of the experiment. For a given monochromator, the resolution is controlled through the use of the defining slits placed before the monochromator and the choice of monochromator crystals. For the experiments in this dissertation, the slits were set to optimize the spectral resolution at a vertical height of 1 mm (unless otherwise stated). By defining the vertical height of the beam to be 1 mm, the experimental resolution is determined by the intrinsic resolution of the monochromator and the core-hole lifetime of the absorber.[30] The resolution is also, in principle, affected by mirrors in the optical path of the beam. The experiments described herein were performed on beam lines where no mirrors were present or were used in such a way that the degradation of resolution did not occur. At the Fe K-edge, using 1 mm pre-monochromator defining slits and a Si(220) double-crystal monochromator, the resolution is about 1.4 eV.[30] A more detailed discussion of all the factors to be considered in XAS data collection can be found in references 30-33 .

1.3.3. Edge Theory and Analysis

Edge structure consists of absorption bands superimposed on the steeply rising continuum absorption caused by transitions of core electrons to discrete bound valence levels. The bound state transitions in the pre-edge and edge region can be interpreted using the X-ray absorption cross-section, σ, given in equation 1.1,[34]

$$\sigma = c\left|\left\langle \phi_f \middle| \hat{O} \middle| \phi_i \right\rangle\right|^2 \qquad (1.1)$$

where c is a constant, $\hat{O}$ is the transition moment operator, and ϕ_f and ϕ_i are the final and initial state wavefunctions, respectively. Pre-edge and edge features are governed primarily by electric dipole selection rules ($\Delta\ell = \pm 1$). The intensity of these features, then, is related to the density of the final states of the appropriate symmetry which have measurable overlap with the initial state wavefunction. Based on a dipole-coupling mechanism, the features in a K-edge spectrum reflect transitions from a core 1s orbital to p-type final states.

XAS spectra of first row transition metal complexes typically have a weak pre-edge feature ~10 eV below the rising edge.[35] This was attributed to the 1s—>3d transition, as spectra of Zn^{2+} (a $3d^{10}$ system) do not have this feature.[36] The 1s—>3d transition is electric dipole forbidden, however, it gains intensity through an allowed quadrupole mechanism and by 4p mixing into the 3d orbitals due to a noncentrosymmetric iron site. An Fe K-edge spectrum typically has a very weak pre-edge feature at ~7112 eV due to the 1s—>3d transition (Figure 1.1). It has been observed that the intensity of this feature increases with decreasing coordination number.[37,38] Decreasing the coordination number distorts the iron site, allowing for 4p mixing into the 3d orbitals, which increases the intensity of the pre-edge feature. A detailed analysis of the energy splittings and intensity pattern of the 1s—>3d pre-edge feature can give information on the spin state, oxidation state, and geometry of the iron site (see Chapter 4).

The abrupt increase in the absorption coefficient at ~7125 eV in an Fe K-edge spectrum is attributed to the electric dipole allowed 1s—>4p transition (Figure 1.1). The energy of the rising edge is dependent on the effective nuclear charge of the iron.[35-37,39-41] An atom with a higher effective nuclear charge has a deeper core level and, thus, a higher photon energy is need to ionize the core electron. On this basis, the position of the edge can be related to the oxidation state of the iron, to a first approximation. Further, for complexes of the same oxidation state, variations in edge energies can be related to differences in the covalency of the ligands. However, one must keep in mind that there are numerous factors that influence the effective nuclear charge including the formal oxidation state of the metal and the number and type of coordinating ligands.

1.3.4. EXAFS Theory and Analysis

1.3.4.1. Information Obtainable from EXAFS. EXAFS spectroscopy is an invaluable technique for investigating the local coordination environment of specific atomic species in systems ranging from metalloproteins[31,42] to catalysts.[43,44] The method is sensitive to short-range order (distances typically within about 4-5 Å of the absorber) and provides information on: 1) the distances to a neighboring atom, 2) the numbers of neighboring atoms, and 3) the types of neighboring atoms. EXAFS has the advantages of focusing on particular atoms and of being applicable to any physical state, including liquid or frozen solutions and amorphous solids. However, the analysis of EXAFS data requires accurately known experimental or theoretical pairwise phase and amplitude functions. Experimental standards have been widely used to extract reliable amplitude and phase functions and used with success to obtain structural information from EXAFS data, particularly for nearest neighbors.[29,31,32] Alternatively, reliable theoretical phases and amplitudes have recently become available that enable more information, including angular distribution, to be obtained from EXAFS analysis.[45-50]

The empirical data-analysis technique[29,31,32] involves the use of phase and amplitude parameters which have been extracted from the EXAFS data of a suitable model complex. The empirical technique allows for the determination of first neighbor distances with high accuracy (typically ± 0.02 Å) but determines with less accuracy the coordination number (one atom in 4 or 5) and the identity of the ligating atoms (not differentiating ± 1 or 2 in Z). The empirical approach is of questionable utility for atoms beyond ~3 Å because of phase and amplitude transferability problems. A break down of the phase and amplitude transferability occurs because of intervening atoms that give rise to multiple-scattering (MS) signals. These MS signals can contribute significantly to the total EXAFS signal and very often interfere with the single-scattering (SS) signal. Moreover, it can be difficult to obtain suitable models for extraction of reliable empirical amplitudes and phases. As a result of these limitations, determination of distances beyond the first coordination shell and of bond angles has been difficult using empirically-derived phase and amplitude parameters.

The alternative to the empirical data-analysis technique is the theoretical technique,[45-50] where the phase and amplitude functions are calculated theoretically. Thus, the reliability of the result is determined by the accuracy of the theory. In this approach, an expected theoretical signal is calculated assuming a structural model for the system under study. The resulting signal is then fit to the experimental data, varying structural and non-structural parameters until a minimum of a selected reliability function is reached. The quality of the fit is determined by visual inspection of EXAFS and Fourier transform (FT) residuals. The theoretical approach is advantageous to the empirical approach in that MS contributions can be modeled and, therefore, bond distance and bond angle information from distant shells of atoms can be determined. Also a theoretical approach is not dependent upon obtaining suitable model compounds to extract phase and amplitude parameters.

1.3.4.2. Single-Scattering Process. This section includes a brief theoretical description of the single-scattering process along with the type of information that can be obtained from a single-scattering analysis. EXAFS results from the interference between the outgoing photoelectron wave from the photoabsorber with the backscattered waves from surrounding atoms (Figure 1.3). The interference generated by each surrounding

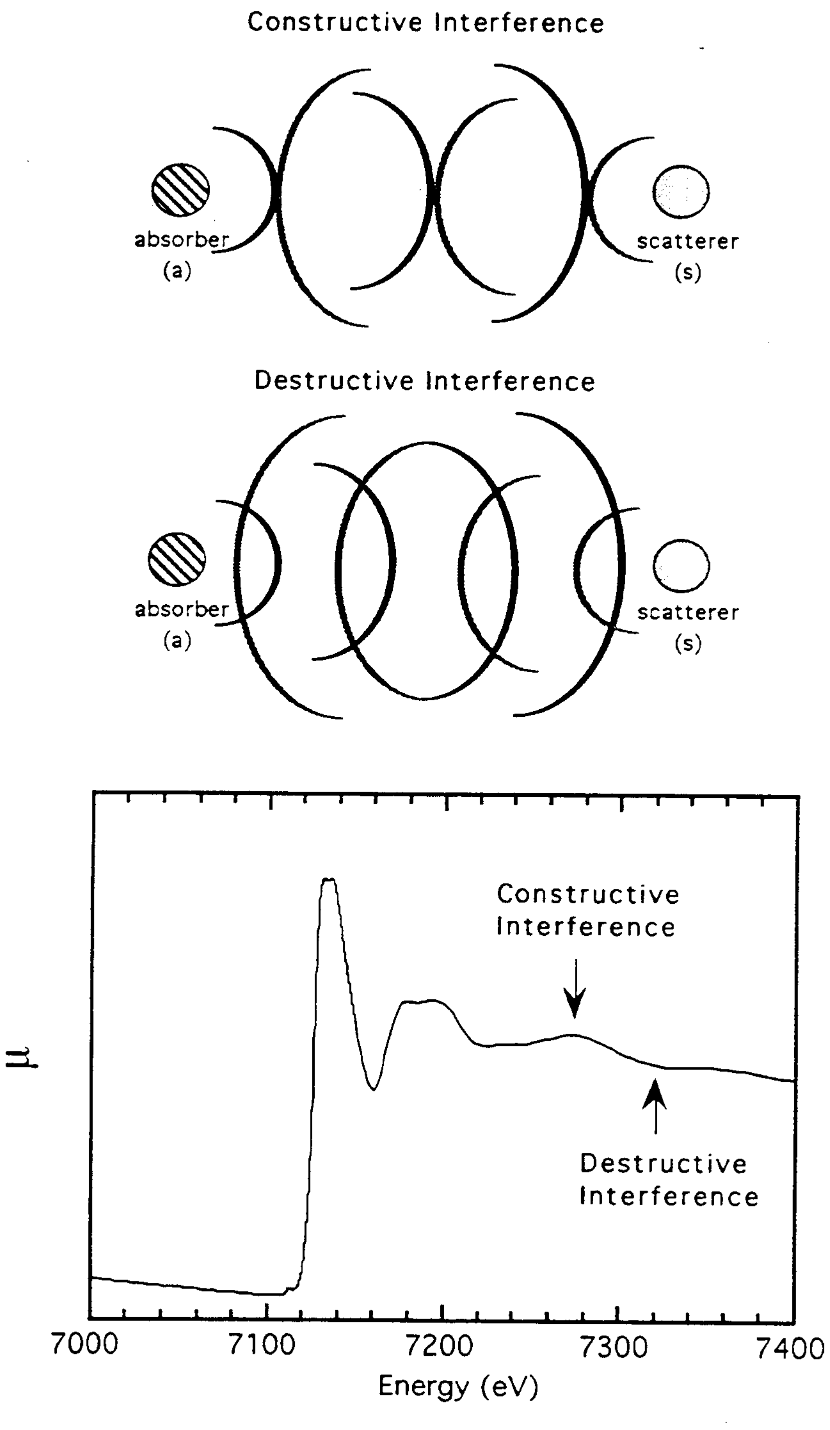

Figure 1.3. Diagram of photoelectron waves generated by X-ray absorption of the absorber. In the top case, the outgoing photoelectron wave constructively interferes with the backscattered wave resulting in a maximum in the absorption coefficient. At slightly higher energy, the outgoing photoelectron wave destructively interferes with the backscattered wave resulting in a minimum in the absorption coefficient.

(scattering) atom contributes a damped sine wave to the overall EXAFS spectrum, where each sine wave can be described by three measurable quantities: frequency, amplitude, and phase. These three observables contain structural information about the nature and location of the scattering atom. The frequency of the sine wave is a measure of the distance between the absorbing atom and the scattering atom, the amplitude of the sine wave is a measure of the number of scattering atoms, and the phase of the sine wave is indicative of the identity of the scattering atom.

EXAFS, denoted here by χ, is the relative modulation of the absorption coefficient, μ, of a particular atom compared to the smooth background absorption coefficient, μ_S, normalized by the absorption coefficient μ_O that would be observed for the free atom. Thus, as defined in reference [51],

$$\chi = \frac{\mu - \mu_s}{\mu_o} \qquad (1.2)$$

Since $\mu_S \equiv \mu_O$, the EXAFS may alternatively be defined by $\chi = (\mu - \mu_O)/\mu_O$ or $(\mu - \mu_S)/\mu_S$. It is now conventional to plot χ versus the photoelectron wave vector, k,

$$k = \left[\left(\frac{2m}{\hbar^2}\right)(E - E_0)\right]^{1/2} \qquad (1.3)$$

where E_0 is the threshold energy for liberation of a photoelectron wave.

The complete mathematical derivation of the single-scattering EXAFS equation is presented in references [51] and [52]. The resultant theoretical single-scattering expression for χ is given by:

$$\chi(k) = \sum_s \frac{N_s |f_s(\pi,k)|}{kR_{as}^2} \exp\left(-R_{as}/\lambda_f\right) \exp(-2\sigma_{as}^2 k^2) \sin[2kR_{as} + \alpha_{as}(k)] \qquad (1.4)$$

where a description of the variables is given in Table 1.1.

Table 1.1. Description of the Variables in the Single-Scattering Expression for χ.

symbol	units	definition
N_S	---	the number of atoms in a shell
$\lvert f_S(\pi,k)\rvert$	---	the inherent backscattering amplitude for this type of scattering atom
R_{as}	Å	the distance between the absorbing atom and the scattering atom
λ_f	Å	the mean free path for inelastic scattering of the photoelectron
σ_{as}^2	Å^2	the rms deviation of R_{as} ($\exp(-2\sigma_{as}^2 k^2)$ is referred to as the Debye-Waller factor)
$\alpha_{as}(k)$	---	the inherent backscattering phase shift for this absorbing atom/scattering atom combination

Equation 1.4 expresses the EXAFS, $\chi(k)$, as a sum of damped sine waves with each term within the summation consisting of an amplitude term, an exponential damping term (Debye-Waller factor) and a sine function to describe the (quasi-periodic) behavior of the EXAFS. The EXAFS for any absorbing atom/scattering atom pair can be represented a damped sine wave with the amplitude ($[N_s|f_s(\pi,k)|\exp(-2\sigma_{as}^2k^2)\exp(-R_{as}/\lambda_f)]/[k(R_{as}^2)]$), frequency ($2R_{as}$), and phase shift ($\alpha_{as}(k)$) characteristic of the atoms involved. The R_{as}^{-2} dependence makes the EXAFS of long-distance shells much weaker than that from nearby atoms. Thus, only atoms within a radius of ~4-5 Å of the absorbing atom contribute significant scattering to the EXAFS. This fall-off of EXAFS amplitude at high R_{as} also has a contribution from inelastic losses of the photoelectron which are more serious for longer distances. This is usually treated by defining a mean free path for the photoelectron, λ_f, and incorporating the $\exp(-R_{as}/\lambda_f)$ term in the equation. Within a shell of scattering atoms, there is some variation in R_{as}, which may be static (a spread in the *a-s* distances from structural distortion or site heterogeneity) or dynamic (due to a stretching vibration in the *a-s* bond). This variation leads to a damping of the EXAFS oscillations which is physically described by σ_{as}^2, a root-mean-square (rms) deviation in the distance R_{as}. The vibrational portion of σ_{as}^2 has a characteristic temperature dependence. It should be noted that the derivation of this expression for χ[51,52] involves a number of approximations that break down at low k values, *i.e.* close to the absorption edge. Therefore, most plane wave single-scattering EXAFS analyses only use the data for $k > 4$ Å^{-1}.

EXAFS data analysis requires accurately known experimental or theoretical absorber/scatterer pair phase and amplitude parameters, $|f_s(\pi,k)|$ and $\alpha_{as}(k)$, respectively. To obtain distances from EXAFS data it is necessary to know the phase shift $\alpha_{as}(k)$. Empirical methods for obtaining phase shifts involve the fitting the EXAFS of a known structure with $\sin[2kR_{as} + \alpha_{as}(k)]$. Typically, $\alpha_{as}(k)$ is parameterized as a quadratic function, $a_0 + a_1k + a_2k^2$, where each of these parameters are optimized in the fitting of the EXAFS of a structure with known R_{as}.[29,31,32] The phase shift parameters are then fixed, and the EXAFS of an unknown structure is fit by varying R_{as}. In a large number of cases this procedure has been shown to yield distances with an accuracy better than 0.03 Å. Alternatively, $\alpha_{as}(k)$ can be calculated from first principles.[53] As can be seen in equation 1.4, the EXAFS amplitude depends on the number of scatterers, N_s, as well as R_{as}, k, $|f_s(\pi,k)|$, and σ_{as}^2. Since R_{as} is obtained from the frequency of the EXAFS and k is known, calculation of the number of scatterers from EXAFS is possible if $|f_s(\pi,k)|$ and σ_{as}^2 are known. The two approaches towards EXAFS amplitude have been: 1) to parameterize $|f_s(\pi,k)|$ and $\exp(-2\sigma_{as}{}^2k^2)$ together and neglect variations in thermal motion in the fits[29,31,32] or 2) to use theoretical values for $|f_s(\pi,k)|$ and to vary both the Debye-Waller factor and the number of scatterers.[54]

1.3.4.3. Multiple-Scattering Process. Thus far only the plane wave single-scattering theory of EXAFS has been discussed. This treatment ignores the possibility that the photoelectron might encounter two (or more) scattering atoms in its "round trip" back to the photoabsorber, as seen in Figure 1.4. A proper analysis of such multiple-scattering processes would enable metrical information to be obtained on second and third shell neighbors. Of particular interest would be the ability to obtain angular information. Multiple-scattering processes cannot by studied with the traditional empirical data analysis approach since the MS effects are incorporated within the empirical parameter approach in such a way that the phase and amplitude parameters reflect the exact geometry of the model compound and cannot be transferred to an unknown of different geometry. Thus, there has been concentrated effort in the last fifteen years to obtain an accurate theoretical approach, so that the multiple-scattering processes can be analyzed properly and exploited.

Multiple-scattering effects in EXAFS can become especially important when atoms are arranged in an approximately collinear array (A-B-C angle > 150°). In such cases, the outgoing photoelectron is strongly forward scattered by the intervening atom, resulting in significant amplitude enhancement. This effect was first observed when theoretical calculations of EXAFS were compared with measurements on copper metal.[52,55] The observed amplitude of the scattered wave for the fourth copper shell was larger than the amplitude calculated from single-scattering theory, and the observed phase shift was off by approximately π from the calculated phase shift. These discrepancies were explained as an effect of first-shell atoms that intervene directly in the absorber-to-scatterer path to the fourth-shell atoms in the face-centered cubic lattice. Rather than occluding the EXAFS from the fourth-shell atoms as might have been expected, the intervening atoms actually accentuate the EXAFS of the shadowed atoms by enhanced forward scattering of both the outgoing and backscattered photoelectron waves. These MS effects also cause additional phase shifts. Multiple-scattering effects have also been observed in many inorganic π-acceptor complexes, where di- or triatomic ligands (*e.g.* CO, CN^-, NCS^-) are linearly bound to the absorbing transition metal.[31,56-59] For example, in $[Mo(NCS)_6]^{3-}$ the amplitude of the carbons and sulfurs of the isothiocyanate ligands are distinctly enhanced in the Fourier transform spectrum.[29] In the case of $Mo(CO)_6$ the amplitude of the oxygen shell is even larger than that of the carbon shell in dramatic contrast to the "normal" $1/R_{as}{}^2$ falloff in the EXAFS amplitude.[29]

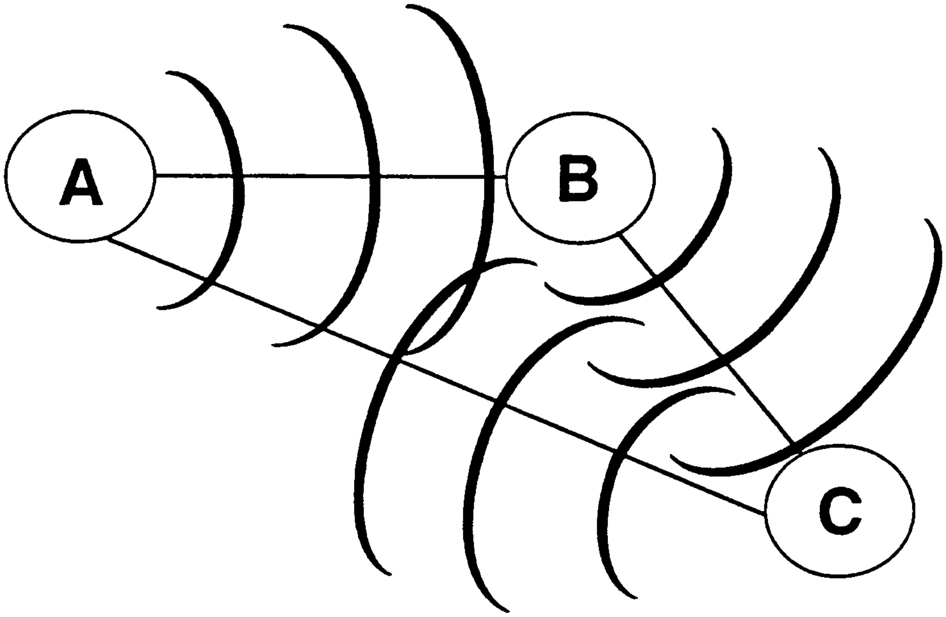

Figure 1.4. A multiple-scattering pathway for a photoelectron generated by X-ray absorption by atom A in the presence of two scattering atoms, B and C. The scattering pathway indicated is A-B-C-A. The multiple-scattering contribution to the EXAFS depends on the distances involved and the A-B-C angle.

Once the effects of multiple-scattering were observed, new EXAFS analysis methods were formulated to take into account multiple-scattering effects. Inclusion of MS contributions could in principle improve the accuracy of the EXAFS analysis and make it possible to exploit the strong angular dependence of multiple-scattering terms. Teo theoretically calculated scattering amplitude and phase functions at various A-B-C scattering angles and assessed the relative importance of various MS pathways as the scattering angle varied.[59] There are three scattering pathways for a three atom A-B-C system (Figure 1.4) where each pathway originates and terminates at the absorbing atom A. Pathway I is the direct backscattering from atom A to C and back. Pathway II is the multiple-scattering via atom B and around the triangle in either direction and pathway III is the multiple-scattering via atom B in both outgoing and incoming trips. When the A-B-C bridging angle is small (~100°) the three pathways are resolvable in a FT of the EXAFS data and can be analyzed separately. When the bridging angle is large (>150°), pathway III is dominant and signified by an amplitude enhancement in the EXAFS. Co and coworkers exploited these effects and studied a series of oxygen-bridged iron complexes.[60] The analysis showed that it was possible to estimate the bridging angle to ±8° and calculate the metal-metal distances to within ±0.05 Å. However, both of these studies indicated that angle determination by EXAFS was only possible when outer-shell peaks are well-resolved in the FT and can be correctly identified. Such cases are infrequent, especially for unknown systems. Thus, a more generally applicable multiple-scattering EXAFS analysis method was needed.

Recently, the proper theoretical formulation of the photoabsorption process has allowed for such a theoretical MS data analysis approach. Currently, there are three widely used theoretical data analysis packages that are capable of computing multiple-scattering processes as well as single-scattering processes . The GNXAS approach (where g_n stands for the n-body distribution function and XAS stands for X-ray absorption spectroscopy) was developed as an integrated theoretical approach to the analysis of EXAFS data.[45] The program EXCURVE was developed at Daresbury.[46] The program FEFF,[47,50] developed at the University of Washington, Seattle, initially was only capable of calculating single-scattering processes, however, later versions incorporated multiple-scattering (FEFF5).[48,49] Chapter 2 of this dissertation presents a detailed description of the GNXAS methodology and then reports the application of GNXAS to iron model complexes. An analysis of the multiple-scattering pathways in $\{FeNO\}^7$ complexes using GNXAS is given in Chapter 3.

1.4. References

(1) *Bioinorganic Catalysis*; Reedijk, J., Ed.; Marcel Dekker, Inc.: New York, 1993.

(2) *Heme Proteins*; Eichorn, G. L.; Marzilli, L. G., Ed.; Elsevier Science Publishing Co., Inc.: New York, 1988; Vol. 7.

(3) Mansuy, D.; Battioni, P. In *Bioinorganic Catalyis*; Reedijk, J., Ed.; Marcel Dekker Inc.: New York, 1993; pp 395.

(4) *Cytochrome P-450: Structure, Mechanism, and Biochemistry*; Ortiz de Montellano, P. R., Ed.; Plenum Press: New York, 1986.

(5) Babcock, G. T.; Wikström, M. *Nature* **1992**, *356*, 301.

(6) Malmström, B. G. *Chem. Rev.* **1990**, *90*, 1247.

(7) *Iron-Sulfur Proteins*; Spiro, T. G., Ed.; John Wiley & Sons: New York, 1982; Vol. 4.

(8) *Inorganic Chemistry of Iron Metabolism*; Crichton, R. R., Ed.; Ellis Horwood Limited: Chichester, 1991.

(9) Evans, D. J.; Henderson, R. A.; Smith, B. E. In *Bioinorganic Catalysis*; Reedijk, J., Ed.; Marcel Dekker, Inc.: New York, 1993; p 89.

(10) Sanders-Loehr, J. In *Iron Carriers and Iron Proteins*; Loehr, T. M., Ed.; VCH Publishers, Inc.: New York, 1989; Vol. 5; p 373.

(11) Brown, C. B.; Remar, G. J.; Musselman, R. L.; Solomon, E. I. *Inorg. Chem.* **1995**, *34*, 688.

(12) Solomon, E. I.; Zhang, Y. *Acc. Chem. Res.* **1992**, *25*, 343.

(13) Que, L., Jr. In *Bioinorganic Catalysis*; Reedijk, J., Ed.; Marcel Dekker, Inc.: New York, 1993; p 467.

(14) Feig, A. L.; Lippard, S. J. *Chem. Rev.* **1994**, *94*, 759.

(15) Solomon, E. I.; Pavel, E. G.; Loeb, K. E.; Campochiaro, C. *Coord. Chem. Rev.* **1995**, in press.

(16) Stoddard, B. L.; Howell, P. L.; Ringe, D.; Petsko, G. A. *Biochemistry* **1990**, *29*, 8885.

(17) Baldwin, J. E.; Bradley, M. *Chem. Rev.* **1990**, *90*, 1079.

(18) Katopodis, A. G.; Wimalasena, K.; Lee, J.; May, S. W. *J. Am. Chem. Soc.* **1984**, *106*, 7928.

(19) Lipscomb, J. D.; Orville, A. M. In *Metals in Biological Systems*; Sigel, H.; Sigel, A., Eds.; Marcel Dekker Inc.: New York, 1992; Vol. 28; p 243.

(20) Batie, C. J.; Lahaie, E.; Ballou, D. P. *J. Biol. Chem* **1987**, *262*, 1510.

(21) Shiman, R. In *Folates and Pterins: Chemistry and Biochemistry of Pterins*; Blakley, R. L.; Benkovic, S. J., Ed.; John Wiley and Sons: New York, 1985; Vol. 2; p 179.

(22) Salowe, S. P.; Marsh, E. N.; Townsend, C. A. *Biochemistry* **1990**, *29*, 6499.

(23) Samuelsson, B.; Dahlén, S.-E.; Lindgren, J. Å.; Rouzer, C. A.; Serhan, C. N. *Science* **1987**, *237*, 1171.

(24) Stubbe, J.; Kozarich, J. W. *Chem. Rev.* **1987**, *87*, 1107.

(25) Petering, D. H.; Byrnes, R. W.; Antholine, W. E. *Chem.-Biol. Interactions* **1990**, *73*, 133.

(26) *X-ray Absorption: Principles, Applications, Techniques of EXAFS, SEXAFS and XANES*; Koningsberger, D. C.; Prins, R., Eds.; John Wiley and Sons Inc.: New York, 1988.

(27) Bianconi, A. In *X-ray Absorption: Principles, Applications, Techniques of EXAFS, SEXAFS and XANES*; Koningsberger, D. C.; Prins, R., Eds.; John Wiley and Sons Inc.: New York, 1988; p 573.

(28) Stern, E. A. In *X-ray Absorption: Principles, Applications, Techniques of EXAFS, SEXAFS and XANES*; Koningsberger, D. C.; Prins, R., Eds.; John Wiley and Sons Inc.: New York, 1988; p 1.

(29) Cramer, S. P.; Hodgson, K. O.; Stiefel, E. I.; Newton, W. E. *J. Am. Chem. Soc.* **1978**, *100*, 2748.

(30) Lytle, F. W. In *Applications of Synchrotron Radiation*; Winick, H.; Xiam, D.; Ye, M.-h.; Huang, T., Eds.; Gordon and Breach Science Publishers: New York, 1989; p 135.

(31) Cramer, S. P.; Hodgson, K. O. *Prog. Inorg. Chem.* **1979**, *25*, 1.

(32) Scott, R. A. *Meth. Enzymol.* **1985**, *117*, 414.

(33) Heald, S. M. In *X-ray Absorption: Principles, Applications, Techniques of EXAFS, SEXAFS and XANES*; Koningsberger, D. C.; Prins, R., Eds.; John Wiley and Sons Inc.: New York, 1988; p 87.

(34) Agarwal, B. K. *X-ray Spectroscopy*; Springer-Verlag: New York, 1979.

(35) Srivastava, U. C.; Nigam, H. L. *Coord. Chem. Rev.* **1973**, *9*, 275.

(36) Shulman, R. G.; Yafet, Y.; Eisenberger, P.; Blumberg, W. E. *Proc. Natl. Acad. Sci. USA* **1976**, *73*, 1384.

(37) Roe, A. L.; Schneider, D. J.; Mayer, R. J.; Pyrz, J. W.; Widom, J.; Que, L., Jr. *J. Am. Chem. Soc.* **1984**, *106*, 1676.

(38) Randall, C. R.; Shu, L.; Chiou, Y.-M.; Hagen, K. S.; Ito, M.; Kitajima, N.; Lachicotte, R. J.; Zang, Y.; Que, L., Jr. *Inorg. Chem.* **1995**, *34*, 1036.

(39) Cramer, S. P.; Eccles, T. K.; Kutzler, F. W.; Hodgson, K. O. *J. Am. Chem. Soc.* **1976**, *98*, 1287.

(40) Wong, J.; Lytle, F. W.; Messmer, R. P.; Maylotte, D. H. *Phys. Rev. B.* **1984**, *30*, 5596.

(41) Kau, L.-S.; Spira-Solomon, D. J.; Penner-Hahn, J. E.; Hodgson, K. O.; Solomon, E. I. *J. Am. Chem. Soc.* **1987**, *109*, 6433.

(42) Cramer, S. P. In *X-ray Absorption: Principles, Applications, Techniques of EXAFS, SEXAFS and XANES*; Koningsberger, D. C.; Prins, R., Eds.; John Wiley and Sons Inc.: New York, 1988; p 573.

(43) Lytle, F. W.; Via, G. H.; Sinfelt, J. H. In *Synchrotron Radiation Research*; Winick, H.; Doniach, S., Eds.; Plenum Press: New York, 1980; Chp. 12.

(44) Iwasawa, Y. *Tailored Metal Catalyst*; D. Reidel Publishing Co.: Dordrecht, 1986.

(45) Filipponi, A.; Di Cicco, A.; Tyson, T. A.; Natoli, C. R. *Solid State Commun.* **1991**, *78*, 265.

(46) Binsted, N.; Campbell, J. W.; Gurman, S. J.; Stephenson, P. C. SERC Daresbury Laboratory EXCURVE 92 program, 1991.

(47) Rehr, J. J.; Mustre de Leon, J.; Zabinsky, S. I.; Albers, R. C. *J. Am. Chem. Soc.* **1991**, *113*, 5135.

(48) Rehr, J. J.; Albers, R. C.; Zabinsky, S. I. *Phys. Rev. Lett.* **1992**, *69*, 3397.

(49) Rehr, J. J. *Jpn. J. Appl. Phys.* **1993**, *32*, 8.

(50) Mustre de Leon, J.; Rehr, J. J.; Zabinsky, S. I.; Albers, R. C. *Phys. Rev. B* **1991**, *44*, 4146.

(51) Stern, E. A. *Phys. Rev. B* **1974**, *10*, 3027.

(52) Ashley, C. A.; Doniach, S. *Phys. Rev. B* **1975**, *11*, 1279.

(53) Lee, P. A.; Teo, B.-K.; Simons, A. L. *J. Am. Chem. Soc.* **1977**, *99*, 3856.

(54) Shulman, R. G.; Eisenberger, P.; Teo, B.-K.; Kincaid, B. M.; Brown, G. S. *J. Mol. Biol.* **1978**, *124*, 305.

(55) Lee, P. A.; Pendry, J. B. *Phys. Rev. B* **1975**, *11*, 2795.

(56) Filipponi, A.; Di Cicco, A.; Zanoni, R.; Bellatreccia, M.; Sessa, V.; Dossi, C.; Psaro, R. *Chem. Phys. Lett.* **1991**, *184*, 485.

(57) Binsted, N.; Cook, S. L.; Evans, J.; Greaves, G. N.; Price, R. J. *J. Am. Chem. Soc.* **1987**, *103*, 3669.

(58) Binsted, N.; Evans, J.; Greaves, G. N.; Price, R. J. *J. Chem. Soc., Chem. Comm.* **1987**, 1130.

(59) Teo, B.-K. *J. Am. Chem. Soc.* **1981**, *109*, 3990.

(60) Co, M. S.; Hendrickson, W. A.; Hodgson, K. O.; Doniach, S. *J. Am. Chem. Soc.* **1983**, *105*, 1144.

Chapter 2

GNXAS,
a New Multiple-Scattering EXAFS Analysis Package, and Its Application to Iron Inorganic Model Complexes

2.1. Introduction

Extended X-ray absorption fine structure (EXAFS) spectroscopy is a valuable technique for investigating the local coordination environment of specific atomic species in systems ranging from metalloproteins[1,2] to catalysts.[3-5] The method is sensitive to short-range order (distances typically within about 3-5 Å of the absorber) and provides information on the distances to, numbers of, and types of neighboring atoms. EXAFS has the advantages of being able to focus on a selected type of atom and of being applicable to any physical state, including liquid or frozen solutions and amorphous solids. However, the analysis of EXAFS data requires accurately known experimental or theoretical pairwise phase and amplitude functions. Experimental standards have been widely used to extract reliable empirical amplitude and phase functions and these have been used with success to obtain structural information from EXAFS data, particularly for nearest neighbors. Alternatively, reliable theoretical phases and amplitudes have recently become available that enable more information, including angular distributions, to be obtained from EXAFS analysis.

The empirical data analysis technique[1,2,6,7] involves the use of pairwise phase and amplitude functions which have been extracted from the EXAFS data of suitable model complexes. The empirical technique allows for the determination of first neighbor distances with high accuracy (typically ± 0.02 Å) but determines with less accuracy the coordination number (one atom in four or five) and the identity of the ligating atoms (not differentiating ± 2 in Z). The empirical approach is of questionable utility for atoms beyond ~3 Å because of phase and amplitude transferability problems. A breakdown of the phase and amplitude transferability occurs because of intervening atoms that give rise to multiple-scattering (MS) signals. These MS signals can contribute significantly to the total EXAFS signal and very often interfere with the single-scattering (SS) signal. The MS effects are particularly evident when an intervening atom lies in a close-to-linear relationship with the absorber and a more distant scatterer, as occurs, for example, in Fe-oxo dimers[8] and metal carbonyls.[2,9-12] Multiple-scattering effects can also be quite prominent for certain rigid ligands such as imidazoles and porphyrins[13,14] and can be of such magnitude that they dominate over SS signals even in structures that are not collinear (*vide infra*). Moreover, it can be difficult to obtain suitable models for extraction of reliable pairwise empirical amplitudes and phases because of the requirement for single well-ordered coordination shells that are separated from other EXAFS contributions. As a result of these limitations, determination of distances beyond the first coordination shell and of bond angles has been difficult using empirically-derived phase and amplitude functions.

An alternative to the empirically-based EXAFS data analysis is to calculate the phase and amplitude functions theoretically. In this approach, an expected theoretical signal is calculated assuming a structural model for the system under study. The resulting signal is then fit to the experimental data, varying the input parameters until a minimum of a selected reliability function is reached. The quality of the fit is further determined by inspection of EXAFS and Fourier transform (FT) residuals. The theoretical approach is advantageous relative to the empirical approach in that MS contributions can be modeled and therefore bond distance and bond angle information from distant shells of atoms can in principle be determined. Also a theoretical approach is not dependent upon obtaining suitable model compounds to extract pairwise phase and amplitude functions. While the reliability of the results are limited by the accuracy of the theory, it is becoming clear that accuracy comparable to that available with the empirical technique is now possible as illustrated by this work and that published in some of the references cited below.

The GNXAS approach (where g_n stands for the n-atom distribution function and XAS stands for X-ray absorption spectroscopy) has recently been developed as an integrated theoretical approach to the analysis of EXAFS data.[15-17] Three distinctive features of the integrated GNXAS approach in comparison with other existing analysis packages (FEFF5[18,19] and EXCURVE[20]) are: (1) an improved solution for the one-particle Green's function equation with complex optical potential of the Hedin-Lundqvist type in the muffin-tin approximation (from which the total photoabsorption cross section is calculated), (2) SS and MS signals are classified according to the appropriate n-atom distribution function with proper treatment of the configurational average of MS terms, and (3) the fit to the experimental spectrum is performed by comparing directly in energy space the raw data with a global model absorption coefficient that includes the structural signal, the edge jump normalization, the post-edge background, and if present, shake-up/shake-off edges, so that the structural signal is optimized together with other components of the absorption spectrum. Since GNXAS is able to calculate all the signals relating to two-, three-, and four-atom correlation functions with the proper treatment of correlated distances and Debye-Waller factors, it is particularly well-suited for the analysis of MS effects and for bond angle determination. GNXAS has been initially used on several simpler systems (including SiX_4, X = F, Cl, and CH_3,[21] $Os_3(CO)_{12}$,[9] Br_2 and HBr,[22] and brominated hydrocarbons[23]) and more recently on a complex polynuclear metal cluster.[24]

In this chapter, the background and brief theoretical description of the GNXAS methodology is presented, along with a description of the GNXAS programs and their use for analysis of molecular systems. The GNXAS methodology is followed by its specific application to three iron coordination complexes.[25] These complexes were chosen to investigate the characteristics, advantages, and limitations of the method, in particular in the study of MS effects in chemical systems. Further, this detailed analysis enables an accurate error assessment by examining the variance between crystallographically known and EXAFS-determined metrical details.

The GNXAS method was applied to Fe K-edge EXAFS data for $Fe(acac)_3$, $Na[Fe(OH_2)EDTA]$, and $K_3Fe(CN)_6$ (where acac = acetylacetonate and EDTA = ethylenediaminetetraacetic acid). The applicability and utility of the GNXAS method was determined by studying the MS effects in the EXAFS data and evaluating the reliability of structural parameters (bond distances and angles) obtained from GNXAS. The study of the magnitude and complexity of MS contributions in the EXAFS data of $Fe(acac)_3$ was of particular interest since $Fe(acac)_3$, due to the regularity of its structure, has been widely used to extract both Fe-O and second shell Fe-C phase and amplitude backscattering parameters for empirical EXAFS analysis. The empirical Fe-O backscattering parameters have been used quite successfully to model first-shell iron-oxygen distances and coordination numbers in many iron-containing models and enzymes,[26-29] while the use of the Fe-C second shell backscattering parameters has met with much more limited success[26,29] due to MS contributions. MS effects are incorporated within the empirical approach in such a way that the phase and amplitude parameters reflect the exact geometry of the model compound and cannot be transferred to an unknown of different geometry. The GNXAS technique was also applied to $Na[Fe(OH_2)EDTA]$ to test the ability of GNXAS to interpret the EXAFS data for a lower-symmetry compound with mixed ligation, such complexes being a better approximation to the situation typically found in metalloenzymes, where the GNXAS approach can prove especially valuable in EXAFS data analysis. Finally, the EXAFS data of $K_3Fe(CN)_6$ was analyzed in detail with GNXAS to study the MS behavior of the linear Fe-C-N unit and to evaluate the use of this analytical approach for angle determination of small molecules liganded to transition metals. The results of these three applications together establish the validity and reliability of GNXAS as an approach for EXAFS data of chemical systems. Given this, the technique may be used to analyze unknown systems, as further elaborated in Chapter 3.

It should be noted here that other groups have developed analysis packages similar in concept to GNXAS. The program EXCURVE, developed at Daresbury, is probably the oldest.[20] The program FEFF,[30,31] developed at the University of Washington, Seattle, came later, roughly at the same time as GNXAS, initially with the possibility of calculating single scattering only, then including multiple scattering in later versions (FEFF5).[18,19] The relationship of these programs to GNXAS shall be briefly discussed in the course of the methodology presentation which follows.

2.2. GNXAS Methodology

2.2.1. Background

Until relatively recently, the lack of a proper theoretical formulation of the photoabsorption process has limited the use of theoretical functions for reliable analysis of EXAFS data. It was necessary to obtain a correct mathematical description of the spherical wave propagation of the photoelectron through the system (in an inner core photoabsorption process the photoelectron is created in an eigenstate of the angular momentum operator or a definite mixture of them) and to use an appropriate optical potential in describing this propagation. Early plane-wave SS theories[32] failed even in the high energy limit[33] and had to be replaced with MS theories with spherical wave propagation.[34-39] It was also realized that the "universal" atomic potentials used to calculate standard theoretical amplitudes and phases were not sufficiently reliable because the electrostatics was not modeled correctly. Therefore, it was necessary to construct a realistic charge density on and around the photoabsorber, as is done in band theory calculations. The Mattheiss[40] prescription of overlapping neutral atom charge densities provided charge densities that are acceptably close to those obtained by self-consistent procedures. The Coulomb, exchange and correlation potentials could then be calculated from this cluster charge density.

Additionally, in the statistical interpretation, the local density approximation of the Hedin-Lundqvist[41,42] (HL) exchange-correlation potential proved to be a good starting point for the photoelectron optical potential. The HL exchange-correlation potential takes into account the energy dependence of the exchange and correlation (Coulomb) hole around the propagating electron in the dispersive (real) part and has an imaginary part capable of reproducing the observed electron mean-free path in metals and semiconductors.[43] The optical potential could be approximated by the self-energy of a uniform interacting electron gas with a density given by the local density of the system. In the spirit of this statistical approximation, Lee and Beni[44] extended the HL potential, which was initially devised to describe exchange and correlation corrections to the

Coulomb potential due to the valence charge only, to the atomic core. When put in context with other components of MS theory correctly formulated in presence of a complex effective potential, this statistical potential proved to be a good starting point for the photoelectron optical potential.[30,45–47] The effect of the intrinsic inelastic channels has not been included in the theory. However, a reasonable estimate of the size of this effect on the amplitude of the EXAFS signal is less than 10% of the total signal, which is acceptable.

Another important aspect for a correct EXAFS analysis is the proper description of structural correlations in a system and the possibility of doing configurational averages. EXAFS has an almost unique advantage over other structural techniques in that it can probe atomic correlation functions of order greater than two, *i.e.* position correlations of more than two atoms at a time. In fact, diffraction techniques only probe the pair correlation function, since the technique is based on the weak coupling between the probe (X-rays, neutrons) and the system under study. The double scattering events of the probe which would allow access to higher order correlations are generally negligible. This is not the case with EXAFS, in that the primary probe (the photon) couples weakly enough with matter so that the simple "golden rule" is sufficient to describe the photoabsorption cross section. However, the secondary probe, *i.e.* the emitted photoelectron, can couple strongly with the atoms of the system so that in addition to SS, MS becomes quite detectable and exploitable in many cases. This feature is shared by other techniques that use electrons either as a secondary probe (as in photoelectron diffraction) or as a primary probe (as in low energy electron diffraction). A good description of the dynamical strong coupling of the electron and matter is not easy to obtain, but once this is achieved, the next step is to have a general method for describing geometric structural correlations. Since the MS series is known to converge slowly, it can be resummed in such a way that the interrelation between the dynamic and the structural parts of the theory is transparent (while at the same time improving the convergence rate). In GNXAS this has been accomplished by summing together all the terms in the series referring to the same set of atoms in all their equivalent configurations with respect to the photoabsorber. This sum is done so as to treat all the MS signals relating to definite structural configurations together to give the various *n*-atom correlation functions.[15–17,45–49] This involves a topological structural analysis that is done on the chemical structure under study. Moreover, an efficient way to perform proper thermal or structural configurational averages, using probability distributions that are either chosen *a priori* or conveniently parameterized, has been devised in this integrated approach to EXAFS analysis.[50]

2.2.2. GNXAS Theoretical and Analytical Approach

Before discussing how the GNXAS package functions, it is useful to present a brief derivation of the photoabsorption cross section for a cluster of atoms in physical terms. It will serve to define concepts, to give an intuitive feeling of what is actually going on in the process, and provides the background for understanding the angle-dependent aspects of MS and how they can be used to obtain geometric information.

In an absorption measurement, the emitted photoelectron is not detected, rather the total number of created holes (the total cross section) is measured. This is equivalent to integrating over all the photoemitted electrons. The integration process suppresses all the electron paths that do not come back to the photoabsorber so that the observed modulations of the absorption coefficient are due to the interference (constructive or destructive according to the photoelectron energy) between the outgoing and returning photoelectronic waves. Only electrons in the completely relaxed (elastic) channel with the maximum available kinetic energy $E = \omega - I_C$ contribute to the effect. Therefore, in studying the modulations in the absorption coefficient, the propagation of the coherent electrons can be described through the introduction of an effective optical potential. In this way a truly many-body problem can be reduced to an effective and tractable one-electron problem. The total many-body absorption cross section can be written as[45]

$$\sigma_{mb}(E) = S_{in}(E)\sigma_e(E) \qquad (1)$$

where $\sigma_e(E)$ is the one-electron absorption cross section in the elastic channel, calculated with the optical potential, and $S_{in}(E)$ describes the inelastic channels. Examples of inelastic channels are the shake-up or shake-off double-electron excitations.[51] These may need to be taken into account since they can distort the EXAFS signal. Notice that in this approach $\sigma_e(E)$ includes the many-body amplitude reduction factor S_o2.[30,45]

As mentioned earlier, the construction of the one-electron optical potential, although in principle feasible, is very difficult. The one-electron optical potential should take into account both the extrinsic and intrinsic effects and their interference. Moreover, the potential needs to be simple and versatile enough to describe the many varied situations encountered in practical applications. On the basis of statistical considerations, it has been found that the HL potential[41,42] is a good starting point for approximating the optical potential.[30,45-47] In this approximation, the optical potential is complex. Its imaginary part $\Gamma(E)$ gives rise to a finite lifetime that describes the attenuation of the photoelectron wave in the elastic coherent channel due to the possibility of inelastic excitations of the system. Therefore, the optical potential acts as a medium that diffracts the coherent electron wave with its real part and attenuates it via the imaginary part.

The attenuation process has the consequence that the actual size of the system probed by a photoelectron with wave vector k and kinetic energy $E = k^2$ reduces to a sphere around the photoabsorber with a radius roughly equal to the mean-free path $\lambda(E)$ of the electron probe at that energy. The mean free path is linked to the imaginary part of the optical potential $\Gamma(E)$ through the relation[52,53]

$$\lambda(E)(au) = \frac{k(au)^{-1}}{\Gamma(E)(Ryd)} \quad \text{or equivalently} \quad \lambda(E)(\mathring{A}) = \frac{E}{\Gamma(E)}\frac{1}{k(\mathring{A})^{-1}} \tag{2}$$

In a one-electron picture it is necessary to start from the description of the potential associated with a cluster of atoms. Since in the statistical approximation the HL potential depends on the local density of the system under study, as does the Coulomb potential, a rapid and efficient way of generating such a density has to be devised. As mentioned before, the Mattheiss[40] prescription of overlapping neutral atom charge densities present in the molecular cluster is able to generate charge densities that are acceptably close to those obtained by self-consistent procedures. At this point, a further approximation is made to the charge density to simplify the solution of the one-electron Schrödinger equation. After partitioning the cluster space into touching spheres around the atoms, an outer sphere encircling all the cluster and an interstitial region in between, one spherically averages the charge density inside the atomic spheres and calculates an averaged charge density in the interstitial region. The potential is set to a constant in this latter region. This approximation is likely to distort the calculated signal within ~30 eV of the absorption edge, but its effects diminish quite rapidly with increasing energy.

Having constructed the potential, the derivation of the one-electron photoabsorption cross section $\sigma_e(E)$ in eq 1 follows from the application of MS theory. The main results relevant to the present discussion are summarized here. The reader is referred to the Appendix in reference 25 for a more detailed derivation. The equation for $\sigma_e(E)$ can be written as

$$\sigma_e(E) = \sigma_0^l(E)\left[1 + \chi^l(E)\right] \tag{3}$$

where $\sigma_0^l(E)$ is the final state l, dipole-allowed, atomic absorption cross section for the photoabsorbing atom and $\chi^l(E)$ represents the contribution due to the other atoms in the cluster. GNXAS uses an improved solution for the one-particle Green's function equation with complex potential in the muffin-tin approximation, from which the photoabsorption cross section is calculated. In this scheme the total cross section can be written as the sum of two contributions, the first one having the form of an "atomic" cross section relative to the muffin-tin sphere of the photoabsorber, the second one being the contribution coming from the neighboring scatterers. However the latter does not factorize into an "atomic" cross section times a dimensionless structure signal, as is the case with a real potential, therefore the structural signal which appears in eq 3 has to be defined as the ratio of the two contributions. This is different from that used in other codes. In most cases, this difference is negligible over almost the entire EXAFS spectrum but it may affect the amplitude of the structural signal in the low-energy part of the spectrum. For more details on this point the reader is referred to reference 45, eq 3.8 - 3.12. In the region of convergence of the MS series the structural term $\chi^l(E)$ can be expressed as[45]

$$\chi^l(E) = \sum_{n=2}^{\infty} \chi_n^l(E) = \sum_{n=2}^{\infty} \sum_{p_n} \Im A_{p_n}^l(E; R_{ij}^{p_n}) \tag{4}$$

where each $\chi_n^l(E)$ term represents the contribution originating from processes in which the excited photoelectron is scattered n-1 times by the surrounding atoms before returning to the photoabsorber. Each $\chi_n^l(E)$ term is obtained by taking the imaginary part ($\Im$) of the scattering amplitudes $A_{p_n}^l(E; R_{ij}^{p_n})$ relative to all the individual paths p_n of order n that involve at most n atoms, including the photoabsorber. The functional form of the contribution of any path p_n is of the type (see Appendix in reference 25)

$$A_n^l(\kappa; R_{ij}^{p_n}) \sin[\kappa R_{p_n}^{tot} + \phi(\kappa; R_{ij}^{p_n})] \tag{5}$$

where $R_{p_n}^{tot}$ is the total length of the path and $A_n^l(\kappa; R_{ij}^{p_n})$ and $\phi(\kappa; R_{ij}^{p_n})$ are, respectively, the amplitude and the phase of the signal associated with it. Due to the use of the optical complex potential *V(r)* the amplitude of the path contains a damping factor which (in the Wentzel-Kramers-Brillouin (WKB) approximation for the potential phase shifts) can be written as

$$\exp[-\Im \oint_{p_n} dr \sqrt{k^2 - V(r)}] \tag{6}$$

where the integral is taken along the closed path of the photoelectron. Therefore the longer the path, the more heavily its contribution is damped. Notice that the complex nature of the central atom phase shift has also been taken into account. In contrast, Lee and Beni[44] and Teo[12] only take into account the complex nature of the phase shifts for the backscattering atoms. These authors also only use the plane-wave approximation for the spherical wave propagators. On the basis of eqs 3-5 the absorption cross section consists of the superposition of various oscillating signals of different amplitudes and periods onto a more or less smooth background given by the atomic absorption. The most important contributions coming from the various paths should be summed, and the resulting signal should be compared to the observed spectrum. However, the criterion of assessing the importance of the various contributions according to the number of scattering events, as suggested by the expansion in eq 4, is not of general validity since in some cases paths running along the same atoms with a different number of scattering events might contribute signals of similar strength. As presented in more detail in the Appendix in reference 25, this might occur because the expansion parameter for the MS series, which is given by $|f(\theta)/(\kappa R)|$ where R is the typical nearest neighbor interatomic distance in the system, has a peculiar behavior as a function of the scattering angle θ. In fact, even at moderately high energies (≥ 200 eV) this quantity falls off quite rapidly from values on the order of unity in a forward cone of aperture ~20° to values typically on the order of less than 0.1. This behavior leads to the so-called "focusing effect", whereby forward scattering events enhance rather than depress the corresponding signal. In the case of a collinear path involving three sites o, i and j at distance R from each other, the ratio of the triple-scattering signal to the double scattering one is $2|f(0)/(\kappa R)|$. Therefore the amplitude of the fourth order path is nearly twice that of the third order which in turn is twice that of second order SS. At lower energies, the scattering becomes more isotropic and $|f(\theta)/(\kappa R)|$ may attain sizable values (~0.2-0.4) for $\sim 30^\circ < \theta < 180^\circ$, as illustrated in Figure 2.1, so that the rate of convergence of the MS series is slower.

From these considerations, it is evident that the rate of convergence of the MS series is controlled by an interplay between (a) the strength of the scattering, which depends on the energy, (b) the number of scattering events and the angles at which the scattering events occur (c) the electron damping, which in turn depends on the energy, the length of the path, and the types of atoms along the path and d) the degeneracy of the various paths. As mentioned in the Background section above, an efficient way to cope with this situation and one that improves the rate of convergence of the MS series is to sum together up to infinite order (or to the necessary order to get convergence) all the terms which refer to the same set of atoms in all their equivalent configurations with

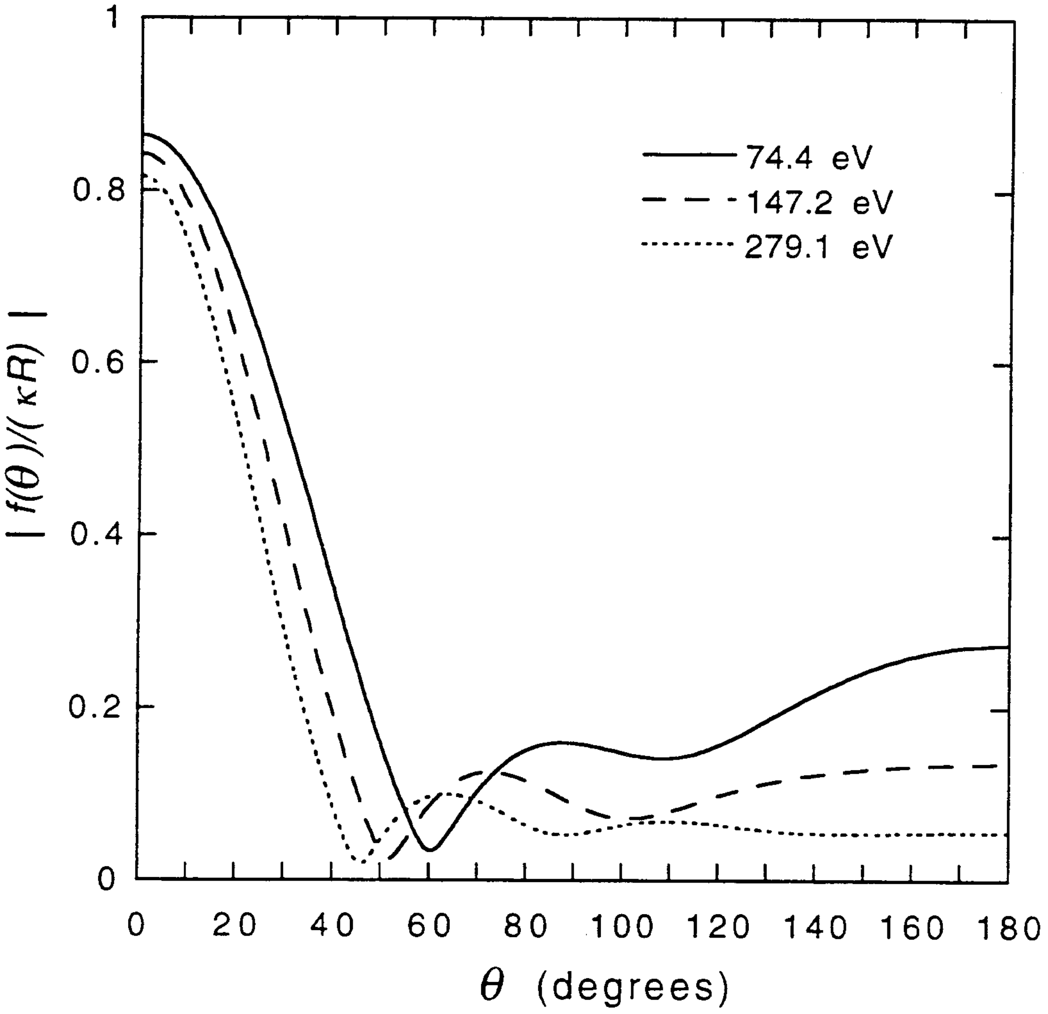

Figure 2.1. Plot of the expansion parameter $|f(\theta)/(\kappa R)|$ as a function of the scattering angle θ at different energies using the oxygen phase shifts and the Fe-O distance R = 1.99 Å for an Fe-O-C scattering pathway. The quantity $|f(\theta)/\kappa|^2$ is the effective scattering cross section for the excited photoelectron impinging onto the O atom at an angle θ away from the incoming Fe-O direction. From inspection of the behavior of this function, it is clear that forward scattering directions are enhanced by factors of 3 - 4. Notice that with this definition of the scattering angle θ the Fe-O-C angle is $180^\circ-\theta$. This latter angle ($180^\circ-\theta$) is the one used throughout this chapter for defining the bond angle in a triangle, besides the two short sides.

respect to the photoabsorber, starting with pairs of atoms, then triplets, quadruplets, and so on.[15-17,48,49] The cut-off distance which limits the size of the model cluster, and therefore the number of structural configurations to be taken into account, can be deduced by inspecting the FT of the experimental absorption spectrum under consideration. A topological structural analysis of the cluster will then provide all the relevant configurations whose path lengths are less than the chosen cut-off distance.

On the basis of these considerations, the structural term, in eq 3, related to a cluster of N atoms with the photoabsorber in site o can be rewritten as[15-17,48,49]

$$\chi^{l}(E)=\sum_{i=1}^{N-1}\gamma^{(2)}_{(o,i)}+\sum_{i=1}^{N-1}\sum_{j>1}^{N-1}\gamma^{(3)}_{(o,i,j)}+\sum_{i=1}^{N-1}\sum_{j>i}^{N-1}\sum_{k>j}^{N-1}\gamma^{(4)}_{(o,i,j,k)}+\ldots=\gamma^{(2)}+\gamma^{(3)}+\gamma^{(4)}+\ldots \qquad (7)$$

where $\gamma^{(2)}{}_{(o,i)}$, $\gamma^{(3)}{}_{(o,i,j)}$, and $\gamma^{(4)}{}_{(o,i,j,k)}$ are the proper two-atom, three-atom, and four-atom signals associated with configurations of two (o,i), three (o,i,j), and four (o,i,j,k) atoms, respectively. The idea here is to sum all the MS signals that refer to the same subclusters of atoms.

In general, the $\gamma^{(n)}$ signals can be defined through the terms of the MS series. For example, in the case of a two-atom signal involving atoms o (photoabsorber) and i

$$\gamma^{(2)}=\chi_{2}^{oio}+\chi_{4}^{oioio}+\chi_{6}^{oioioio}+\chi_{8}^{oioioioio}+\ldots O(\chi_{10}) \qquad (8a)$$

where the leading term is the SS process with obvious meaning of the superscripts. Similarly for a $\gamma^{(3)}$ signal involving sites o, i, and j one has

$$\gamma^{(3)}=2\chi_{3}^{oijo}+2\chi_{4}^{oiojo}+\chi_{4}^{oijio}+\chi_{4}^{ojijo}+\ldots O(\chi_{5}) \qquad (8b)$$

where the coefficients count the time reversal degeneracy of the paths. Usually $\gamma^{(2)}$ and χ_2 differ very little since the higher order MS contributions are very small, thus the $\gamma^{(2)}$ signal often is referred to as the SS contribution. However $\gamma^{(3)}$ and $2\chi_3$ can be quite different due to the sizable contributions from the higher order terms.

For higher-order $\gamma^{(n)}$ signals, only the terms $\chi_m(E)$, with $m \geq n$, appear in the infinite summation. Higher-order terms are meaningful only when the MS series converges (see Appendix in reference 25). Nevertheless, the n-body $\gamma^{(n)}$ signals can be defined independently. In a system with only two atoms, the $\gamma^{(2)}$ signal coincides with the total structural term χ (E). For such a system, one can carry out the matrix inversion of eq A12 of the Appendix in reference 25.

For a triplet of atoms (*o,i,j*), the proper three-atom signal is defined by subtracting the lower-order terms

$$\gamma^{(3)}_{(o,i,j)} = \chi^{(o,i,j)} - \gamma^{(2)}_{(o,i)} - \gamma^{(2)}_{(o,j)} \tag{9}$$

This procedure can be used to define the higher-order $\gamma^{(n)}$ signals. In general, the evaluation of the *n*-atom terms $\gamma^{(n)}$ is obtained by calculating the total signal for *n* atoms and subtracting all the lower-order $m < n$ terms. The exact calculation of the $\gamma^{(n)}$ signals is obtained by performing matrix inversions for defined sets of two, three, or four atoms. A very fast algorithm based on the continued fraction expansion has been developed to calculate the total *n*-atom signals,[49] since it is difficult to perform such inversions at high energies, due to the high number of angular momenta needed. It is assumed that the rearranged MS series in eq 7 always converges, especially after proper configurational averaging of the individual terms.

Since the MS series can now be written in terms of *n*-atom signals, an average over all the configurations, whether thermal or structural, in the system can be written as[16,17,48]

$$\begin{aligned}
\langle\chi(E)\rangle &= \rho_0\int_0^\infty 4\pi r^2 dr g_2(r)\gamma^{(2)}(r;E) + \\
&\rho_0^2\int 8\pi^2 r_1^2 r_2^2 \sin\theta dr_1 dr_2 d\theta g_3(r_1,r_2,\theta)\gamma^{(3)}(r_1,r_2,\theta;E) + \\
&\rho_0^3\int 8\pi^2 r_1^2 r_2^2 r_3^2 \sin\theta dr_1 dr_2 dr_3 d\theta d\omega g_4(r_1,r_2,\theta,r_3,\omega)\gamma^{(4)}(r_1,r_2,\theta,r_3,\omega;E) + \ldots
\end{aligned} \tag{10}$$

where the various g_n are the *n*-atom correlation functions which give the probability of the occurrence of a given configuration as seen from the absorbing site. The distances r_i and angles θ and ω are the structural variables, which parameterize the relative position of *n* atoms at a time, and ρ_0 is the average density of the system. Since the various g_n are not known *a priori*, unless a definite model to describe thermal or structural disorder is known, a decomposition can be made of the distribution functions into sums of well defined peaks associated with particular *n*-atom configurations. To each peak there corresponds a $\gamma^{(n)}$ signal which is dependent on peak shape, where the peak shape is defined by a certain number of parameters that can be varied during the fitting procedure. An initial background structural model must exist to establish such a decomposition. For molecules of biological interest, the various bond lengths and the angle between the bonds are the natural variables to describe thermal disorder and the various peaks can be described in terms of correlated Gaussian distributions. In this case, correlation variances and average distances and angles describing the various configurations can be fitted directly to the experimental signal.

Other ways of path selection and configuration averaging are obviously possible and each code uses different criteria. FEFF5,[18,19] for example, retains only the most significant MS paths in order to avoid unnecessary computations. The default presorting criterion for retaining a path is that the amplitude of the contribution of a given path, estimated in the plane wave approximation, is above 2.5% of the first-shell amplitude. Configurational averages are made via the method of cumulant expansion,[18,19] where the cumulants of various order enter among the fitting parameters. For instance, the first cumulant is the linear phase shift, the second is the Debye-Waller factor, the third is the cubic phase shift, *etc.* As is apparent from the previous discussion GNXAS classifies the MS paths according to a physical criterion that improves the convergence of the MS series and at the same time is suitable for configurational averaging. This approach has three advantages: (1) the number of structural parameters to be fit can be minimized (*e.g.* two bond lengths and an angle can serve to parameterize two SS scattering contributions and a MS contribution), (2) bond lengths and angles can be chosen as variables in the configuration space or given fixed values, and (3) correlations between the variables can be taken into account. In this respect, the cumulant expansion method is one of the possible choices in the GNXAS package for performing configurational averages.

The GNXAS program set incorporates all the advances described above on *ab-initio* calculations of the X-ray absorption cross section and configurational averages and directly fits the theoretical results with the experimental EXAFS data. Raw data are compared directly in E space with a model absorption coefficient $\alpha_{\mathrm{mod}}(E)$

$$\alpha_{\mathrm{mod}}(E) = J\alpha_0(E)[1+\chi(E)]+\beta(E) \tag{11a}$$

composed of an atomic absorption of hydrogenic type $\alpha_0(E)$, a structural $\chi(E)$ term and an appropriate function $\beta(E)$. The function $\beta(E)$ accounts for remaining background effects and can include many-body features like double-electron excitation channels (the $S_{in}(E)$ factor in eq 1). J is the absorption coefficient jump which takes into account thickness and density of the photoabsorbing centers of the particular sample. The comparison of the experiment with the theoretical cross section also requires the inclusion of a few parameters which do not have direct structural meaning. The XAS experiment is not a measure of the pure K-edge or L-edge absorption as there is always a background present mainly due to lower energy excitations and to instrumental effects. A smooth background is taken into account as a sum of polynomial functions. Also there are often spikes, steps, or small edges arising from instrumental effects or from intrinsic photoabsorption phenomena which are necessary to identify and to remove in the definition of the structural signal. It is possible to exclude particular energy regions affected by glitches, spikes, *etc.*, and contributions coming from multi-electron excitation channels can be included with arc-tangent, step-like or Lorentzian line shapes.

The procedure of fitting a global model absorption coefficient directly to the raw data is unique to the GNXAS package. In the usual approach, a structural signal $\chi(E)$ is separated from the measured absorption cross section $\alpha(E)$ according to the formula

$$\chi(E) = \{\alpha(E) - \alpha_0(E)\}/\alpha_0(E) \tag{11b}$$

where $\alpha_0(E)$ is the absorption of an isolated embedded atom. This separation is achieved in three steps: (a) a pre-edge background removal that eliminates the energy dependence of the absorption other than the one under investigation; (b) a normalization to an edge jump that takes into account the thickness and density of the photoabsorbing atoms; and (c) a post-edge background removal that eliminates the energy dependence due to the absorption from an isolated atom. This last step is the most crucial one as it can affect the final form of the structural signal. Up until recently, the practice followed was to perform the three steps without optimization in a partially subjective way. Recently a method has been suggested[54] that for the third step subtracts a spline that best eliminates the nonstructural, low-R portion of $\chi(R)$, the Fourier transform of $\chi(E)$, through an iterative procedure. Instead, GNXAS optimizes all three steps in E space, since the three contributions cannot be separately defined in an unambiguous way, neither theoretically nor experimentally. The atomic cross section of the photoabsorber, for example, is a concept that can be defined theoretically in the framework of multiple scattering theory only in the muffin-tin approximation for the cluster potential. However, the cross section so calculated contains unphysical oscillations due to the truncation of the atomic potential. In a non-muffin-tin approach of MS theory, there is no way to define unambiguously the central atom absorption, since this latter depends on the scattering amplitude of the region of space surrounding the photoabsorber, which is not well defined. The ideal situation would be to have a reliable theory that calculates altogether the pre-edge, edge, and post-edge absorptions, including the structural signal and shake-up/shake-off processes, to be fitted to the experiment. Unfortunately, this is too complicated and the present status of the theory is not yet sufficiently developed.

However, this concept is retained in GNXAS by constructing a global model signal to fit to the whole absorption. It is true that the β term in eq 11a, which contains the pre-edge contribution plus shake-up/shake-off edges, couples this background to the structural model, but this is unavoidable and physical. In fact the method suggested in reference 54 has the drawback that it misrepresents the intensity and the shape of the double-excitations channels. Indeed these spectral features peak in the low-R region of configuration space, since they contain high frequency components. By trying to minimize this low-R nonstructural portion of $\chi(R)$ in order to define an optimal atomic background absorption, one is bound to misrepresent this contribution, since the intensity and the shape of the double excitations channels are determined by the physics of the process.

The nonlinear fitting procedure is applied to the unfiltered data by a residual function

$$R_{N-n}(x_1,x_2 \ldots x_n) = \frac{N}{N-n} \frac{\sum_{i=1}^{N} \left[\alpha(k_i) - \alpha_{\text{mod}}(k_i; x_1, x_2 \ldots x_n)\right]^2 k_i^p}{\sum_{i=1}^{N} \left[\alpha(k_i)\right]^2 k_i^p} \qquad (12)$$

which is a χ^2-like statistical function dependent on the structural and background parameters ($x_1,x_2,\ldots x_n$) and on the noise level. This function is not a true statistical χ^2 function since a true χ^2 function weights the data inversely according to the variance of each data point. However, the two functions can be roughly proportional in a situation in which the collection times are such that all data points, at low and high k, have roughly the same variance, the latter being determined by calculating the standard deviation during averaging of the experimental spectra. This requires a careful selection of the experimental count times to ensure that high- and low-k data contribute significantly to the spectrum. In any case, in the GNXAS package, there is also the capability for generating error bars for each data point and constructing a true χ^2 function. In eq 12 $k = \sqrt{E}$, N is the number of experimental points, and n is the number of fitting parameters. Structural parameters, such as equilibrium distances, angles, and Debye-Waller factors, can be refined around model values by using a Taylor expansion of phases and amplitudes up to sufficient-order to calculate the theoretical signals relative to each new configuration in the refinement procedure. Signals need to be recalculated only when the structural parameters vary significantly (typically 10% or more) from the starting values. For details on applied nonlinear multiparametric fitting procedures, see reference 55.

It is useful to consider the number of independent data points present in a spectrum for comparison with the number of fit variables. At first sight, it would seem from eq 12 that this number is the total number of points; however, this is not so. In fact, doubling the number of points in a set of sinusoidal signals defined in k space does not lead to a doubling of the information content in the spectrum, especially if one has already enough points to determine the phases and amplitudes. More quantitatively, if δk is the interval in k space where the spectrum is defined and if this latter is analyzed only on a finite interval δR of the conjugate variable R, then it has recently been shown[56] that the number of truly independent points N_I in a spectrum is given by $N_I = (2\delta k\delta R/\pi)+2$. This conclusion does not contradict the procedure of nonlinear least-squares minimization in k space, since this latter is in principle able to lead to the determination not only of the number but also of the type of parameters relevant to the fit. In fact, trying to fit more parameters than the number allowed by the above formula will result in some of them being determined with very large errors, indicating which parameters are relevant. A parameter which is not relevant will not lead to a decrease of the squared residual function of the type shown in eq 12. Of course, it is very useful to have an *a priori* estimate of the number of parameters one can reasonably fit to a spectrum as a guide, but in principle, this is not essential. In the data analysis section, the independent data-to-parameter ratio, which is an indication of the degree of determinacy of the fit, is presented for each compound.

The inclusion of three-atom signals provides for determination of quantities such as bond angles, angle variances, and bond-bond and bond-angle correlations. The structural parameters associated with a pair of atoms are the distance R and the variance σ_R^2 (*i.e.* the mean square variation of the distance R) if a Gaussian distribution of distances is used.[50] By considering the explicit contributions associated with triplets of atoms, one has to include three average quantities to define the triangle (*e.g.*, the two short sides R_1 and R_2 and θ, the angle between them). Thermal and configurational Gaussian disorder is taken into account through six parameters

$$M = \begin{pmatrix} \sigma_{R_1}^2 & \sigma_{R_1R_2}^2 & \sigma_{R_1\theta}^2 \\ \sigma_{R_1R_2}^2 & \sigma_{R_2}^2 & \sigma_{R_2\theta}^2 \\ \sigma_{R_1\theta}^2 & \sigma_{R_2\theta}^2 & \sigma_{\theta}^2 \end{pmatrix} \tag{13}$$

which belong to the symmetric covariance matrix. In the case of a pair of atoms, the symmetric covariance matrix is represented by the variance σ_R^2. In a simple vibrational model for the two atoms, the DW factor in the EXAFS formula is given by $\exp(-2\sigma_R^2 k^2)$. For a more complete treatment of configurational averages of a general EXAFS signal, the reader is referred to reference 50.

Besides the above structural parameters, other nonstructural parameters are to be refined in the fit (although their variation is limited by theoretical considerations). One of these nonstructural parameters is E_0, which aligns the experimental energy spectrum to the theoretical one. Physically E_0 is the origin of the photoelectron kinetic energy and should be defined as the core ionization threshold (vacuum level) so that $E = \omega - E_0$. Even though in the theoretical treatment an internal photoelectron wavenumber κ is defined relative to a muffin-tin origin $\overline{V}_0$, this origin is energy dependent (since the HL potential is energy dependent) and the only reason for its existence is that the true molecular potential has been approximated by its muffin-tin counterpart. Since non-self-consistent molecular charge densities are used, E_0 can be estimated only within an uncertainty of 2-3 eV. Self-consistent calculations might provide a more accurate determination of this quantity. However, the ionization threshold I_C is very seldom experimentally determined in current measurements of absorption spectra. Therefore, in practice, it is convenient to leave E_0 as a parameter in the fit. Another nonstructural parameter that can be varied in the fit is the many-body amplitude reduction factor S_0^2. The presence of S_0^2 is justified since intrinsic processes are not incorporated in the optical potential as described by the HL potential. The magnitude of S_0^2 should be related to the weight of the intrinsic processes in the absorption spectrum, which should be typically less than ~0.1. An additional source of broadening of the experimental spectra comes from the core hole width Γ_c that adds to the imaginary part of the potential. The value of Γ_c in the fit is usually kept fixed to some experimentally-determined value or good theoretical estimate.[57] Finally, the calculated signal should be convoluted with the experimental resolution function as determined by the specific optics of the experimental system used to measure the data.[58] In practice this function is modeled as a Gaussian with standard deviation E_r, which is allowed to vary in a range of 1-2 eV around the expected value.

Standard statistical concepts can be used to estimate the error affecting the fitted values of the parameters since the data analysis is performed using raw absorption spectra.[59,60] By neglecting systematic errors in the experimental data and in the theoretical calculations, the definition of the residual function given by eq 12 allows one to estimate parameter values, statistical standard deviations, and the quality of the fit.

The expected value of this expression can be calculated in terms of the variance of the experimental and model signals. In particular, for $p = 0$, the expected value is the variance of the experimental points which is usually on the order of 10^{-6}-10^{-8}. This is the lower limit of the residual. Therefore, the quality of the fit is measured by the value of the residual. In the limit of a "perfect" simulation, the quality of the fit is on the order of the variance of the experimental data. Once the residual is near the variance of the experimental data, the statistical standard deviation of a specific structural parameter can be estimated by the increase of the residual as the parameter is varied. This kind of procedure is commonly used in multi-parametric nonlinear fitting procedures. The statistical significance of the inclusion of particular fitting parameters can be tested by using the well-known F-test, valid for χ^2 distributions.

These considerations do not take into account correlations between different fitting parameters. Correlation effects can increase the standard deviation of the measured parameters. A rigorous way to account for these effects is by estimating correlation through contour plots in parameter space.[61] However, the size of correlation effects can be greatly reduced by extending the number of independent points in the fitting procedure. Calculation of correlation among all the parameters is time consuming for standard data analysis. For EXAFS spectra recorded over a wide energy range and composed of a reasonable number of points, one can reasonably assume that correlations are within 3σ of the estimated standard deviation (σ). Error bars are estimated as three times the statistical standard deviation, an assumption that tends to overestimate the error. Usually the statistical errors determined are quite small. Systematic errors in the experimental data collection and the intrinsic limitation of the theory (arising mainly from the approximations) give rise to errors that can be much larger than the statistical ones. When GNXAS is applied to a particular class of unknown systems, the best indication would be the variance between GNXAS results on a number of similar structures for which crystallographic results are known. A thorough study of the effects of the approximations on the derived structural data is currently under way. According to comparisons in fits to known, less complex structures, theoretical cross sections are quite accurate for the determination of distances and angles (on the order of 0.01 Å for bond distances, around 1° for bond angles) and are less accurate in the determination of covariance matrices (errors up to 10-20% for bond variances σ_R^2 have been observed). These limits are explored further in the applications described below for much more complex multishell transition metal complexes.

2.2.3. The GNXAS Program Set

The GNXAS package consists of five independent subprograms, each performing a specific task in the general layout of the method described above. Briefly, in the order of application, the CRYMOL subprogram (a) generates a cluster of sufficient size to count all the two-, three-, and four-atom configurations associated with any nonequivalent photoabsorber up to a given cutoff with the correct degeneracy, so that one can define all the SS and MS paths involving up to four atoms and (b) selects the various types of atoms differing in atomic number, types of neighbors, and distances within a given tolerance to build appropriate miniclusters to be used in the construction of the overlapped charge density to obtain the potential.

The PHAGEN subprogram takes the minicluster generated by CRYMOL, defines muffin-tin radii according to Norman's criterion,[62] and uses the Mattheiss prescription to overlap self-consistent atomic charge densities to construct the cluster charge density. In order to model the charge relaxation around the core hole and to mimic the screening of the excited photoelectron, the self-consistent charge density of the photoabsorbing atom with one core hole and one electron added to the first nonoccupied valence state is used. On the basis of the cluster charge density obtained, the Coulomb and the HL exchange and correlation potential are generated, the latter being recalculated at each new energy point. Finally, the radial Schrödinger equation is solved with the complex potential and the t atomic matrix elements calculated on the basis of eq A13 in the Appendix in reference 25 for any nonequivalent atom in the cluster.

The GNPEAK subprogram accepts as input a file generated by CRYMOL specifying the type, position, and neighbors of all the atoms in the cluster and searches for all two-, three-, and four-atom local configurations around each nonequivalent photoabsorber which are associated with SS and MS contributions to the absorption coefficient. These atomic configurations are referred to as peaks of the two-atom (g_2), three-atom (g_3), and four-atom (g_4) distribution functions. This information is passed to the GNXAS subprogram. The GNXAS subprogram also reads the atomic t matrix file generated by PHAGEN and calculates all the $\gamma^{(n)}$ signals relative to all the configurations calculated by GNPEAK.

Finally, the subprogram FITHEO builds up a model absorption signal (see eq 11) composed of an appropriate background plus the oscillatory structural contribution $\chi(E)$ already calculated by GNXAS. The parameters contained in the model absorption signal are then refined during a fitting procedure that tries to minimize the difference between the calculated and experimental signals. The function minimized is given by eq 12. Fits are done directly in E space. A standard statistical procedure commonly used in multiparametric nonlinear fitting is implemented here to perform χ^2 and F-tests in order to answer typical questions arising in model refinements.

A comment is relevant on the relationship of GNXAS to other theoretical-parameter based EXAFS analysis programs. EXCURVE, FEFF5, and GNXAS all have conceptual similarities regarding the calculation of SS and MS signals. All three programs at present use a theoretical scheme consisting of the reduction of the photoabsorbtion many-body problem to a one-particle problem with a complex Hedin-Lundqvist effective potential based on a charge distribution obtained by overlapping atomic charge densities following the Mattheiss prescription[40] in a muffin-tin approximation. The calculated signals are therefore in general very similar, with the differences arising from the definition of the muffin-tin parameters and the different way of defining the central atom absorption cross section mentioned above.

2.3. Applications to Iron Complexes

2.3.1. Sample Preparation and Data Collection

$Fe(acac)_3$ was purchased from Aldrich, $K_3Fe(CN)_6$ was purchased from J. T. Baker, and $Na[Fe(OH_2)EDTA]$ was prepared according to the published procedures.[63] The crystalline samples were ground into a fine powder and diluted with BN. The BN powder mixture was pressed into a 1 mm thick slotted Al spacer and sealed with Mylar tape windows. The X-ray absorption spectra were recorded at the Stanford Synchrotron Radiation Laboratory on unfocused beamlines 7-3 and 4-3 during dedicated conditions (3 GeV, 25-90 mA). The radiation was monochromatized using a Si(220) double-crystal monochromator detuned to 50% at 7998 eV to minimize harmonic contamination. The X-ray beam was defined to be 1 mm vertically by pre-monochromator slits. An Oxford Instruments continuous-flow liquid helium CF1208 cryostat was used to maintain a constant temperature of 10 K. Data were measured in transmission mode with three nitrogen-filled ionization chambers, using an Fe foil between the second and third ionization chambers for internal energy calibration. The spectra were calibrated by assigning the first inflection point of the Fe foil spectrum to 7111.2 eV. The data represent an average of two to four scans. The effects of a quartet monochromator glitch were removed from the averaged data by four single point replacements at around k = 11.8, 12.1, 12.3, and 12.6 Å^{-1}.

2.3.2. GNXAS Data Analysis

The following approach was used for the GNXAS analysis of the three iron complexes. The atomic coordinates were input into CRYMOL, and the appropriate cluster was determined. Phase shifts were calculated in PHAGEN using the standard muffin-tin approximation with the entire cluster and up to an energy limit of 70 Ry (950 eV) above the Fe K edge. The muffin-tin radii were chosen by scaling Norman radii of the cluster atoms by a factor of about 0.8 in such a way as to match the nearest neighbor distance. The GNPEAK program was then run to identify and select the relevant peaks in the g_n distribution functions and associate each atom with the appropriate phase shifts. GNXAS calculated the various signals from each g_n contribution. Least-square fits were performed in the subprogram FITHEO on the averaged, energy-calibrated, raw absorption data without prior background subtraction or Fourier filtering. The minimization program uses the MINUIT subroutine of the CERN Library. The residual function is minimized by refining parameters for which specified intervals can be input. The nonstructural parameters, E_0, S_0^2, Γ_c, and E_r were, as usual, calibrated on model compounds and allowed to vary within narrow intervals, observing if they refined to one of the hard limits.[57,58] The structural parameters varied in the refinements were the distance and the associated bond variance σ_R^2 for each two-atom configuration and the distances, the angle, and the covariance matrix elements for the three-atom configurations (unless stated otherwise). Distances and angles were allowed to vary within a preset range, typically ±0.05 Å and ±5°, respectively. Bond and angle variances and the off-diagonal covariance elements were also allowed to vary in restricted ranges: ±0.005 Å^2, ±50 (degrees)^2 and ±0.5, respectively. The results were carefully monitored to ensure that all parameters refined inside the allowed range. The coordination numbers were kept fixed to known values.

2.3.3. Results and Discussion

2.3.3.1. Fe(acac)$_3$. The GNXAS method was applied to Fe(acac)$_3$ Fe K-edge EXAFS data to determine the feasibility of studying the metrical details of inorganic compounds. The ability of GNXAS to provide an accurate description of the MS contributions in the EXAFS data of a compound with a non-collinear arrangement of atoms and the reliability of the structural parameters obtained from GNXAS were evaluated. The GNXAS set of programs were used to generate theoretical EXAFS signals corresponding to both two-atom- and three-atom scattering processes. The structure of Fe(acac)$_3$ has been determined by X-ray diffraction.[64] The iron atom is in an octahedral arrangement (Figure 2.2) surrounded by six oxygen atoms at 1.99 Å, six carbons (C$_1$) at 2.95 Å, three carbons (C$_2$) at 3.34 Å, and six carbons (C$_3$) at 4.32 Å (where the ranges of the distances are given in Table 2.1). The atomic coordinates of Fe(acac)$_3$ were entered into CRYMOL and the appropriate cluster (neglecting the hydrogens) was determined (shown in Figure 2.2). In this case, the cut-off distance was 4.4 Å since the longest Fe-C distance is 4.32 Å and the FT showed no significant features beyond this value. The reduced Norman sphere radii used to calculate the phase shifts were 1.13 Å for Fe, 0.873 Å for O, and 0.899 Å for C. The prototypical two-atom and three-atom configurations (g_2 and g_3 peaks) were identified in the cluster up to 4.4 Å and averaged with a frequency tolerance of 0.1 Å. The resultant coordinates of the atomic configurations were used to calculate the various signals associated with two-atom and three-atom contributions. The signal associated with four two-atom configurations were generated: Fe-O, Fe-C$_1$, Fe-C$_2$, and Fe-C$_3$. Five signals associated with three-atom configurations were calculated: Fe-O-C$_1$, O-Fe-O (90°), O-Fe-O (180°), Fe-O-C$_2$, and Fe-O-C$_3$ (where the three-atom configuration is defined by the two short distances and the intervening angle). The appropriate crystallographic distances and angles for the above mentioned two- and three-atom configurations are listed in Table 2.1. The fitting program used at the final step of the data analysis built the theoretical absorption spectrum by summing all the two-atom and three-atom contributions. The final spline was in three segments of order 4, 4, 4 with defining energy points of 7147, 7269, 7577, and 7999 eV. The least-squares fits were done with k^3 weighting over the k range of 2.4 - 15.1 Å^{-1}.

To analyze the MS effects in Fe(acac)$_3$, signals from two-atom configurations were systematically replaced with the appropriate three-atom contributions, while monitoring the residual in the EXAFS and the components in the FT. For these fits all the distances and angles were fixed to the crystallographic values while permitting the associated variances and nonstructural parameters to vary. Fit A (Figure 2.3A) contains only two-atom contributions from Fe-O, Fe-C$_1$, Fe-C$_2$, and Fe-C$_3$. The R value for Fit A is 0.181×10^{-4}, and the EXAFS residual clearly contains high frequency components. In Fit A, the first peak of the FT of the data is fit fairly well by the FT of the theoretical signal, but the intensity of the theoretical signal does not match the experimental intensity above 2 Å. The second fit, Fit B, includes three-atom signals from Fe-O-C$_1$, O-Fe-O (90°), and O-Fe-O (180°) while the second and third shells of carbon are still treated as two-atom configurations (Figure 2.3B). The R value of Fit B is 0.635×10^{-5}, almost a factor of three better than the R value in Fit A, indicating the importance of treating

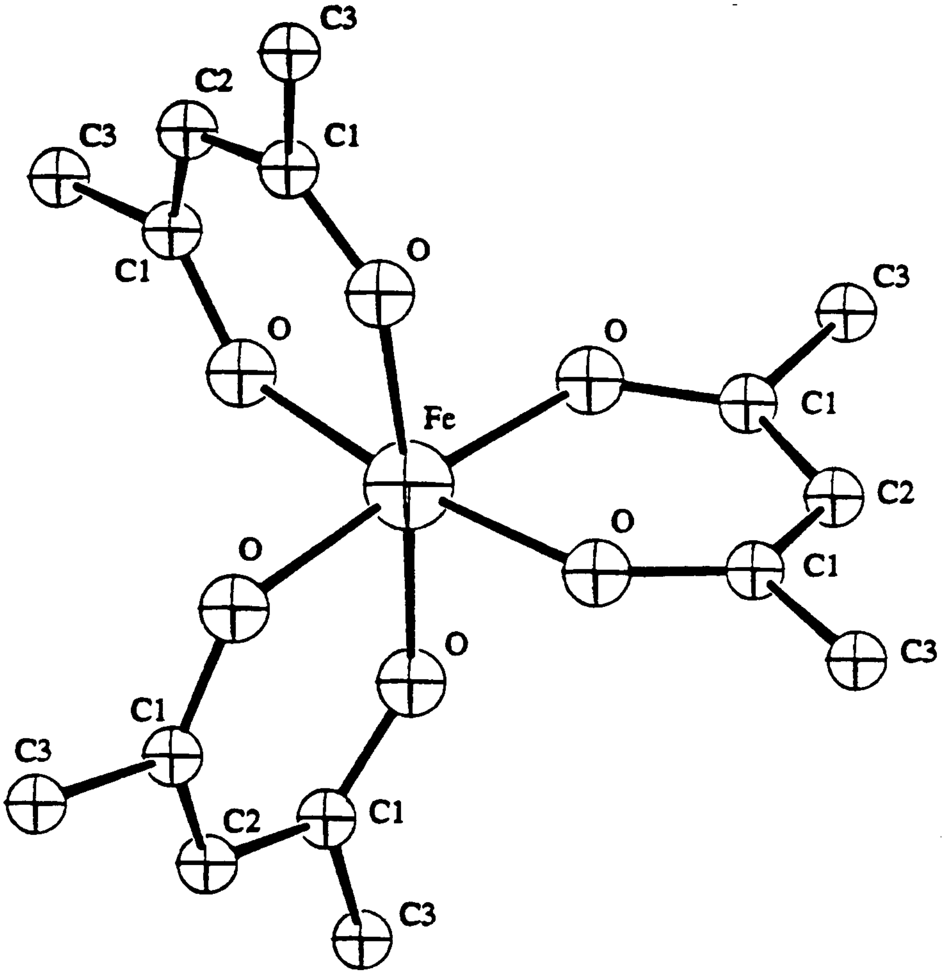

Figure 2.2. Molecular structure of Fe(acac)$_3$ with atom designations as used in the text.

Table 2.1. Comparison of Fe(acac)3 GNXAS Distance and Angle Fitting Results to Crystallographic Values.

structural feature (# of configurations in complex)	GNXAS distances/angles	GNXAS bond variance (σ_R^2)/ angle variance (σ_θ^2)^a	crystallographic distances/angles average [range]
Fe-O (6)	1.99 Å	0.002	1.99 Å [1.99-2.00]
Fe-C_1 (6)	(2.98 Å)*	----	2.95 Å [2.93-2.97]
Fe-C_2 (3)	(3.37 Å)*	----	3.34 Å [3.29-3.43]
Fe-C_3 (6)	(4.34 Å)*	----	4.32 Å [4.30-4.33]
O-C_1 (6)	1.22 Å	0.001	1.26 Å [1.24-1.28]
O-C_2 (6)	2.38 Å	0.006	2.34 Å [2.31-2.39]
O-C_3 (6)	2.38 Å	0.008	2.36 Å [2.34-2.38]
Fe-O-C_1 (6)	134°	1×10^1	128° [128-130]
Fe-O-C_2 (6)	101°	4×10^1	101° [99-103]
Fe-O-C_3 (6)	165°	3×10^1	165° [164-166]
O-Fe-O (6)	89°	6×10^1	91° [87-94]
O-Fe-O (3)	175°	3×10^1	175° [174-176]

^{a} Bond and angle variances are reported in Å^2 and degrees^2, respectively.

* values were calculated using the fitted Fe-O bond length, O-C bond length, and Fe-O-C angle.

Figure 2.3. Comparison of the theoretical and experimental signals of the k^3-weighted EXAFS data and the FT of Fit A, Fit B, Fit C, and Fit D of Fe(acac)$_3$. The top portion of the figure contains the non-phase-shift-corrected FT of the k^3-weighted EXAFS data of the experimental data (——) and that of the total theoretical signal (----). Also shown is the FT of the residual (····). The lower portion of the figure presents the EXAFS signals for the individual contributions. The total theoretical signal is also shown (——) and compared with the experimental data (····) with the residual being the difference between the experimental and the theoretical EXAFS. (The ordinate scale is 10 between two consecutive tick marks.) Fit A contains only $\gamma^{(2)}$ contributions. The residual in Fit A contains many high frequency components, and the fit does not match the data between 2 Å and 4 Å in the FT. Fit B includes contributions from Fe-O-C$_1$ and 90° and 180° O-Fe-O configurations. Notice the reduction of the residual in the low k-region of the EXAFS and the improvement of the fit to the FT between 2 and 3 Å. Fit C includes contributions from Fe-O-C$_2$. There is no noticeable improvement in the fit to the data since the Fe-O-C$_2$ signal is weak. Fit D includes contributions from Fe-O-C$_3$. Note the considerable improvement in the fit to the data between 3.5 and 4.1 Å in the FT.

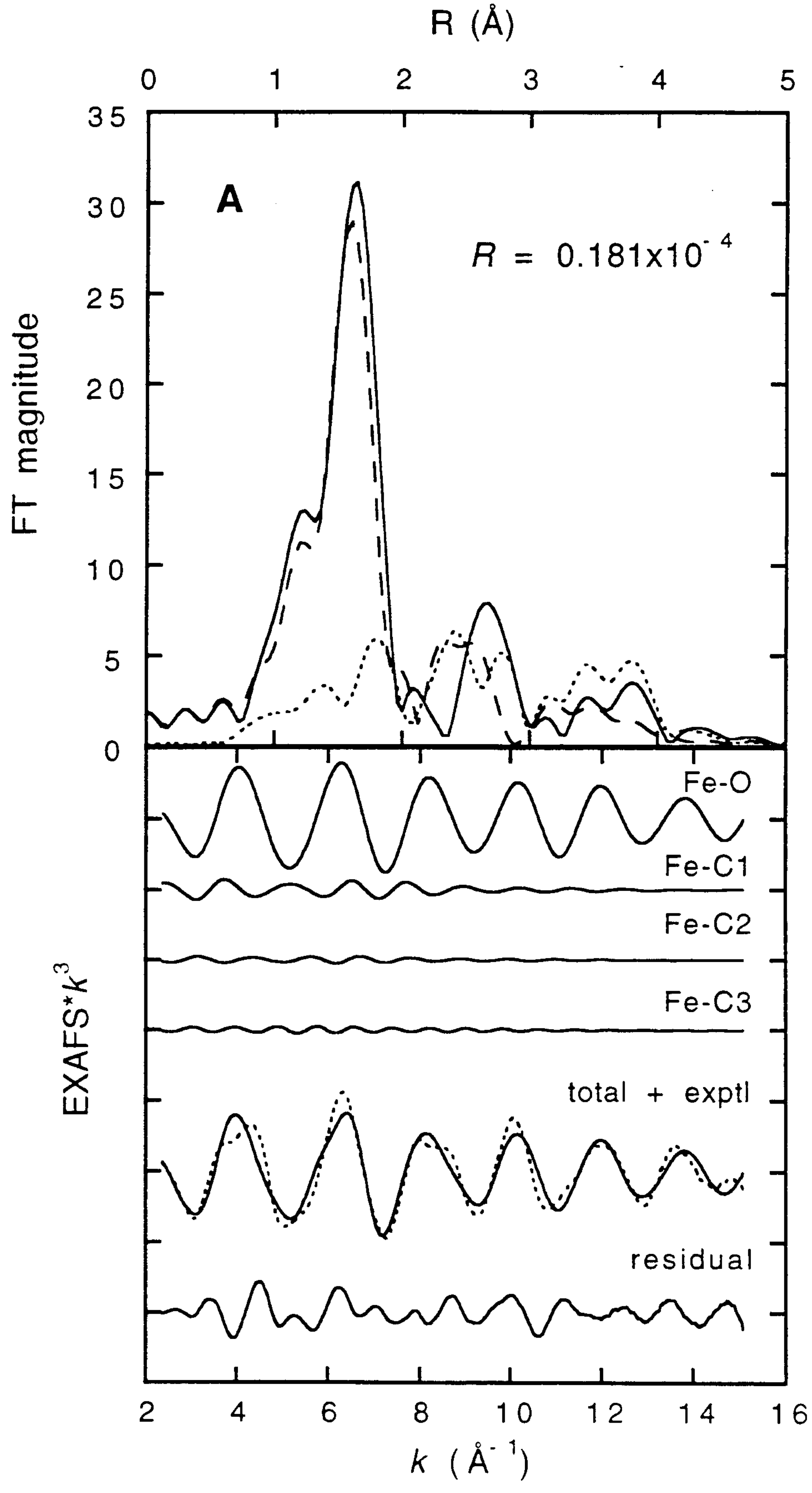
R (Å)
0
1
2
3
4
5
35
30
25
20
15
10
5
0
FT magnitude
A
R = 0.181x10^{-4}
Fe-O
Fe-C1
Fe-C2
Fe-C3
total + exptl
residual
EXAFS*k^3
2
4
6
8
10
12
14
16
k (Å^{-1})

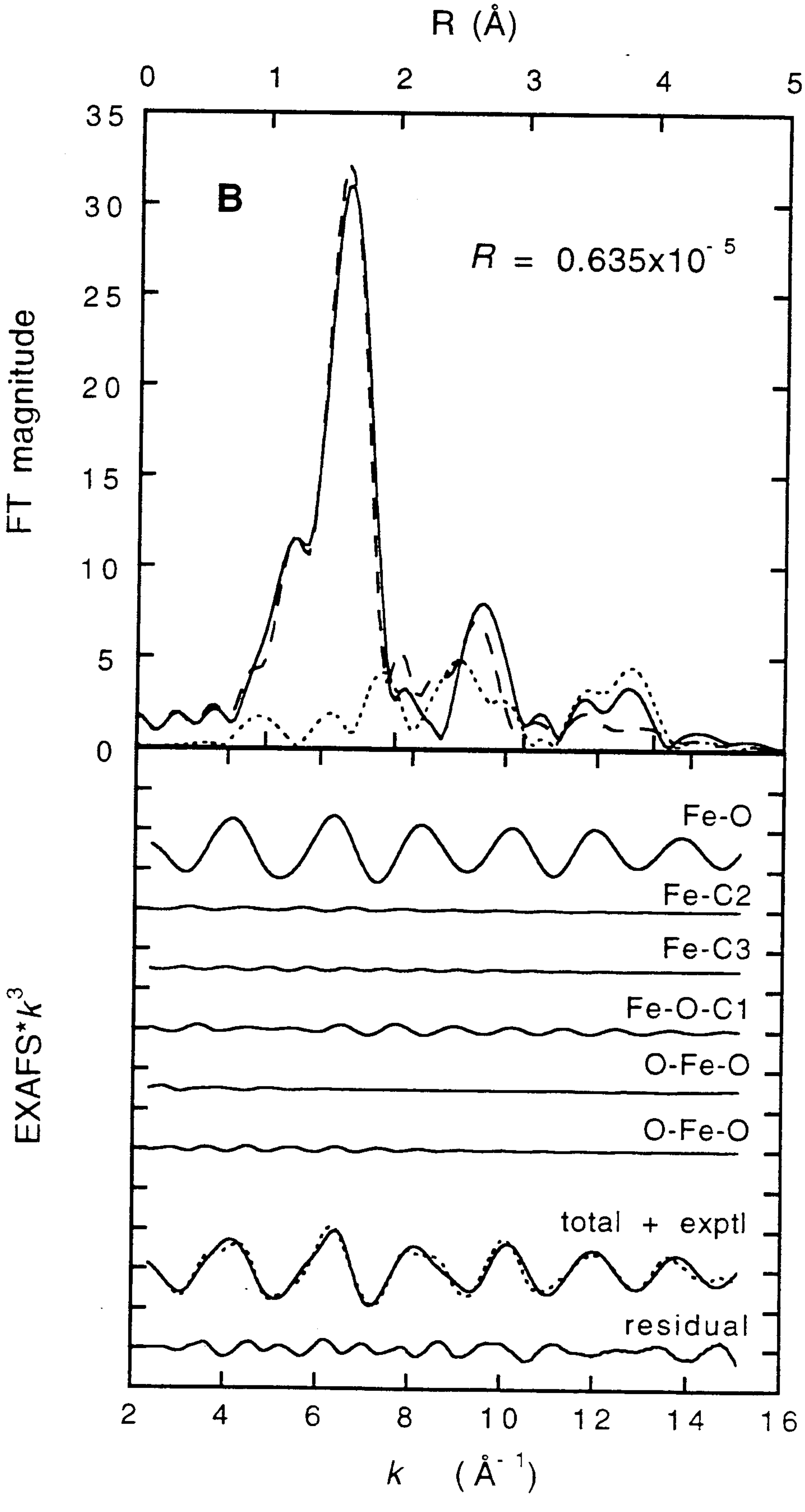
R (Å)
0
1
2
3
4
5
35
30
25
20
15
10
5
0
FT magnitude
B
R = 0.635x10^{-5}
EXAFS*k^3
Fe-O
Fe-C2
Fe-C3
Fe-O-C1
O-Fe-O
O-Fe-O
total + exptl
residual
2
4
6
8
10
12
14
16
k (Å^{-1})

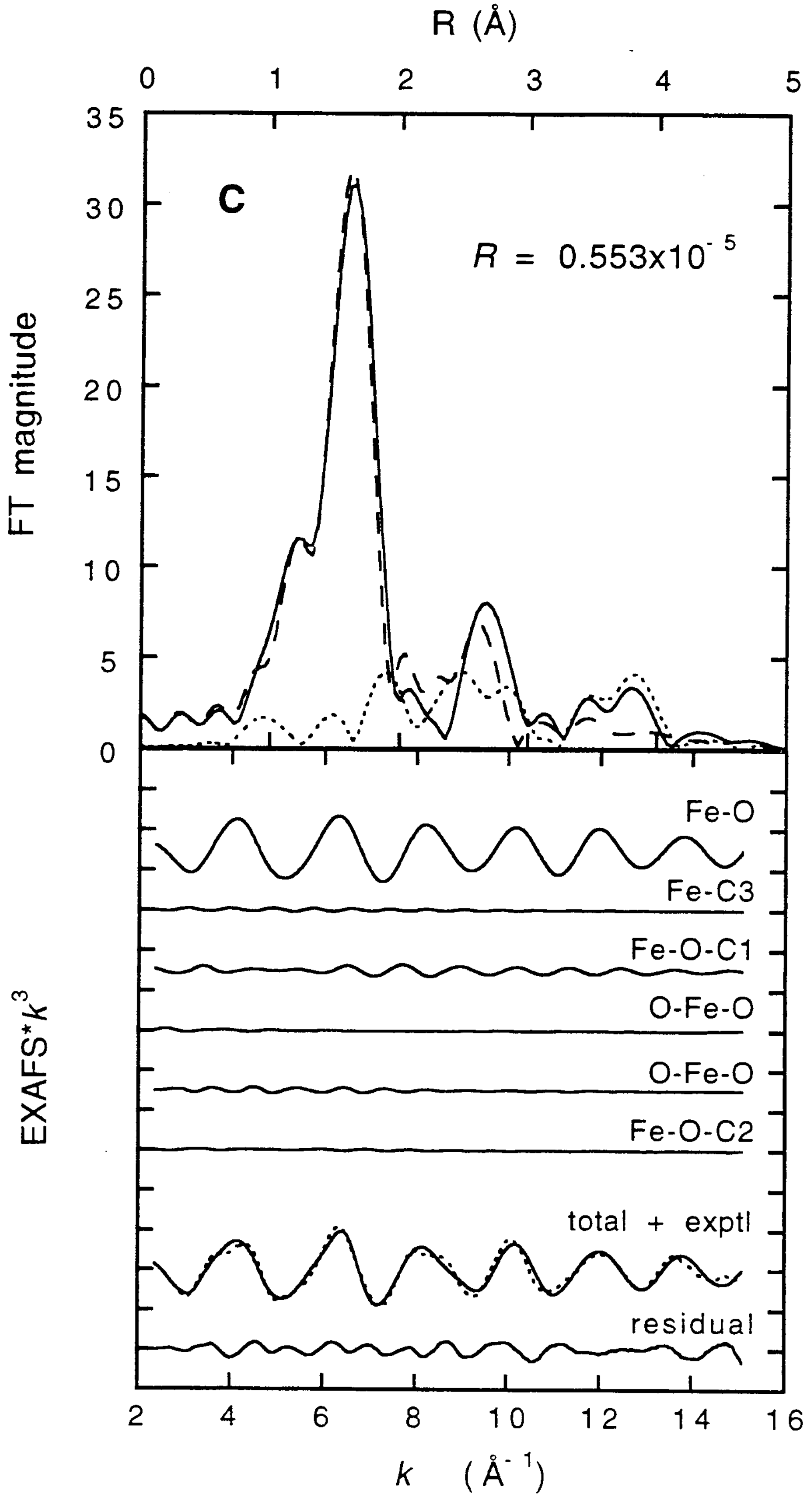
R (Å)
0
1
2
3
4
5
35
30
25
20
15
10
5
0
C
R = 0.553x10⁻⁵
FT magnitude
EXAFS*k³
Fe-O
Fe-C3
Fe-O-C1
O-Fe-O
O-Fe-O
Fe-O-C2
total + exptl
residual
2
4
6
8
10
12
14
16
k (Å⁻¹)

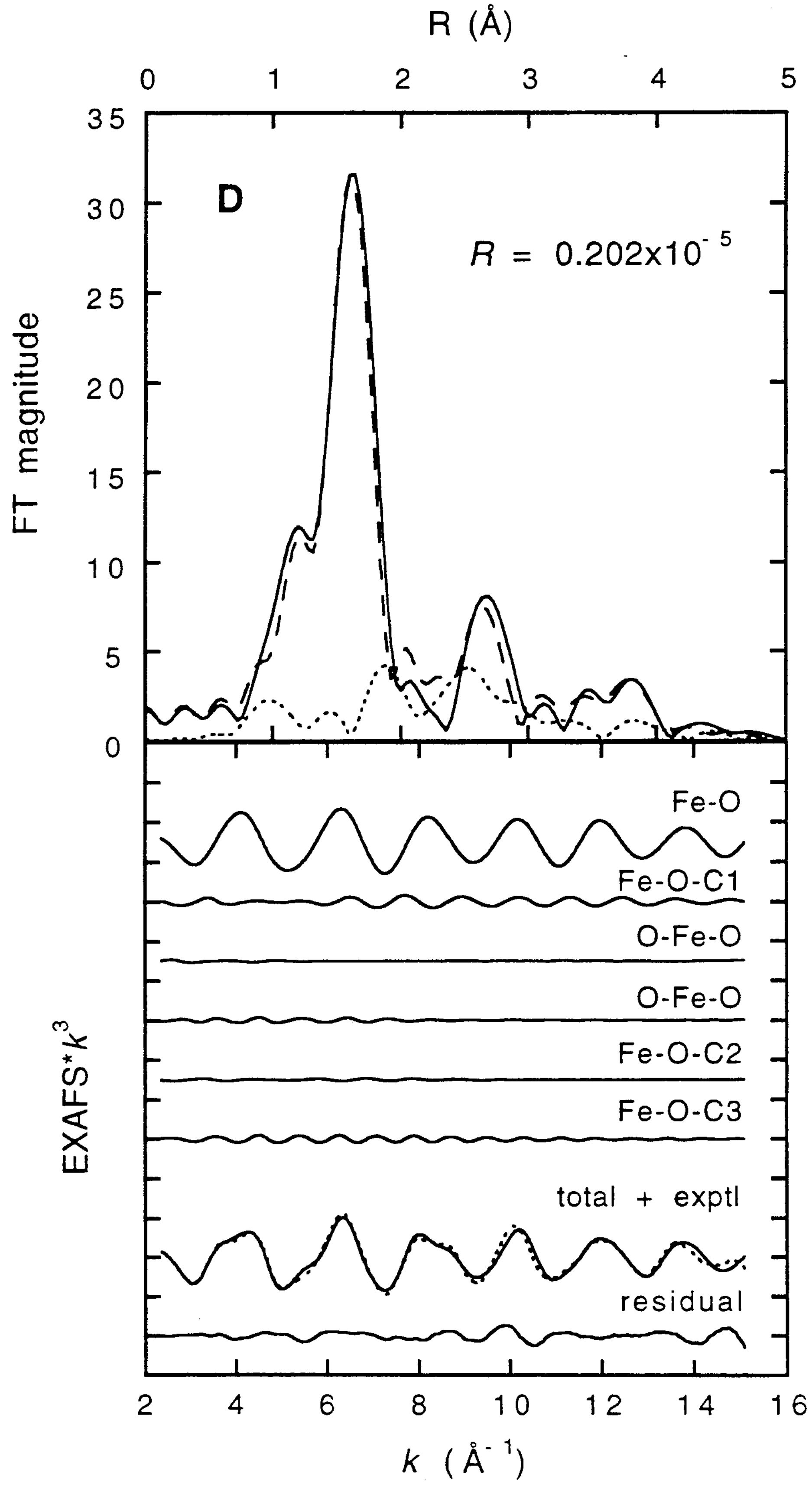
R (Å)
0
1
2
3
4
5
35
30
25
20
15
10
5
0
D
R = 0.202x10^{-5}
FT magnitude
Fe-O
Fe-O-C1
O-Fe-O
O-Fe-O
Fe-O-C2
Fe-O-C3
total + exptl
residual
EXAFS*k^3
2
4
6
8
10
12
14
16
k (Å^{-1})

Fe-O-C_1 as a three-atom configuration. Also notice the significant improvement in the fit to the low-*k* region of the EXAFS, where the Fe-$C_1 \gamma^{(2)}$ signal and the Fe-O-$C_1 \gamma^{(3)}$ signals differ the most (Figure 2.4). The contributions from the 90° and 180° O-Fe-O configurations are relatively small as seen by comparison of their amplitudes with the total Fe-O-C_1 signal. The EXAFS residual in Fit B still contains some high frequency components, but the FT of the theoretical signal of Fit B begins to match the second peak in the FT of the experimental data at ~2.6 Å. In Fit C the second shell of carbons is treated with a three-atom signal. The *R* value of Fit C is 0.553×10^{-5}. Fit C is not a significant improvement over Fit B because the signal generated by the Fe-O-C_2 configuration is negligible (Figure 2.3C). Both the EXAFS data and the FT look very similar to those in Fit B. In Fit D a signal from Fe-O-C_3 is included. The signal from Fe-O-C_3 is fairly strong, and the *R* value of Fit D decreased to 0.202×10^{-5}. All of the distinguishable regular high frequency components have been removed in the Fit D residual, and the FT of theoretical signals is in very good agreement with the experimental FT up to ~4 Å (Figure 2.3D). Notice that even though the Fe-C_3 distance is longer than 4 Å the Fe-O-C_3 signal is significant. This enhancement is in part due to a focusing effect since the Fe-O-C_3 angle is relatively large (165°). Figure 2.5 displays the individual contributions of each signal in the FT. The dominant feature in the FT is the Fe-O signal with the Fe-O-C_1 and O-Fe-O (180°) and Fe-O-C_3 signals contributing at higher *R* values.

The ability of the GNXAS method to accurately determine bond distances and angles was also evaluated. Fits were done by varying the distances and angles and applying constraints to keep them within 5% of the crystallographic values. The initial covariance matrix elements were obtained from Fit D and were allowed to vary within 10% of those values. A comparison of the crystallographic values with the distances and angles obtained from the best fit to the data is presented in Table 2.1. The *R* value of this fit was 0.142×10^{-5} (slightly better than Fit D) and the bond distances and angles were quite close to the crystallographic values. The fit to the experimental data looks very similar to Fit D with a slight improvement of the fit in the Fourier transformed data between 2.5 and 3.0 Å. The bond distances and angles obtained from the GNXAS fit to the experimental data are within the range of the crystallographic values as given in Table 2.1 with a few exceptions. The values obtained from the Fe-O-C_1 signal deviate from the range of crystallographic values by 0.02 Å for the O-C_1 distance and 4° for the Fe-O-C_1 angle, causing the Fe-C_1 distance to deviate from the crystallographic value by 0.03 Å.

The level of accuracy in this fit indicates that the theory is quite reliable in reproducing the phase of the experimental signal, as has been confirmed by previous

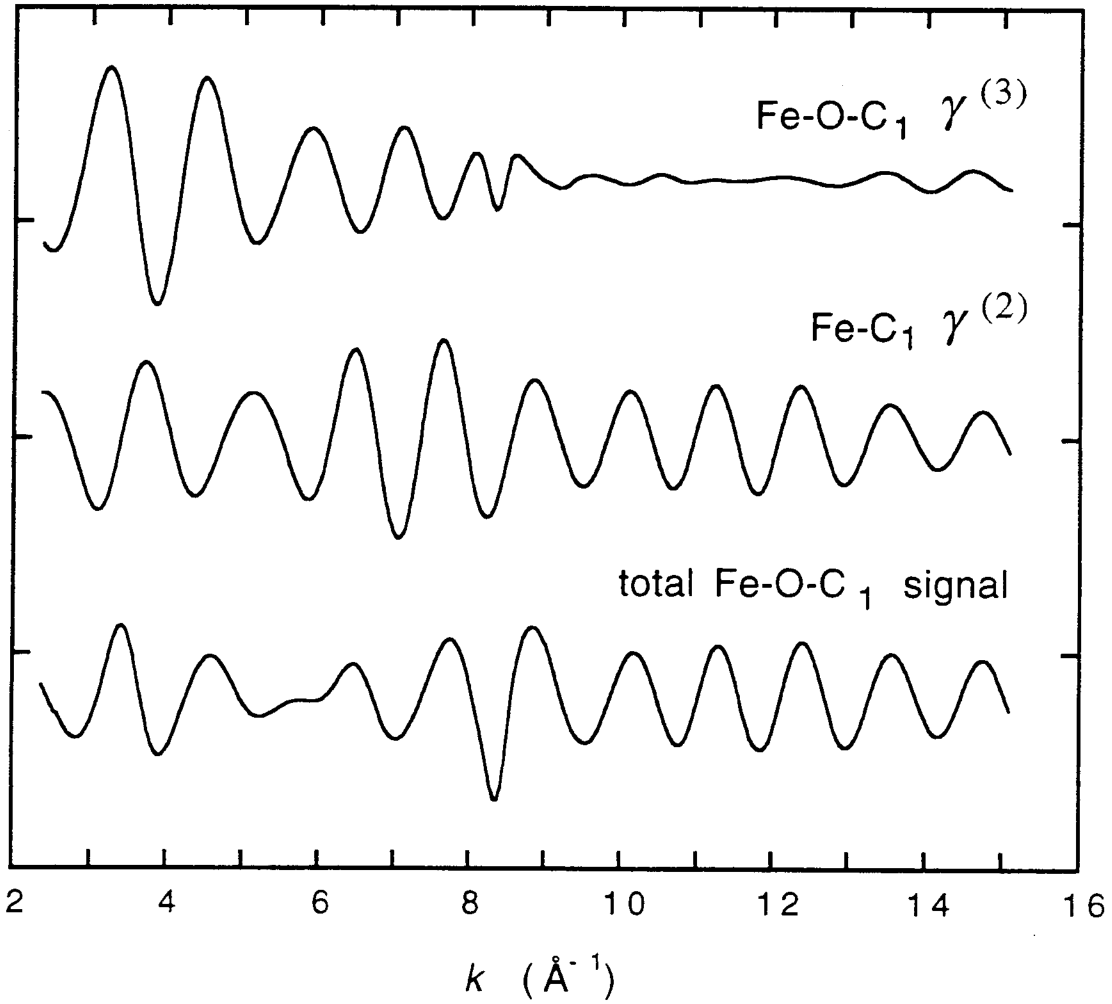

Figure 2.4. Comparison of the Fe-C$_1$ $\gamma^{(2)}$ EXAFS signal to the Fe-O-C$_1$ $\gamma^{(3)}$signal and the total Fe-O-C$_1$ signal. The anomalous behavior of the Fe-O-C$_1$ $\gamma^{(3)}$ signal near 8 Å^{-1} is due to the existence of a deep minimum in the amplitude function of the three-atom signal. Note that the Fe-O-C$_1$ $\gamma^{(3)}$ signal is out of phase with the Fe-C$_1$ $\gamma^{(2)}$ signal between 2.5 and 7.5 Å^{-1}. The low-k EXAFS can only be properly accounted for when the first shell of carbons (C$_1$) is treated in a three-atom configuration (Fe-O-C$_1$), including both the SS and MS contributions. (The ordinate scale is 5 between two consecutive tick marks.)

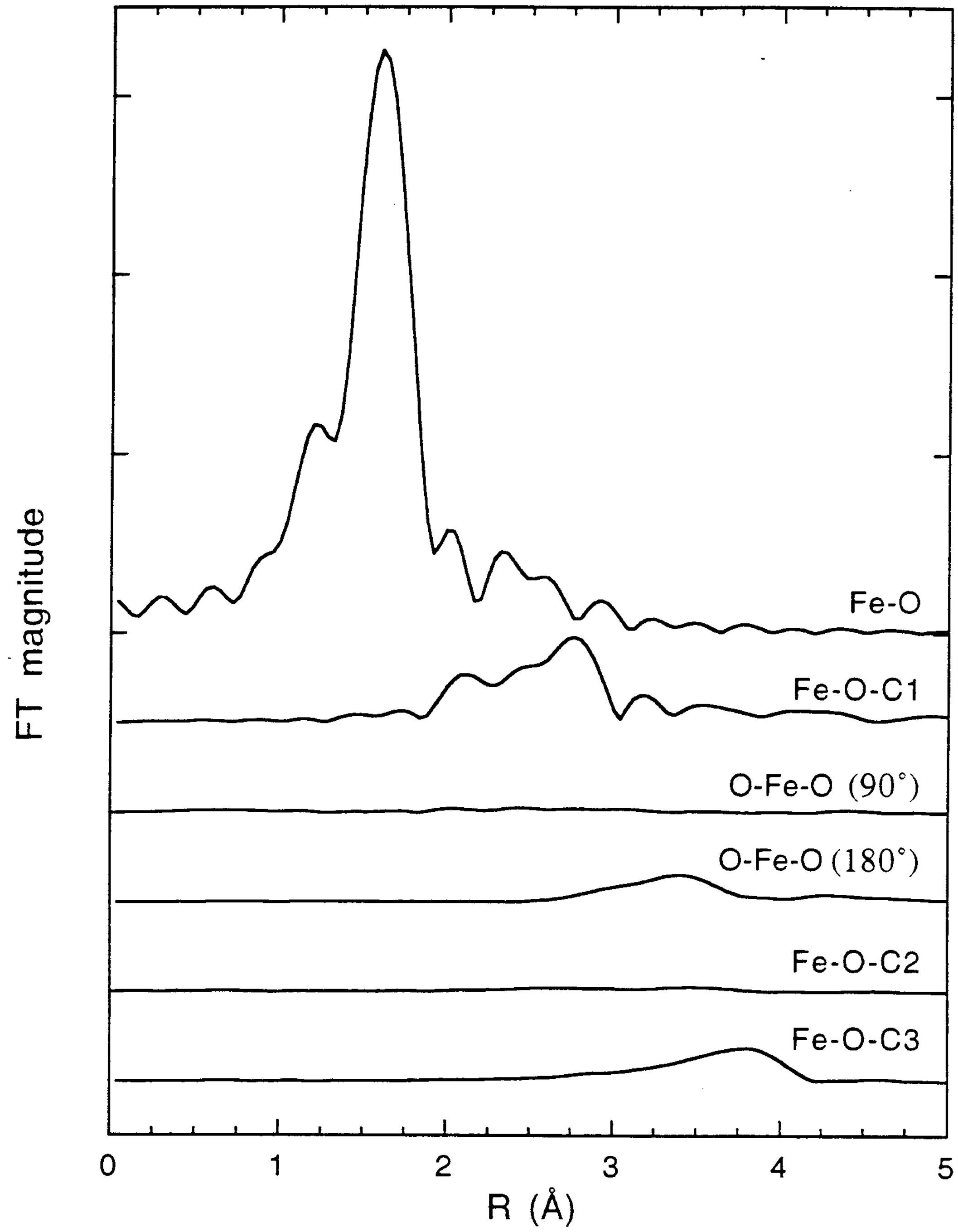

Figure 2.5. FT of the EXAFS signals of Fe(acac)$_3$ for the individual contributions shown in Figure 2.3D. This display is a useful way to determine which signals contribute in which regions and shows clearly the significant and complex contributions from Fe-O-C$_1$ and Fe-O-C$_3$. (The ordinate scale is 10 between two consecutive tick marks.)

experiments.[21-25] Over a large number of fits varying the nonstructural parameters and spline and differing the number of contributions, the Fe-O distance varied by less than 0.01 Å and the Fe-O-C angles by less than 1°, while the O-C_1 distance varied up to 0.04 Å, the O-C_2 distance 0.1 Å, and the O-C_3 distance 0.02 Å. The stronger the signal the smaller the variation in the distance/angle between fits. The amplitude of the signal is determined with slightly less accuracy because amplitudes are affected in the fits by several variables which can be strongly correlated (S_0^2, E_r, Γ_c, bond variances, and the covariance matrix elements). However, the variations of the above-mentioned parameters were confined in narrow ranges determined by physical constraints. In the Fe(acac)$_3$ case, values for the bond variances are not well known since a theoretical approximation of the molecular vibrations is not available. However, fitted values followed reasonable trends with the Fe-O distance having the lowest variance of all the $\gamma^{(2)}$ contributions in Fit A. In a comparison of the variances for the O-C distances, O-C_1 had the lowest variance, O-C_2 had a much higher variance with the static disorder in the O-C_2 distances being over twice that of the O-C_1 distances, and O-C_3 (with C_3 being the carbon in the methyl groups) had the highest mean square deviation.

The EXAFS signal generated by GNXAS matches closely that of the experimental signal of Fe(acac)$_3$ when all the MS contributions were added into the theoretical signal. A comparison of the FT in Figure 2.3A, where only the two-atom signals were taken into account, with the FT in Figure 2.3D, where the three-atom signals were also used, shows the importance of including MS contributions from the three shells of carbon atoms. Not only does the GNXAS theoretical fit match the experimental data but the bond distances and angles in the final fit were within 4% of the crystallographic average values with the majority of the bond distances and angles being within the range of the crystallographic values (see Table 2.1). The number of parameters used in the fit is 18 (two parameters for each bond, the length and its variance, and two for each angle, the angle and its variance, since in this application the off-diagonal elements of the correlation matrix have been fixed to zero) plus 3 (S_0^2, E_r, and Γ_c), for a total of 21. This number can be compared with the number of independent data points $N_I = (2\delta k \delta R/\pi) + 2 = 36$, for $\delta k = 12$ Å^{-1} and $\delta R = 4.5$ Å. Notice that the the number of neighbors has been fixed and that the two-body parameters are also associated with three-body signals. In this manner, the same parameters can be associated with both a strong and a weak signal. The independent data-to-parameter ratio determined above shows that the fit is overdetermined by nearly a factor of two, pointing to the reliability of the fit. A point worth mentioning is that the three-atom MS signal from Fe-O-C_1 is out of phase with the Fe-C_1 signal between 2.5 and 7.5 Å^{-1} (the Fe-O-C_1 signal dies off after 7.5 Å^{-1}) (this can be seen in Figure 2.4). This has implications when using SS Fe-C second-shell parameters in empirical fits. One can only assume phase and amplitude transferability in the second shell if the two distances and *the angle* of the model are very close to the comparable distances and angle in the unknown. Therefore, the GNXAS method is advantageous in that it can account for the strength and the complexity of MS contributions in an inorganic compound with a noncollinear arrangement of atoms. Once the MS signals are modeled correctly, reliable bond distances and angles can be obtained not only from the first-shell but also from second- and third- shell neighbors without dependence on obtaining suitable models from which to extract such empirical parameters.

2.3.3.2. $Na[Fe(OH_2)EDTA]$. Similar methodology was applied to $Na[Fe(OH_2)EDTA]$ Fe K-edge EXAFS data to evaluate the ability of GNXAS to theoretically analyze the EXAFS data of a lower symmetry coordination complex with mixed ligation. The structure of $[Fe(H_2O)EDTA]^-$ (shown in Figure 2.6) is not as well-ordered as that of $Fe(acac)_3$ and more like the structures of metalloenzymes for which it is expected that the GNXAS methodology will be particularly useful. The crystal structure of $Li[Fe(OH_2)EDTA]\cdot 2H_2O$ was previously reported.[63] The iron atom is surrounded by five oxygens and two nitrogens in the first shell with two O_1's at 1.97 Å, two O_2's at 2.11 Å, a water at 2.11 Å, and two N's at 2.32 Å. Each oxygen (except for the water) is bound to a carbon which is bound to another oxygen. Each nitrogen is bound to three carbons that link the hexadentate ligand. The crystallographic values of $Li[Fe(OH_2)EDTA]\cdot 2H_2O$ were used to generate the two-atom and three-atom configurations up to 4.5 Å with a frequency tolerance of 0.1 Å. The reduced Norman sphere radii used in the phase shift calculation were 1.17 Å for Fe, 0.730 Å for O, 0.751 Å for N, and 0.772 Å for C. The peaks in the two-atom distribution include two short Fe-O_1 distances, two long Fe-O_2 distances, one Fe-OH_2 distance, two Fe-N distances, ten Fe-C distances between 2.83 and 3.16 Å, and four Fe-O_3 distances between 3.91 and 4.22 Å. There were approximately 30 unique three-atom contributions which ranged in distance from 3.04 Å to 4.5 Å. The signals attributed to each of the two- and three-atom configurations were calculated. Due to the complexity of the structure, contributions to the fits were systematically introduced. The spline was in three segments of order 3,4,4 with defining energy points of 7155, 7250, 7600, and 7999 eV. Least-squares fits were done with k^3 weighting over the k range 2.8-15.1 $Å^{-1}$.

The first-shell fit contained waves from the following two-atom configurations: Fe-O_1 [2] at 1.97 Å, Fe-O_2 [3] at 2.11 Å, and Fe-N [2] at 2.32 Å, where the number in the brackets indicates the coordination number (see Table 2.2 for the range of

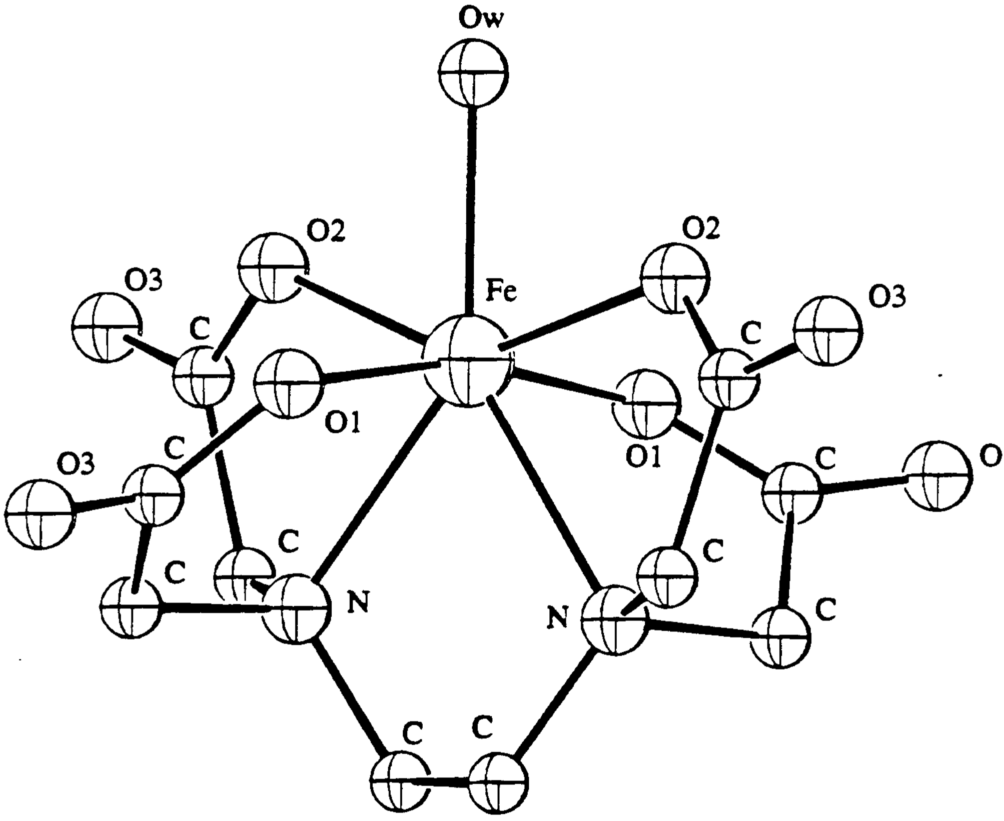

Figure 2.6. Molecular structure of [Fe(OH$_2$)EDTA]$^-$ with atom designations as used in the text.

Table 2.2. Comparison of the Na[Fe(OH_2)EDTA] GNXAS Values to the Crystallographic Values of Li[Fe(OH_2)EDTA]·$2H_2O$.

structural feature (# of configurations in complex)	Na[Fe(OH_2)EDTA] GNXAS distances/angles	Na[Fe(OH_2)EDTA] GNXAS bond variance (σ_R^2)/ angle variance (σ_θ^2)[a]	Li[Fe(OH_2)EDTA]· $2H_2O$ crystallographic distances/angles average [range]
Fe-O_1 (2)	1.97 Å	0.003	1.97 Å [1.94-2.00]
Fe-O_2 (3)	2.10 Å	0.004	2.11 Å [2.11-2.13]
Fe-N (2)	2.33 Å	0.003	2.32 Å [2.30-2.35]
O_1-C (2)	1.33 Å	0.005	1.28 Å [1.27-1.29]
O_2-C (2)	1.30 Å	0.004	1.26 Å [1.26-1.27]
N-C (6)	1.48 Å	0.002	1.47 Å [1.47-1.48]
$O_{1,2}$-O_3 (4)	2.30 Å	0.006	2.23 Å [2.20-2.25]
C-O_3 (4)	1.27 Å	0.006	1.23 Å [1.21-1.25]
Fe-C (4)	2.91 Å	0.008	2.91 Å [2.79-2.99]
Fe-O_1-C (2)	121°	3×10^1	120° [119-121]
Fe-O_2-C (2)	119°	6×10^1	122° [121-123]
Fe-N-C (6)	106°	1×10^1	108° [103-112]
O_1-Fe-O_1 (1)	170°	1×10^1	166°
O_2-Fe-O_2 (1)	150°	2×10^0	145°
Fe-O_1-O_3 (2)	150°	5×10^1	145° [142-148]
Fe-O_2-O_3 (2)	155°	5×10^1	149° [148-150]
Fe-C-O_3 (4)	158°	1×10^1	158° [153-161]

[a] Bond and angle variances are reported in Å^2 and degrees^2, respectively.

crystallographic distances). The Fe-OH_2 and long Fe-O_2 distances were treated together since they both have a distance of 2.11 Å. All five oxygens could not be averaged and treated as a single shell because the EXAFS signals from the short Fe-O_1 and longer Fe-O_2 strongly interfere at higher k (Figure 2.7). This first-shell fit (not shown) gave an R value of 0.118×10^{-4} with good agreement between the FT of the experimental data and the fit signal up to 2.0 Å (corresponding to ~2.4 Å in the cluster when the phase shift is taken into account). The major contributions in the EXAFS signal were accounted for using the three first-shell distances, with especially good agreement at higher k. The next fit included signals from three-atom configurations: Fe-O_1-C, Fe-O_2-C, and Fe-N-C. The R value decreased to 0.437×10^{-5}. The total theoretical EXAFS signal fits extremely well to the experimental EXAFS above $k = 8$ Å^{-1}, and there were several peaks between 2.0 and 3.0 Å in the FT. However, peaks above 3.0 Å in the FT were not being fit well and high frequency components could be seen in the EXAFS residual, especially at lower k. Therefore other three-atom components were examined for signals that were relatively strong and of the same frequency as those in the residual.

All the ~90° signals associated with O-Fe-O, O-Fe-N, and N-Fe-N were extremely weak. Both the O_1-Fe-O_1 and O_2-Fe-O_2 MS signals contributed only a small amount at low k. The Fe-O_1-O_3 and Fe-O_2-O_3 signals were significant. However, the Fe-C-O_3 contribution was found to be extremely strong and largely responsible for the peak in the FT at ~3.5 Å. The best fit was obtained when the last five mentioned contributions were included. The results of this fit are shown in Figure 2.7, and a comparison of the distances and angles to the Li[Fe(OH_2)EDTA]·$2H_2O$ crystallographic values are given in Table 2.2. The individual contributions to the FT are shown in Figure 2.8. With an R value of 0.735×10^{-6}, this fit was a factor of 6 better than the fit that included the first neighbors and Fe-O_1-C, Fe-O_2-C, and Fe-N-C signals. The fit compares extremely well to the experimental EXAFS with the exception of high frequency components between 7.5 and 12 Å^{-1} (see results in Figure 2.7). These higher frequency components can possibly be attributed to intermolecular signals that were not accounted for because the cluster was only generated up to 4.5 Å. The FT of the theoretical fit is in close agreement with the FT of the experimental data up to 4.0 Å. The low-frequency EXAFS is dominated by three waves from the g_2 contributions: Fe-O_1, Fe-O_2, and Fe-N. The EXAFS distances for these three shells show excellent agreement with the Li[Fe(OH_2)EDTA]·$2H_2O$ crystallographic values, deviating by <0.01 Å. The Fe-O_1-C, Fe-O_2-C, and Fe-N-C waves have significant contributions in the FT region between 2.0 and 3.0 Å, with Fe-N-C having the largest signal because of the 6-fold degeneracy. The

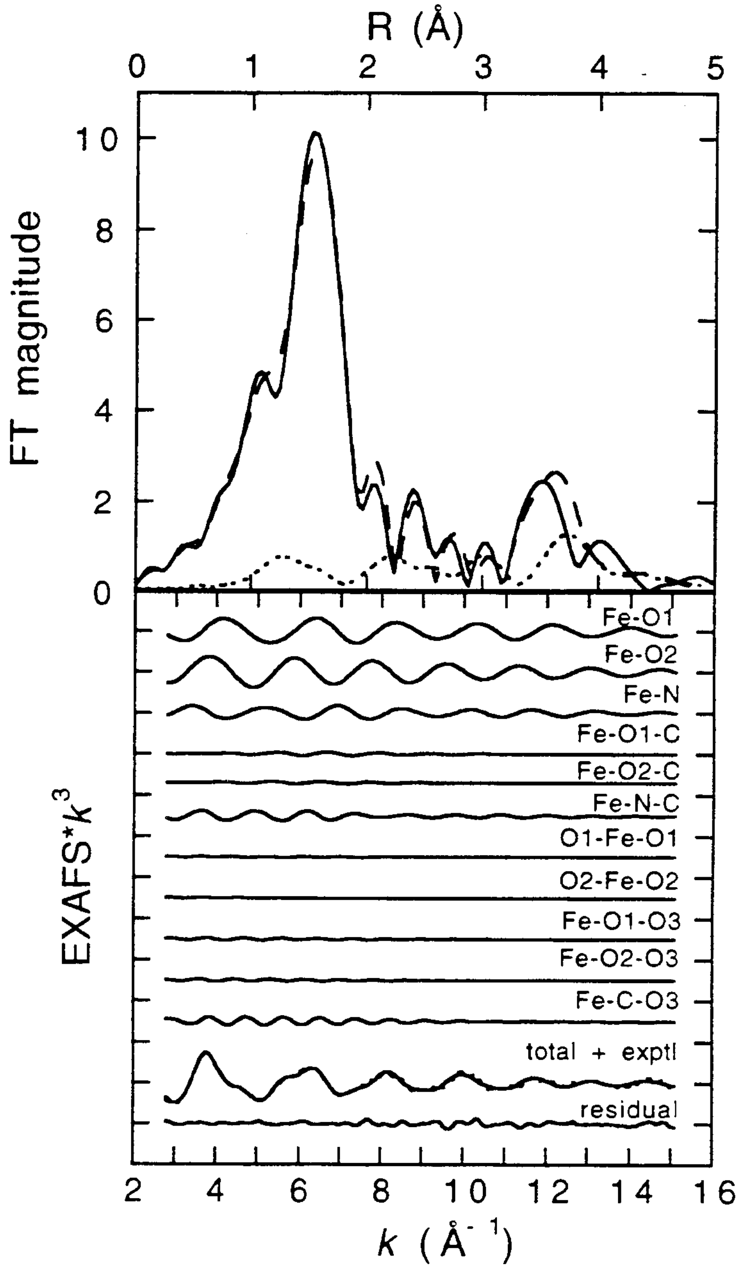

Figure 2.7. Comparison of the GNXAS theoretical signal with experimental data of Fe K-edge k^3-weighted EXAFS data between 7155 and 7999 eV of Na[Fe(OH$_2$)EDTA]. The top portion of the figure contains the non-phase shift corrected FT of the k^3-weighted experimental EXAFS data (——) and that of the total theoretical signal (----). Also shown is the FT of the residual (····). The lower portion of the figure presents the EXAFS signals for the individual contributions. The total theoretical signal is also shown (——) and compared with the experimental data (····) with the residual being the difference between the experimental and the theoretical EXAFS. (The ordinate scale is 10 between two consecutive tick marks.)

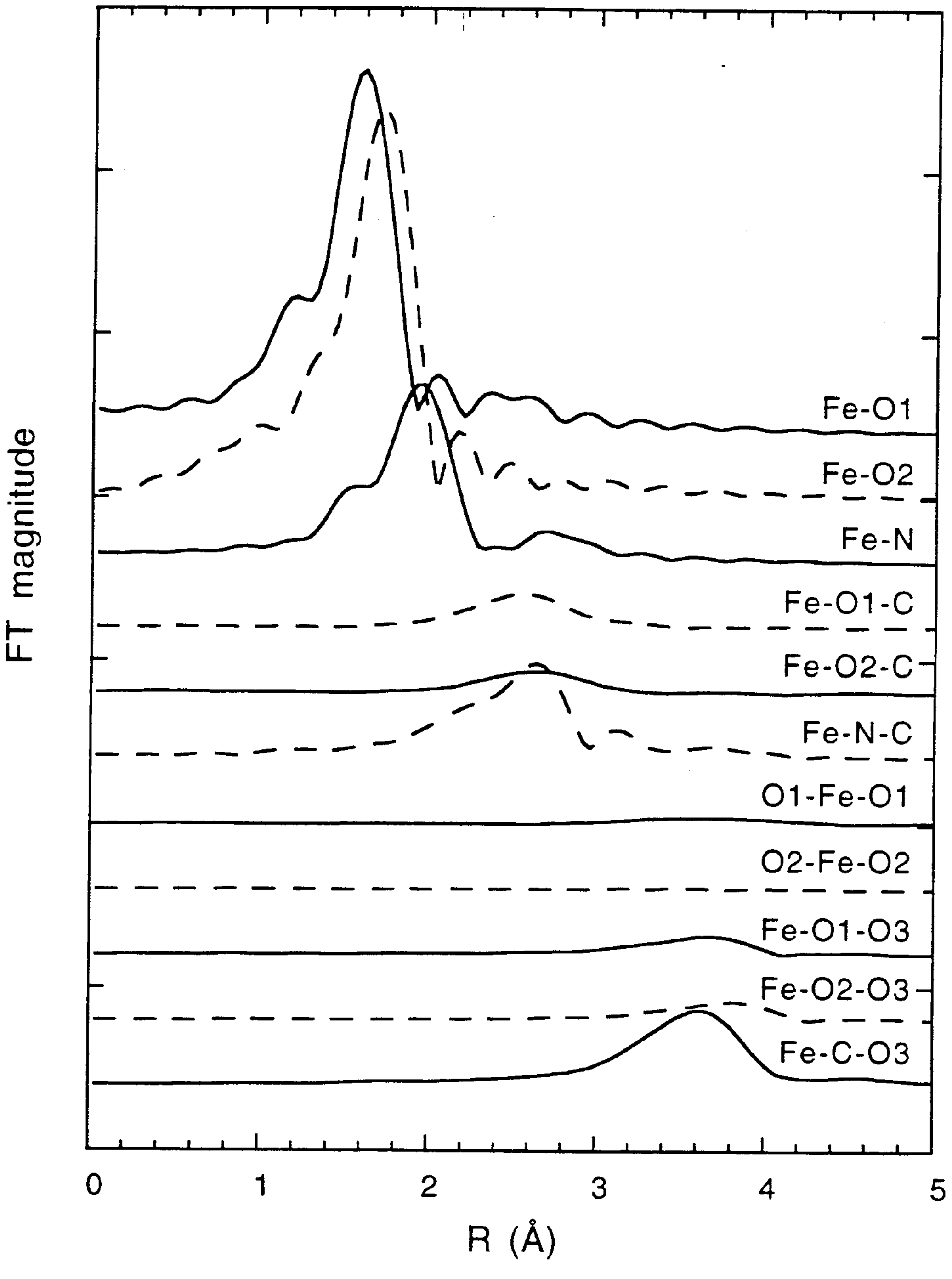

Figure 2.8. FT of the EXAFS signals of Na[Fe(OH_2)EDTA] for the individual contributions shown in Figure 2.7. The first-shell signals contribute significantly below 2.5 Å with the Fe-O_1-C, Fe-O_2-C, and Fe-N-C signals contributing between 2.5 and 3.2 Å. The main contribution above 3.0 Å comes from Fe-C-O_3. (The ordinate is 5 between two consecutive tick marks.)

higher frequency region is dominated by the Fe-C-O_3 signal. A focusing effect occurs because of the large Fe-C-O_3 angle (161°).

Not only are the structural values obtained from the GNXAS fit consistent with the crystallographic values but the GNXAS total EXAFS signal compared to the data and the respective FT of the fit and the data agree remarkably well for a low-symmetry coordination complex with mixed ligation. The fitted parameters are in substantially good agreement with crystallographic data, even though the fit is slightly under-determined (37 fitting parameters compared to 36 independent points). The bond distances obtained from GNXAS for the three first neighbors distance are all within 0.01 Å of the crystallographic values (see Table 2.2). The GNXAS bond distances and angles that make up the g_3 contributions are within 4% of the average crystallographic values, with the strength of the signal influencing the goodness of the match. The configurations with stronger signals have distances and angles that are closer to the crystallographic values than the configurations with weaker signals. For example, the first shell has the strongest contributions and the calculated distances are within the range of the Li[Fe(OH_2)EDTA]·$2H_2O$ crystallographic values. The Fe-N-C signal is much stronger than the Fe-O-C signals. The difference between the crystallographic and calculated N-C distance is 0.01 Å while the difference between the crystallographic and calculated O-C distance is 0.05 Å. Since the Fe-C-O_3 signal is strong, accurate distances and angles are obtainable, even though the O_3 atoms are over 4 Å away from the Fe atom. GNXAS also proved to be internally consistent, in that the first-shell distances varied <0.01 Å, the low-*Z* bond distances (*i.e.*, O-C and N-C) varied ±0.04 Å, and the bond angles varied ±3° over a large number of fits with varying contributions, splines, and nonstructural parameters.

2.3.3.3. $K_3Fe(CN)_6$. The GNXAS programs were applied to $K_3Fe(CN)_6$ EXAFS data to investigate the MS of the linear Fe-C-N unit and to test the feasibility of using GNXAS for angle determination studies for low-*Z* diatomics coordinated to transition metal centers. The iron atom in $K_3Fe(CN)_6$ is in an octahedral environment[65] with an average Fe-C bond distance of 1.94 Å and a range of 1.93 - 1.94 Å. The Fe-C-N angle ranges from 177 to 179° with a C-N distance of 1.15 Å. The crystallographic values of $K_3Fe(CN)_6$ were used to characterize the two-atom and three-atom configurations up to 4.5 Å with a frequency tolerance of 0.1 Å. The reduced Norman sphere radii used in the phase shift calculation were 0.946 Å for Fe, 0.654 Å for C, and 0.668 Å for N. The two-atom configurations included Fe-C while the three-atom configurations included Fe-C-N, C-Fe-C (90°), and C-Fe-C (180°). The two-region spline had orders of 3, 4 with defining energy points of 7160, 7300, and 7999 eV. The coordination numbers were fixed to the known values, and the Fe-C and C-N distances were allowed to vary along with the respective variances. The independent points to parameters ratio is 36 to 19, indicating that the fit to the data will be overdetermined by almost a factor of 2. A comment has to be made for collinear configurations. In the GNXAS programs, a Taylor expansion of amplitudes and phases is used during the fitting procedure with first order derivatives. For a collinear structure (θ = 180°), the first order derivative is zero and therefore the program uses the second-derivative. Thus, the thermal and configurational averages of the Fe-C-N contributions were performed using a second-order Taylor expansion for the amplitude and phase around $\theta = 180°$, as described elsewhere.[9] The agreement with the experimental data was found to be much worse with fits having angles $\theta < 178°$, thus indicating a strong sensitivity of the signal to the geometry of the collinear configuration. In addition, the angles around the iron were constrained to be octahedral. Least-squares fits were done with k^3 weighting over the k range of 2.9-15.1 Å^{-1}.

The best fit gave an Fe-C distance of 1.92 Å and a C-N distance of 1.18 Å. The EXAFS contributions and the FT of the best fit are presented in Figure 2.9 and show good agreement to the experimental data. The Fe-C SS signal and the Fe-C-N MS signal dominate the EXAFS spectrum. The angular sensitivity of the Fe-C-N signal was investigated by fixing all the distances and variances and generating the MS signal from Fe-C-N and the SS signal from Fe-N as a function of the Fe-C-N angle (Figure 2.10). The MS signal from the Fe-C-N unit shows considerable amplitude enhancement for angles greater than about 150°, as reported in earlier papers for Fe-O-Fe and metal carbonyl systems.[8-12] This indicates that GNXAS can be used to analyze MS effects as a function of angle, and where the angular dependent amplitude/phase effects become significant (above about 150°), angles can be fairly accurately determined for Fe-C-N configurations. This should also be the case for similar systems such as nitrosyl and dioxygen complexes even when contributions from other outer shell scatterers may be present.

2.4. Summary

In this chapter an *ab initio*, integrated approach to EXAFS data analysis, called GNXAS, has been described. The characteristics and advantages of this approach were investigated by applying the method to Fe K-edge EXAFS data of three iron coordination complexes of known structure. Accurate structural results were obtained by using a fitting procedure which takes into account two-atom and three-atom MS signals. The raw

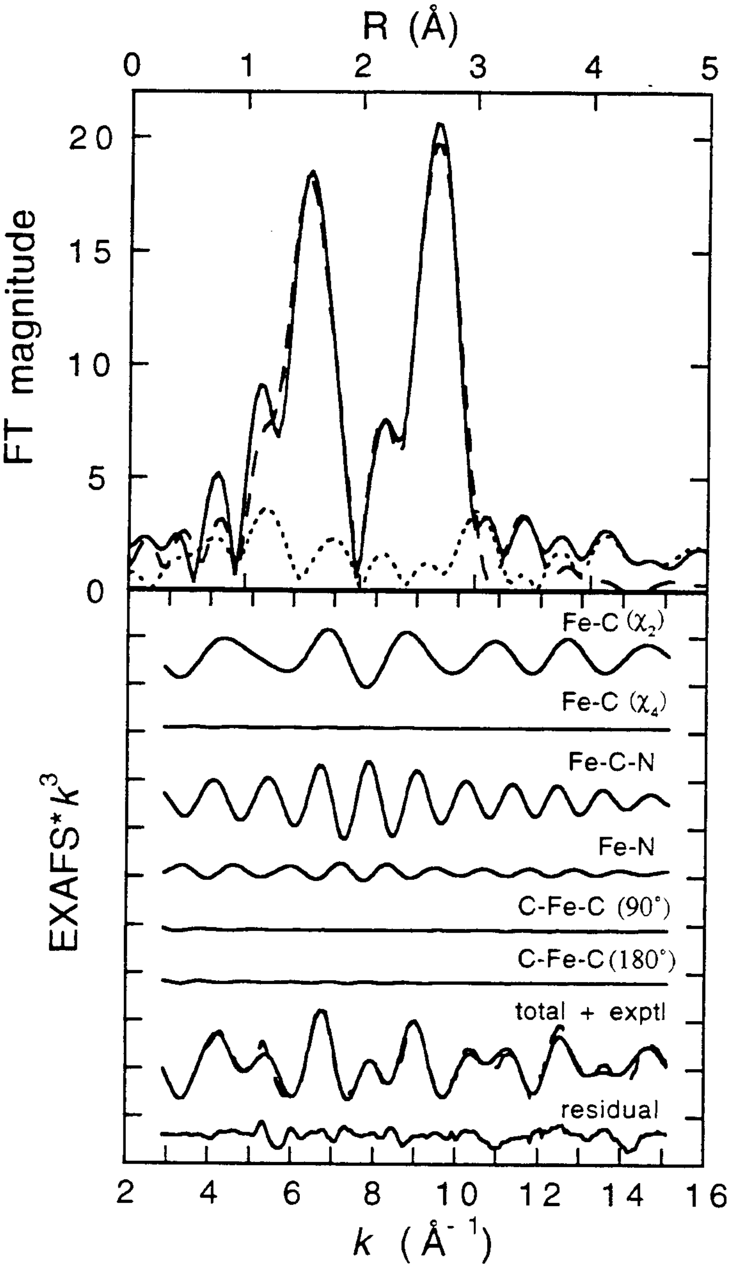

Figure 2.9. Comparison of the GNXAS theoretical signal with experimental data of Fe K-edge k^3-weighted EXAFS data between 7160 and 7999 eV of $K_3Fe(CN)_6$. The top portion of the figure contains the non-phase shift corrected FT of the k^3-weighted experimental EXAFS data (——) and that of the total theoretical signal (----). Also shown is the FT of the residual (····). The lower portion of the figure presents the EXAFS signals for the individual contributions. The total theoretical signal is also shown (——) and compared with the experimental data (····) with the residual being the difference between the experimental and the theoretical EXAFS. (The ordinate scale is 10 between two consecutive tick marks.

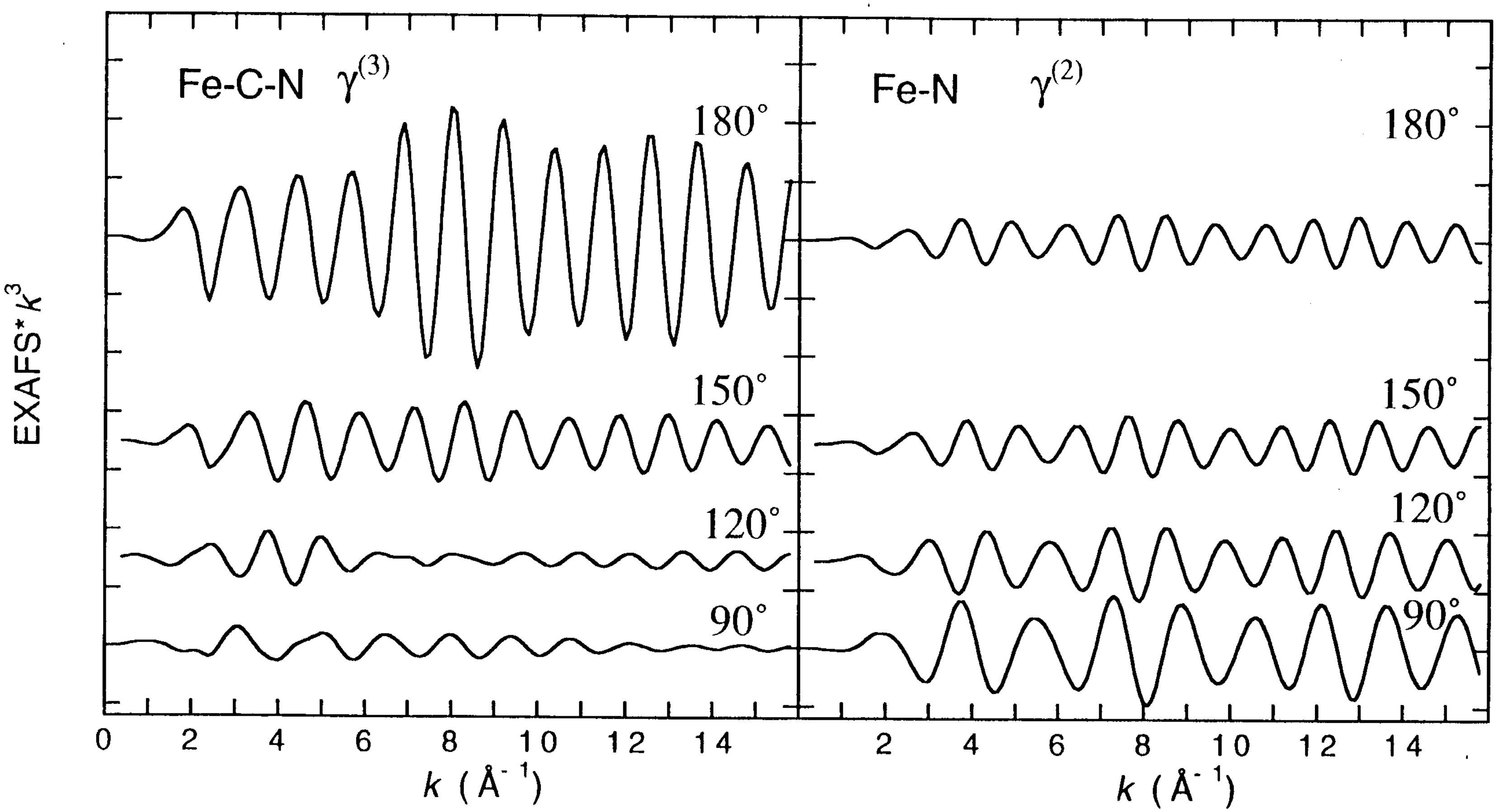

Figure 2.10. Comparison of the EXAFS signals of the $\gamma^{(3)}$ Fe-C-N contribution to the $\gamma^{(2)}$ Fe-N contribution when the Fe-C-N angle equals 180°, 150°, 120°, and 90°. Notice the increased amplitude enhancement of the $\gamma^{(3)}$ Fe-C-N signal above 150°. This indicates that GNXAS can be used to determine angles fairly accurately above 150° for Fe-C-N configurations and other similar systems where diatomics may be coordinated to a transition metal center. (The ordinate scale is 10 between two consecutive tick marks.)

data were fit in a way that reduces the tedious standard preanalysis of manual spline-background removal and without dependence on obtaining suitable models from which to extract empirical phase and amplitude parameters. First neighbor distances deviated less than 0.01 Å from the crystallographic values, which is comparable or better than that which can be obtained by empirical-based methods. Bond distances and angles of second (and in some cases third) neighbors were also obtained due to the accurate modeling of MS contributions. The second and third neighbor distances and angles were found to be in good agreement with crystallographic values, typically within the crystallographic range and varying only 4% in distance and angle from the average. These findings are of general importance for structural studies of chemical systems, including inorganic complexes and metalloproteins. Further, they demonstrate that a proper treatment of the MS components in the EXAFS signal is necessary to get reliable structural information on distant neighbors. Moreover, accurate bond angle determination for angles over about 150° is feasible for Fe-C-N and other similar systems using the GNXAS approach to accurately analyze MS effects.

2.5. Acknowledgments

This research was supported by grants from the NIH (RR01209, K.O.H.; GM40392, E.I.S.) and NSF (CHE91-21576, K.O.H.). Stanford Synchrotron Radiation Laboratory is supported by the Department of Energy, Office of Basic Energy Science, Divisions of Chemical Science and Material Science, and in part by the National Institutes of Health, National Center of Research Resources, Biomedical Research Technology Program (RR-01209) and DOE's Office of Health and Environmental Research. Rino Natoli, Andrea Di Cicco and Adriano Filipponi (who are supported by the Italian INFN and CNR research institutions) are gratefully acknowledged for providing the GNXAS program set and for their help in introducing me to the intricacies of the this data analysis package.

2.6. References and Notes

(1) Cramer, S. P. In *X-ray Absorption: Principles, Applications, Techniques of EXAFS, SEXAFS and XANES*; Koningsberger, D. C, Prins, R., Eds.; John Wiley and Sons Inc.: New York, 1988; p 573.

(2) Cramer, S. P.; Hodgson, K. O. *Prog. Inorg. Chem.* **1979**, *25*, 1.

(3) Lytle, F. W.; Via, G. H.; Sinfelt, J. H. In *Synchrotron Radiation Research*; Winick, H., Doniach, S. Eds.; Plenum Press: New York, 1980; Chapter 12.

(4) Lagarde, P.; Dexpert, H. *Adv. Phys.* **1984**, *33*, 567.

(5) Iwasawa, Y. *Tailored Metal Catalysts;* D. Reidel Publishing Co.: Dordrecht, The Netherlands, 1986.

(6) Cramer, S. P.; Hodgson, K. O.; Stiefel, E. I.; Newton, W. E. *J. Am. Chem. Soc.* **1978**, *100*, 2748.

(7) a) Scott, R. A. *Methods Enzymol.* **1985**, *117*, 414.
b) Shulman, R.G.; Eisenberger, P.; Kincaid, B.M. *Ann. Rev. Biophys. Bioeng.* **1978**, *7*, 559.

(8) Co, M. S.; Hendrickson, W. A.; Hodgson, K. O.; Doniach, S. *J. Am. Chem. Soc.* **1983**, *105*, 1144.

(9) Filipponi, A.; Di Cicco, A.; Zanoni, R.; Bellatreccia, M.; Sessa, V.; Dossi, C.; Psaro, R. *Chem. Phys. Lett.* **1991**, *184*, 485.

(10) Binsted, N.; Cook, S. L.; Evans, J.; Greaves, G. N.; Price, R. J. *J. Am. Chem. Soc.* **1987**, *109*, 3669.

(11) Binsted, N.; Evans, J.; Greaves, G. N.; Price, R. J. *J. Chem. Soc., Chem. Commun.* **1987**, 1130.

(12) Teo, B. -K. *J. Am. Chem. Soc.* **1981**, *103*, 3990.

(13) Co, M. S.; Scott, R. A.; Hodgson, K. O. *J. Am. Chem. Soc.* **1981**, *103*, 986.

(14) Hasnain, S. S.; Strange, R. W. In *Synchrotron Radiation and Biophysics;* Hasnain, S. S., Ed.; Ellis Horwood: Chichester, U.K., 1990; Chapter 4 and references therein.

(15) Filipponi, A.; Di Cicco, A.; Tyson, T. A.; Natoli, C. R. *Solid State Commun.* **1991**, *78*, 265.

(16) Filipponi, A.; Di Cicco, A. *Synchrotron Radiation News* **1993**, *6*, 13.

(17) Filipponi, A.; Di Cicco, A. Unpublished data.

(18) a) Rehr, J. J.; Albers, R. C.; Zabinsky, S. I. *Phys. Rev. Lett.* **1992**, *69*, 3397.
b) Rehr, J. J. *Jpn. J. Appl. Phys.* **1993**, *32*, 8.

(19) a) Frenkel, A. I.; Stern, E. A.; Qian, M.; Newville, M. *Phys. Rev. B* **1993**, *48*, 12449.
b) Frenkel, A. I.; Stern, E. A.; Voronel, A.; Qian, M.; Newville, M. *Phys. Rev. Lett.* **1993**, *71*, 3485.

(20) Binsted, N.; Campbell, J. W.; Gurman, S. J.; Stephenson, P. C. *"SERC Daresbury Laboratory EXCURVE92 program"* 1991.

(21) Di Cicco, A.; Stizza, S.; Filipponi, A.; Boscherini, F.; Mobilio, S. *J. Phys. B: At. Mol. Opt. Phys.* **1992**, *25*, 2309.

(22) D'Angelo, P.; Di Cicco, A.; Filipponi, A.; Pavel, N. V. *Phys. Rev. A* **1993**, *47*, 2055.

(23) Burattini, E.; D'Angelo, P.; Di Cicco, A.; Filipponi, A.; Pavel, N. V. *J. Phys. Chem.* **1993**, *97*, 5486.

(24) Nordlander, E.; Lee, S. C.; Cen, W.; Wu, Z. Y.; Natoli, C. R.; Di Cicco, A.; Filipponi, A.; Hedman, B.; Hodgson, K. O.; Holm, R. H. *J. Am. Chem. Soc.* **1993**, *115*, 5549.

(25) Westre, T. E.; Di Cicco, A.; Filipponi, A.; Natoli, C. R.; Hedman, B.; Solomon, E. I.; Hodgson, K. O. *J. Am. Chem. Soc.* **1995**, *117*, 1566.

(26) DeWitt, J. G.; Bentsen, J. G.; Rosenzweig, A. C.; Hedman, B.; Green, J.; Pilkington, S.; Papaefthymiou, G. C.; Dalton, H.; Hodgson, K. O.; Lippard, S. J. *J. Am. Chem. Soc.* **1991**, *113*, 9219.

(27) Hedman, B.; Co, M. S.; Armstrong, W. H.; Hodgson, K. O.; Lippard, S. J. *Inorg. Chem.* **1986**, *25*, 3708.

(28) Tsang, H. -T.; Batie, C. J.; Ballou, D. P.; Penner-Hahn, J. E. *Biochemistry* **1989**, *28*, 7233.

(29) Scarrow, R. C.; Maroney, M. J.; Palmer, S. M.; Que, L., Jr.; Roe, A. L.; Salowe, S. P.; Stubbe, J. *J. Am. Chem. Soc.* **1987**, *109*, 7857.

(30) Mustre de Leon, J.; Rehr, J. J.; Zabinsky, S. I.; Albers, R. C. *Phys. Rev. B* **1991**, *44*, 4146.

(31) Rehr, J. J.; Mustre de Leon, J.; Zabinsky, S. I.; Albers, R. C. *J. Am. Chem. Soc.* **1991**, *113*, 5135.

(32) Lee, P. A.; Citrin, P. H.; Eisenberger, P.; Kincaid, B. M. *Rev. Mod. Phys.* **1981**, *53*, 769.

(33) Rehr, J. J.; Albers, R. C.; Natoli, C. R.; Stern, E. A. *Phys. Rev. B* **1986**, *34*, 4350.

(34) Müller, J. E.; Schaich, W. L. *Phys. Rev. B* **1983**, *27*, 6489.

(35) Schaich, W. L. *Phys. Rev. B* **1984**, *29*, 6513.

(36) Lee, P. A.; Pendry, J. B. *Phys. Rev. B* **1975**, *11*, 2795.

(37) Natoli, C. R.; Benfatto, M. *J. Phys.* **1986**, *47*, C8.

(38) Vvedensky, D. D.; Saldin, D. K.; Pendry, J. B. *Comput. Phys. Commun.* **1986**, *40*, 421.

(39) Durham, P. J.; Pendry, J. B.; Hodges, C. H. *Solid State Commun.* **1981**, *38*, 159.

(40) Mattheiss, L. F. *Phys. Rev.* **1964**, *134*, A970.

(41) Hedin, L.; Lundqvist, S. *Solid State Phys.* **1969**, *23*, 1.

(42) Lundqvist, B. I. *Phys. Kondens. Materie* **1967**, *6*, 193.

(43) Penn, D. R. *Phys. Rev. B* **1987**, *35*, 482.

(44) Lee, P. A.; Beni, G. *Phys. Rev. B* **1977**, *15*, 2862.

(45) Tyson, T. A.; Hodgson, K. O.; Natoli, C. R.; Benfatto, M. *Phys. Rev. B* **1992**, *46*, 5997.

(46) Natoli, C. R. In *X-ray Absorption Fine Structure*; Hasnain, S. S., Ed.; Ellis Horwood: Chichester, U.K., 1991; p 6.

(47) Tyson, T. A.; Benfatto, M.; Natoli, C. R.; Hedman, B.; Hodgson, K. O. *Physica B* **1989**, *158*, 425.

(48) Filipponi, A.; Di Cicco, A.; Benfatto, M.; Natoli, C. R. *Europhys. Lett.* **1990**, *13*, 319.

(49) Filipponi, A. *J. Phys.: Condens. Matter* **1991**, *3*, 6489.

(50) Benfatto, M.; Natoli, C. R.; Filipponi, A. *Phys. Rev. B* **1989**, *40*, 9626.

(51) Stern, E. A.; Bunker, B. A.; Heald, S. M. *Phys. Rev. B* **1980**, *21*, 5521.

(52) Müller, J. E.; Jepsen, O.; Wilkins, J. W. *Solid State Commun.* **1982**, *42*, 365.

(53) Müller, J. E.; Wilkins, J. W. *Phys. Rev. B* **1984**, *29*, 4331.

(54) Newville, M.; Livins, P.; Yacoby, Y.; Rehr, J. J.; Stern, E. A. *Phys. Rev. B* **1993**, *47*, 14126.

(55) Bevington, P. R.; Robinson, D. K. *Data Reduction and Error Analysis for the Physical Sciences*; McGraw-Hill: New York, 1992.

(56) Stern, E. A. *Phys. Rev. B* **1993**, *48*, 9825.

(57) Krause, M. O.; Oliver, J. H. *J. Phys. Chem. Ref. Data* **1979**, *8*, 329.

(58) The principal determining factor is the monochromator and associated vertical slit opening, with the resolution determined by the relationship $\Delta E/E = \cot(\Theta)\Delta\Theta$, where Θ is a function of the Darwin width and the vertical angular acceptance of the monochromator. The value at the Fe K-edge for the experimental conditions used for these experiments were ~1.4 eV. Lytle, F. W. In *Applications of Synchrotron Radiation*; Winick, H.; Xiam, D.; Ye, M.-h; Huang,T., Eds.; Gordon and Breach Science Publishers: New York, 1989; p. 135.

(59) Di Cicco, A. Ph.D. Thesis, *University of Rome "La Sapienza"*, 1991.

(60) Di Cicco, A.; Filipponi, A. Unpublished.

(61) Joyner, R. W.; Martin, K. J.; Meehan, P. *J. Phys. C* **1987**, *20*, 4005.

(62) Norman, J. G., Jr. *Mol. Phys.* **1976**, *31*, 1191.

(63) Lind, M. D.; Hamor, M. J.; Hamor, T. A.; Hoard, J. L. *Inorg. Chem.* **1964**, *3*, 34.

(64) Iball, J.; Morgan, C. H. *Acta Crystallogr.* **1967**, *23*, 239.

(65) Figgis, B. N.; Skelton, B. W.; White, A. H. *Aust. J. Chem.* **1978**, *31*, 1195.

Chapter 3

Determination of the Fe-N-O Angle in $\{FeNO\}^7$ Complexes Using Multiple-Scattering EXAFS Analysis by GNXAS

3.1. Introduction

Mononuclear high spin non-heme ferrous centers are present in the catalytic active sites of a large number of enzymes involved in the binding and activation of molecular dioxygen.[1] An understanding of the reactivity of these enzymes requires knowledge of the geometric and electronic structures of the active sites as well as their interactions with substrate, dioxygen, and other molecules of relevance to catalysis. Understanding the oxygen intermediates involved in catalysis is key to obtaining molecular insight into the mechanism of the reaction. Unfortunately, these intermediates are often too unstable to allow detailed spectroscopic study. Nitric oxide reversibly binds to the ferrous active site of the native form of many of these non-heme iron enzymes to generate stable nitrosyl complexes.[2] These enzyme-NO complexes can serve as analogs of the possible dioxygen intermediates involved in catalysis and can be readily studied spectroscopically to determine geometric and electronic structure differences which could provide insight into differences in oxygen activation by the enzymes.

However, in order to use the NO derivative of these non-heme iron enzymes as a probe of electron distribution related to dioxygen reactivity, a detailed understanding of the electronic and geometric structure of the $\{FeNO\}^7$ unit[3] is required. $\{FeNO\}^7$ complexes have been described in the literature as having different electronic structures for different geometric structures, linear Fe-N-O being viewed as Fe^+ and NO^+ and bent Fe-N-O as Fe^{3+} and NO^-. Enzyme-NO complexes as well as several $\{FeNO\}^7$ model compounds (in particular FeEDTA-NO, *vide infra*) exhibit an unusual S=3/2 EPR signal.[2] A wide range of bonding descriptions have appeared[4] to describe this S=3/2 signal including $[Fe^+d^7(S=3/2)$ - $NO^+(S=0)]$, $[Fe^{2+}d^6(S=2)$ - $NO^0(S=1/2)]$ antiferromagnetically coupled, $[Fe^{3+}d^5(S=1/2)$ - $NO^-(S=1)]$ ferromagnetically coupled, and $[Fe^{3+}d^5(S=3/2)$ - $NO^-(S=0)]$. Recently a combination of spectroscopic and theoretical methods was used to determine that the appropriate description of the S=3/2 $\{FeNO\}^7$ unit is high spin Fe^{3+}(S=5/2) antiferromagnetically coupled to an NO^- (S=1) to produce the S=3/2 ground state.[5]

In the present study, extended X-ray absorption fine structure (EXAFS) data on a series of $\{FeNO\}^7$ model compounds were measured and analyzed to characterize the geometric structure of the Fe-N-O unit. Multiple-scattering effects from distant shells can contribute significantly to the EXAFS of inorganic molecules,[6] and these effects have been used in a few favorable cases to obtain angular information.[7] The effects are particularly evident when an intervening atom nears a linear relationship with an absorber and a distant scatterer, as occurs in Fe-oxo dimers[7b] and metal carbonyls.[8] An empirical data analysis approach was utilized to determine the Fe-O-Fe angle in oxygen-bridged iron complexes.[7b] The analysis demonstrated that it was possible to estimate the Fe-O-Fe bridging angle to within ±8° and calculate the Fe-Fe distance to ±0.05 Å. In the present study, the same traditional empirical EXAFS technique was initially applied to the $\{FeNO\}^7$ systems to determine the Fe-N-O angle. However, determination of the Fe-N-O angle using the empirical technique was not found to be possible because the oxygen of the Fe-N-O is not a heavy back-scatterer, the quality of empirical Fe-N and Fe-O (second shell) phases and amplitudes is poor, and other low Z atoms are at approximately the same distance as the Fe-O (second shell).[9] Since angle determination by empirical methods did not prove to be feasible, a new theoretical EXAFS data analysis package, GNXAS,[10] was utilized to probe the Fe-N-O bond angle using a multiple-scattering analysis and establish the generality of the approach for angle determination of low-Z small molecules liganded to transition metal complexes.

The GNXAS package provides a new integrated approach to the analysis of EXAFS data based on full curved-wave, multiple-scattering theoretical analysis. It incorporates direct fitting of theoretical spectra (calculated by utilizing the Hedin-Lundqvist complex exchange and correlations potential[11]) to the experimental data and utilizes single- and multiple-scattering signals with the proper treatment of correlated distances and Debye-Waller factors. GNXAS has been evaluated on simpler systems (including SiX_4 (X = F, Cl, CH_3),[12] $Os_3(CO)_{12}$,[8d] Br_2 and HBr,[13] and brominated hydrocarbons[14]) and a more complex heterometal cluster.[15] It has been demonstrated in the previous chapter that the GNXAS method can provide accurate bond distances and angles for second and third neighbors for Fe complexes.[16]

In this study, the EXAFS data of a series of crystallographically-characterized $\{FeNO\}^7$ compounds with varying Fe-N-O angles were analyzed using the GNXAS method to examine the sensitivity of this method to Fe-N-O angle determination. The compounds studied were $[Fe(TMC)NO](BF_4)_2$[17] (where TMC = 1,4,8,11-tetramethyl-1,4,8,11-tetraazacyclotetradecane), which has an Fe-N-O bond angle of 177.5(5)°, $Fe(TACN)(N_3)_2NO$[4e] (where TACN = *N*,*N*',*N*"-trimethyl-1,4,7-triazacyclononane) which has an angle of 156(1)°, and Fe(salen)NO[18] (where salen = *N*,*N*'-ethylenebis(salicylideneiminato)), which has a bond angle of 127(6)° at -175 °C and 147(5)° at 23 °C.

EXAFS data for FeEDTA-NO (whose crystal structure is not known due to lack of suitable crystals) were obtained and analyzed to determine the unknown Fe-N-O bond angle. In order to use the GNXAS method to calculate the theoretical EXAFS spectrum, an initial structural model is needed. Such a model for this unknown structure was obtained by comparing first-shell empirical fits of the EXAFS data of $[Fe(H_2O)EDTA]^-$, $[Fe(H_2O)EDTA]^{2-}$, and FeEDTA-NO. The Fe-O and Fe-N distances of the EDTA ligand in FeEDTA-NO were much closer to the distances in $[Fe(H_2O)EDTA]^-$ than the respective distances in $[Fe(H_2O)EDTA]^{2-}$, consistent with our description of the FeEDTA-NO complex as having a ferric center.[5] Thus bond distances and angles from the crystallographically-characterized $[Fe(H_2O)EDTA]^-$ were used as an initial structural model in the GNXAS analysis with NO substituted for the bound water.[19] Since the EXAFS data for FeEDTA-NO were collected as a frozen solution, EXAFS data were also collected for $Na[Fe(OH_2)EDTA]$ as a solution as well as a powder to determine if the metrical details differed in the two states. The results of this study establish that EXAFS analysis by GNXAS can provide reliable angular information and serve as the basis for its application to NO complexes of non-heme iron protein active sites.

3.2. Experimental Section

3.2.1. Sample Preparation and Data Collection

X-ray absorption (XAS) spectra were recorded at the Stanford Synchrotron Radiation Laboratory on unfocused beamlines 7-3 and 4-3 during dedicated conditions (3 GeV, 25-75 mA). The radiation was monochromatized using a Si(220) double-crystal monochromator detuned 50% at 7998 eV to minimize harmonic contamination. An Oxford Instruments continuous-flow liquid helium CF 1208 cryostat was used to maintain a constant temperature. The XAS spectra were calibrated using an internal Fe foil standard,[20] assigning the first inflection point to 7111.2 eV.

$[Fe(TMC)NO](BF_4)_2$,[17] $Fe(TACN)(N_3)_2NO$,[4e] Fe(salen)NO,[18] and $Na[Fe(OH_2)EDTA]$[19] were prepared as described in the literature. $[Fe(TMC)NO](BF_4)_2$, $Fe(TACN)(N_3)_2NO$, and Fe(salen)NO are air-sensitive and were handled in a nitrogen-filled inert atmosphere dry glove box during the following sample preparation. The crystalline samples were mixed with BN and ground into a fine powder. The BN/sample mixture was pressed into a 1 mm thick Al spacer that was sealed with 63.5 μm Mylar tape windows. Immediately after preparation, the samples were frozen in liquid nitrogen. Data were measured in transmission mode at 10 K with nitrogen-filled ionization chambers. Since Fe(salen)NO undergoes a spin and structural transition at 180 K, EXAFS data were also collected at 220 K.

The $[Fe(OH_2)EDTA]^{2-}$ solution, 50 mM in Fe, was prepared by anaerobically adding ferrous ammonium sulfate to a 50 mM solution of Na_2EDTA in pH = 6.5, 0.1 M deoxygenated phosphate buffer. Oxidizing this solution produced $[Fe(OH_2)EDTA]^-$. An FeEDTA-NO solution was prepared by purging an $[Fe(OH_2)EDTA]^{2-}$ solution with NO gas under anaerobic conditions. To form an ice-free glass, the XAS solution samples were prepared by adding 50% (by volume) glycerol to the previously prepared solutions resulting in solutions 25 mM in Fe. These samples were loaded into 140 μL Lucite EXAFS cells (23 x 2 x 3 mm) with 37 μm Kapton windows in an anaerobic wet box under nitrogen. The samples were frozen in liquid nitrogen and were subsequently stored in a liquid nitrogen refrigerator until use. Data were collected in fluorescence mode at 10 K. The fluorescence signal was collected by an argon-filled ionization chamber,[21] equipped with Soller slits and a Mn filter.

Data were also collected for $Fe(acetylacetonate)_3$ and $[Fe(1,10\text{-phenanthroline})_3](ClO_4)_3$ at 10 K to extract Fe-O and Fe-N backscattering parameters for empirical analysis. $Fe(acetylacetonate)_3$ was purchased from Aldrich and $[Fe(1,10\text{-phenanthroline})_3](ClO_4)_3$ was prepared according to the published procedure.[22] The samples were prepared in air in an identical manner to the solids mentioned above. Data were measured in transmission mode with nitrogen-filled ionization chambers.

The EXAFS data were measured to k = 15 Å^{-1} with 2 mm high pre-monochromator beam-defining slits for the $Na[Fe(OH_2)EDTA]$, $Na_2[Fe(OH_2)EDTA]$, and FeEDTA-NO solutions and 1 mm high pre-monochromator slits for all the powder samples. Two to seven scans were averaged for each transmission sample, while eight to twenty scans were averaged for the fluorescence samples. The effects of a quartet monochromator glitch were removed from the averaged data by four single point replacements at around k = 11.8, 12.1, 12.3 and 12.6 Å^{-1}.

3.2.2. GNXAS Data Analysis

As described in detail in Chapter 2 and elsewhere,[10,16] the GNXAS programs generate model EXAFS signals for each shell around the photoabsorber based on an initial structural model. Both single-scattering and multiple-scattering contributions are summed to generate a theoretical spectrum for the model which is then fit to the non-Fourier-filtered experimental data.[10,16]

The crystallographic coordinates were used as input for $[Fe(TMC)NO](BF_4)_2$,[17] $Fe(TACN)(N_3)_2NO$,[4e] and Fe(salen)NO[18] at high and low temperatures (Figure 3.1 shows the structure of each compound). Phase shifts were calculated using the standard

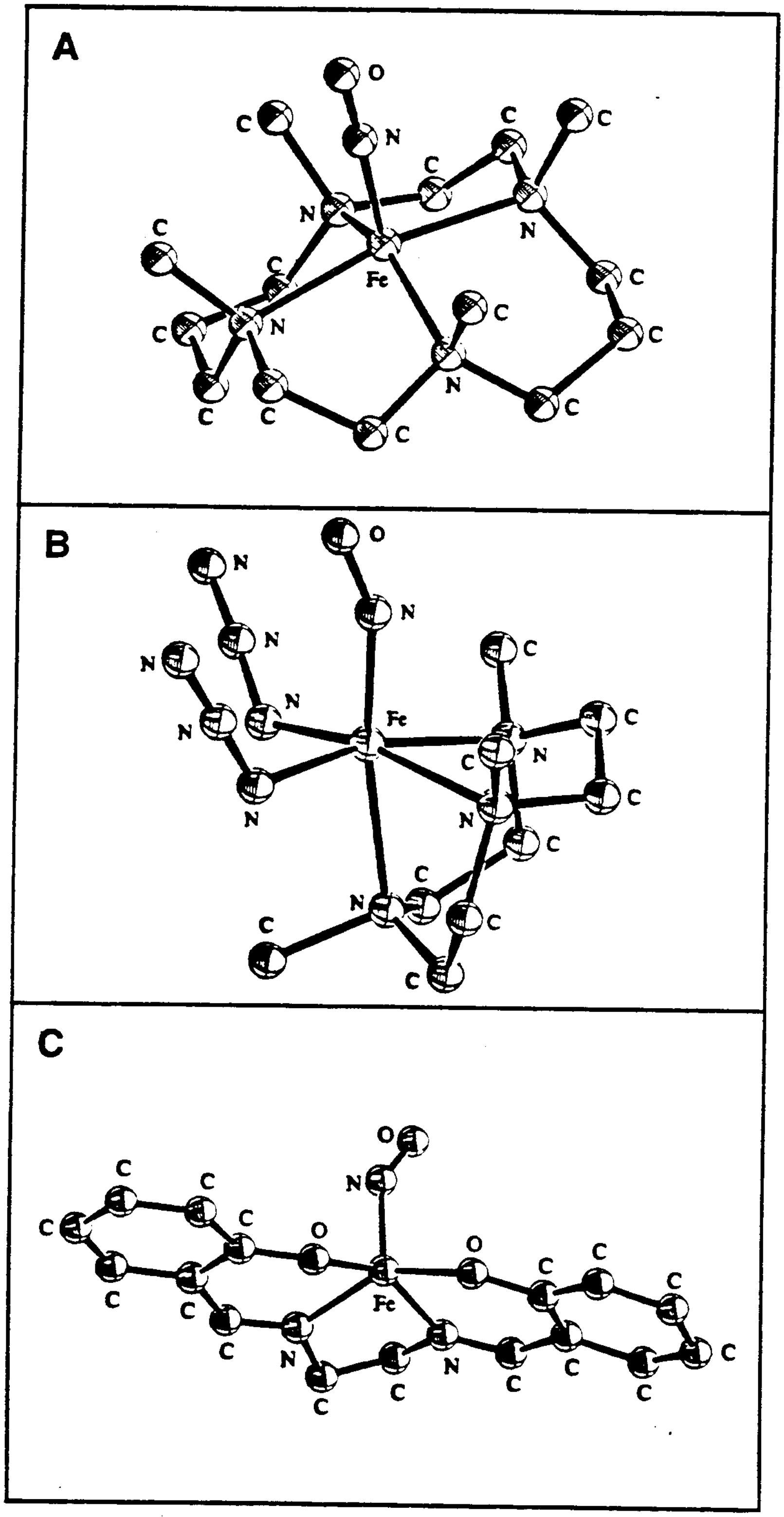

Figure 3.1. Molecular structures of (A) $[Fe(TMC)NO](BF_4)_2$, (B) $Fe(TACN)(N_3)_2NO$ and (C) Fe(salen)NO at 23°C.

muffin-tin approximation with all the atoms associated with each compound and up to an energy limit of 70 Ry (950 eV) above the Fe K edge. The Mattheiss prescription[23] of overlapping, self-consistent atomic charge densities of the atoms of the cluster was used to construct the Coulomb portion of the effective one-electron potential. Proper account of the charge relaxation around the core hole was taken. The Hedin-Lundqvist plasmon-pole approximation was used to model its exchange and correlation part.[11] The imaginary part of the latter takes into account inelastic scattering processes of the photoelectron propagating out of the system and models *a priori* its mean-free path. The muffin-tin radii were chosen by scaling Norman radii of the cluster atoms by a factor of about 0.8 as to match the nearest neighbor distance.

The theoretical EXAFS spectrum was calculated to include contributions from two-atom and three-atom configurations. Within each n-atom configuration, all the MS contributions were taken into account.[10,16] The two-atom and three-atom configurations were identified in each cluster up to 4.4 Å and averaged with a frequency tolerance of 0.1 Å. The resultant information was used to calculate the various EXAFS $\gamma^{(2)}$ and $\gamma^{(3)}$ signals associated with each two-atom and three-atom contribution using the crystallographic bond lengths and distances.

The GNXAS fitting program constructs the theoretical absorption spectrum by summing all the $\gamma^{(2)}$ and $\gamma^{(3)}$ signals and compares this theoretical spectrum with the experimental absorption spectrum with the residual function R being a measure of the quality of the fit.[16] Least-square fits are performed on the averaged, energy-calibrated, raw absorption data without prior background subtraction or Fourier filtering. Raw data are compared directly with a model absorption coefficient composed of an appropriate background plus the oscillatory structural contribution from the theoretically calculated EXAFS.[16] A spline of orders 3,4,4 with defining energy points of 7155, 7250, 7600, and 7998 eV was used for most cases. If there was low-frequency noise in the Fourier transform (FT) the first defining energy point was adjusted by a maximum of 5 eV until the noise was minimized. Least-squares fits were done with k^3 weighting where the first and the last spline points determined the range of the fit.

The structural parameters varied in the refinements were the distance (R) and the bond variance $\left(\sigma_R^2\right)$, the mean square variation in the bond distance, for each two-atom configuration and the distances, the angle and the covariance matrix elements[10,16] for the three-atom configurations. Distances and angles were allowed to vary within a preset range, typically ±0.05 Å and ±5°. Bond and angle variances and the off-diagonal covariance matrix elements were also allowed to vary in restricted ranges: ±0.005 Å^2, ±50 (degrees)^2 and ±0.5, respectively. The coordination numbers were kept fixed to known crystallographic values. The nonstructural parameters in the fits were E_o (a parameter that aligns the experimental energy scale to the theoretical energy scale), $S_0{}^2$ (many-body amplitude reduction factor), Γ_c (core-hole lifetime), and E_r (experimental resolution). These parameters were refined within narrow limits around expected values.[24,25]

3.2.3. Empirical EXAFS Analysis

Data reduction and analysis using empirical phase and amplitude parameters was performed to obtain first-shell fits of the Na[Fe(OH_2)EDTA] powder and solution, Na_2[Fe(OH_2)EDTA] solution, and FeEDTA-NO solution according to the methods described previously[8a,26] and briefly summarized here. A pre-edge subtraction was performed by fitting the EXAFS region with a smooth second order polynomial function which was extrapolated into the pre-edge region and subtracted. A three segment spline approximately even in k-space with orders of two, three, and three was fit to the EXAFS region and subtracted and the data normalized to an edge jump of one at 7130 eV. The polynomial spline was chosen so that it minimized residual low-frequency noise but did not reduce the amplitude of the EXAFS, as judged by monitoring the FT of the EXAFS as a function of the spline fitting process. The normalized data were converted to k-space. The photoelectron wave vector, k, is defined by $[2m_e(E-E_0)/\hbar^2]^{1/2}$ where m_e is the electron mass, E is the photon energy, $\hbar$ is Planck's constant divided by 2π, and E_o is the threshold energy of the absorption edge, which was defined to be 7130 eV for the Fe K absorption edge. The empirical EXAFS data analyses were performed with nonlinear least-square curve-fitting[8a,20,26] techniques using empirical phase and amplitude parameters. The following models were used to obtain the empirical Fe-X backscattering parameters of interest: Fe-O from [Fe(acetylacetonate)$_3$][27] and Fe-N from [Fe(1,10-phenanthroline)$_3$](ClO_4)$_3$.[22]

Fourier transforms (from k to R space) were performed for the data range 3.5-14.5 $Å^{-1}$ with a Gaussian window of 0.1 $Å^{-1}$. The window widths used in the backtransforms (from R to k space) are presented in the Results and Discussion section. The window widths were kept as similar as possible to the windows used to extract amplitude and phase parameters from the model compounds to minimize artifacts introduced by the Fourier filtering technique. All curve-fitting was based on k^3-weighted data and applied to the individual filtered shell of interest. Only the structure-dependent parameters, the distance and coordination number, were varied. A "goodness of fit" parameter, F, was calculated as $F = \{[k^6(\text{data - fit})^2]/(\text{no. of points})\}^{1/2}$ for each fit.

3.3. Results and Discussion

3.3.1. GNXAS Fits of $\{FeNO\}^7$ Complexes with Known Fe-N-O Angles

The GNXAS approach was used to fit the experimental EXAFS data of $[Fe(TMC)NO](BF_4)_2$, $Fe(TACN)(N_3)_2NO$, and Fe(salen)NO at 10 and 220 K. EXAFS contributions for each two-atom and three-atom configuration were calculated using crystallographic distances and bond angles. The individual contributions were then summed to generate a theoretical EXAFS spectrum which was then fit to the non-Fourier filtered experimental EXAFS data without prior background subtraction. In the fits, the crystallographic bond distances and angles were allowed to vary to fit the experimental EXAFS data. A comparison of the theoretical EXAFS spectrum to the experimental data (along with the individual EXAFS signal from each contribution) for each compound is presented in Figures 3.2 - 3.5. A comparison of the bond distances and angles obtained from the GNXAS fits to the crystallographic values is given in Table 3.1.

The best fit to the EXAFS data of $[Fe(TMC)NO](BF_4)_2$ is presented in Figure 3.2, with the corresponding FT presented in Figure 3.6A. The total EXAFS spectrum was accounted for by four contributions: Fe-N(O), Fe-N(TMC), Fe-N-O, and Fe-N-C [throughout this chapter, signals from three-atom configurations contain contributions from the three-atom multiple-scattering pathways ($\gamma^{(3)}$ signal) and a two-atom contribution ($\gamma^{(2)}$ signal) from the distant atom[16]. The GNXAS bond distances and angles match extremely well with the crystallographic values, deviating less than 0.01 Å and 1°, respectively (Table 3.1). The linear Fe-N-O multiple-scattering signal is very strong due to the intervening atom focusing effect,[16] allowing for very accurate bond angle determination. The crystallographic Fe-N-O bond angle is 177.5(5)° and the Fe-N-O bond angle obtained from the GNXAS fit is 178°. In the numerous fits that were calculated the bond distances varied by <0.02 Å and the bond angles varied by <1°.

The EXAFS data of $Fe(TACN)(N_3)_2NO$ and the best fit to the data are presented in Figure 3.3 and the FT is shown in Figure 3.7B. The EXAFS spectrum is dominated by three two-atom signals: Fe-N(O), Fe-N(N_2) and Fe-N(TACN). The significant three-atom signals come from Fe-N-O, Fe-N-N and Fe-N-C groups. The resultant bond distances and angles are all within 5% of the crystallographic values (see Table 3.1) with the Fe-N-O angle equal to 157° (as compared to the crystallographic value of 156(1)°).

The fit to the Fe(salen)NO EXAFS data at 10 K with an Fe-N-O angle of 131° is presented in Figure 3.4, with the FT of this fit to the data shown in Figure 3.8C. The two-atom and three-atom contributions included in the fit to the data were Fe-N(O),

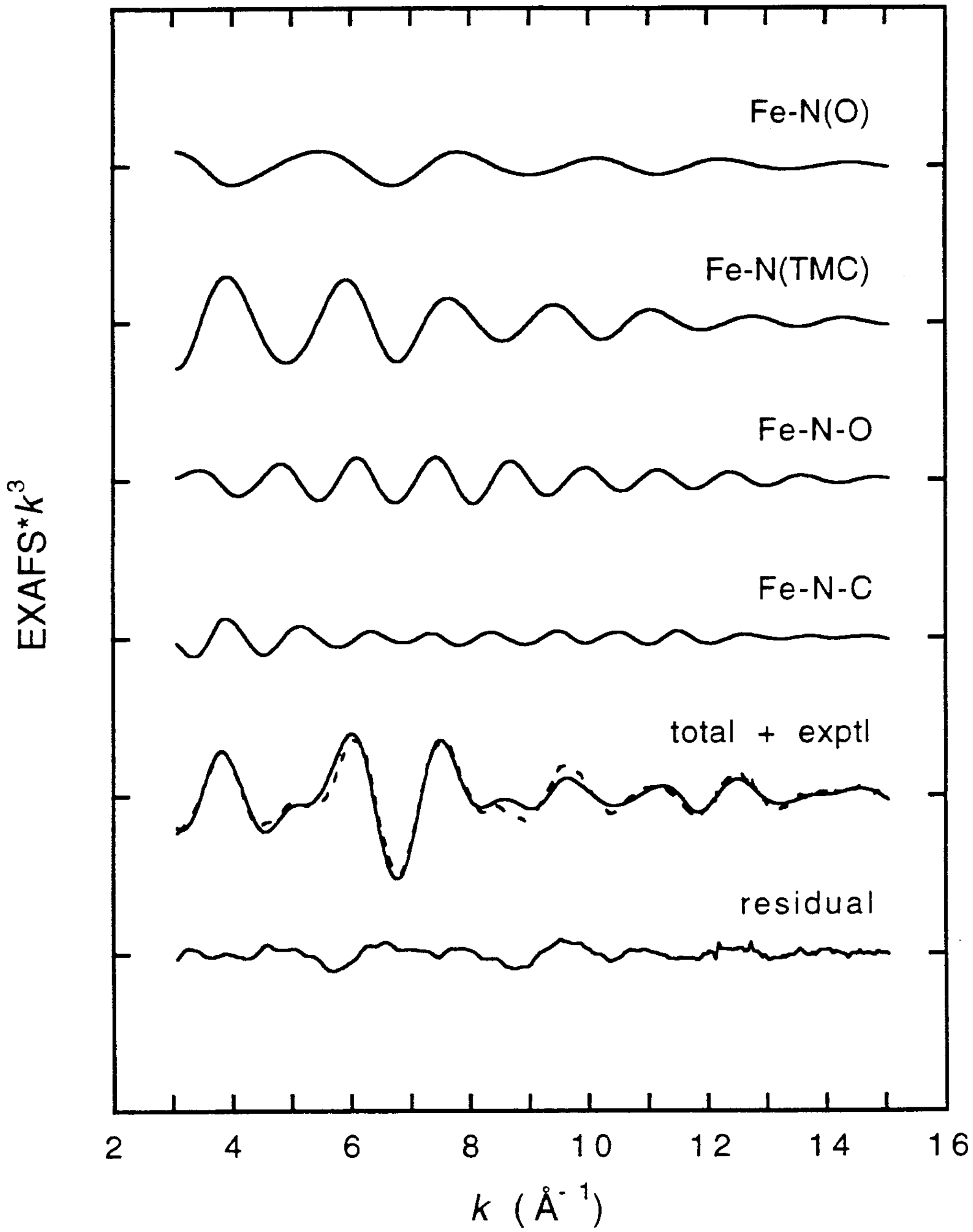

Figure 3.2. EXAFS signals for individual contributions in the best fit for the [Fe(TMC)NO](BF_4)$_2$ data. The total signal (——) is also shown and compared with the experimental data (---) with the residual being the difference between the experimental EXAFS and the theoretical EXAFS. (The ordinate scale is 10 between two consecutive tick marks.) Note the strength of the Fe-N-O contribution.

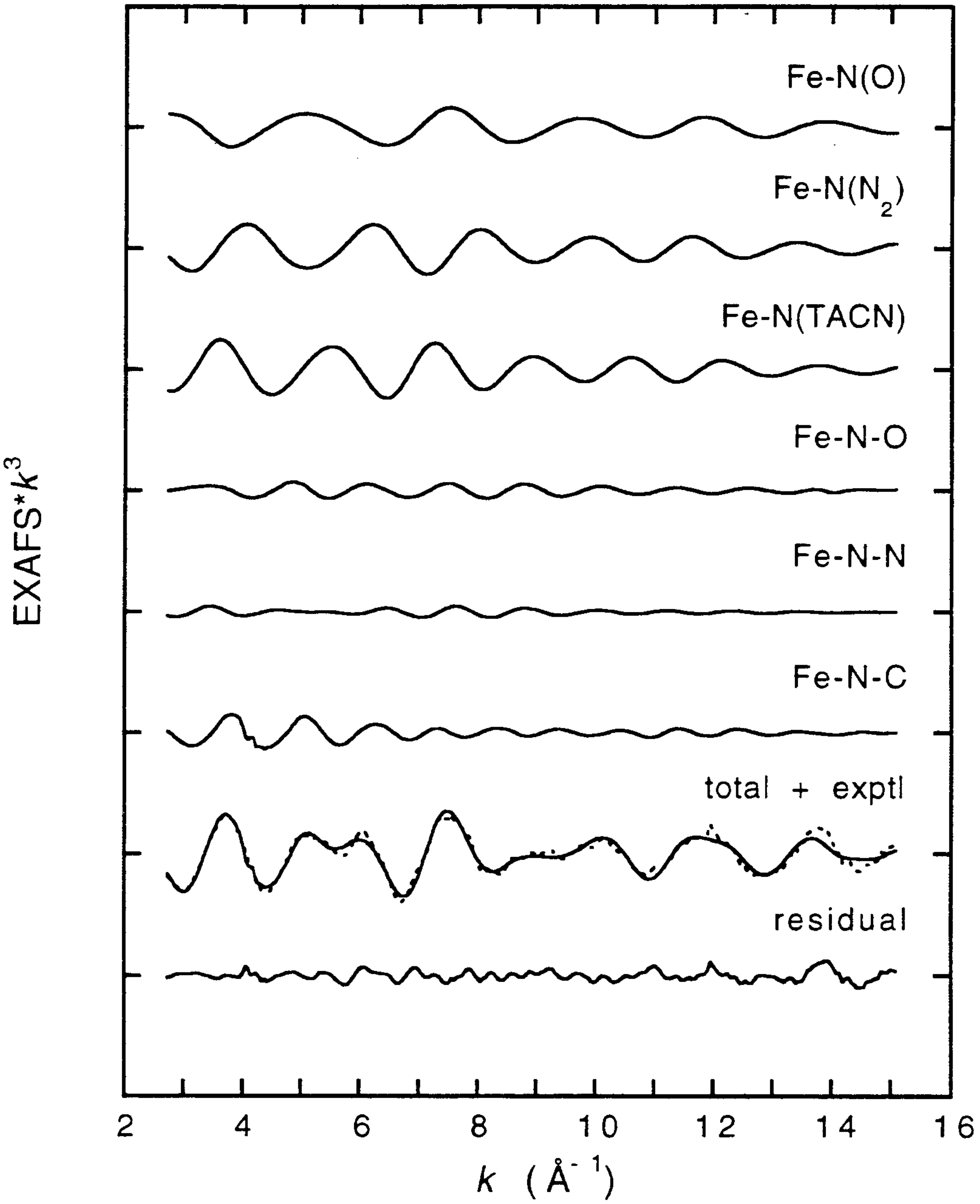

Figure 3.3. EXAFS signals for individual contributions in the best fit for the Fe(TACN)(N$_3$)$_2$NO data. The total signal (——) is also shown and compared with the experimental data (---) with the residual being the difference between the experimental EXAFS and the theoretical EXAFS. (The ordinate scale is 10 between two consecutive tick marks.)

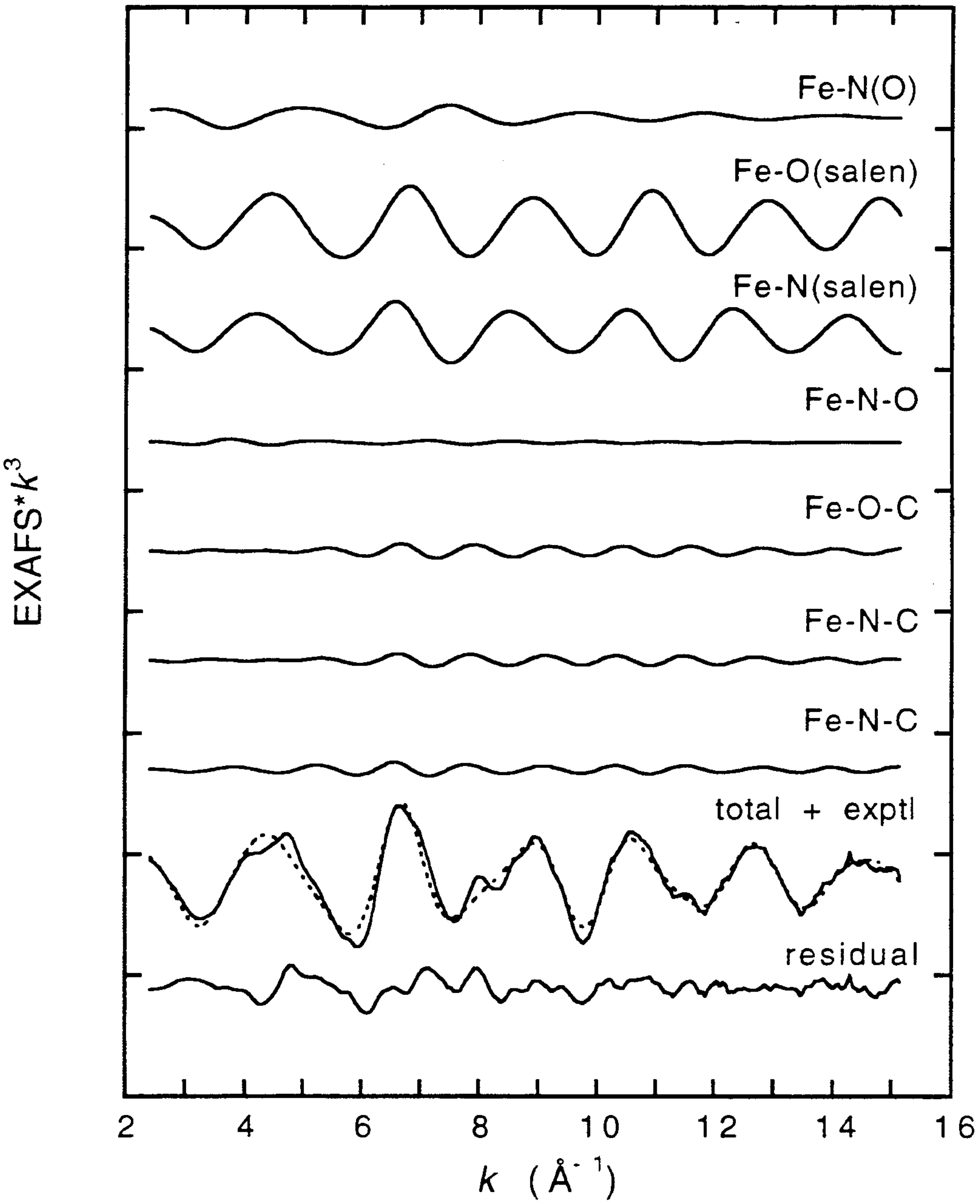

Figure 3.4. EXAFS signals for individual contributions in the best fit for the Fe(salen)NO at 10 K data. The total signal (——) is also shown and compared with the experimental data (---) with the residual being the difference between the experimental EXAFS and the theoretical EXAFS. (The ordinate scale is 10 between two consecutive tick marks.)

Table 3.1. Crystallographic Bond Distances and Angles Compared to GNXAS Results for $\{FeNO\}^7$ Complexes with Known Fe-N-O Angles.

compound	structural feature (CN[a])	GNXAS distance/ angle	GNXAS bond variance (σ_R^2)/ angle variance (σ_θ^2)[b]	crystallographic values [range]
$[Fe(TMC)NO](BF_4)_2$	Fe-N (1)	1.73 Å	0.005	1.74 Å
	Fe-N (4)	2.17 Å	0.007	2.16 Å [2.15-2.18]
	N-O (1)	1.14 Å	0.001	1.14 Å
	N-C (4)	1.49 Å	0.004	1.49 Å [1.48-1.50]
	Fe-N-O (1)	178.0°	2×10^1	177.5°
	Fe-N-C (12)	110.7°	8×10^1	110° [109-114]
$Fe(TACN)(N_3)_2NO$	Fe-N (1)	1.77 Å	0.003	1.74 Å
	Fe-N (2)	2.06 Å	0.004	2.05 Å [2.03-2.08]
	Fe-N (3)	2.25 Å	0.005	2.25 Å [2.24-2.27]
	N-O (1)	1.10 Å	0.001	1.14 Å
	N-N (2)	1.22 Å	0.002	1.19 Å [1.19-1.20]
	N-C (9)	1.43 Å	0.003	1.5 Å [1.4-1.6]
	Fe-N-O (1)	156.7°	4×10^0	156°
	Fe-N-N (2)	127.7°	3×10^0	124° [121-127]
	Fe-N-C (9)	109.0°	8×10^1	108° [104-112]
Fe(salen)NO 10K[d]	Fe-N (1)	1.77 Å	0.006	1.8 Å
	Fe-O (2)	1.87 Å	0.001	1.90 Å [1.87-1.93]
	Fe-N (2)	1.95 Å	0.001	1.97 Å [1.97-1.98]
	N-O (1)	1.16 Å	0.003	1.15 Å[c]
	O-C (2)	1.36 Å	0.003	1.36 Å [1.35-1.37]
	N-C (2)	1.28 Å	0.003	1.28 Å [1.26-1.31]
	N-C (2)	1.49 Å	0.003	1.50 Å [1.49-1.51]
	Fe-N-O (1)	131°	1×10^1	127°
	Fe-O-C (2)	127°	1×10^0	127° [126-128]
	Fe-N-C (2)	124°	1×10^0	124° [123-125]
	Fe-N-C (2)	114°	1×10^0	114° [114-115]
Fe(salen)NO 220K[e]	Fe-N (1)	1.76 Å	0.004	1.78 Å
	Fe-O (2)	1.90 Å	0.003	1.91 Å [1.89-1.92]
	Fe-N (2)	2.08 Å	0.012	2.08 Å [2.07-2.08]
	N-O (1)	1.10 Å	0.001	1.11 Å
	O-C (2)	1.31 Å	0.005	1.31 Å [1.30-1.32]
	N-C (2)	1.26 Å	0.004	1.26 Å [1.24-1.27]
	N-C (2)	1.47 Å	0.001	1.45 Å [1.45-1.46]
	Fe-N-O (1)	149°	3×10^1	147°
	Fe-O-C (2)	132°	3×10^1	130° [126-133]
	Fe-N-C (2)	127°	1×10^0	125° [124-126]
	Fe-N-C (2)	116°	1×10^1	114° [112-116]

[a] CN = number of configurations in the complex. [b] Bond and angle variances are reported in $Å^2$ and $degrees^2$, respectively. [c] value was fixed in the crystal structure. [d] The crystal structure was determined at -175 °C and the EXAFS was measured at 10 K. [e] The crystal structure was determined at 23 °C and the EXAFS was measured at 220 K.

Fe-O(salen), Fe-N(salen), Fe-N-O, Fe-O-C, and two Fe-N-C signals. The distances and angles obtained from the GNXAS fits were all within 1% of the crystallographic values, Table 3.1. In the Fe(salen)NO EXAFS data at 10 K the two-atom signals from the O and N of the salen ligand were very strong relative to the signal from the N of the nitrosyl ligand. The bond variances $\left(\sigma_R^2\right)$ are 0.001 Å^2 for the Fe-O(salen) and Fe-N(salen) contributions and 0.006 Å^2 for the Fe-N(O) signal. The high bond variance and the associated weak signal for the Fe-N(O) contribution could be due to the fact that the nitrosyl group is disordered.[18] The crystal structure of Fe(salen)NO at -175 °C shows a strongly disordered nitrosyl group with the standard deviation of the Fe-N(O) distance being 0.1 Å and a 1 σ variation of the Fe-N-O angle ranging from 115° to 137°. Not only is the nitrosyl group disordered, but the Fe-N-O angle is below 150.° Significant enhancement of the multiple-scattering signal results when the atoms are arranged in approximately a collinear array, in which case the outgoing photoelectron is strongly forward scattered by the intervening atom. This effect drops off very rapidly for bond angles below ~150°.[6,7,16] Since the Fe-N(O) contribution has a high bond variance and the Fe-N-O angle is low (~130°), the Fe-N-O signal is extremely weak.

The best fit to the Fe(salen)NO EXAFS data at 220 K is presented in Figure 3.5, with the FT of the best fit to the data shown in Figure 3.9B. The two-atom and three-atom contributions included in the fit to the data were Fe-N(O), Fe-O(salen), Fe-N(salen), Fe-N-O, Fe-O-C and two Fe-N-C signals. The distances and angles obtained from the GNXAS fits were all within 1% of the crystallographic values, Table 3.1. The crystal structure of Fe(salen)NO taken at 23 °C was more accurately determined than the structure at -175 °C, although the oxygen of the nitrosyl group showed some disorder. Two oxygens (OA and OB) were introduced into the crystallographic model with fixed occupancies of 0.5; the Fe-N-OA angle is 144(5)° and the Fe-N-OB angle is 150(4)°. The Fe-N-O angle obtained from the GNXAS fit to the EXAFS data in Figure 3.5 was 149° with an angle variance of 31 (degrees)^2, see Table 3.1. Predictably, the bond variances were higher for the Fe(salen)NO data collected at 220 K, which is also seen in the lower magnitude at high *k* in the EXAFS data (Figures 3.4 and 3.5).

Once best fits were obtained for each $\{FeNO\}^7$ complex, the sensitivity of the fit to the Fe-N-O angle was tested by fixing all the distances, angles, and nonstructural parameters and calculating a theoretical EXAFS spectrum with Fe-N-O angles ranging from 90° to 180°. The FTs of relevant calculated spectra for each compound are presented in Figures 3.6 - 3.9. Plots of log(*R* values) *vs* Fe-N-O angle for each complex are shown in Figure 3.10 (the log function allows the plots to be scaled for comparison). A minimum in these plots is indicative of a better fit to the experimental EXAFS data.

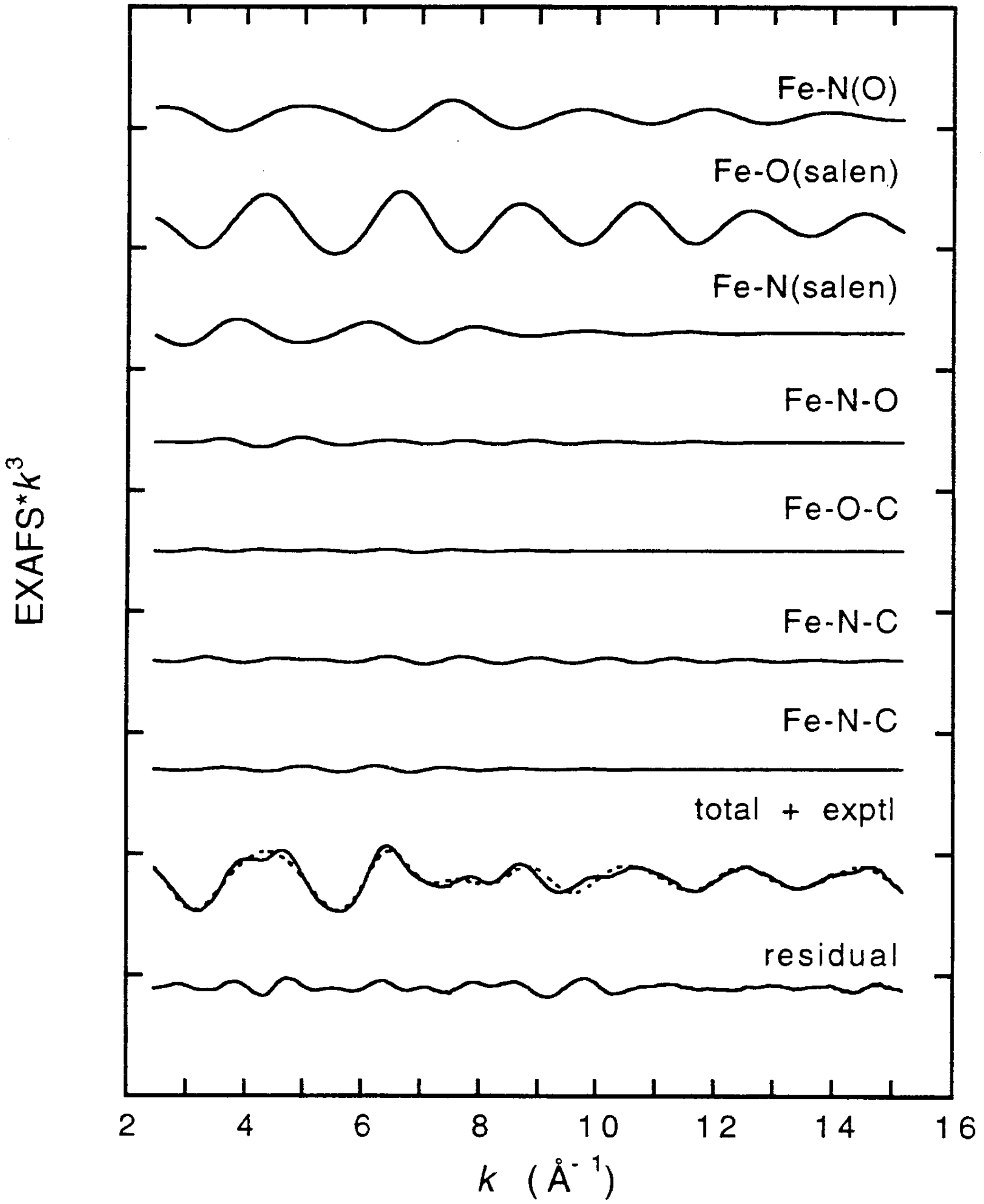

Figure 3.5. EXAFS signals for individual contributions in the best fit for the Fe(salen)NO at 220 K data. The total signal (——) is also shown and compared with the experimental data (---) with the residual being the difference between the experimental EXAFS and the theoretical EXAFS. (The ordinate scale is 10 between two consecutive tick marks.)

The FTs of the calculated GNXAS spectra with the Fe-N-O angles of 178° (best fit), 150°, and 120° for the [Fe(TMC)NO]$(BF_4)_2$ data are presented in Figure 3.6. The second peak in the FT at 2.5 Å, which is due to the Fe-N-O multiple-scattering signal, cannot be accounted for without an Fe-N-O angle that is close to linear. The *R* value dramatically increases in calculated spectra where the Fe-N-O angle is below 170° (Figure 3.10A). Due to the strength of the multiple-scattering signal from an approximately linear Fe-N-O unit, the calculated spectrum is extremely sensitive to the Fe-N-O angle.

Figure 3.7 shows the FTs of calculated spectra for Fe(TACN)$(N_3)_2$NO with an Fe-N-O angle of 180°, 157°(best fit), and 120°. The FT of the calculated spectrum with Fe-N-O equal to 180° does not match the FT of the experimental EXAFS data. When the log(*R* value) is plotted *vs* the Fe-N-O angle there is a minimum between 155° and 160° (Figure 3.10B) with the crystallographic Fe-N-O angle for Fe(TACN)$(N_3)_2$NO being 156°. There is a second shallower minimum in the *R* value at 110°. Upon inspection of the Fe-N-O multiple-scattering signal and the Fe-O (of the Fe-N-O) single-scattering signal, it was observed that in the low-*k* region the Fe-O signal with an Fe-N-O angle of 110° was in-phase and of the same order of magnitude as the Fe-N-O multiple-scattering signal with an Fe-N-O angle equal to 156°. Therefore the single-scattering Fe-O signal with a Fe-N-O angle of 110° was able to mimic the multiple-scattering Fe-N-O signal with a Fe-N-O angle equal to 156° for *k* less than 6 $Å^{-1}$, giving a false minimum in the log(*R* value) *vs* Fe-N-O angle plot. The multiple-scattering contribution for a three-atom configuration dominates for angles above 150°, while the single-scattering signal is important for values below 150°.[6,7,16] Thus, due to the sinusoidal nature of EXAFS, a double minimum occurs when the log(*R* value) is plotted *vs* the Fe-N-O angle, where in one case the single-scattering signal (Fe-O) has a phase and amplitude that matches the experimental data and in the other case the multiple-scattering signal (Fe-N-O) has a phase and amplitude that matches the data.

The FTs for calculated spectra of Fe(salen)NO at 10 K with Fe-N-O values of 180°, 150°, and 131° are shown in Figure 3.8. Since the theoretical spectra were calculated using the bond distances, angles, and the covariance matrix elements of the fit in Figure 3.4, the bond variance associated with the Fe-N(O) signal was very high, 0.006 $Å^2$. The high Fe-N(O) bond variance made the Fe-N-O signal extremely weak at all angles, even at 180°. Due to the weak Fe-N-O signal, the *R* values of these fits are all very similar and insensitive to the Fe-N-O angle (Figure 3.10D). Thus, a signal from a three-atom configuration must be a significant component in the total EXAFS signal in order for GNXAS to provide angular information.

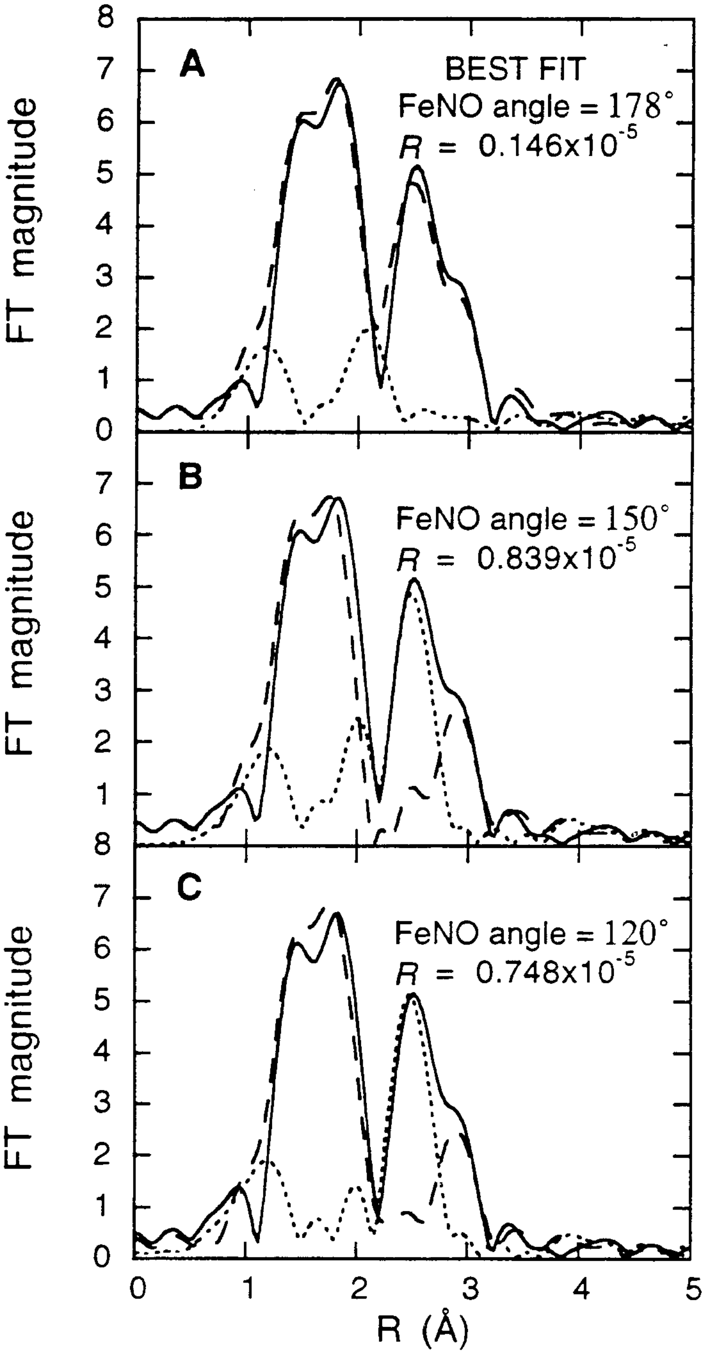

Figure 3.6. A comparison of the theoretical (---) and experimental (——) non-phase shift corrected FT of [Fe(TMC)NO](BF$_4$)$_2$ EXAFS data, along with the FT of the EXAFS residual (····). The R value is an indication of the goodness of the fit. Calculated spectra for several different Fe-N-O bond angles are shown: (A)178° (best fit), (B) 150°, and (C) 120°. This {FeNO}^{7} complex has a crystallographic Fe-N-O bond angle of 177.5(5)°.

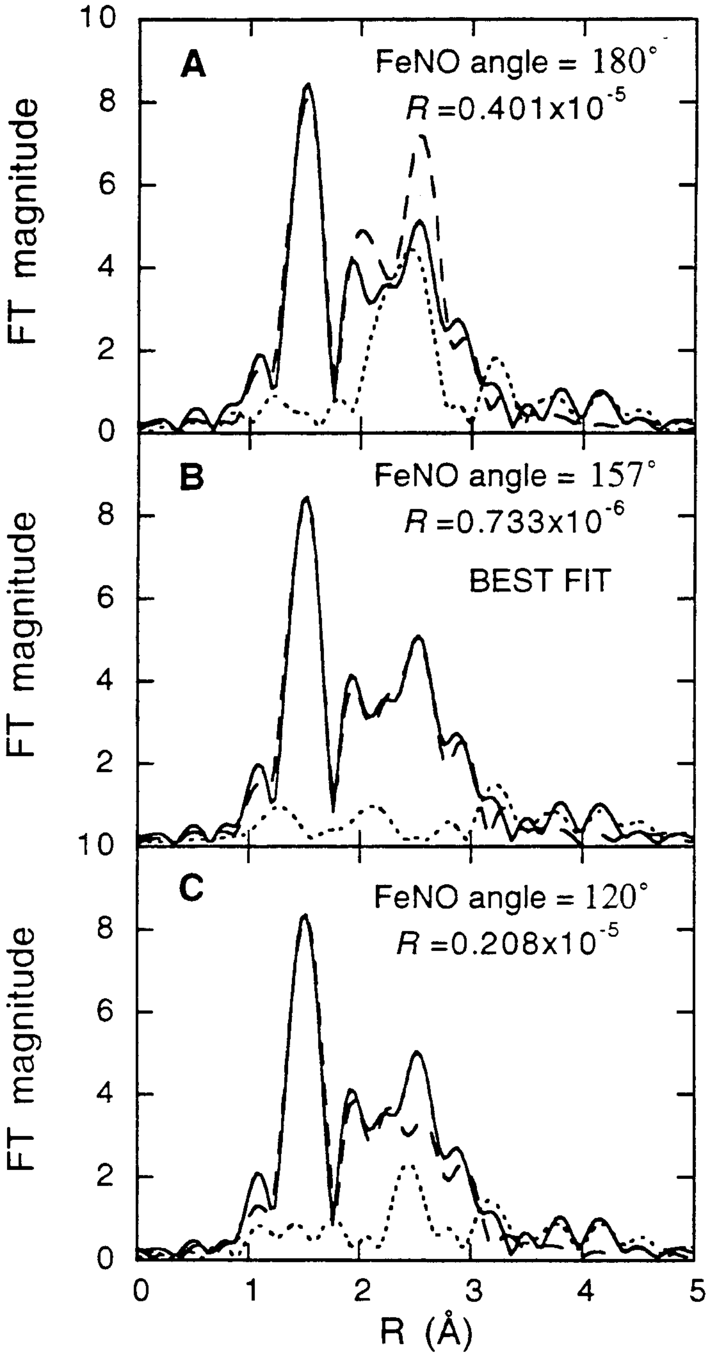

Figure 3.7. A comparison of the theoretical (---) and experimental (——) non-phase shift corrected FT of Fe(TACN)(N_3)$_2$NO EXAFS data, along with the FT of the EXAFS residual (····). The R value is an indication of the goodness of the fit. Calculated spectra for several different Fe-N-O bond angles are shown: (A) 180°, (B) 157° (best fit), and (C) 120°. This {FeNO}^{7} complex has a crystallographic Fe-N-O bond angle of 156(1)°.

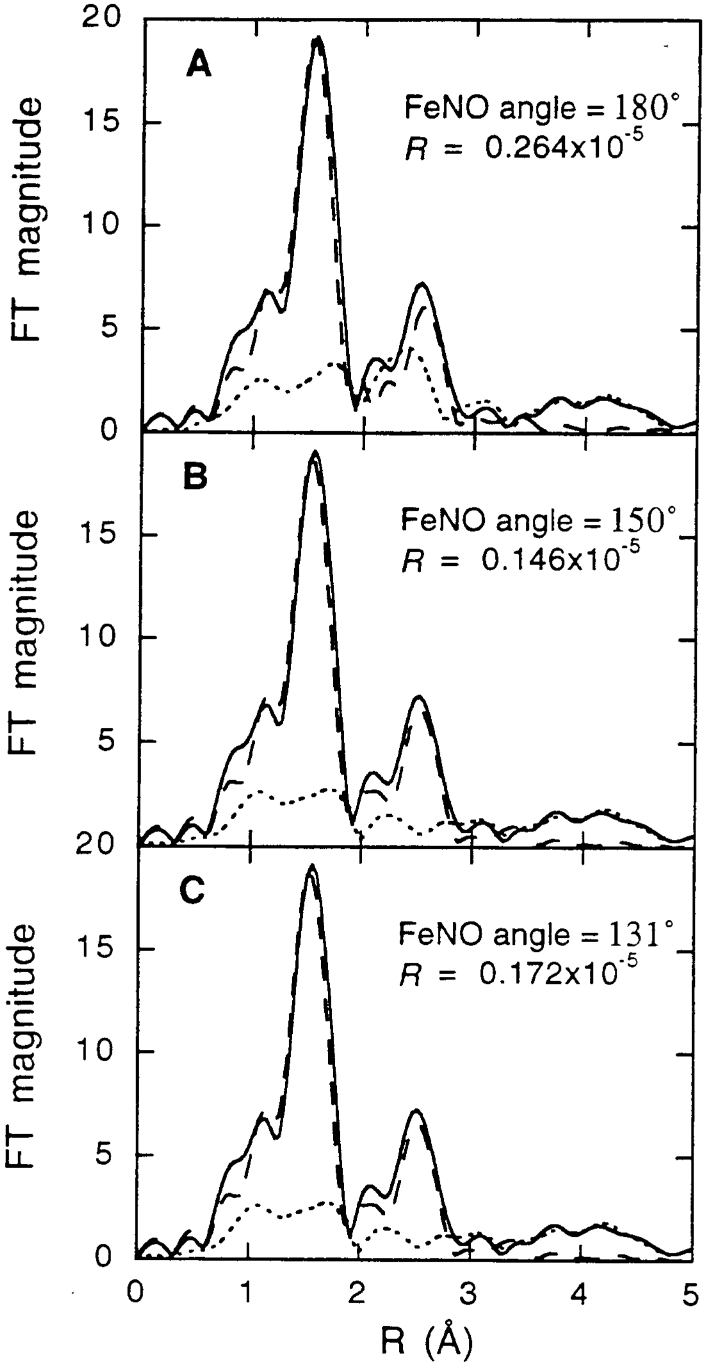

Figure 3.8. A comparison of the theoretical (---) and experimental (——) non-phase shift corrected FT of Fe(salen)NO at 10 K EXAFS data, along with the FT of the EXAFS residual (····). The *R* value is an indication of the goodness of the fit. Calculated spectra for several different Fe-N-O bond angles are shown: (A) 180°, (B) 150°, and (C) 131°. This $\{FeNO\}^7$ complex has a crystallographic Fe-N-O bond angle of 127(6)°.

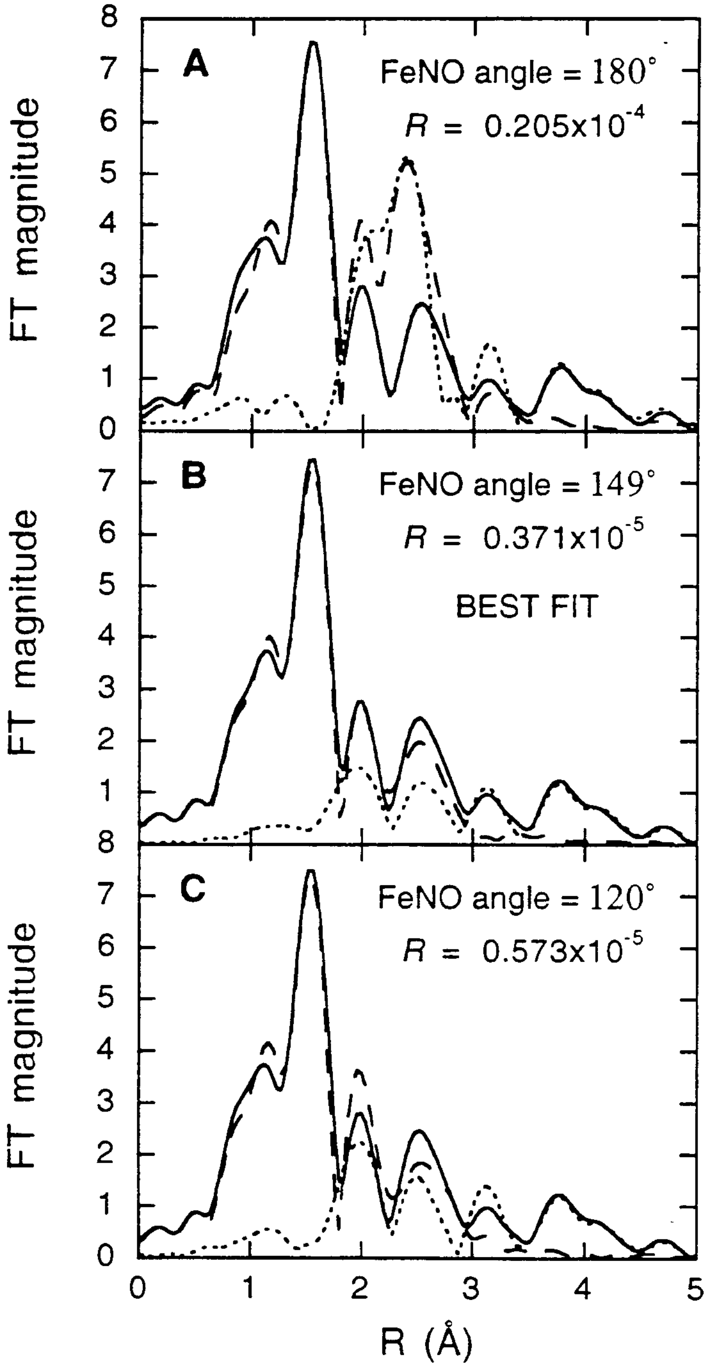

Figure 3.9. A comparison of the theoretical (---) and experimental (——) non-phase shift corrected FT of Fe(salen)NO at 220 K EXAFS data, along with the FT of the EXAFS residual (····). The R value is an indication of the goodness of the fit. Calculated spectra for several different Fe-N-O bond angles are shown: (A) 180°, (B) 149° (best fit), and (C) 120°. This model compound has a crystallographic bond angle of 147(5)°.

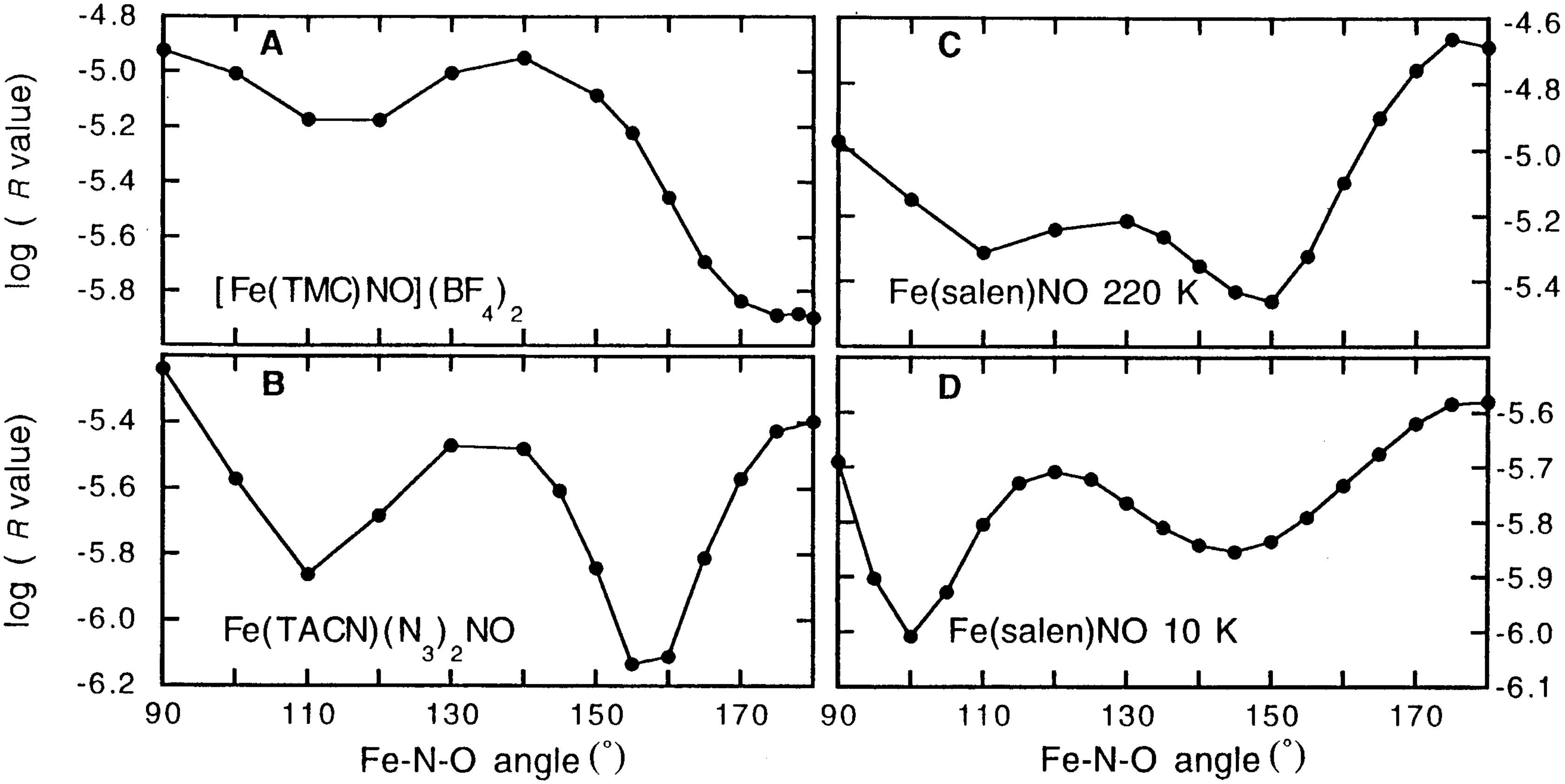

Figure 3.10. Plots of the log(*R* value) *vs* Fe-N-O angle for (A) [Fe(TMC)NO](BF$_4$)$_2$, (B) Fe(TACN)(N$_3$)$_2$NO and (C) Fe(salen)NO at 220 K and (D) 10 K where each point represents a match of the calculated EXAFS spectrum to the data. The lower the *R* value the better the fit. The deep minimum in the [Fe(TMC)NO](BF$_4$)$_2$ data at high angles indicates the Fe-N-O angle must be over 170 °. The plot for the Fe(TACN)(N$_3$)$_2$NO data has a double minimum with the dominant minimum being around 155°. The minimum in the Fe(salen) 220 K data is at ~150°, while *R* values for the Fe(salen)NO at 10 K were nearly insensitive to variations of the Fe-N-O angle due to the weak Fe-N-O signal.

The FTs for calculated spectra of Fe(salen)NO at 220 K with Fe-N-O angles of 180°, 149° (best fit), and 120° are shown in Figure 3.9. Fits above 155° have relatively high *R* values, however the *R* values for all the fits below 155° are very similar (Figure 3.10C). In this case, application of GNXAS to the data only allows an upper limit of 155° to be set for the Fe-N-O angle.

3.3.2. Fe-N-O Angle Determination of an $\{FeNO\}^7$ Complex of Unknown Structure

GNXAS analysis was used to investigate the Fe-N-O angle of FeEDTA-NO, a complex whose structure is unknown. GNXAS requires an initial structural model. Therefore, EXAFS data of several FeEDTA complexes were obtained and compared to FeEDTA-NO to determine a suitable initial structural model. Using the empirical EXAFS data analysis method, first-shell distances were obtained for Na[Fe(OH_2)EDTA] powder, Na[Fe(OH_2)EDTA] solution, Na_2[Fe(OH_2)EDTA] solution, and FeEDTA-NO solution. The EXAFS of both the powder and solution forms of Na[Fe(OH_2)EDTA] were studied to determine if there is any significant structural change between solid and solution forms. The results of the first-shell empirical fits are given in Table 3.2 and Figure 3.11.

The first-shell distances obtained from the best fit, Fit #1, to the Na[Fe(OH_2)EDTA] powder data match extremely well to the crystallographic values of Li[Fe(OH_2)EDTA]·$2H_2O$[19] (Table 3.3) with two shells of O at ~2.0 and ~2.1 Å and 2 N at ~2.3 Å. The first-shell distances obtained from the best fit, Fit #2, to the Na[Fe(OH_2)EDTA] solution data are very similar to those of the powder sample. The shorter Fe-O distance was elongated by 0.02 Å in the solution sample and the coordination numbers were slightly different. It appears that there are no major changes in the first shell of the Na[Fe(OH_2)EDTA] structure between the solution and the powder since both the difference in the short Fe-O distance and the differences in the coordination numbers are within the uncertainty of the technique. The first-shell distances obtained from the best fit, Fit #3, to the Na_2[Fe(OH_2)EDTA] EXAFS data are given in Table 3.2. While the presence of two shells of O could not be resolved in the reduced form, an average distance of 2.17 Å was obtained which is 0.12 Å longer than the average Fe-O distance in Na[Fe(OH_2)EDTA].

Two fits (Fits #4 and #5) are shown (Figure 3.11) for the FeEDTA-NO solution, one fit with and one without a short Fe-N bond from the Fe-N-O unit. Fit #4, which includes the short Fe-N bond, is substantially better than Fit #5, without the short Fe-N bond, with the *F* value being over a factor of 2 lower for Fit #4. The best fit to the

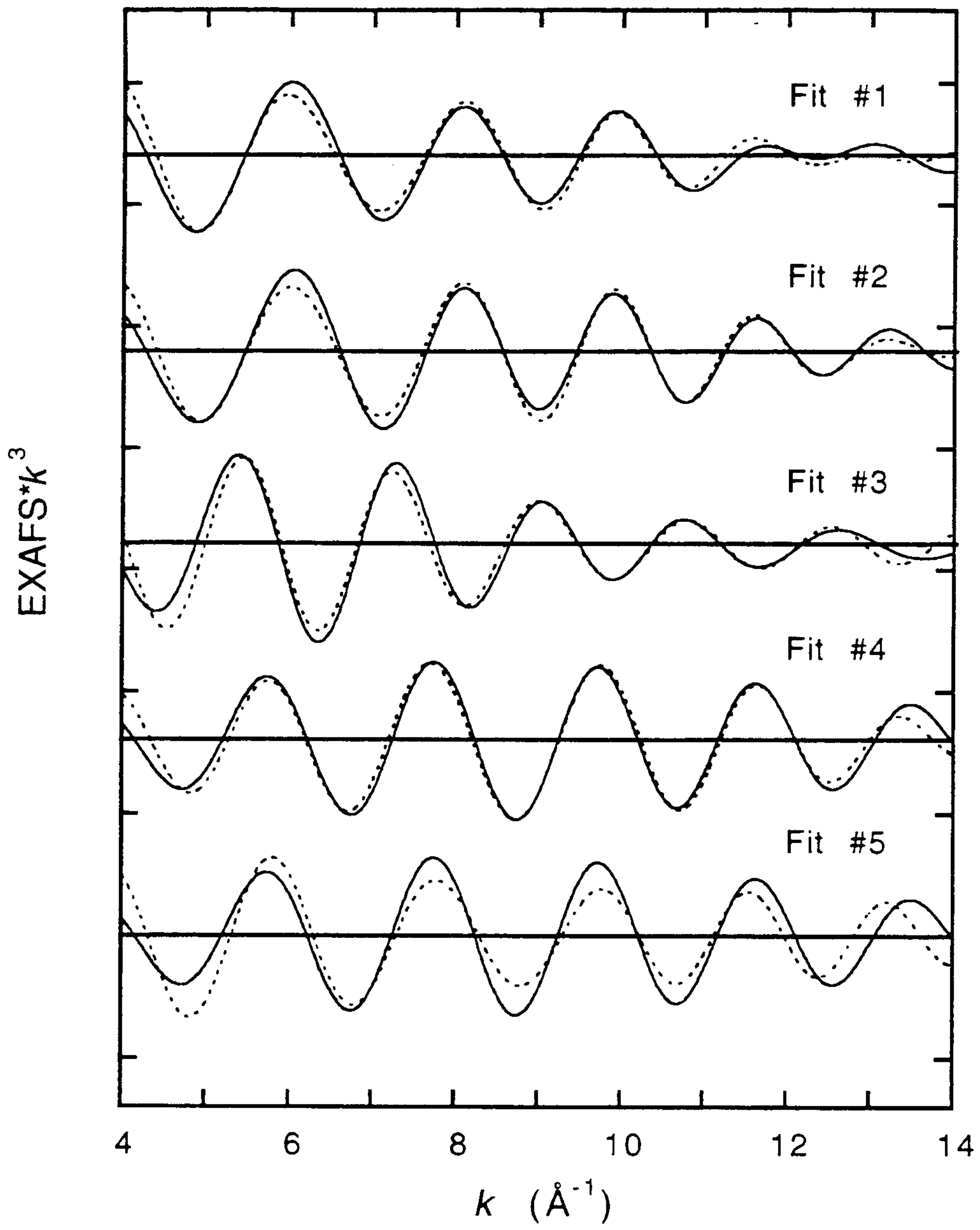

Figure 3.11. Empirical first-shell fits to the Fourier-filtered EXAFS data with the solid line representing the experimental data and the dashed line representing the fit to the data. Fits #1, #2, and #3 are the best empirical fits to the Na[Fe(OH_2)EDTA] powder data (Table 3.2), to the Na[Fe(OH_2)EDTA] solution data, and to the Na_2[Fe(OH_2)EDTA] solution data, respectively. Fits #4 and #5 are fits to the FeEDTA-NO data with Fit #4 containing a short Fe-N distance. (The ordinate scale is 5 between consecutive tick marks with solid horizontal lines going through the zero point of each plot.)

Table 3.2. First Shell Empirical Fits of FeEDTA Complexes.

sample	Fit #	FT window width (Å)	element	CN[a]	bond length (Å)	F[b]
Na[Fe(OH_2)EDTA] (powder)	#1	[0.8-2.2]	O	2.5	1.98	0.40
			O	2.5	2.12	
			N	1.8	2.34	
Na[Fe(OH_2)EDTA] (solution)	#2	[0.8-2.2]	O	2.7	2.00	0.40
			O	1.6	2.12	
			N	1.6	2.34	
Na_2[Fe(OH_2)EDTA] (solution)	#3	[1.0-2.2]	O	3.4	2.17	0.46
			N	1.9	2.34	
FeEDTA-NO (solution)	#4	[1.1-2.0]	N	1.1	1.76	0.39
			O	3.2	2.05	
			N	1.5	2.27	
	#5		O	3.5	2.06	0.85
			N	1.9	2.28	

[a] CN = coordination number. [b] $F = \{[k^6(\text{data-fit})^2]/(\text{no. of points})\}^{1/2}$.

Table 3.3. Comparision of the Li[Fe(OH$_2$)EDTA]·2H$_2$O Crystallographic Bond Distances and Angles to the GNXAS and Empirical Fitted Bond Distances and Angles for Na[Fe(OH$_2$)EDTA] Solution and Powder and FeEDTA-NO.

	Li[Fe(OH$_2$)EDTA]·2 H$_2$O	Na[Fe(OH$_2$)EDTA] Powder			Na[Fe(OH$_2$)EDTA] Solution			FeEDTA-NO Solution		
structural feature(CN)^a	crystallographic values [range]	GNXAS distances/ angles	GNXAS variances^b	empirical first shell distances	GNXAS distances/ angles	GNXAS variances^b	empirical first shell distances	GNXAS distances/ angles	GNXAS variances^b	empirical first shell distances
Fe-O$_1$ (2)	1.97 Å [1.94-2.00]	1.97 Å	0.003	1.98 Å	1.98 Å	0.003	2.00 Å	2.03 Å	0.002	2.05 Å^d
Fe-O$_2$ (3)	2.11 Å [2.11-2.13]	2.10 Å	0.004	2.12 Å	2.09 Å	0.006	2.12 Å	2.11 Å^c	0.006^c	----
Fe-N (2)	2.32 Å [2.30-2.35]	2.33 Å	0.003	2.34 Å	2.35 Å	0.002	2.34 Å	2.33 Å	0.010	2.27 Å
O$_1$-C (2)	1.28 Å [1.27-1.29]	1.33 Å	0.005	----	1.33 Å	0.006	----	1.29 Å	0.004	----
O$_2$-C (2)	1.26 Å [1.26-1.27]	1.30 Å	0.004	----	1.30 Å	0.005	----	1.31 Å	0.005	----
N-C (6)	1.47 Å [1.47-1.48]	1.48 Å	0.002	----	1.47 Å	0.002	----	1.47 Å	0.003	----
O$_{1,2}$-O$_3$(4)	2.23 Å [2.20-2.25]	2.30 Å	0.006	----	2.27 Å	0.006	----	----	----	----
C-O$_3$ (4)	1.23Å [1.21-1.25]	1.27 Å	0.002	----	1.28 Å	0.007	----	1.29 Å	0.008	----
Fe-C (4)	2.90 Å [2.79-2.99]	2.91 Å	0.008	----	2.92 Å	0.008	----	2.96 Å	0.010	----
Fe-N (1)	----	----	----	----	----	----	----	1.78 Å	0.003	1.76 Å
N-O (1)	----	----	----	----	----	----	----	1.10 Å	0.001	----
Fe-N-O (1)	----	----	----	----	----	----	----	156°	2×10^0	----
Fe-O$_1$-C (2)	120° [119-121]	121°	3×10^1	----	123°	3×10^1	----	122°	3×10^1	----
Fe-O$_2$-C (2)	122° [121-123]	119°	6×10^1	----	124°	6×10^1	----	122°	6×10^1	----
Fe-N-C (6)	108° [103-112]	106°	1×10^1	----	106°	1×10^1	----	104°	6×10^1	----
O$_1$-Fe-O$_1$(1)	166°	170°	7×10^0	----	170°	1×10^1	----	----	----	----
O$_2$-Fe-O$_2$ (1)	145°	150°	2×10^0	----	150°	2×10^0	----	----	----	----
Fe-O$_1$-O$_3$ (2)	145° [142-148]	150°	5×10^1	----	150°	5×10^1	----	----	----	----
Fe-O$_2$-O$_3$ (2)	149° [148-150]	155°	5×10^1	----	155°	6×10^1	----	----	----	----
Fe-C-O$_3$ (4)	158° [153-161]	158°	1×10^1	----	159°	1×10^1	----	158°	2×10^1	----

[a] CN = number of configurations in the complex. [b] Bond variances $\left(\sigma_R^2\right)$ and angle variances $\left(\sigma_\theta^2\right)$ are reported in Å^2 and degrees^2, respectively.

[c] coordination number was fixed at 2. [d] average of both Fe-O shells

FeEDTA-NO data has 1.1 N at 1.76 Å, 3.2 O at 2.05 Å, and 1.5 N at 2.27 Å. The short 1.76 Å Fe-N distance is typical for the {FeNO}^{7} systems.[4] The Fe-O distance appears to be an average of two Fe-O shells, which could not be resolved given the range of available data. A fit with four contributions was attempted (Fe-N at ~1.8 Å, Fe-O at 2.0 Å, Fe-O at ~2.1 Å and Fe-N at ~2.3) but both Fe-O distances coalesced at 2.05 Å with an F value identical to that for Fit #4.

The Fe-O and Fe-N distances of the EDTA ligand in FeEDTA-NO are more similar to the respective distances in $Na[Fe(OH_2)EDTA]$ than those in $Na_2[Fe(OH_2)EDTA]$. In addition, the XAS edge of FeEDTA-NO is more similar to the edge of $Na[Fe(OH_2)EDTA]$ than to that of $Na_2[Fe(OH_2)EDTA]$.[5] The coordination number of the oxygens varies in a chemically reasonable way for the solid $Na[Fe(OH_2)EDTA]$, solution $Na[Fe(OH_2)EDTA]$, and FeEDTA-NO. The crystallographically-characterized $[Fe(OH_2)EDTA]^-$ has 5 oxygens in the first shell and the best fits to the $Na[Fe(OH_2)EDTA]$ powder and solution data give an oxygen coordination number of 5.0 and 4.3, respectively. The somewhat lower coordination number in solution could be related to an increased disorder in the solution. The NO seems to take the place of the H_2O at 2.11 Å, since the oxygen coordination number has decreased to 3.2 in the best FeEDTA-NO fit.

The GNXAS approach was used to analyze EXAFS data of $Na[Fe(OH_2)EDTA]$ powder and solution to ensure that the MS contributions could be properly accounted for and that reliable second and third shell bond distances and bond angles could be obtained. The results of the fits to the $Na[Fe(OH_2)EDTA]$ solution data also provided values for bond and angle variances and the off-diagonal covariance matrix elements for the fits to the FeEDTA-NO data.

The best fit to the $Na[Fe(OH_2)EDTA]$ powder data is presented and discussed in Chapter 2. The low-frequency EXAFS is dominated by three waves from two-atom contributions: Fe-O_1, Fe-O_2 and Fe-N, where O_1 refers to the oxygen at 1.97 Å and O_2 refers to the oxygen at 2.11 Å. The EXAFS distances for these three shells show excellent agreement with the crystallographic values of the $Li[Fe(OH_2)EDTA]\cdot 2H_2O$,[19] deviating by <0.01 Å (Table 3.3). There were approximately 30 unique three-atom configurations which ranged in distance from 3.0 to 4.5 Å. The eight main contributions were from Fe-O_1-C, Fe-O_2-C, Fe-N-C, O_1-Fe-O_1, O_2-Fe-O_2, Fe-O_1-O_3, Fe-O_2-O_3, and Fe-C-O_3, where O_3 refers to the oxygen outside the first shell. The GNXAS determined bond distances and angles that make up the three-atom contributions are within 5% of the crystallographic values, with the strength of the signal influencing the goodness of the match.[16] Contributions with stronger signals have distances and angles that match closer to the crystallographic values than do contributions with weaker signals. Over a large number of fits with varying contributions, splines, and nonstructural parameters the first-shell distances varied by <0.01 Å, the low-*Z* bond distances (*i.e.* O-C and N-C) varied by ±0.04 Å, and the bond angle varied by ±3°. The GNXAS first-shell distances are within 0.02 Å of the empirical first-shell distances, with the GNXAS distances being slightly closer to the crystallographic values.

The EXAFS data and the FT of the best fit to the Na[Fe(OH_2)EDTA solution data are presented in Figure 3.12 and the bond distances and angles from that fit are given in Table 3.3. The main contributions to the EXAFS are the same as for the Na[Fe(OH_2)EDTA] powder. The best fit shows excellent agreement with the experimental EXAFS as does the FT of the experimental data and the fit. The bond distances obtained from the best fit to the Na[Fe(OH_2)EDTA] solution data are within 0.02 Å of the Na[Fe(OH_2)EDTA] powder values and the bond angles are all within 2° with two exceptions. There is a 0.03 Å difference in the $O_{1,2}$-O_3 distance and a 5° difference in the Fe-O_2-C angle. However, both the $O_{1,2}$-O_3 distance and the Fe-O_2-C angle show large disorder, with a bond variance of 0.006 Å^2 and an angle variance of 60 (degrees)^2 (Table 3.3). The bond and angle variances are very similar, but slightly larger than the powder values, which is expected since there should be more disorder in solution. The increase in the solution variances is also consistent with the fact that in the empirical analysis (where the Debye-Waller factors are fixed) the coordination numbers for the solution were lower than those of the powder. The similarities in bond lengths, bond angles, and the respective variances indicate that the [Fe(OH_2)EDTA]$^-$ unit is structurally the same in the powder and the solution form. Therefore it is a reasonable approximation to initially model FeEDTA-NO in the solution form using the crystallographic coordinates of Li[Fe(OH_2)EDTA]·2H_2O with NO replacing the H_2O.

The best fit to the EXAFS of the FeEDTA-NO solution data is shown in Figure 3.13 and the bond distances and angles are presented in Table 3.3. The FT of the EXAFS data of the best fit is shown in Figure 3.14B. The initial [Fe(OH_2)EDTA]$^-$ structural model was modified by including a short Fe-N distance (~1.8 Å) and fixing the coordination number for the 2.1 Å Fe-O distance at two. Fits were done using $\gamma^{(2)}$ signals exclusively to determine first-shell distances. Once a reasonable fit was obtained, the first-shell distances were fixed and a Fe-N-O signal was added to the fit. Fe-N-O signals were calculated every 10° between 90° and 180°, fixing the Fe-N distance at 1.8 Å and the N-O distance at 1.1 Å. Fits were then performed including the Fe-N-O signal at each angle. Reasonable fits were obtained for Fe-N-O angles between 150° and 160°. At this point, other three-atom signals were included in the fits allowing the distances,

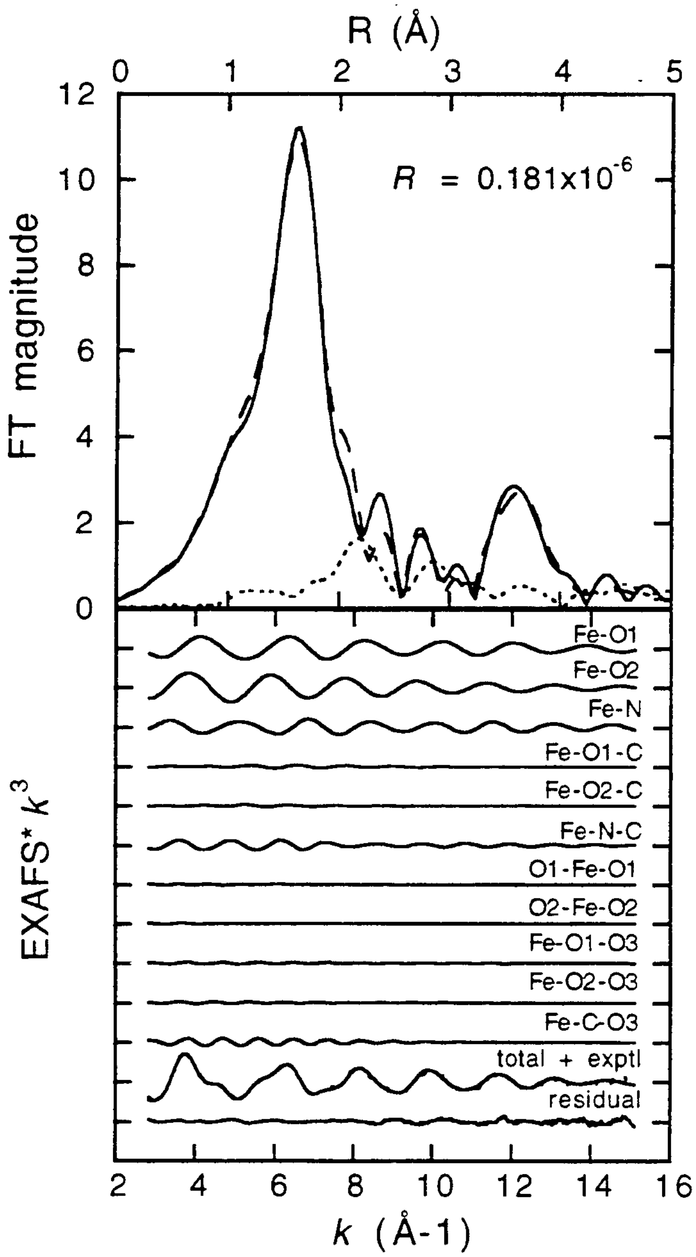

Figure 3.12. Comparison of the GNXAS theoretical signal with the experimental data of Fe K-edge k^3-weighted EXAFS of Na[Fe(OH$_2$)EDTA] solution data. The top portion of the figure contains the non-phase shift corrected FT of the k^3-weighted EXAFS data of the experimental data (——) and that of the total theoretical signal (---). Also shown is the FT of the residual (····). The lower portion of the figure presents the EXAFS signals for the individual contributions. The total theoretical signal is also shown (——) and compared with the experimental data (····) with the residual being the difference between the experimental EXAFS and the theoretical EXAFS. (The ordinate scale is 10 between two consecutive tick marks.)

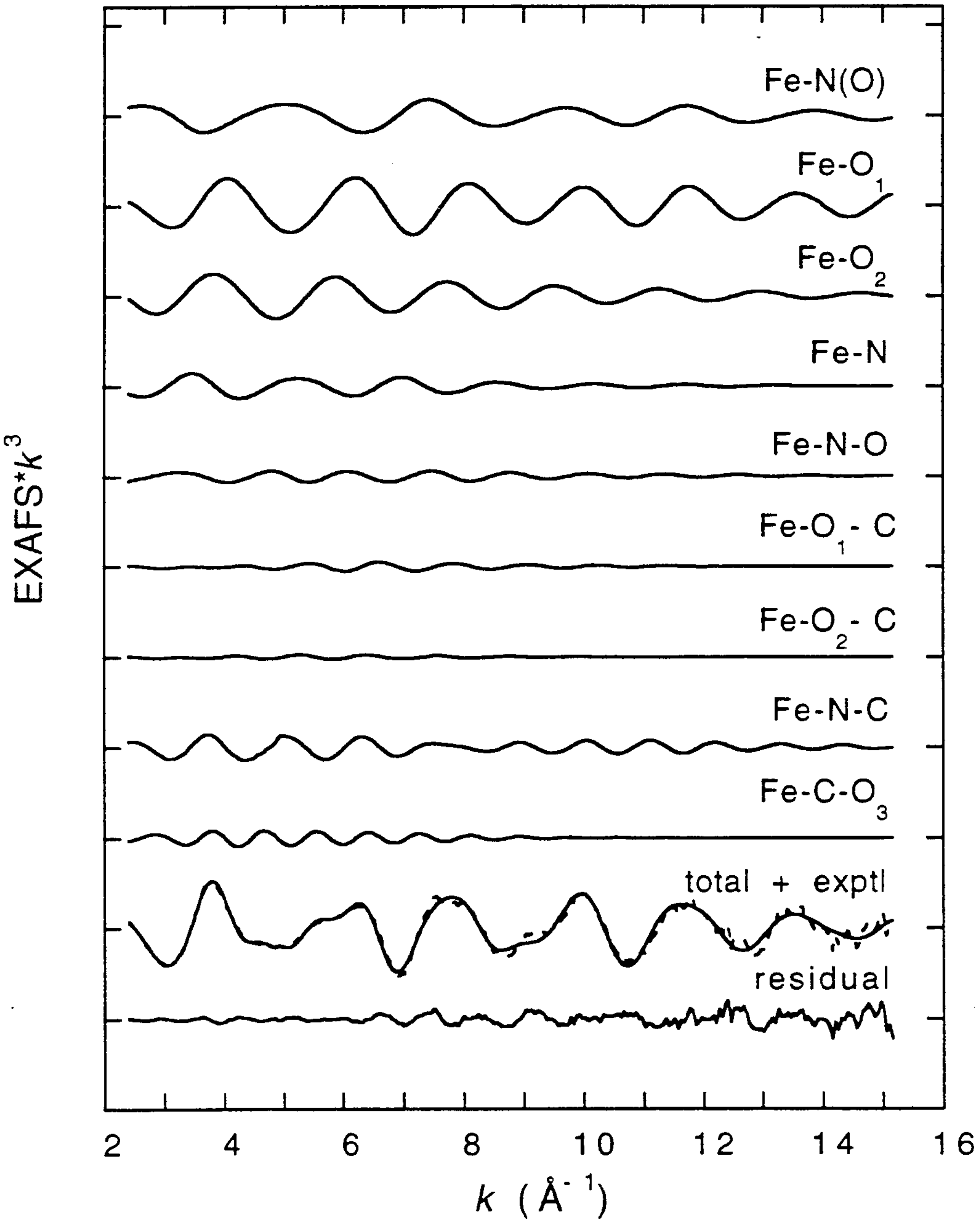

Figure 3.13. EXAFS signals for individual contributions in the best fit for the FeEDTA-NO data. The total signal (——) is also shown and compared with the experimental data (---) with the residual being the difference between the experimental EXAFS and the theoretical EXAFS. (The ordinate scale is 10 between two consecutive tick marks.)

angles, and elements of the covariance matrix to vary within a restricted range. The Fe-N-O angle was allowed to vary between 145° and 165°. Several of the three-atom contributions included in the fit to the Na[Fe(OH_2)EDTA] solution data (Figure 3.12) were left out of the FeEDTA-NO fits (O_1-Fe-O_1, O_2-Fe-O_2, Fe-O_1-O_3, and Fe-O_2-O_3), since the signals were relatively weak and only increased the number of variables in the fit. The distances and bond angles obtained from the GNXAS final fit are very similar to the distances and bond angles from the GNXAS fits of the Na[Fe(OH_2)EDTA] powder and solution data as can be seen in Table 3.3. The complicated EXAFS spectrum in Figure 3.13 is dominated by four waves of lower frequency: Fe-N(O), Fe-O_1, Fe-O_2 and Fe-N. However, the longer Fe-N contribution is much weaker than in the Na[Fe(OH_2)EDTA] powder and solution EXAFS with a bond variance that is three to four times higher indicating that the bond between the Fe-N at ~2.3 Å may be weakened when the NO binds. The Fe-N-O signal is fairly strong compared to the other three-atom signals. The Fe-N(O) and N-O bond distances obtained from the GNXAS fit were 1.78 and 1.10 Å, respectively. These distances are consistent with other Fe-N(O) and N-O bond distances in $\{FeNO\}^7$ systems.[4] A fit with an Fe-N-O angle of 156° shows excellent agreement with the experimental EXAFS data, Figure 3.13, and with the Fourier transformed data, Figure 3.14B, up to 3.5 Å. The discrepancy between the theoretical and experimental signal in the FT beyond 3.5 Å can be attributed to the fact that several three-atom contributions associated with weaker signals in that region were not included in the fit.

As was done with the crystallographically-characterized $\{FeNO\}^7$ complexes, the sensitivity of the calculated spectrum to the EXAFS data for FeEDTA-NO was tested as a function of Fe-N-O angle. The FTs for FeEDTA-NO with Fe-N-O values of 180°, 156° (best fit), and 120° are shown in Figure 3.14. A plot of log(*R* value) *vs* Fe-N-O angle (Figure 3.15) of the FeEDTA-NO data displays a minimum at 156°. This looks extremely similar to the plot of the Fe(TACN)(N_3)$_2$NO data, where Fe(TACN)(N_3)$_2$NO has an Fe-N-O angle of 156°. It is not surprising that the geometric structures of the Fe-N-O unit in Fe(TACN)(N_3)$_2$NO and FeEDTA-NO are similar since both compounds exhibit very similar optical spectroscopy.[5]

3.4. Summary

Multiple-scattering signals from three-atom configurations are accurately modeled by GNXAS to obtain angular information on the Fe-N-O unit of $\{FeNO\}^7$ complexes. The GNXAS fits to the $\{FeNO\}^7$ model compounds are sensitive to the Fe-N-O angle

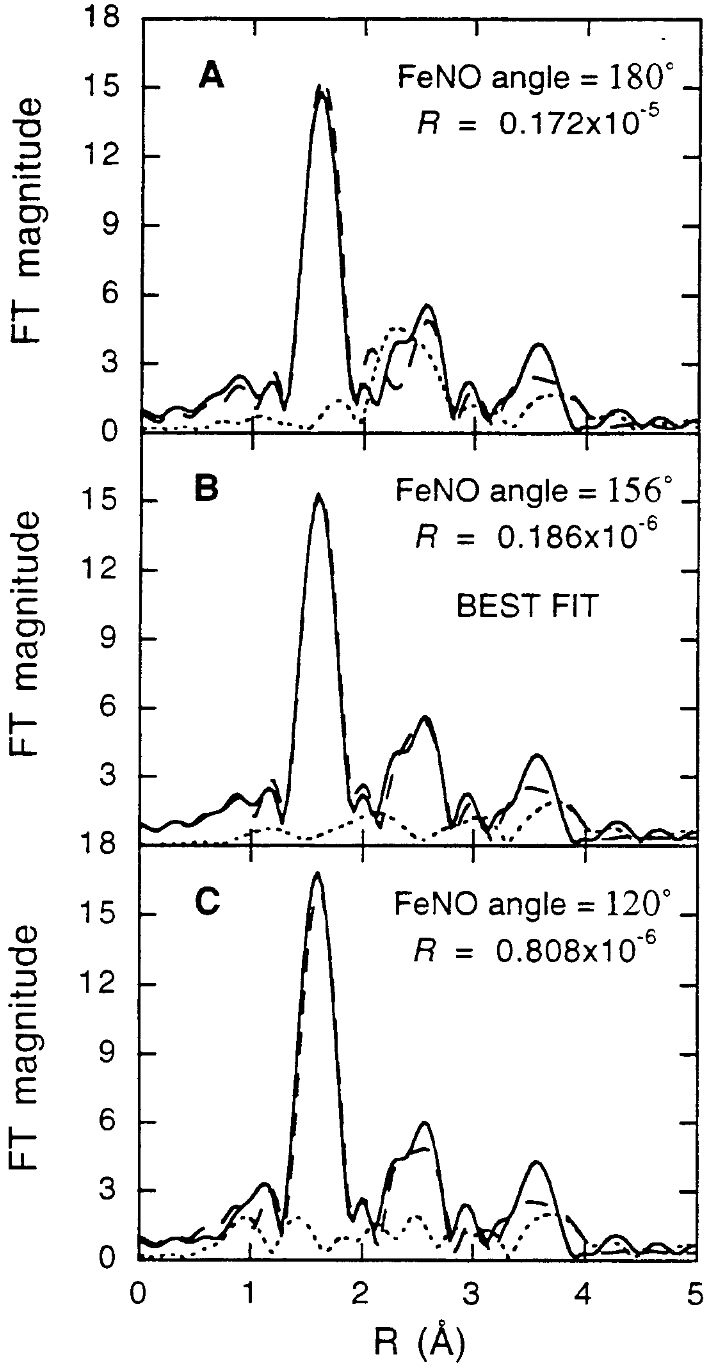

Figure 3.14. A comparison of the theoretical (---) and experimental (——) non-phase shift corrected FT of FeEDTA-NO EXAFS data, along with the FT of the EXAFS residual (····). The R value is an indication of the goodness of the fit. Calculated spectra are for Fe-N-O bond angles of: (A)180°, (B) 156° (best fit), and (C) 120°.

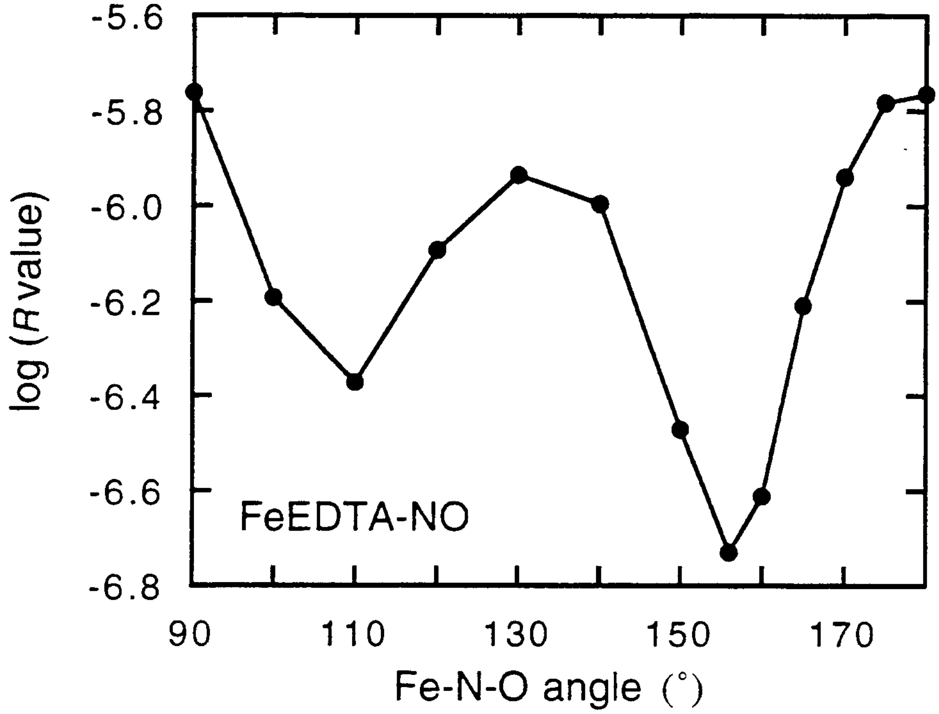

Figure 3.15. Plot of the log(R value) *vs* Fe-N-O angle for FeEDTA-NO where each point represents a match of the calculated EXAFS spectrum to the data. The lower the R value the better the fit. This plot of FeEDTA-NO calculated spectra exhibits similar behavior to the plot of the Fe(TACN)$(N_3)_2$NO calculated spectra (Figure 3.10B) with the dominant minimum being around 155°.

when the Fe-N-O signal is significant in comparison with the total EXAFS signal. It is possible to determine whether the Fe-N-O unit is linear or bent and estimate the Fe-N-O angle, with the GNXAS fits being very sensitive when the angle is between 150° and 180°. The Fe-N-O angle of a crystallographically-uncharacterized $\{FeNO\}^7$ model complex was determined. Using this method the Fe-N-O angle of FeEDTA-NO is determined to be bent, and close to 156°. The results of this study establish that EXAFS analysis using GNXAS can provide reliable angular information on low-*Z* small molecules liganded to transition metal complexes. This work provides the basis for studying NO complexes with transition metal active sites in metalloproteins. It is also straightforward to extend this methodology to study other diatomics such as O_2^- or O_2^{2-} liganded to transition metal sites.

3.5. Acknowledgments

The $Na[Fe(OH_2)EDTA]$, $Na_2[Fe(OH_2)EDTA]$, and FeEDTA-NO solutions were prepared and provided by Yan Zhang and Mark Pavlosky. This research was supported by grants from the NIH (RR01209, K.O.H., GM40392, E.I.S) and NSF (CHE91-21576, K.O.H.). The Stanford Synchrotron Radiation Laboratory is supported by the Department of Energy, Office of Basic Energy Sciences, Divisions of Chemical Science and Material Science, and in part by the National Institutes of Health, National Center of Research Resources, Biomedical Research Technology Program and DOE's Office of Health and Environmental Research. Rino Natoli, Andrea Di Cicco, and Adriano Fillipponi (who are funded by the Italian INFN and CNR research institutions) should be thanked for providing the GNXAS data analyis package, as well as for their help in installing the package and providing insight into the intricacies of GNXAS fitting.

3.6. References and Notes

(1) (a) Solomon, E. I.; Zhang, Y. *Acc. Chem. Res.* **1992**, *25*, 343. (b) Smith, W. L.; Lands, W. E. M. *J. Biol. Chem.* **1972**, *247*, 1038. (c) Kohlmiller, N. A.; Howard, J. B. *J. Biol. Chem.* **1979**, *254*, 7302. (d) Nozaki, M.; Kagamiyama, H.; Hayaishi, O. *Biochem. Z.* **1963**, *338*, 582. (e) Burger, R. M.; Peisach, J.; Blumberg, W. E.; Wittenberg, J. B.; Sausville, E. A.; Horwitz, S. B. *Electron Transport and Oxygen Utilization*; Elsevier: New York, 1982; p 319. (f) Shiman, R. *Folates and Pterins*; Wiley: New York, 1984; Vol. 2, p 179. (g) Lindstedt, S.; Odelhög, B.; Rundgren, M. *Biochemistry* **1977**, *16*, 3369. (h) Ruettinger, R. T.; Griffith, G. R.;

Coon, M. J. *Arch. Biochem. Biophys.* **1977**, *183*, 528. (i) Batie, C. J.; LaHaie, E.; Ballou, D. P. *J. Biol. Chem.* **1987**, *262*, 1510. (j) Pang, C. -P.; Chakravarti, B.; Adlington, R. M.; Ting, H. -H.; White, R. L.; Jayatilake, G. S.; Baldwin, J. E.; Abraham, E. P. *Biochem. J.* **1984**, *222*, 789. (k) Slykhouse, T. O.; Fee, J. A. *J. Biol. Chem.* **1976**, *251*, 5472.

(2) (a) Nelson, M. J. *J. Biol. Chem.* **1987**, *262*, 12137. (b) Rich, P. R.; Salerno, J. C.; Leigh, J. S.; Bonner, W. D. *FEBS Lett.* **1978**, *93*, 323. (c) Arciero, D. M.; Lipscomb, J. D. *J. Biol. Chem.* **1986**, *261*, 2170. (d) Arciero, D. M.; Orville, A. M.; Lipscomb, J. D. *J. Biol. Chem.* **1985**, *260*, 14035. (e) Twilfer, H.; Bernhardt, F.-H.; Gersonde, K. *Eur. J. Biochem.* **1985**, *147*, 171. (f) Chen, V.J .; Orville, A. M.; Harpel, M. R.; Frolik, C. A.; Surerus, K. K.; Münck, E.; Lipscomb, J. D. *J. Biol. Chem.* **1989**, *264*, 21677.

(3) The Feltham-Enemark formalism for $\{MNO\}^x$ complexes is used here in which x is the number of d type electrons in the system when the nitrosyl ligand is formally considered as NO^+ (Enemark, J. H.; Feltham, R. D. *Coord. Chem. Rev.* **1974**, *13*, 339).

(4) (a) Wells, F. V.; McCann, S. W.; Wickman, H. H.; Kessel, S. L.; Hendrickson, D. N.; Feltham, R. D. *Inorg. Chem.* **1982**, *21*, 2306. (b) Bill, E.; Bernhardt, F. -H.; Trautwein, A. X.; Winkler, H. *Eur. J. Biochem.* **1985**, *147*, 177. (c) Earnshaw, A.; King, E. A.; Larkworthy, L. F. *J. Chem. Soc. (A) Inorg. Phys. Theor.* **1969**, 2459. (d) Salerno, J. C.; Siedow, J. N. *Biochim. Biophys. Acta* **1979**, *579*, 246. (e) Pohl, K.; Wieghardt, K.; Nuber, B.; Weiss, J. *J. Chem. Soc., Dalton Trans.* **1987**, 187.

(5) (a) Zhang, Y.; Pavlosky, M. A.; Brown, C. A.; Westre, T. E.; Hedman, B.; Hodgson, K. O.; Solomon, E. I. *J. Am. Chem. Soc.* **1992**, *114*, 9189. (b) Brown, C. A.; Pavlosky, M. A.; Westre, T. E.; Zhang, Y.; Hedman, B.; Hodgson, K. O.; Solomon, E. I. *J. Am. Chem. Soc.* **1995**, *117*, 715.

(6) (a) Ashley, C. A.; Doniach, S. *Phys. Rev. B* **1975**, *11*, 1279. (b) Lee, P. A.; Pendry, J. B. *Phys. Rev. B* **1975**, *11*, 2795. (c) Cramer, S. P. Ph.D. Thesis, Stanford University, 1978.

(7) (a) Teo, B. -K. *J. Am. Chem Soc.* **1981**, *103*, 3990. (b) Co, M. S.; Hendrickson, W. A.; Hodgson, K. O.; Doniach, S. *J. Am Chem. Soc.* **1983**, *105*, 1144.

(8) (a) Cramer, S. P.; Hodgson, K. O.; Stiefel, E. I.; Newton, W. E. *J. Am. Chem Soc.* **1978**, *100*, 2748. (b) Binsted, N.; Evans, J.; Greaves, G. N.; Price, R.J . *J. Chem. Soc., Chem. Commun.* **1987**, 1330. (c) Binsted, N.; Cook, S. L.; Evans, J.; Greaves, G. N.; Price, R. J. *J. Am. Chem. Soc.*, **1987**, *109*, 3669. (d) Filipponi, A.;

Di Cicco, A.; Zanoni, R.; Bellatreccia, M.; Sessa, V.; Dossi, C.; Psaro, R. *Chem. Phys. Lett.* **1991**, *184*, 485.

(9) Westre, T. E.; Hedman, B.; Solomon, E. I.; Hodgson, K. O. Unpublished data.

(10) (a) Filipponi, A.; Di Cicco, A.; Tyson, T. A.; Natoli, C. R. *Solid State Commun.* **1991**, *78*, 265. (b) Filipponi, A.; Di Cicco, A. *Synchrotron Radiation News* **1992**, *6*, 13.

(11) Hedin, L.; Lundqvist, S. *Solid State Phys.* **1969,** *23*,1.

(12) Di Cicco, A.; Stizza, S.; Filipponi, A.; Boscherini, F.; Mobilio, S. *J. Phys. B: At. Mol. Opt. Phys.* **1992**, *25*, 2309.

(13) D'Angelo, P.; Di Cicco, A.; Filipponi, A.; Pavel, N. V. *Phys. Rev. A* **1993**, *47*, 2055.

(14) Burattini, E.; D'Angelo, P.; Di Cicco, A.; Filipponi, A.; Pavel, N. V. *J. Phys. Chem.* **1993**, *97*, 5486.

(15) Nordlander, E.; Lee, S. C.; Cen, W.; Wu, Z. Y.; Natoli, C. R.; Di Cicco, A.; Filipponi, A.; Hedman, B.; Hodgson, K. O.; Holm, R. H. *J. Am. Chem. Soc.* **1993**, *115*, 5549.

(16) Westre, T. E.; Di Cicco, A.; Filipponi, A.; Natoli, C. R.; Hedman, B.; Solomon, E. I.; Hodgson, K. O. *J. Am. Chem. Soc.* **1995**, *117*, 1566.

(17) Hodges, K. D.; Wollman, R. G.; Kessel, S. L.; Hendrickson, D. N.; Van Derveer, D. G.; Barefield, E. K. *J . Am. Chem. Soc.* **1979**, *101*, 906.

(18) Haller, K. J.; Johnson, P. L.; Feltham, R. D.; Enemark, J. H. *Inorg. Chim. Acta* **1979**, *33*, 119.

(19) Lind, M. D.; Hamor, M. J.; Hamor, T. A.; Hoard, J. L. *Inorg. Chem.* **1963**, *3*, 34.

(20) Scott, R. A.; Hahn, J. E.; Doniach, S.; Freeman, H. C.; Hodgson, K. O. *J. Am. Chem. Soc.* **1982**, *104*, 5364.

(21) (a) Stern, E. A.; Heald, S. M. *Rev. Sci. Instrum.* **1979**, *50*, 1579. (b) Lytle, F. W.; Greegor, R. B.; Sandstrom, D. R.; Marques, E. C.; Wong, J.; Spiro, C. L.; Huffman, G. P.; Huggins, F. E. *Nucl. Instrum. Meth. Phys. Res.* **1984**, *226*, 542.

(22) Johansson, L. *Chem. Scr.* **1976**, *9*, 30. The crystal structure of the perchlorate salt has not been determined, but the $[Fe(phenanthroline)_3]^{2+}$ complex structure can be assumed to be identical with that of the corresponding iodide salt (Johansson, L.; Molund, M.; Oskarsson, Å. *Inorg. Chim. Acta* **1978**, *31*, 117).

(23) Mattheiss, L. F. *Phys. Rev.* **1964**, *134*, A970.

(24) Krause, M. O.; Oliver, J. H. *J. Phys. Chem. Ref. Data* **1979**, *8*, 329.

(25) The principal determining factor for E_r is the monochromator and associated vertical slit opening, with the resolution determined by the relationship $\Delta E/E$ =

cot(Θ)ΔΘ, where Θ is a function of the Darwin width and the vertical angular acceptance of the monochromator. The value at the Fe K-edge for the experimental conditions used for these experiments were ~1.4 eV. Lytle, F. W. In *Applications of Synchrotron Radiation*; Winick, H.; Xiam, D.; Ye, M.-h; Huang,T., Eds.; Gordon and Breach Science Publishers: New York, 1989; p. 135.

(26) (a) Cramer, S. P.; Hodgson, K. O. *Prog. Inorg. Chem.* **1979**, *25*, 1. (b) Scott, R. A. *Methods Enzymol.* **1985**, *117,* 414.

(27) (a) Iball, J.; Morgan, C. H. *Acta Crystallogr.* **1967**, *23*, 239. (b) Roof, R. B., Jr. *Acta Crystallogr.* **1956**, *9*, 781.

Chapter 4

A Multiplet Analysis of Fe K-Edge 1s—>3d Pre-Edge Features of Iron Complexes

4.1. Introduction

X-ray absorption spectroscopic (XAS) studies have been used extensively to characterize the iron active sites in both mononuclear and binuclear non-heme iron enzymes.[1-18] While extended X-ray absorption fine structure (EXAFS) analysis provides information on the types of ligating atoms and very accurate first-shell iron-ligand distances, it determines with less accuracy the coordination number and in general gives little or no information on the active site geometry. However, complementary information can be obtained from the edge region of the XAS spectra. In particular, the features in region of the 1s—>3d transition have been shown to be sensitive to the oxidation state and geometry of the iron atom.[19] Additionally, the total intensity of this transition has been shown to increase with decreasing coordination number for iron model complexes due to the loss of inversion symmetry at the iron site.[1,20] Analysis of the 1s—>3d pre-edge feature has already proven useful in the determination of the coordination number of the non-heme iron active sites in ovotransferrin,[1] catechol 1,2-dioxygenase,[1] protocatechuate 3,4-dioxygenase,[1,8] uteroferrin,[11] soybean lipoxygenase,[13,16] rabbit lipoxygenase,[16] human lipoxygenase,[16] and bleomycin.[15] Previously, the splitting of the pre-edge feature was used to characterize the oxidation state and spin state of the iron site in activated bleomycin.[17] The feature from the 1s->3d transition has also been shown to change with differing bridging ligation in binuclear model complexes, with μ-oxo bridged complexes having a fairly intense pre-edge feature with a distinctive shape.[21]

XAS edge spectra of first-row transition metals have a weak pre-edge feature ~10 eV below the absorption edge. This feature was unequivocally assigned as originating from the 1s—>3d transition by Shulman *et. al.* when they observed that Zn(II), a d^{10} system, did not have this feature.[19] A dipole-coupled 1s—>3d transition is forbidden by parity considerations for complexes in a centrosymmetric environment. Yet, experimentally, a very weak pre-edge feature is still observed for complexes in a centrosymmetric environment. In such molecules, the most likely 1s—>3d transition intensity mechanism is electric quadrupole coupling which is theoretically calculated to be two orders of magnitude weaker than electric dipole coupling.[22,23] Experimentally, the quadrupole nature of the 1s—>3d pre-edge feature in D_{4h} $CuCl_4^{2-}$ was determined by Hahn *et. al.* by analysis of the angular dependence of the 1s—>3d transition using polarized radiation and oriented single crystals.[24] Complexes in noncentrosymmetric environments have more intense pre-edge features.[1,20,24-28] The increase in intensity has been attributed to metal 4p mixing into the 3d orbitals which provides some 1s—>4p character to the transition which is electric dipole allowed. Since the quadrupole-coupled mechanism is two orders of magnitude weaker than the dipole-coupled mechanism, only a few percent of 4p mixing into the 3d orbitals can have a dramatic effect on the intensity of the 1s—>3d pre-edge feature.

In this study, XAS Fe K-edge data on high and low spin ferrous and ferric inorganic model complexes with varying geometries, as well as binuclear complexes with varying oxidation states, geometries, and bridging ligation, have been measured in order to establish a detailed understanding of the 1s—>3d pre-edge feature and its sensitivity to the electronic and geometric structure of the iron site. The energy splitting and intensity distribution of the pre-edge features of these complexes vary with spin state, oxidation state, geometry, and bridging ligation (in the binuclear complexes). A methodology for interpreting this energy splitting and intensity distribution of the 1s—>3d pre-edge features is developed for high spin ferrous and ferric complexes in octahedral, tetrahedral and square pyramidal environments and low spin ferrous and ferric complexes in octahedral environments. In each case, the allowable many-electron excited states are determined using ligand field theory. The energies of the excited states are calculated and compared to the measured energy splitting in the 1s—>3d pre-edge features. The relative intensities of transitions into the many-electron excited states are obtained and also compared to the observed intensity pattern of the pre-edge feature. The effect of distorting the iron site to tetrahedral and square-pyramidal geometries is analyzed. The contribution to the pre-edge intensity from both an electric quadrupole and an electric dipole (from 4p-3d mixing) intensity mechanism is determined for these distorted cases where the amount of 4p mixing is experimentally obtained and compared to a theoretical estimate of the amount of 4p mixing determined from density functional calculations.

4.2. Experimental Section

4.2.1. Sample Preparation

FeF_2, $FeCl_2$, $FeBr_2$, FeI_2, $FeSiF_6 \cdot 6H_2O$, $(NH_4)_2Fe(SO_4)_2 \cdot 6H_2O$, FeF_3, $FeCl_3$, $FeBr_3$, $Fe(acac)_3$, $(NH_4)Fe(SO_4)_2 \cdot 12H_2O$, $K_3Fe(CN)_6$, and $K_4Fe(CN)_6$ were purchased from Aldrich in >98% purity and used without further purification. FeF_2, $FeCl_2$, $FeBr_2$, FeI_2, $FeSiF_6 \cdot 6H_2O$, and $(NH_4)_2Fe(SO_4)_2 \cdot 6H_2O$ are air-sensitive and, therefore, these complexes were shipped in Ar-filled bottles and immediately placed in an inert atmosphere glove box upon delivery. All other model complexes were prepared as previously described (see references in Tables 4.1, 4.2, and 4.3). The crystalline samples were each mixed with boron nitride (BN) and ground into a fine powder. The BN/sample mixture was pressed into a 1 mm thick Al spacer that was sealed with 63.5 μm Mylar tape windows. All air-sensitive complexes were prepared in an inert atmosphere nitrogen-filled glove box and immediately frozen in liquid nitrogen.

4.2.2. XAS Data Collection and Reduction

X-ray absorption spectra were recorded at the Stanford Synchrotron Radiation Laboratory (SSRL) and the National Synchrotron Light Source (NSLS) on beamlines 2-3, 4-2, 4-3, 7-3, and X19A, during dedicated conditions (3 GeV, 30-100 mA/2.5 GeV, 100-200 mA, respectively). Tables 4.1, 4.2, and 4.3 give the respective beamlines and temperatures at which the data were collected for each sample.[29] In all cases, the radiation was monochromatized using a Si(220) double-crystal monochromator. For the majority of the data, the vertical aperature of the pre-monochromator slits was 1 mm. The only exception was for the $(BF_4)[Fe(TMC)X]$ series (where X = Cl^-, Br^-, CH_3CN^-, and N_3^-) in which case the pre-monochromator slit opening was 1.5 mm vertically. Data were measured in transmission mode with N_2 filled ionization chambers to $k = 9.5$ Å^{-1}, detuning the monochromator 50% at 7474 eV to minimize harmonic contamination (in some cases the data were measured to $k = 15$ Å^{-1} in order to obtain EXAFS data as well). In general, two to five scans were measured for each sample. A smooth pre-edge background was removed from each averaged spectrum by fitting a first order polynomial to the pre-edge region and subtracting this polynomial from the entire spectrum. A two-segment spline of order two was fit to the EXAFS region and the data normalized to an edge jump of one at 7130 eV. Energies were calibrated using an internal Fe foil standard, assigning the first inflection point to 7111.2 eV.[30] The spectrometer energy resolution was approximately 1.4 eV[31] with reproducibility in edge position determination of < 0.2 eV.

4.2.3. Data Analysis

The intensities and energies of pre-edge features of the model complexes were quantitated by least-squares fits to the data. The fitting program EDG_FIT, which utilizes the double precision version of the public domain MINPAK fitting library[32] was used. EDG_FIT was written by Dr. Graham N. George of the SSRL. Pre-edge features were modeled by pseudo-Voigt line shapes (simple sums of Lorentzian and Gaussian functions).[31,33-35] A fixed 50:50 ratio of Lorentzian to Gaussian contribution for the pre-edge feature successfully reproduced these spectral features. Functions modeling the background underneath the pre-edge features were chosen empirically to give the best fit and included a pseudo-Voigt feature that mimicked the white line and in some cases pseudo-Voigt features that mimicked shoulders on the rising edge. Furthermore, the second derivative of the data was compared to the second derivative of the fit and only fits where a good overall match was obtained were accepted. In all cases, a number of acceptable fits, typically eight, were obtained which equally well reproduced the data and the second derivative varying the energy range over which the data was fit and the background functions used. All spectra were fit over three energy ranges: 7108 - 7116 eV, 7108 - 7117 eV, and 7108 - 7118 eV. Typically, only functions modeling the pre-edge peaks and one function modeling the background were needed to obtain a good match to the data over the range 7108 - 7116 eV, while functions modeling shoulders on the rising edge were needed to obtain a good match to the data over the range 7108 - 7118 eV. The value reported for the area of a fitted feature (where the peak area was approximated by the height x full width at half-maximum (FWHM)) is the average of all the pseudo-Voigt functions that fit the pre-edge features from all the successful fits. To quantitate the error, the standard deviations for the peak energies and areas were calculated from all the pseudo-Voigt functions that fit the pre-edge features from all the successful fits for each sample.

4.3. Results and Analysis

Fe K-edge XAS data were measured for approximately 50 monomeric and dimeric iron model complexes. The energies and areas of the 1s—>3d pre-edge features were determined by fits to the data and are presented in Tables 4.1 (high spin iron complexes), 4.2 (binuclear complexes), and 4.3 (low spin iron complexes). A multiplet analysis was used to explain the energy splitting and intensity patterns of the pre-edge features for the various cases: high spin ferrous complexes (O_h, T_d and C_{4v} geometries), high spin ferric complexes (O_h, T_d and C_{4v} geometries), binuclear complexes, and O_h low spin ferrous and ferric complexes. In each case, the strong field many-electron states were determined for the $d^{(n+1)}$ excited state[36] where the only effect of the core 1s hole should be an increase in the potential since it is spherically symmetric.[37] The energies of the many-electron states were determined by using reasonable values for 10Dq, B, and C (*vide infra*) and solving the Tanabe-Sugano matrices.[38] The intensity of the pre-edge features due to the transition into each many-electron state was analyzed in terms of both a quadrupole intensity and a dipole intensity (*i.e.* 4p mixing into the 3d orbitals) mechanism. In the cases where the iron atom was in a noncentrosymmetric environment, the amount of 4p mixing into the 3d orbitals was determined and compared to the theoretical estimate from density functional calculations.

4.3.1. High Spin Ferrous Complexes

4.3.1.1. O_h Geometry. Fe K-edge XAS data were collected for eight high spin ferrous octahedral model complexes with varying ligation: F^-, Cl^-, Br^-, I^-, H_2O, and imidazole. All of these complexes have an iron atom in an approximately octahedral site. FeF_2 has the largest distortion away from O_h with the axial ligands being 0.1 Å closer to the iron than the equatorial ligands.[39] The other seven complexes have iron sites that are nearly O_h with ligand distances that differ by less than 0.05 Å. The XAS edge spectra for FeF_2, $FeCl_2$, $FeBr_2$, and FeI_2 are shown in Figure 4.1 and the spectra for rinneite, $FeSiF_6{\bullet}6H_2O$, $(NH_4)_2Fe(SO_4)_2{\bullet}6H_2O$, and $[Fe(imidazole)_6]Cl_2$ are shown in Figure 4.2. The lowest energy transitions are the weak 1s—>3d pre-edge peaks at approximately 7112 eV followed by the 1s—>4p transition at approximately 7125 eV. An expanded view of the 1s—>3d pre-edge region is shown as insets in Figures 4.1 and 4.2. The energies and areas of the pre-edge features are presented in Table 4.1. All eight high spin ferrous octahedral model complexes have two very weak pre-edge features that are split by ~2 eV at ~7111.5 and 7113.5 eV.

The 1s—>3d transition is formally electric dipole forbidden, but can gain intensity through an allowed quadrupole transition and by 4p mixing into the 3d states as a result of a noncentrosymmetric environment of the metal site. Since all eight of these complexes have a nearly centrosymmetric octahedral iron site, the only intensity mechanism available is the allowed quadrupole transition. The splitting of the high spin ferrous pre-edge feature has been observed before,[19] and has been attributed to the free ion splitting of the ^4F and ^4P terms (which is ~2 eV). However, the iron atom in these complexes is affected by an octahedral ligand field which causes the 3d orbitals to split into a t_2 and an e set. Removing the degeneracy of the 3d orbitals causes the free ion terms to split into four many-electron states: $^4T_1$, $^4T_2$, $^4T_1$, and $^4A_2$.[36] The ground state of a high spin ferrous atom in an O_h ligand field has an electronic (hole) configuration of $t_2^2e^2$. Promoting an electron from a 1s orbital into the 3d manifold gives the t_2e^2 and t_2^2e configurations (Scheme 1).

Table 4.1. XAS Pre-Edge Energies and Areas for High Spin Iron Model Complexes.

compound	oxidation state	ligation	beamline, temperature	pre-edge peak energy[a]	pre-edge peak area[a,b]	total pre-edge peak area[b]	peak energy differences[c]	peak area ratio[d]	reference
$(Et_4N)_2[FeCl_4]$	ferrous	4 Cl	SSRL 7-3, 10 K	7111.60 (0.02) 7113.12 (0.02)	8.6 (0.4) 4.3 (0.7)	12.9 (0.6)	1.5	0.67	53
Cs_3FeCl_5	ferrous	4 Cl	SSRL 2-3, 10 K	7111.60 (0.01) 7113.11 (0.01)	9.8 (0.3) 3.3 (0.3)	13.1 (0.4)	1.5	0.75	54
$Fe(HB(3,5\text{-}i\text{Pr}_2pz)_3)Cl$	ferrous	3 N, 1 Cl	SSRL 2-3, 10 K	7111.64 (0.02) 7113.17 (0.02)	14.2 (0.5) 5.6 (0.9)	19.8 (0.9)	1.5	0.72	55
gillespite ($BaFeSi_4O_{10}$)	ferrous	4 O	SSRL 4-3, 100 K	7111.74 (0.02) 7113.25 (0.03)	4.1 (0.3) 1.2 (0.2)	5.3 (0.3)	1.5	0.78	56,57
$(BF_4)[Fe(TMC)Cl]$	ferrous	4 N, 1 Cl	SSRL 7-3, 300 K	7111.41 (0.01) 7113.43 (0.02)	10.9 (0.1) 2.0 (0.3)	12.9 (0.2)	2.0	0.84	58
$(BF_4)[Fe(TMC)Br]$	ferrous	4 N, 1 Br	SSRL 7-3, 300 K	7111.35 (0.01) 7113.24 (0.04)	9.0 (0.3) 2.1 (0.4)	11.1 (0.3)	1.9	0.81	58
$(BF_4)[Fe(TMC)CH_3CN]$	ferrous	4 N, 1 C (CH_3CN)	SSRL 7-3, 300 K	7111.52 (0.04) 7113.30 (0.12)	10.5 (0.8) 2.2 (1.2)	12.7 (0.5)	1.8	0.83	58
$(BF_4)[Fe(TMC)N_3]$	ferrous	4 N, 1 N (N_3)	SSRL 7-3, 300 K	7111.47 (0.01) 7113.30 (0.05)	12.4 (0.5) 1.0 (0.2)	13.4 (0.3)	1.8	0.92	58
FeF_2	ferrous	6 F	SSRL 7-3, 10 K	7111.38 (0.03) 7112.28 (0.09) 7113.48 (0.06)	2.2 (0.2) 1.0 (0.1) 1.2 (0.2)	4.4 (0.2)	2.1	0.73	39
$FeCl_2$	ferrous	6 Cl	SSRL 7-3, 10 K	7111.32 (0.05) 7112.05 (0.11) 7113.42 (0.05)	1.9 (0.4) 1.4 (0.6) 0.9 (0.2)	4.3 (0.2)	2.1	0.78	59
$FeBr_2$	ferrous	6 Br	SSRL 7-3, 10 K	7111.32 (0.03) 7111.98 (0.25) 7113.15 (0.04)	2.5 (0.6) 0.7 (0.8) 0.6 (0.1)	3.8 (0.3)	1.8	0.84	60
FeI_2	ferrous	6 I	SSRL 4-3, 30 K	7111.35 (0.05) 7112.70 (0.1)	2.2 (0.2) 0.8 (0.2)	3.1 (0.2)	1.3	0.73	60
rinneite ($K_3NaFeCl_6$)	ferrous	6 Cl	SSRL 7-3, 10 K	7111.32 (0.06) 7111.81 (0.19) 7113.38 (0.04)	1.2 (0.9) 1.8 (1.2) 0.6 (0.1)	3.6 (0.2)	2.1	0.84	61

$FeSiF_6 \cdot 6H_2O$	ferrous	6 O	SSRL 2-3, 10 K	7111.34 (0.07) 7112.26 (0.08) 7113.60 (0.04)	2.2 (0.5) 0.7 (0.3) 1.1 (0.3)	4.0 (0.5)	2.3	0.73	62,63
$(NH_4)_2Fe(SO_4)_2 \cdot 6H_2O$	ferrous	6 O	SSRL 2-3, 10 K	7111.18 (0.07) 7112.03 (0.15) 7113.58 (0.03)	1.5 (0.6) 1.6 (0.7) 0.9 (0.2)	3.9 (0.3)	2.4	0.77	64
$[Fe(imidazole)_6]Cl_2$	ferrous	6 N	SSRL 2-3, 10 K	7111.24 (0.03) 7112.35 (0.16) 7113.66 (0.02)	1.6 (0.5) 1.6 (0.8) 0.6 (0.2)	3.8 (0.3)	2.4	0.85	65,66
$(Et_4N)[FeCl_4]$	ferric	4 Cl	SSRL 7-3, 10 K	7113.16 (0.00)	20.7 (0.8)	20.7 (0.8)	---	---	67
Fe(salen)Cl	ferric	2 O, 2 N, 1 Cl	SSRL 7-3, 10 K	7112.91 (0.01) 7114.25 (0.07)	12.9 (0.3) 1.5 (0.4)	14.4 (0.6)	1.3	0.89	68
FeF_3	ferric	6 F	SSRL 4-3, 55 K	7113.38 (0.02) 7114.79 (0.02)	3.3 (0.2) 1.9 (0.2)	5.3 (0.3)	1.4	0.63	69
$FeCl_3$	ferric	6 Cl	SSRL 4-3, 30 K	7112.60 (0.02) 7113.77 (0.03)	2.2 (0.2) 1.8 (0.2)	4.0 (0.2)	1.2	0.54	70
$FeBr_3$	ferric	6 Br	SSRL 4-3, 30 K	7112.37 (0.02) 7113.52 (0.03)	2.6 (0.2) 1.8 (0.2)	4.4 (0.2)	1.1	0.59	70
$[FeCl_6][Co(NH_4)_6]$	ferric	6 Cl	SSRL 7-3, 10 K	7112.78 (0.03) 7114.02 (0.03)	2.6 (0.3) 1.4 (0.1)	4.0 (0.2)	1.2	0.65	61,62
$Fe(acac)_3$	ferric	6 O	SSRL 4-3, 55 K	7112.79 (0.02) 7114.31 (0.04)	2.7 (0.3) 1.9 (0.1)	4.6 (0.3)	1.5	0.59	63
$[Fe(urea)_6](ClO_4)_3$	ferric	6 N	SSRL 7-3, 10 K	7112.97 (0.02) 7114.44 (0.02)	2.6 (0.2) 1.9 (0.1)	4.5 (0.3)	1.5	0.58	64
$(NH_4)_3[Fe(malonate)_3]$	ferric	6 O	SSRL 2-3, 10 K	7112.92 (0.03) 7114.44 (0.03)	3.1 (0.3) 2.4 (0.3)	5.5 (0.1)	1.5	0.57	65
$K_3[Fe(oxalate)_3]$	ferric	6 O	SSRL 2-3, 10 K	7112.93 (0.00) 7114.41 (0.01)	4.9 (0.1) 2.4 (0.1)	7.3 (0.2)	1.5	0.67	66
$(NH_4)Fe(SO_4)_2 \cdot 12H_2O$	ferric	6 O	SSRL 2-3, 10 K	7113.14 (0.02) 7114.57 (0.01)	2.7 (0.1) 2.2 (0.2)	4.9 (0.2)	1.4	0.56	67

---

[a] Pre-edge energies and intensities were determined by fits to the data (see the Experimental Section for details on the fitting procedure). [b] The values reported for the pre-edge areas were multiplied by 100. [c] Peak energy differences are the energy differences between the lowest energy and the highest energy pre-edge feature. [d] Peak area ratios are the area of the first pre-edge feature divided by the total pre-edge area.

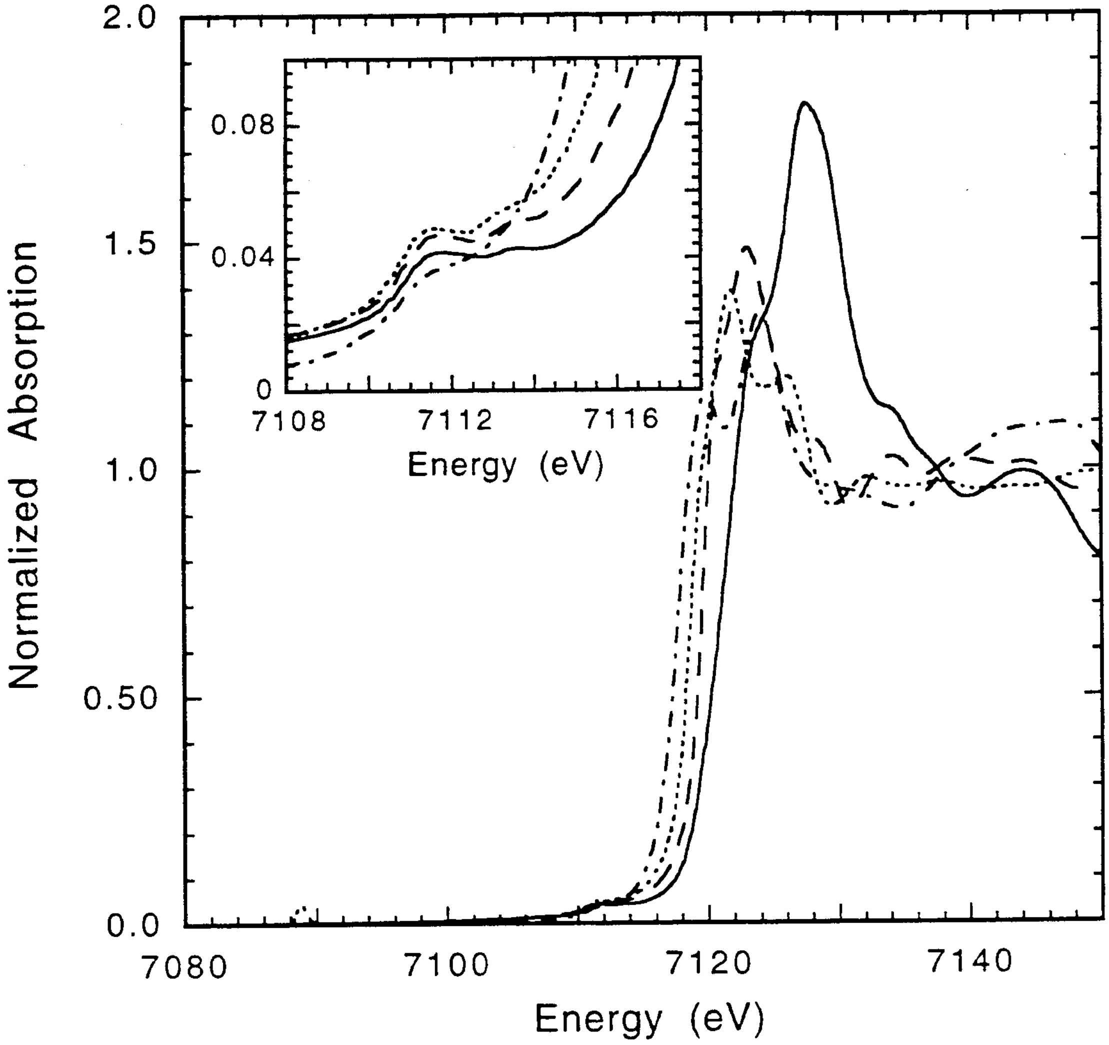

Figure 4.1. Fe K-edge XAS spectra of FeF_2 (—), $FeCl_2$ (---), $FeBr_2$ (·····), and FeI_2 (— -), where the inset is an expansion of the 1s—>3d pre-edge region.

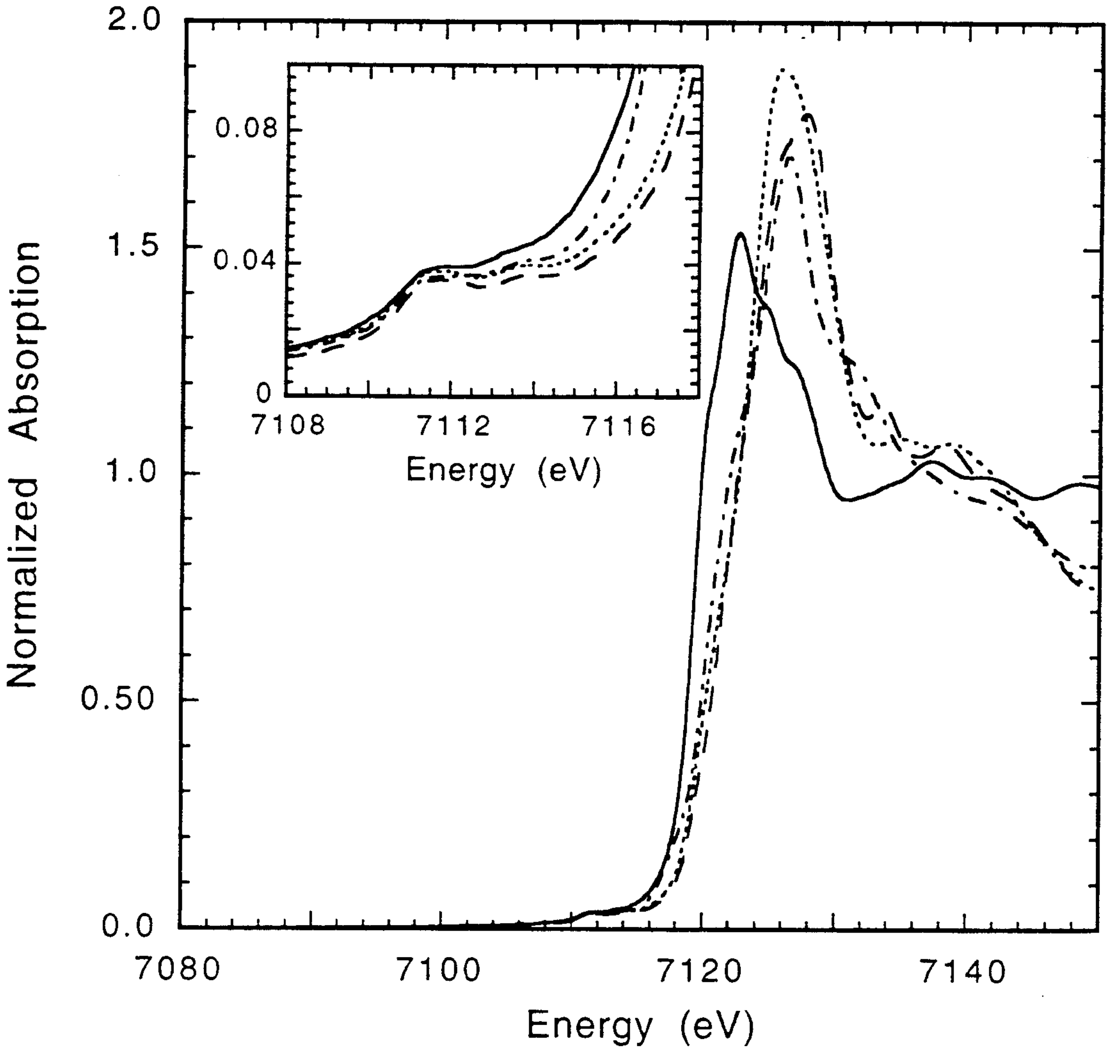

Figure 4.2. Fe K-edge XAS spectra of rinneite (—), $FeSiF_6 \cdot 6H_2O$ (---), $(NH_4)_2Fe(SO_4)_2 \cdot 6H_2O$ (·····), and $[Fe(imidazole)_6]Cl_2$ (— -), where the inset is an expansion of the 1s—>3d pre-edge region.

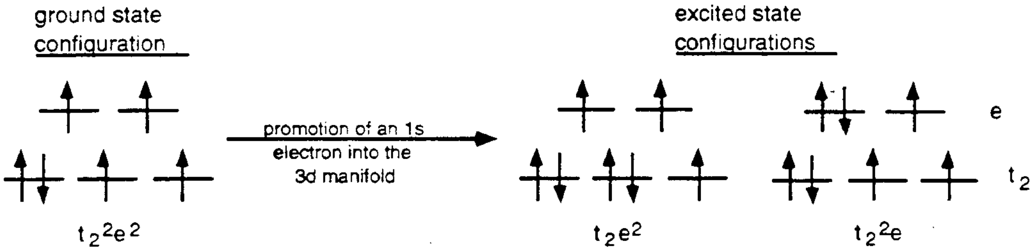

Scheme 1

To obtain the strong-field many-electron excited states the holes in each of these configurations must be coupled. The t_2e^2 configuration gives rise to a $^4T_1$ many-electron state, while the t_2^2e configuration gives a $^4T_1$ and a $^4T_2$ state. The $^4A_2$ state originates from a t_2^3 configuration and thus is forbidden from a $t_2^2e^2$ ground state as it would involve a two-electron transition and it cannot mix with any other quartet state due to symmetry constraints. (Note that coupling of the 1s hole to the these $d^{(n+1)}$ final states gives a set of $^5T_1$, $^5T_2$, and $^5T_1$ states and a set of $^3T_1$, $^3T_2$, and $^3T_1$ states. Only the quintet states are spin allowed and these will have the same relative energy splittings as the parent $d^{(n+1)}$ states. Thus, only the $d^{(n+1)}$ state nomenclature is used further.)

The energies of the $^4T_1$, $^4T_2$, and $^4T_1$ states can be determined by solving the Tanabe-Sugano matrices[38] with appropriate values for the ligand field parameters, 10Dq, B, and C. Ground state 10Dq values can be obtained from optical spectroscopy, however, excited state 10Dq values will be reduced in this case because of the addition of an electron into the d-manifold. It has been found that 10Dq values obtained from charge transfer transition energies are 63% of the values obtained from ligand field transitions.[40] In this case, however, the excited state 10Dq should not be reduced as much due to the increase in the effective nuclear charge from the 1s hole. The energies of the many-electron states were calculated with a 10Dq that is 80% of the ground state value as was experimentally determined from fits to the high spin ferric octahedral model complex data (*vide infra*). The B value used was a $d^{(n+1)}$ free ion B value reduced by 10% to include covalency effects. The C/B ratio was kept fixed at 4.0. High spin ferrous complexes typically have ground state 10Dq values of ~10,000 cm^{-1}.[41] Using a 10Dq value of 8000 cm^{-1}, a B value of 780 cm^{-1}, and a C value of 3120 cm^{-1}, the energies of the $^4T_1$, $^4T_2$, and $^4T_1$ states were determined. The lowest energy excited state is the $^4T_1(0.08|t_2^2e> + 0.92|t_2e^2>)$ state, 0.9 eV higher in energy is the $^4T_2(|t_2^2e>)$ state, and 1.3 eV higher in energy than the $^4T_2$ state is the $^4T_1(0.92|t_2^2e> + 0.08|t_2e^2>)$state. Therefore, from ligand field theory one would expect that a high spin ferrous complex in an octahedral ligand field would have three pre-edge features of equal intensity split by 0.9 and 1.3 eV (see Figure 4.3B). However, the first two features would be barely experimentally resolvable as the energy resolution at the Fe K-edge is ~ 1.4 eV.[31]

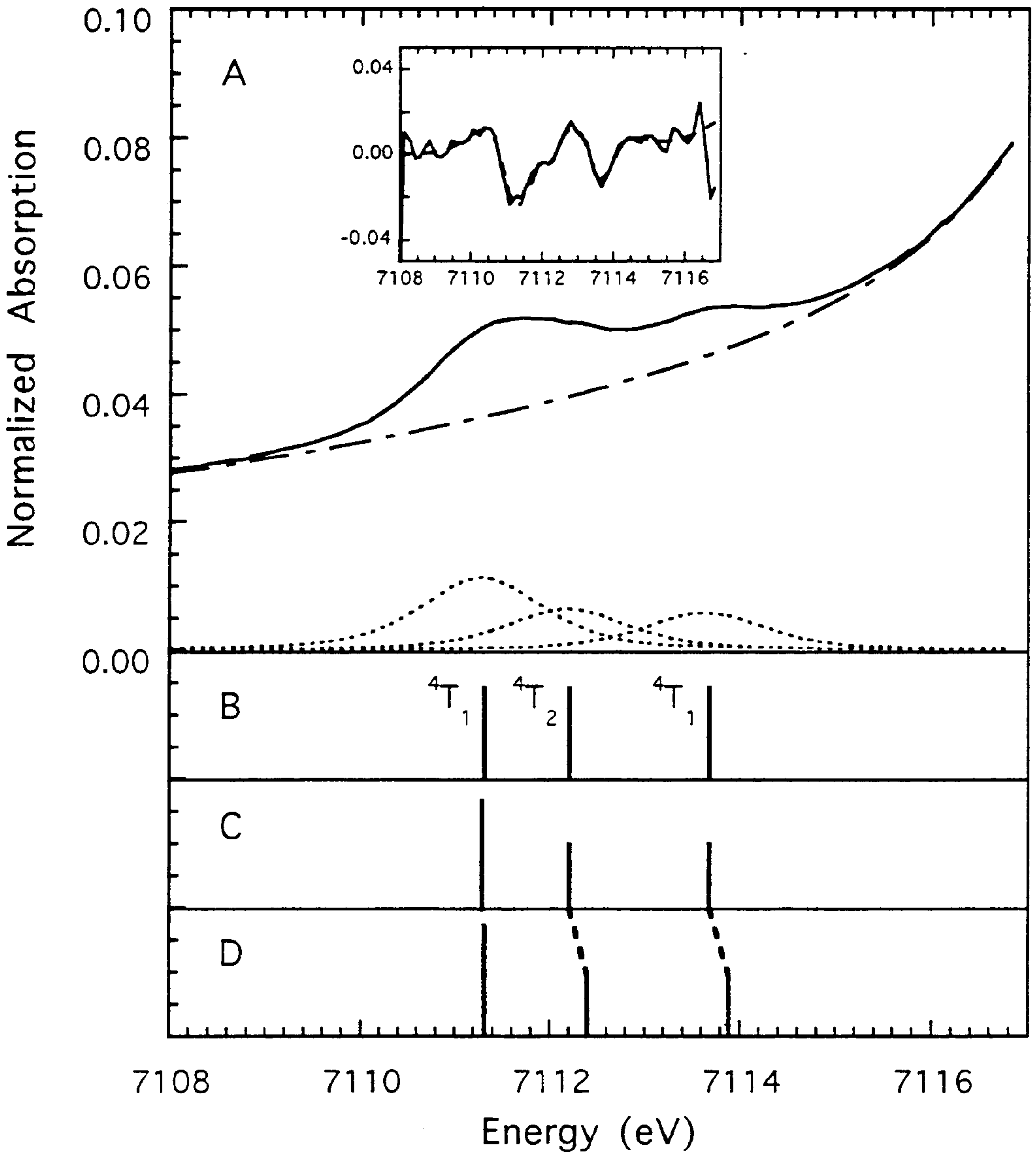

Figure 4.3. A) Fit to the Fe K-edge XAS pre-edge region of $FeSiF_6•6H_2O$ where the solid line is the data, the dashed line is the fit to the data, the dashed-dot line is the background function, and the dotted lines are the individual pre-edge peaks. The inset is the second derivative of the data (—) and the second derivative of the fit to the data (---). B) The energy splitting and the quadrupole intensity distribution of the $^4T_1$, $^4T_2$ and $^4T_1$ states. C) The energy splitting and the quadrupole intensity distribution of the $^4T_1$, $^4T_2$ and $^4T_1$ states when covalency effects are included. D) The effect of increased 10Dq on the energy splitting of the $^4T_1$, $^4T_2$ and $^4T_1$ states.

Furthermore, the intensity of the three features should also reflect covalency effects. The e set of 3d orbitals is more covalent than the t_2 set due to σ bonding interactions with the ligands and, thus, states containing a t_2e^2 component should be more intense than states containing a t_2^2e component as there is more d-character in the t_2 set of orbitals. In the high spin ferrous case, only the lowest energy $^4T_1$ state contains a t_2e^2 component. Thus, the lowest energy feature (arising from the transition to the lowest energy $^4T_1$ state) should be more intense than the two features higher in energy (see Figure 4.3C). All of the ferrous high spin octahedral model complex pre-edge features needed to be fit with three peaks (with the exception of FeI_2 which was adequately fit with two features) with the lower energy feature being more intense than the other two features (see Table 4.1 and Figure 4.3).

The total normalized pre-edge intensities of the octahedral high spin ferrous complexes range from 3.1 - 4.4 with an average intensity of 3.9. This is consistent with the quadrupole intensity observed for D_{4h} $CuCl_4^{2-}$.[24,42,43] The pre-edge feature of an isotropic sample of $(\text{creatininium})_2CuCl_4$ (which has been shown to be quadrupole in character)[24] was fit using the same criteria as for the iron complexes. The results of the fit give a pre-edge feature at 8978.8(0.1) eV with an intensity of 1.5(0.3). Cu(II) complexes are $3d^9$ systems that have only one hole in the 3d manifold. Therefore, to compare the total intensity of the Cu(II) complex to that of the Fe(II) complexes that are $3d^6$ systems, the total pre-edge intensity has to be scaled by 4 and by (Z_{eff}^2 for Fe(II))/(Z_{eff}^2 for Cu(II)) as the quadrupole transition increases as Z_{eff}^2. Z_{eff}, estimated from Slater's rules,[44] is 7.85 for Cu(II) and 5.90 for Fe(II). Thus, the predicted quadrupole intensity for a ferrous complex is 3.4(0.7) which is close to the experimental average intensity of 3.9. One would expect that the experimental value would be higher than the predicted quadrupole intensity as some of the complexes are slightly distorted from O_h symmetry.

Trends in the pre-edge splittings of the three features in these complexes can be related to ligand field strength: $Fe(II)(\text{imidazole})_6 > Fe(II)(H_2O)_6 > FeF_2 \sim FeCl_2 > FeBr_2 > FeI_2$. This is the same trend that is observed for 10Dq values obtained from optical spectroscopy along the spectrochemical series.[41] It is worth noting that the splittings of the pre-edge features observed for $FeSiF_6 \bullet 6H_2O$ are identical to the calculated splittings of the states when using a 10Dq value that is 80% of the ground state 10Dq value of $FeSiF_6 \bullet 6H_2O$. Increasing 10Dq from 7500 to 13,000 cm^{-1}, increases the splitting between the $^4T_1$ and $^4T_2$ states by 0.5 eV and the splitting between the lowest and highest $^4T_1$ states by 0.4 eV.

4.3.1.2. T_d Geometry. Fe K-edge XAS data were collected for three tetrahedral ferrous complexes: $(Et_4N)_2[FeCl_4]$, Cs_3FeCl_5, and Fe(HB(3,5-*i*Pr_2pz)$_3$)Cl. The iron environment in $(Et_4N)_2[FeCl_4]$ is very close to T_d in geometry, Cs_3FeCl_5 is D_{2d} distorted, and Fe(HB(3,5-*i*Pr_2pz)$_3$)Cl is C_{3v} distorted. The XAS edge spectra for these three complexes are shown in Figure 4.4 with an expanded view of the 1s—>3d pre-edge region presented in the inset. All three complexes have a relatively intense pre-edge feature that is split by 1.5 eV with the lower energy feature being more intense than the higher energy feature (Table 4.1). The Fe(HB(3,5-*i*Pr_2pz)$_3$)Cl pre-edge peaks are more intense than those of $(Et_4N)_2[FeCl_4]$ and Cs_3FeCl_5 (Figure 4.4 and Table 4.1).

The 1s—>3d pre-edge features of $(Et_4N)_2[FeCl_4]$, Cs_3FeCl_5, and Fe(HB(3,5-*i*Pr_2pz)$_3$)Cl can gain intensity both through an allowed quadrupole transition and by 4p mixing into the 3d orbitals, since these complexes have a noncentrosymmetric environment around the iron site. In changing the symmetry from O_h to T_d, the e set of the 3d orbitals is lower in energy than the t_2 set with 10Dq of the T_d systems being 4/9 that of the O_h 10Dq. In the T_d case, the ground state has a hole configuration of t_2^3e and, therefore, the only allowed excited states are those containing the t_2^3 or t_2^2e configurations (Scheme 2).

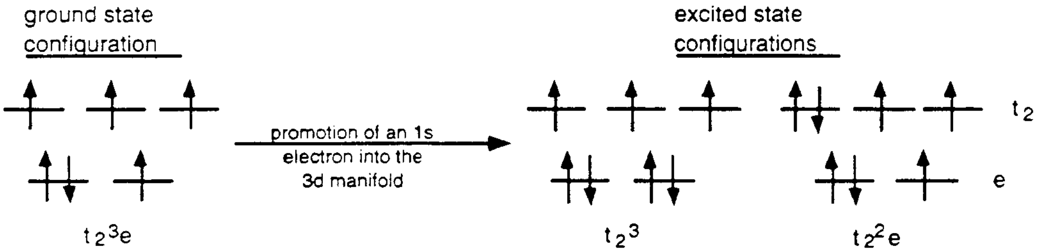

Scheme 2

A t_2e^2 configuration would involve a forbidden two-electron transition. Coupling the three t_2 holes gives a $^4A_2$ many-electron state, while coupling the holes in the t_2^2e configuration give $^4T_1$ and $^4T_2$ states. The t_2e^2 configuration (arising from a two-electron transition) also gives rise to a $^4T_1$ state. Since the two $^4T_1$ states are allowed to mix by symmetry, both $^4T_1$ states will have an allowed t_2^2e component. The $^4A_2$ and the $^4T_2$ states only contain t_2^3 or t_2^2e components, respectively, and transitions into these states are fully allowed.

Energies of the four many-electron states were calculated using a 10Dq value of 3280 cm^{-1} (80% of the ground state 10Dq of $(Et_4N)_2[FeCl_4]$),[45] a B value of 780 cm^{-1} (90% of the $d^{(n+1)}$ B), and a C value of 3120 cm^{-1}. The $^4A_2$ ($|t_2^3>$)state is the lowest energy excited state; the $^4T_2$ ($|t_2^2e>$) state is 0.4 eV higher in energy; a $^4T_1$ ($0.31|t_2^2e>$ +

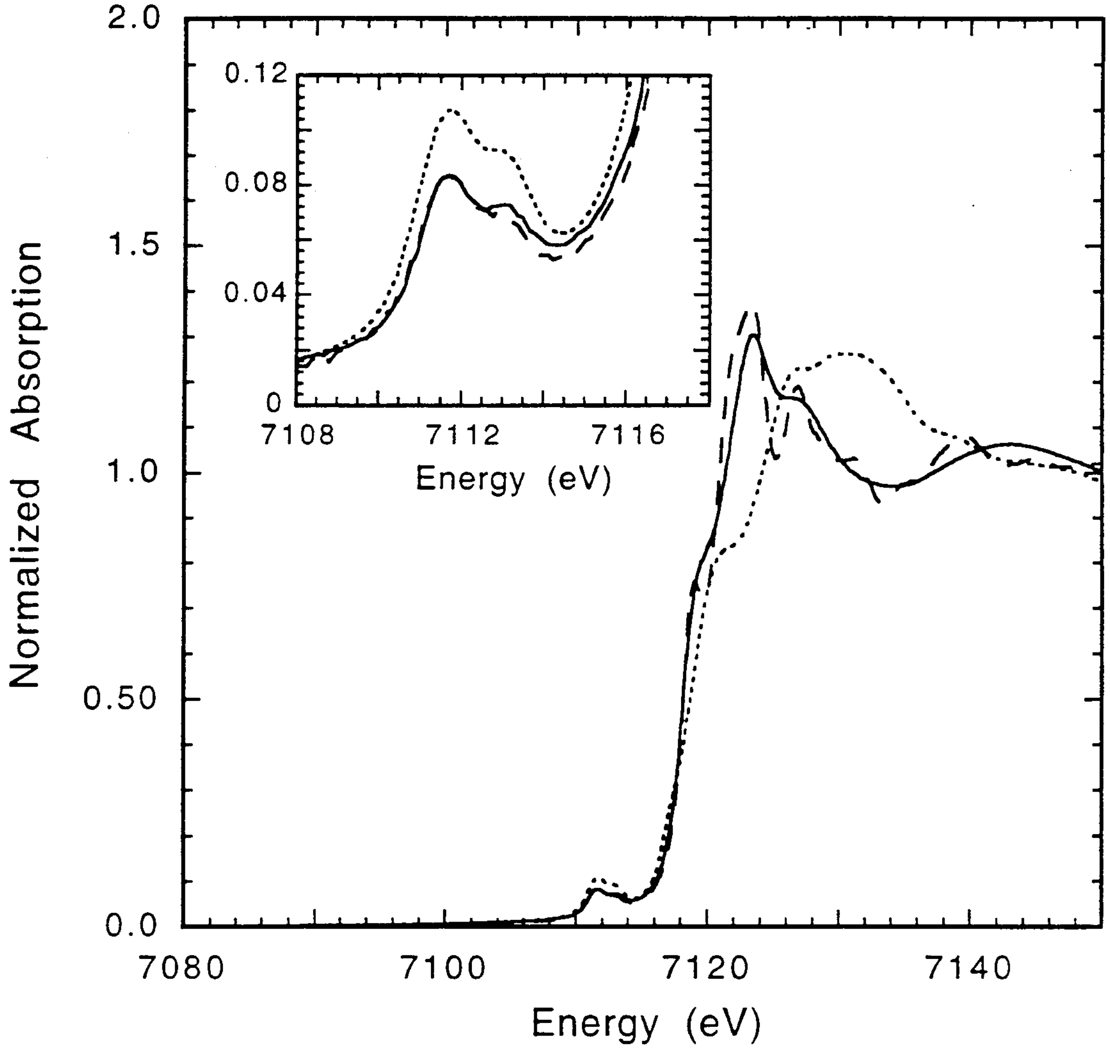

Figure 4.4. Fe K-edge XAS spectra of $(Et_4N)_2[FeCl_4]$ (—), Cs_3FeCl_5 (---), and Fe(HB(3,5-*i*Pr_2pz)$_3$)Cl (·····), where the inset is an expansion of the 1s—>3d pre-edge region.

$0.69|t_2e^2>$) state is 0.3 eV higher in energy (than the $^4T_2$ state); and a $^4T_1$ ($0.69|t_2^2e> + 0.31|t_2e^2>$) state is 1.3 eV higher in energy than the other $^4T_1$ state. Since the t_2e^2 configuration requires a two-electron transition, only the t_2^2e components of the $^4T_1$ states are allowed. The three lower energy states ($^4A_2$, $^4T_2$, and $^4T_1$) are all within 0.7 eV of one another and, thus, will not be resolvable at the Fe K-edge, while the higher energy $^4T_1$ state is positioned 2 eV higher than the $^4A_2$ state and should be resolvable.

The quadrupole intensity is divided between these states according to the degeneracy of the state and the percentage of the one-electron allowed strong field component (in the case of the $^4T_1$ states), so that the quadrupole intensity ratio of the $^4A_2$:$^4T_2$:$^4T_1$:$^4T_1$ is 1:3:0.31x3:0.69x3 (see Figure 4.5B). The pre-edge features of these tetrahedral complexes will also gain intensity from 4p mixing into the 3d orbitals. However, the 4p states transform as t_2[46] so there will only be mixing into the 3d t_2 set and, thus, only the $d^{(n+1)}$ states that have t_2^2e components will have electric dipole intensity from 4p mixing into the 3d orbitals. The $^4T_2$, $^4T_1$, and $^4T_1$ states have a t_2^2e component and will have an electric dipole intensity ratio of 3:0.31x3:0.69x3, respectively (see Figure 4.5C). Consequently, two pre-edge features are expected, with the first feature containing transitions into the $^4A_2$,$^4T_2$, and $^4T_1$ states and the second feature containing the transition into the higher energy $^4T_1$ state. The intensity pattern of the data can be explained when both the quadrupole intensity and the dipole intensity from 4p character mixing into the 3d t_2 orbitals are taken into account (see Figure 4.5). Using a total quadrupole intensity of 3.4(0.7) (the value calculated for the quadrupole contribution), the dipole intensity of $(Et_4N)_2[FeCl_4]$, which has a total intensity of 12.9(0.6) (Table 4.1), is 9.5(0.9). Taking the proper intensity ratio for each state (given above), the intensity of the first feature divided by the total intensity is 0.66 which is very close to the intensity ratio of 0.67 experimentally obtained for the pre-edge features of $(Et_4N)_2[FeCl_4]$ (Table 4.1).

The percentage of 4p mixing into the 3d orbitals was also obtained. The dipole intensity (allowed by 4p mixing into the 3d t_2 set of orbitals) is 9.5(0.9) for $(Et_4N)_2[FeCl_4]$. The quadrupole intensity is ~1% of the dipole intensity as has been calculated by Blair and Goddard[22] and experimentally observed for $CuCl_4^{2-}$.[42,43] A more rigorous figure can be obtained from an analysis of the pre-edge features of $(creatininium)_2CuCl_4$, a D_{4h} complex, and Cs_2CuCl_4, a D_{2d} complex. The fitted 1s->3d pre-edge areas of these two complexes are 1.5(0.3) and 7.1(0.5), respectively. The pre-edge feature of $(creatininium)_2CuCl_4$ only has quadrupole intensity from a transition into $3d_{x^2-y^2}$ as the copper is in a centrosymmetric environment, while the pre-edge feature of Cs_2CuCl_4 has both quadrupole intensity from a transition into $3d_{x^2-y^2}$ and

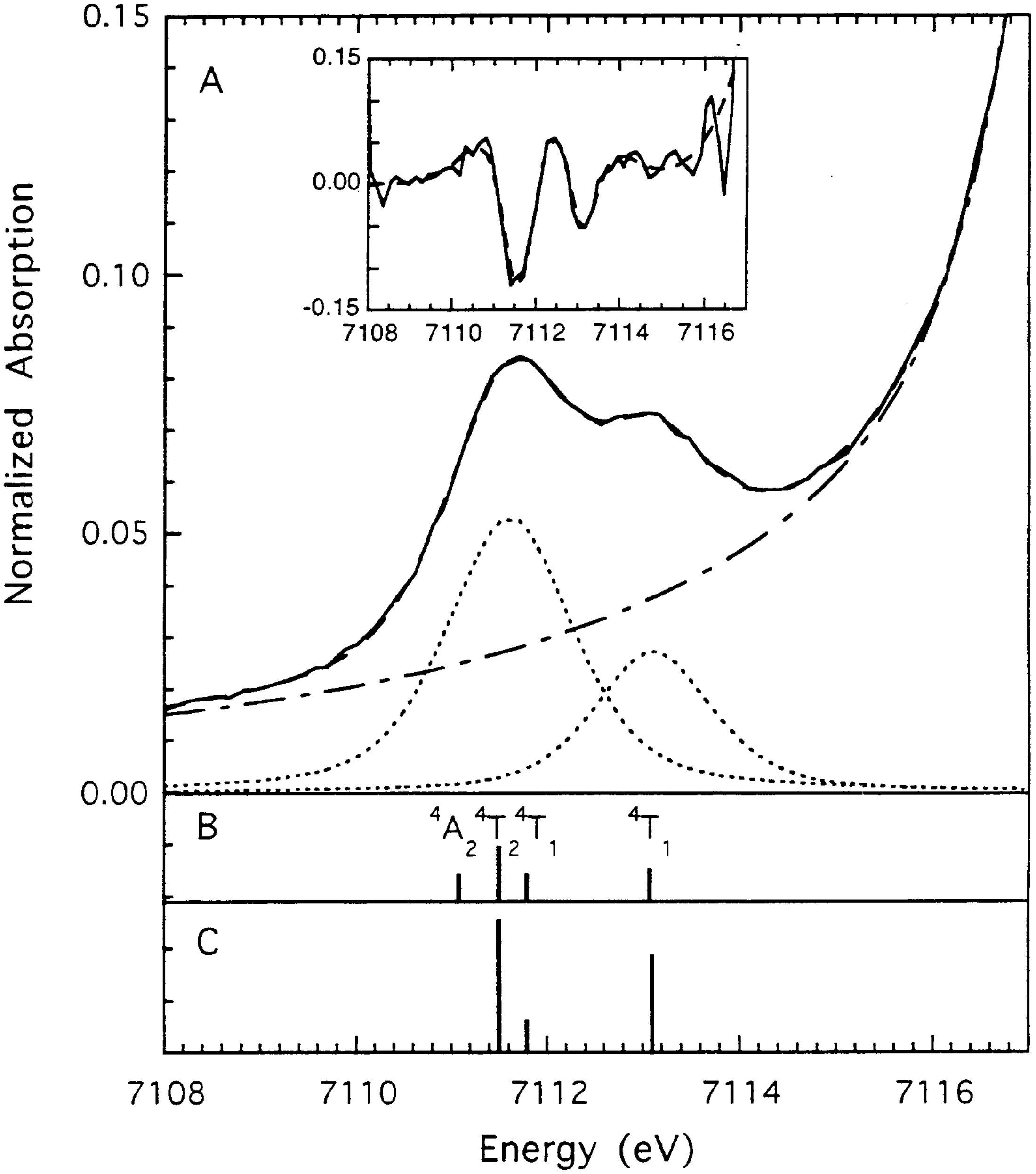

Figure 4.5. A) Fit to the Fe K-edge XAS pre-edge region of $(Et_4N)_2[FeCl_4]$, where the solid line is the data, the dashed line is the fit to the data, the dashed-dot line is the background function, and the dotted lines are the individual pre-edge peaks. The inset is the second derivative of the data (—) and the second derivative of the fit to the data (---). B) The energy splitting and the quadrupole intensity distribution of the $^4A_2$, $^4T_2$, $^4T_1$, and $^4T_1$ states. C) The energy splitting and the dipole intensity distribution (allowed by 4p mixing into the 3d states) of the $^4A_2$, $^4T_2$, $^4T_1$, and $^4T_1$ states.

dipole intensity from $4p_z$ mixing into the $3d_{x^2-y^2}$ orbital. The pre-edge feature of Cs_2CuCl_4 should also have ~1.5(0.3) units of quadrupole intensity from a transition into $3d_{x^2-y^2}$, however, self-consistent field-Xα-scattered wave calculations indicate that the $3d_{x^2-y^2}$ component of the lowest unoccupied molecular orbital is 61% for (creatininium)$_2CuCl_4$ and 67% for Cs_2CuCl_4.[42,43] Taking into account the differences in d character in the lowest unoccupied molecular orbital, the amount of quadrupole intensity in the pre-edge feature of Cs_2CuCl_4 should be 1.65 (0.3). Thus, the amount of dipole intensity in the pre-edge feature of Cs_2CuCl_4 should be 5.45(0.6), 7.1(0.5) minus 1.65(0.3). The amount of $4p_z$ mixing into the lowest unoccupied molecular orbital is known to be 3.8(1.5)% from an analysis of the Cu 1s—>4p + ligand-to-metal charge-transfer shakedown transition.[42,43] Hence, 3.8(1.5)% $4p_z$ mixing into the lowest unoccupied molecular orbital provides for 5.45(0.6) units of pre-edge intensity. In other words, 1% 4p mixing yields 1.43(0.6) units of 1s—>3d pre-edge intensity. Using this ratio, the percentage of 4p mixing into the 3d orbitals was obtained for $(Et_4N)_2[FeCl_4]$. Since the dipole intensity of the pre-edge feature for $(Et_4N)_2[FeCl_4]$ is 9.5(0.9) units, the amount of 4p mixing into the 3d orbitals is 9.5(0.9)/1.43(0.6), or 6.6(2.8)%. A density functional calculation on $(Et_4N)_2[FeCl_4]$ predicts 2 - 3% 4p mixing into each of the 3d orbitals with t_2 symmetry, indicating that the total amount of 4p mixing into the 3d manifold is 6 - 9%.[47]

4.3.1.3. C_{4v} Geometry. Fe K-edge XAS data were collected for four square pyramidal high spin ferrous model complexes: $(BF_4)[Fe(TMC)Cl]$, $(BF_4)[Fe(TMC)Br]$, $(BF_4)[Fe(TMC)CH_3CN]$, and $(BF_4)[Fe(TMC)N_3]$. The spectra of these four complexes are shown in Figure 4.6 with the inset showing an expanded view of the 1s—>3d pre-edge region. All four of these square pyramidal complexes have an intense feature at ~7111.5 eV, with a second much weaker feature at ~7113.3 eV where the second feature is visible in the second derivative. $(BF_4)[Fe(TMC)N_3]$ has the most intense pre-edge feature while that of $(BF_4)[Fe(TMC)Br]$ is the least intense (Table 4.1).

An iron atom in a C_{4v} site has a noncentrosymmetric environment and thus the 1s—>3d pre-edge transition gains intensity both from the allowed quadrupole and from dipole (associated with 4p mixing into the 3d orbitals) mechanisms. A C_{4v} site can be treated as a distorted O_h site, in which the $^4T_2$ $d^{(n+1)}$ state (*vide supra*) splits into a $^4B_2$ and a ^4E state and the two $^4T_1$ states split into a $^4A_2$ and a ^4E state. If the ground state orbital splitting is as shown in Scheme 3, then promotion of a 1s electron into the 3d manifold produces three $d^{(n+1)}$ allowed excited state configurations: ea_1b_1, e^2b_1, and e^2a_1 (Scheme 3).

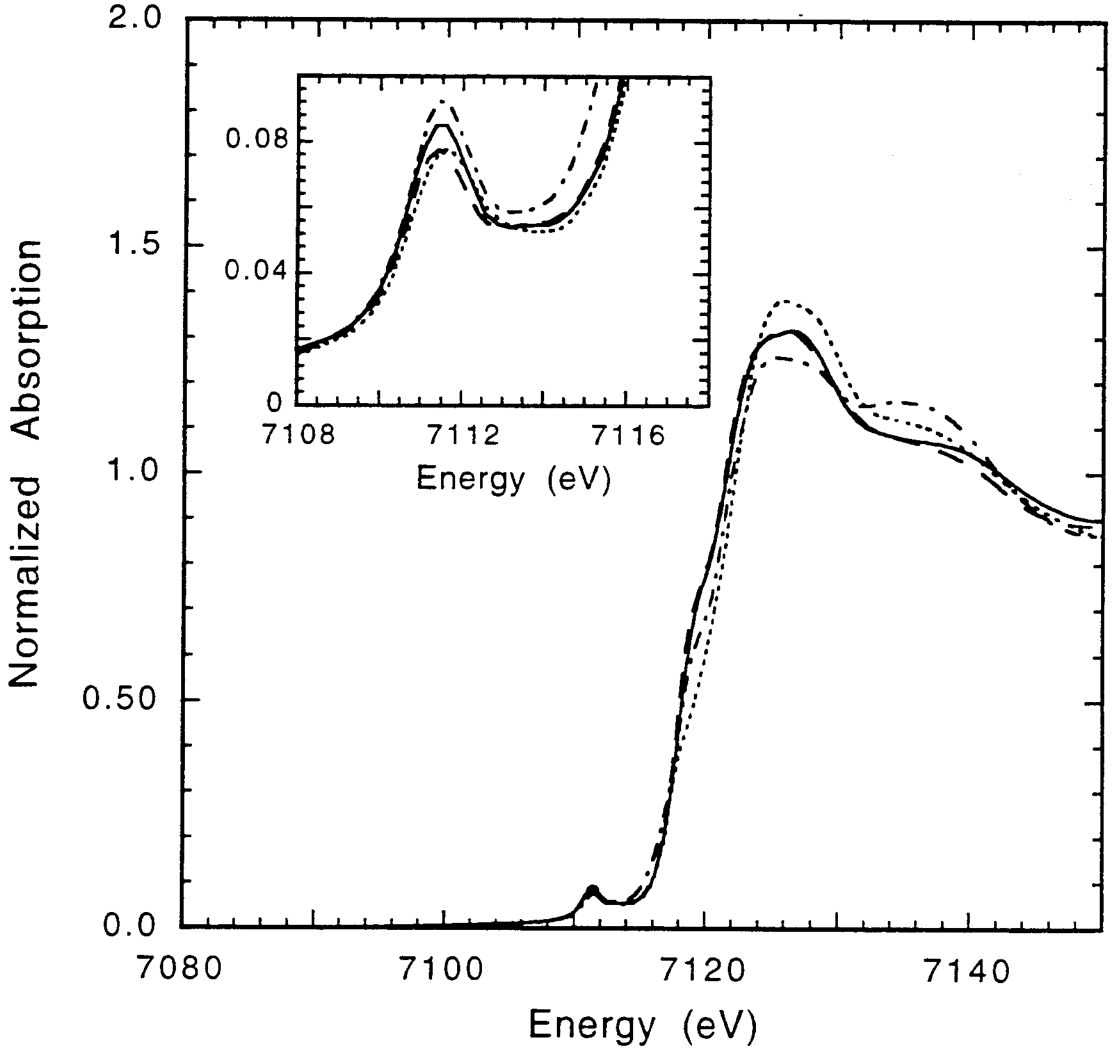

Figure 4.6. Fe K-edge XAS spectra of (BF$_4$)[Fe(TMC)Cl] (—), (BF$_4$)[Fe(TMC)Br] (---), (BF$_4$)[Fe(TMC)CH$_3$CN] (·····), and (BF$_4$)[Fe(TMC)N$_3$] (— -), where the inset is an expansion of the 1s—>3d pre-edge region.

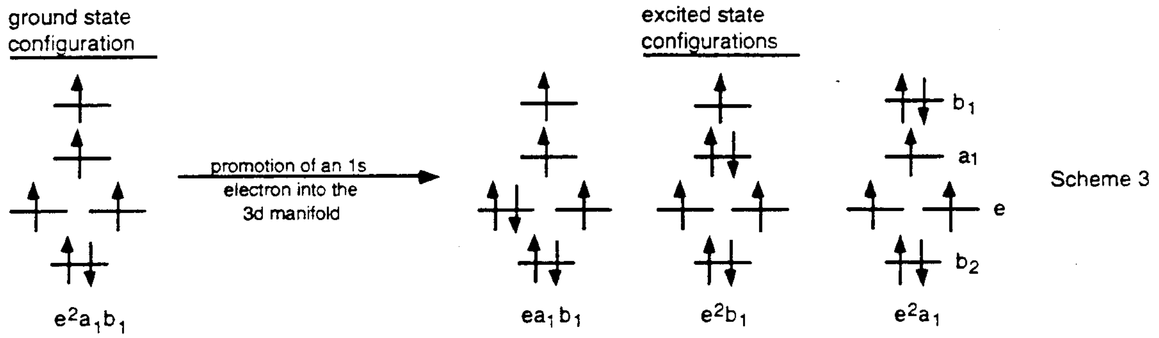

The relative energies of these configurations have been determined from density functional calculations[47] and are consistent with values obtained from optical absorption experiments for square pyramidal ferrous complexes.[41] From these calculations, the e^2b_1 configuration (which contributes to the $^4B_2$ state from the O_h $^4T_2$ state) is the lowest in energy, with the ea_1b_1 configuration (which contributes to the ^4E state from the lower energy O_h $^4T_1$ state) being 0.4 eV higher in energy, and the e^2a_1 configuration (which contributes to the $^4A_2$ state from the higher energy O_h $^4T_1$ state) being 1.6 eV higher than the ea_1b_1 configuration.[47] Thus, the many-electron states that involve one-electron transitions are the $^4B_2$, ^4E, and $^4A_2$ states. The quadrupole intensity of these states will have an intensity ratio of 1:2:1, respectively (see Figure 4.7B).

The pre-edge features of these square pyramidal complexes can gain additional intensity from 4p mixing into the 3d orbitals. In the C_{4v} case, the 4p orbitals transform as e ($4p_{x,y}$) and a_1 ($4p_z$). As the main distortion is along the z axis, one would predict that the $4p_z$ orbital mixing into the d_{z^2} orbital of a_1 symmetry will be the dominant effect. Thus, the transition to the $^4B_2$ state that contains the e^2b_1 component should be the most intense. This is consistent with the data where the lower energy feature is much more intense than the higher energy feature (see Figure 4.7). The density functional calculation for $(BF_4)[Fe(TMC)Cl]$ also shows that the d_{z^2} orbital contains $4p_z$ character, while the d_{xz} and d_{yz} e orbitals contained no significant $4p_{xy}$ character.[47] The amount of $4p_z$ mixing into the d_{z^2} orbital can be estimated from the experimental data. The total pre-edge intensity for $(BF_4)[Fe(TMC)Cl]$ is 12.9(0.2) (Table 4.1). If 3.4(0.7) units are attributed to the quadrupole transition, then 9.5(0.7) units originate from $4p_z$ (dipole allowed) character in the d_{z^2} orbital. If 1% 4p mixing account for 1.43(0.6) units of area (*vide supra*), the amount of $4p_z$ mixing into the $3d_{z^2}$ orbital is 9.5(0.7)/1.43(0.6), or 6.6(2.8)%. The density functional calculation for $(BF_4)[Fe(TMC)Cl]$ shows 9% $4p_z$ mixing into the d_{z^2} orbital.[47]

Considering that there is only one state that gains intensity from the $4p_z$ mixing into the d_{z^2} orbital, the axial interaction will be reflected in the intensity and position of

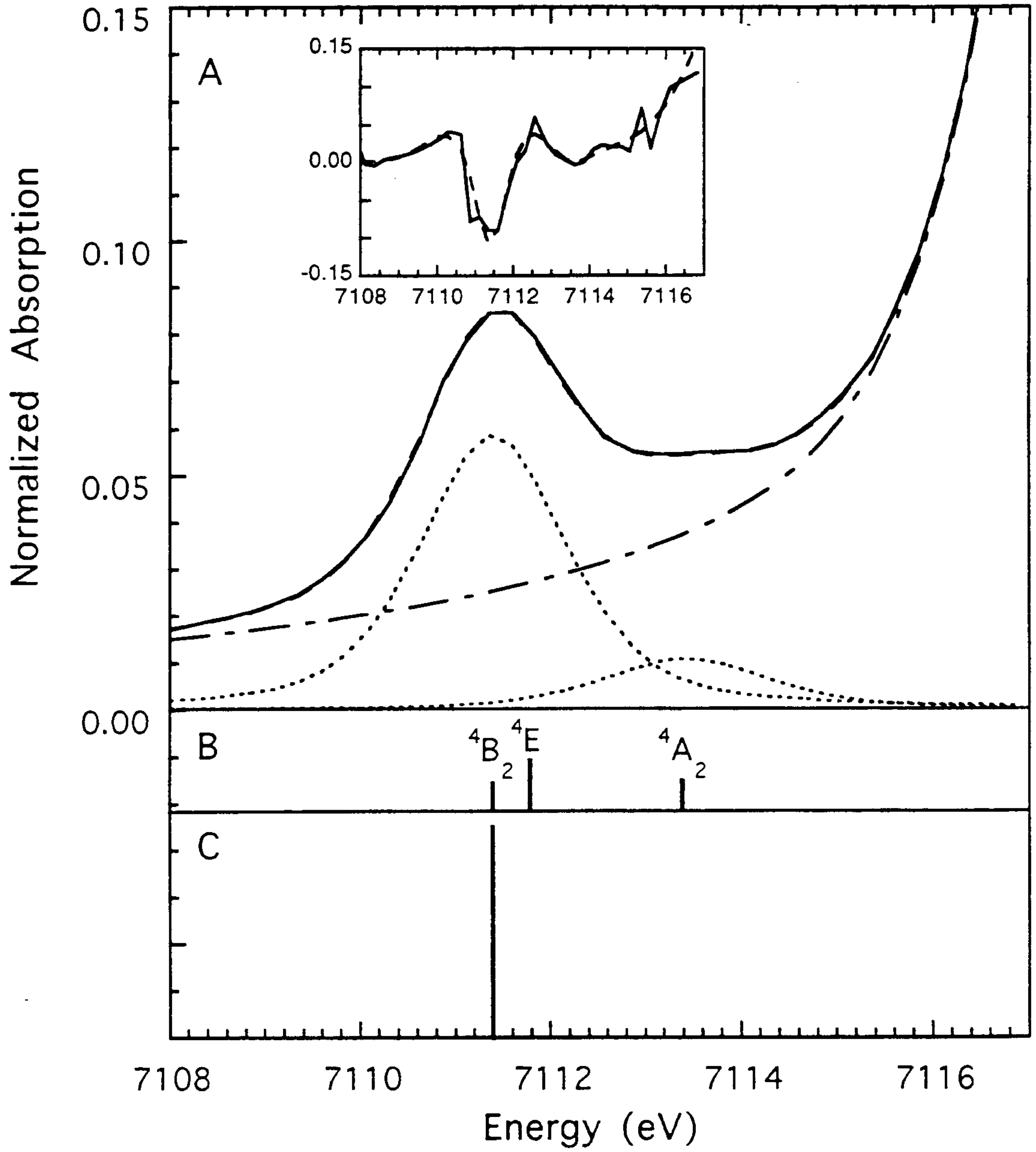

Figure 4.7. A) Fit to the Fe K-edge XAS pre-edge region of $(BF_4)[Fe(TMC)Cl]$, where the solid line is the data, the dashed line is the fit to the data, the dashed-dot line is the background function, and the dotted lines are the individual pre-edge peaks. The inset is the second derivative of the data (—) and the second derivative of the fit to the data (---). B) The energy splitting and the quadrupole intensity distribution of the $^4B_2$, ^4E, and $^4A_2$ states. C) The energy splitting and the dipole intensity distribution (allowed by 4p mixing into the 3d states) of the $^4B_2$, ^4E, and $^4A_2$ states.

the most intense pre-edge feature. For example, the intensity of this pre-edge feature of the high spin ferrous complexes in this study decreases as: $(BF_4)[Fe(TMC)N_3] > (BF_4)[Fe(TMC)Cl] > (BF_4)[Fe(TMC)CH_3CN] > (BF_4)[Fe(TMC)Br]$. This trend matches the strength of the axial ligand with the azide having the strongest interaction and the bromide having the weakest.

It is important to note that both T_d $(Et_4N)_2[FeCl_4]$ and C_{4v} $(BF_4)[Fe(TMC)Cl]$ have the same pre-edge intensity. Thus, one would not be able to determine the site symmetry of the iron solely on the basis of total pre-edge intensity.[1,20] However, the distribution of intensity over the multiplet features of T_d and C_{4v} complexes is very different. In the T_d case, the dipole intensity (from 4p mixing into the t_2 d orbitals) is distributed over both pre-edge features (Figure 4.5), while in the C_{4v} case (where one axial ligand is removed), the dipole intensity from $4p_z$ mixing into the $d_z{}^2$ orbital is located only in the lowest energy pre-edge features since removing an axial ligand lowers the energy of d_z2 (Figure 4.7).

4.3.2. High Spin Ferric Complexes

4.3.2.1. O_h Geometry. Fe K-edge XAS data were collected for nine high spin ferric octahedral model complexes with varying ligation: F^-, Cl^-, Br^-, and O and N from acac, malonate, oxalate, urea, and H_2O. The XAS edge spectra for FeF_3, $FeCl_3$, $FeBr_3$, and $[FeCl_6][Co(NH_4)_6]$ are shown in Figure 4.8 and the spectra for $Fe(acac)_3$, $(NH_4)_3Fe(malonate)_3$, $(NH_4)Fe(SO_4)_2 \bullet 12H_2O$, and $Fe(urea)_6(ClO_4)_3$ are shown in Figure 4.9. The lowest energy transitions are the weak 1s—>3d pre-edge peaks, which are expanded and shown as insets in Figures 4.8 and 4.9. All nine complexes have a low intensity split pre-edge feature (Table 4.1).

Since all nine of these complexes have a centrosymmetric octahedral iron site, the only intensity mechanism available for the 1s—>3d feature is the allowed quadrupole transition. In the high spin ferric case, there are five 3d electrons in the ground state with a $t_2{}^3e^2$ configuration. Promotion of a 1s electron into the 3d manifold produces two excited state configurations, a $t_2{}^2e^2$ and $t_2{}^3e$ (Scheme 4).

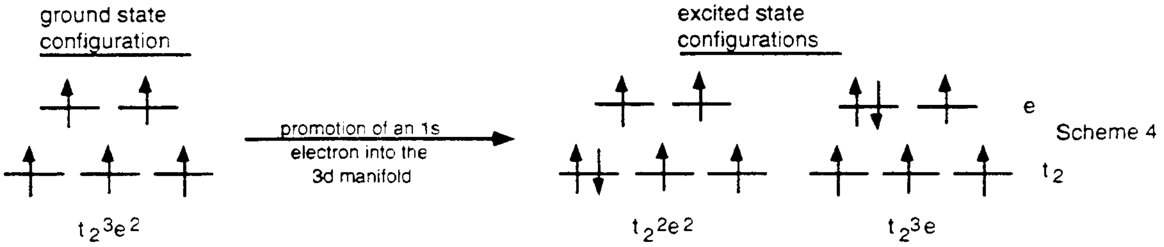

Scheme 4

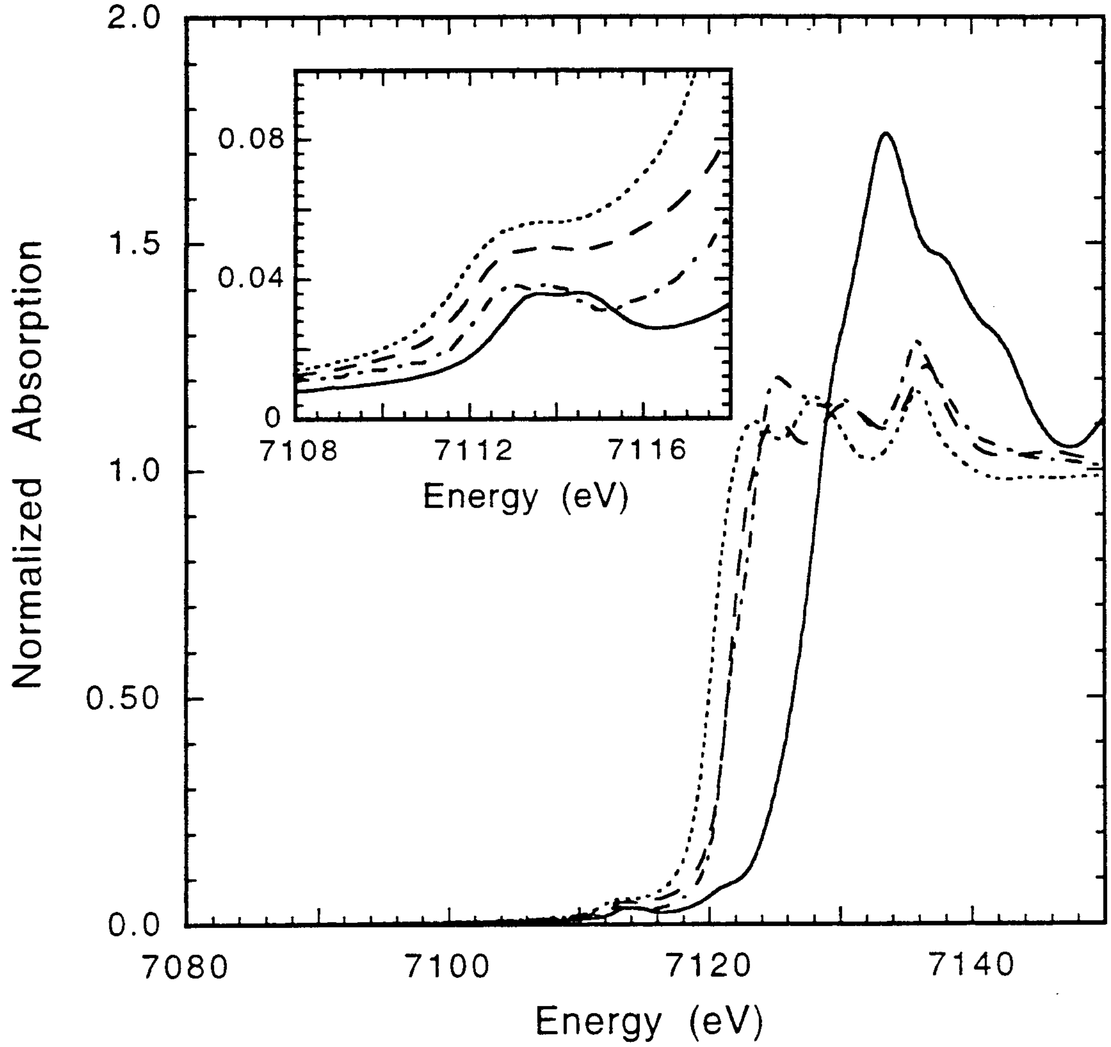

Figure 4.8. Fe K-edge XAS spectra of FeF_3 (—), $FeCl_3$ (---), $FeBr_3$ (·····), and $[FeCl_6][Co(NH_4)_6]$ (— -), where the inset is an expansion of the 1s->3d pre-edge region.

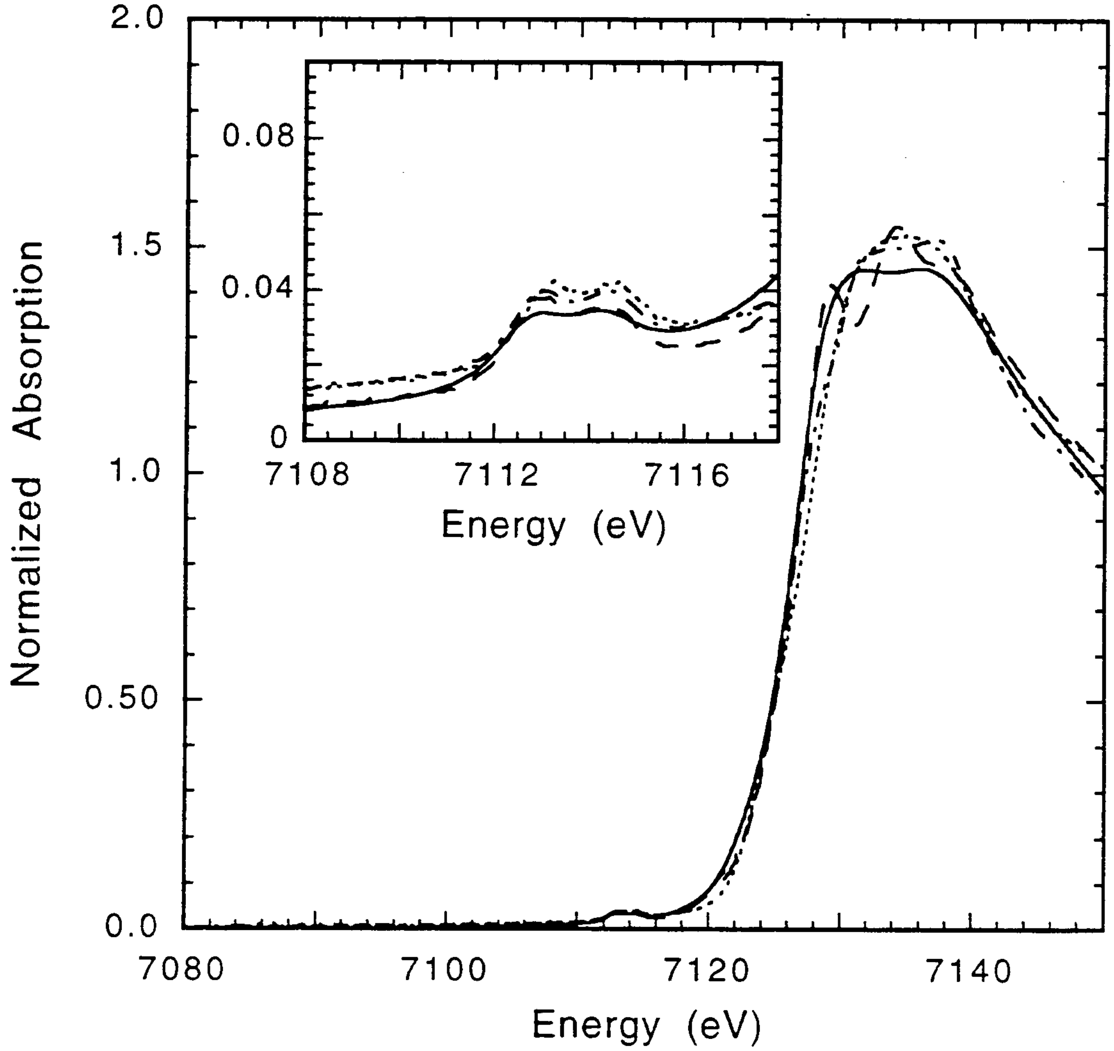

Figure 4.9. Fe K-edge XAS spectra of Fe(acac)$_3$ (—), (NH$_4$)$_3$Fe(malonate)$_3$ (---), (NH$_4$)Fe(SO$_4$)$_2$•12H$_2$O (·····), and Fe(urea)$_6$(ClO$_4$)$_3$ (— -), where the inset is an expansion of the 1s—>3d pre-edge region.

Coupling of the holes in the $t_2^2e^2$ and t_2^3e configurations gives a $^5T_2$ and a ^5E state, respectively.[36] Therefore, one predicts an octahedral high spin ferric complex to have two pre-edge features split by an excited state 10Dq with a quadrupole intensity ratio of 3:2. Fits to the data show that there are indeed pre-edge two features with an intensity ratio of ~3:2 and splittings that range from 1.1 to 1.5 eV (Figure 4.10 and Table 4.1). The energy splitting between the two pre-edge features is a direct measurement of the 10Dq value of the $d^{(n+1)}$ final state. In comparing these energy splitting with ground state 10Dq values from optical data,[41] the excited state 10Dq values are 80% of the ground state values. The splitting of the two pre-edge features in these complexes can be related to ligand field strength with the splittings following the trend Fe-O/Fe-N > FeF_3 > $FeCl_3$ > $FeBr_3$.

The total pre-edge intensities of the octahedral high spin ferric complexes range from 4.0 to 7.3 with the average intensity being 4.9. As was done for the high spin ferrous complexes in an O_h field, an estimate of the quadrupole intensity was calculated using the area of the pre-edge feature for D_{4h} $CuCl_4^{2-}$ of 1.5(0.3). That value was scaled by 5 for the number of 3d electrons and multiplied by (Z_{eff}^2 for Fe(III))/(Z_{eff}^2 for Cu(II)) where Z_{eff} is 7.85 for Cu(II) and 6.25 for Fe(III) giving a predicted quadrupole intensity for a ferric complex of 4.7(0.9) which is very similar to the experimental averaged intensity of 4.9. One would expect that the experimental value would be higher than the predicted quadrupole intensity as some of the complexes are distorted from O_h symmetry.

4.3.2.2. T_d Geometry. Fe K-edge XAS data were collected for one high spin ferric tetrahedral complex, $(Et_4N)[FeCl_4]$. The XAS spectrum is shown in Figure 4.11 (solid line) with the 1s—>3d pre-edge region expanded and shown in the inset. $(Et_4N)[FeCl_4]$ has a very intense single pre-edge feature (Table 4.1).

The 1s—>3d pre-edge feature of $(Et_4N)[FeCl_4]$ gains intensity both through an allowed quadrupole transition and dipole transition from 4p mixing into the 3d orbitals, since this complex has a noncentrosymmetric environment around the iron site. In changing symmetry from O_h to T_d, the e set of the 3d orbitals is lower in energy than the t_2 set with 10Dq of the T_d systems being 4/9 that of the O_h 10Dq. As in the high spin ferric octahedral case, there are two one-electron allowed excited state configurations, $t_2^2e^2$ and t_2^3e (Scheme 5), that produce two many-electron states, $^5T_2$ and ^5E, respectively.

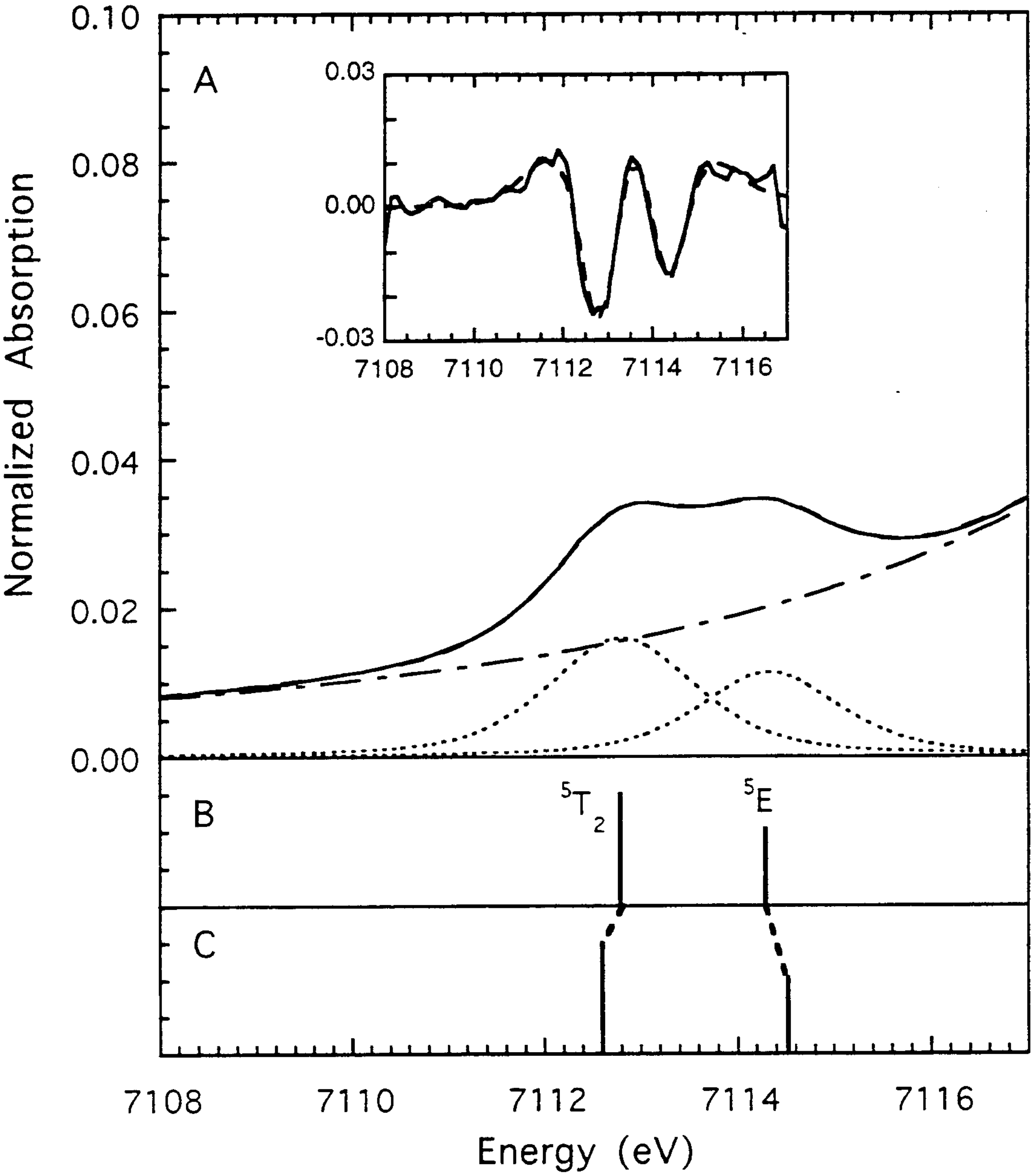

Figure 4.10. A) Fit to the Fe K-edge XAS pre-edge region of Fe(acac)$_3$, where the solid line is the data, the dashed line is the fit to the data, the dashed-dot line is the background function, and the dotted lines are the individual pre-edge peaks. The inset is the second derivative of the data (—) and the second derivative of the fit to the data (---). B) The energy splitting and the quadrupole intensity distribution of the $^5T_2$ and ^5E states. C) The effect of increased 10Dq on the energy splitting of the $^5T_2$ and ^5E states.

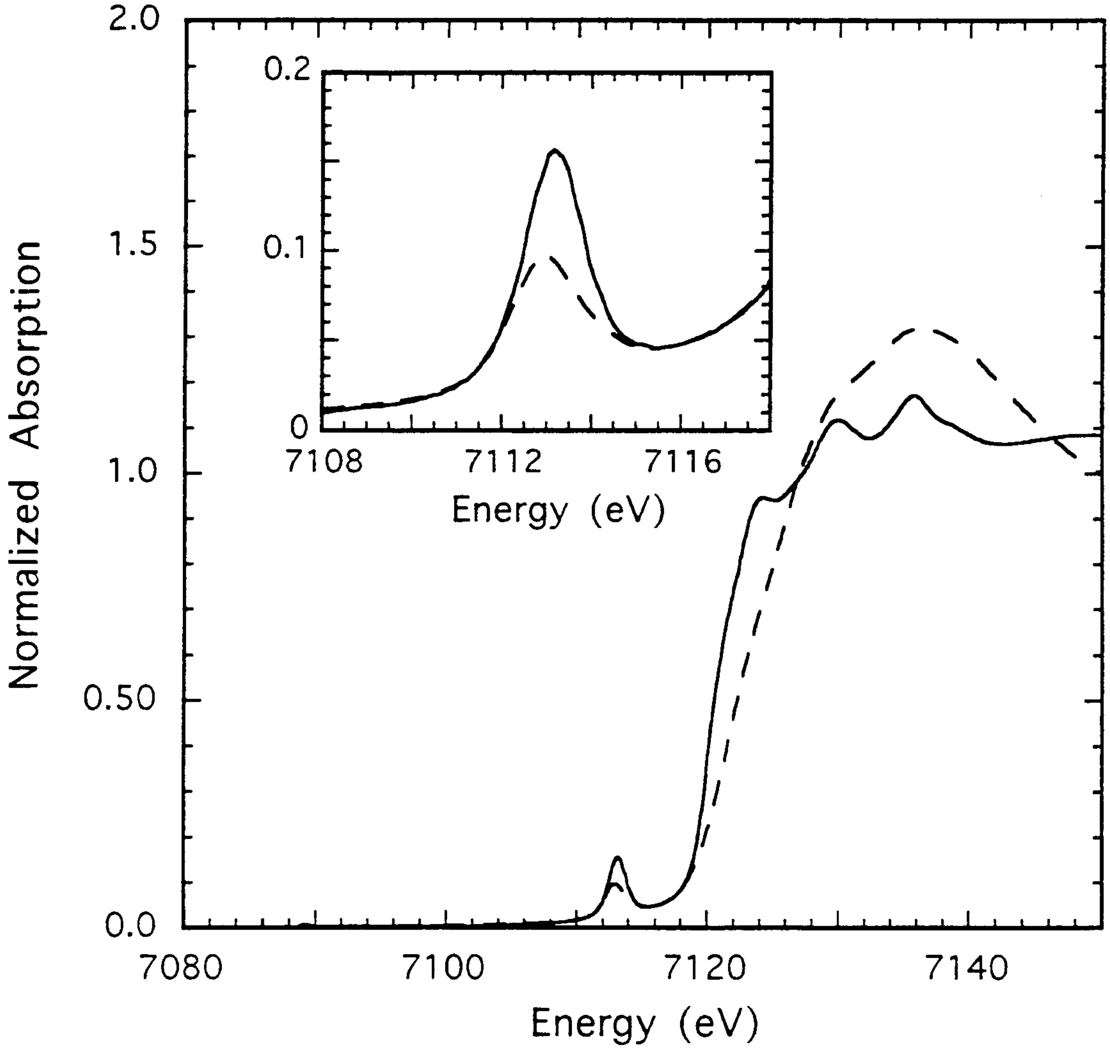

Figure 4.11. Fe K-edge XAS spectra of (Et$_4$N)[FeCl$_4$] (—) and Fe(salen)Cl (---), where the inset is an expansion of the 1s—>3d pre-edge region.

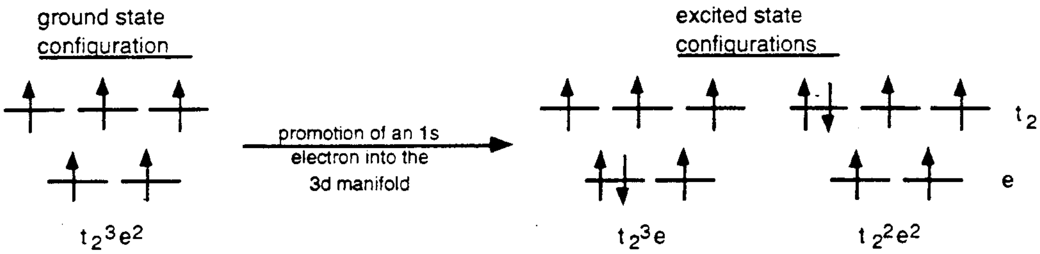

Scheme 5

Consequently, a tetrahedral high spin ferric complex can have a transition to the doubly degenerate ^5E state and also to a triply degenerate $^5T_2$ state at 10Dq higher in energy. Energies of the many-electron states were calculated using a 10Dq value of 5200 cm^{-1} (80% of the ground state 10Dq of $(Et_4N)[FeCl_4]$)[48], a B value of 950 cm^{-1} (90% of the $d^{(n+1)}$ B), and a C value of 3800 cm^{-1}. Using these values the energy splitting between the ^5E and $^5T_2$ states is 0.6 eV (Figure 4.12) which is not resolvable at the Fe K-edge.

The pre-edge features of tetrahedral complexes also gain intensity from 4p mixing into the 3d orbitals. The 4p orbitals transform as t_2 so there is only mixing into the 3d t_2 set which contributes to the intensity of the transition into the $^5T_2$ state (see Figure 4.12). If the total quadrupole intensity is 4.7(0.9) (the value calculated above for ferric complexes) then for $(Et_4N)[FeCl_4]$ which has a total intensity of 20.7(0.8) (Table 4.1) the dipole intensity is 16.0(1.2). Thus, the total amount of 4p mixing into the t_2 set of orbitals observed experimentally is 11.2(4.7)% (*i.e.* 16.0(1.2)/1.43(0.6)). A density functional calculation on $(Et_4N)[FeCl_4]$ predicts 2-3% 4p mixing into each of the 3d orbitals of t_2 symmetry, giving a total of 6-9%.[47]

4.3.2.3. C_{4v} Geometry. Fe K-edge data were collected for one square pyramidal high spin ferric complex, Fe(salen)Cl. The XAS spectrum of Fe(salen)Cl is shown in Figure 4.11 with the pre-edge region expanded and shown in the inset. The pre-edge feature of Fe(salen)Cl appears to be a relatively intense single feature (Table 4.1).

When the iron atom is in a C_{4v} site it is in a noncentrosymmetric environment and thus the 1s—>3d pre-edge transition can gain intensity both from the allowed quadrupole transition and also from 4p mixing into the 3d orbitals. A C_{4v} site can be treated as a distorted O_h site, in which the $d^{(n+1)}$ $^5T_2$ state splits into a $^5B_2$ and a ^5E state and the ^5E state splits into a $^5A_1$ and a $^5B_1$ state. Due to the reduced ligand repulsion along the z-axis (from removing an axial ligand), the d_{xz}, d_{yz} and the d_{z^2} orbitals will be lower in energy with respect to the d_{xy} and $d_{x^2-y^2}$ orbitals. There are four one-electron allowed excited state configurations: $eb_2a_1b_1$, $e^2a_1b_1$, $e^2b_2b_1$, and $e^2b_2a_1$.

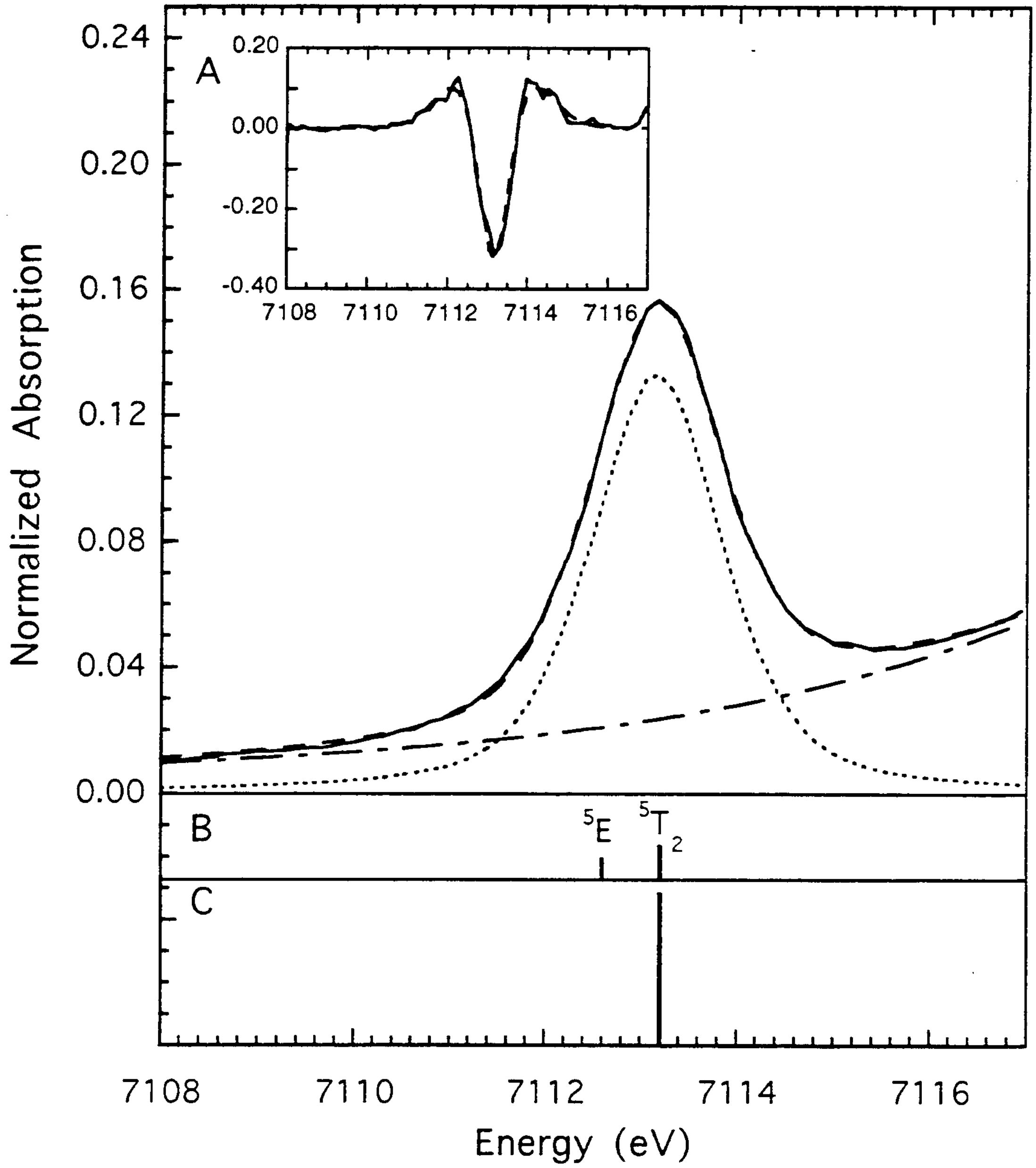

Figure 4.12. A) Fit to the Fe K-edge XAS pre-edge region of (Et$_4$N)[FeCl$_4$], where the solid line is the data, the dashed line is the fit to the data, the dashed-dot line is the background function, and the dotted lines are the individual pre-edge peaks. The inset is the second derivative of the data (—) and the second derivative of the fit to the data (---). B) The energy splitting and the quadrupole intensity distribution of the ^{5}E and ^{5}T$_2$ states. C) The energy splitting and the dipole intensity distribution (allowed by 4p mixing into the 3d states) of the ^{5}E and ^{5}T$_2$ states.

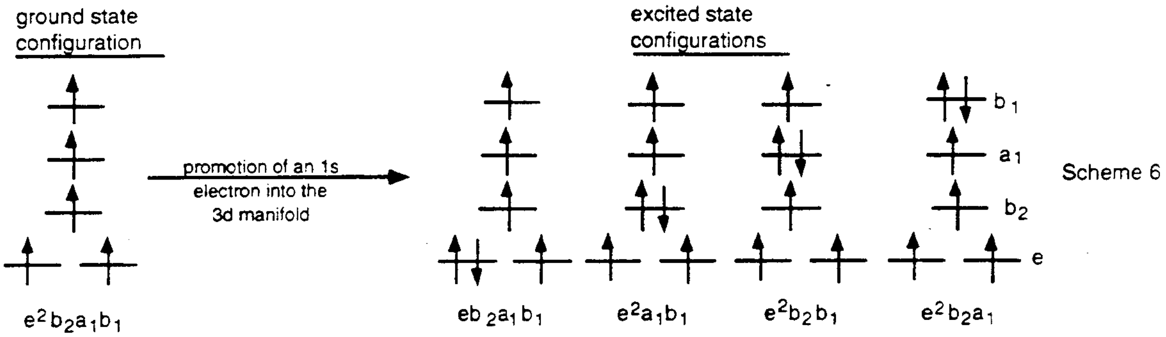

Scheme 6

The relative energies of these configurations can be determined from density functional calculations and from experimental observations of the 3d orbital energies.[41] From these calculations, the $e^2a_1b_1$ configuration (which comprises the $^5B_2$ state) is the lowest in energy, with the $eb_2a_1b_1$ configuration (which comprises the ^5E state) being 0.2 eV higher in energy, the $e^2b_2b_1$ configuration (which comprises the $^5A_1$ state) being 0.45 eV above the $eb_2a_1b_1$ configuration, and the $e^2b_2a_1$ (which comprises the $^5B_1$ state) being 1.05 eV above the $e^2b_2b_1$ configuration.[47] The quadrupole intensity into these states will have an intensity ratio of 1:2:1:1, respectively (see Figure 4.13B).

The pre-edge features of square pyramidal complexes gains additional intensity from 4p mixing into the 3d orbitals. In the C_{4v} case, the 4p orbitals transform as e and a_1. However, the main distortion is along the z axis, and one would thus predict that the $4p_z$ orbital (of a_1 symmetry) will mix into the d_{z^2} orbital of a_1 symmetry. In this scenario the transition to the $^5A_1$ state that contains the $e^2b_2b_1$ component should be the most intense. This is consistent with the pre-edge data where the lower energy feature is much more intense than the higher energy feature (see Figure 4.13). The density functional calculation on Fe(salen)Cl also shows that the d_{z^2} orbital contains $4p_z$ character, while the d_{xz} and d_{yz} orbitals do not contain significant $4p_{xy}$ character.[47] The amount of $4p_z$ mixing into the d_{z^2} orbital can be estimated experimentally as follows. The total pre-edge intensity for Fe(salen)Cl is 14.4(0.6); if 4.7(0.9) units are attributed to quadrupole intensity, then 9.7(1.1) units come from $4p_z$ (dipole allowed) character in the d_{z^2} orbital. The amount of $4p_z$ mixing into the d_{z^2} orbital is 9.7(1.1)/1.43(0.6), or 6.8(2.9)%. The density functional calculation of $(BF_4)[Fe(TMC)Cl]$ shows 9% $4p_z$ mixing into the d_{z^2} orbital. As in the high spin ferrous square pyramidal case, there is only one state that gains intensity from the $4p_z$ mixing into the d_{z^2} orbital; thus, the axial interaction will be reflected in the intensity and position of the most intense pre-edge feature.

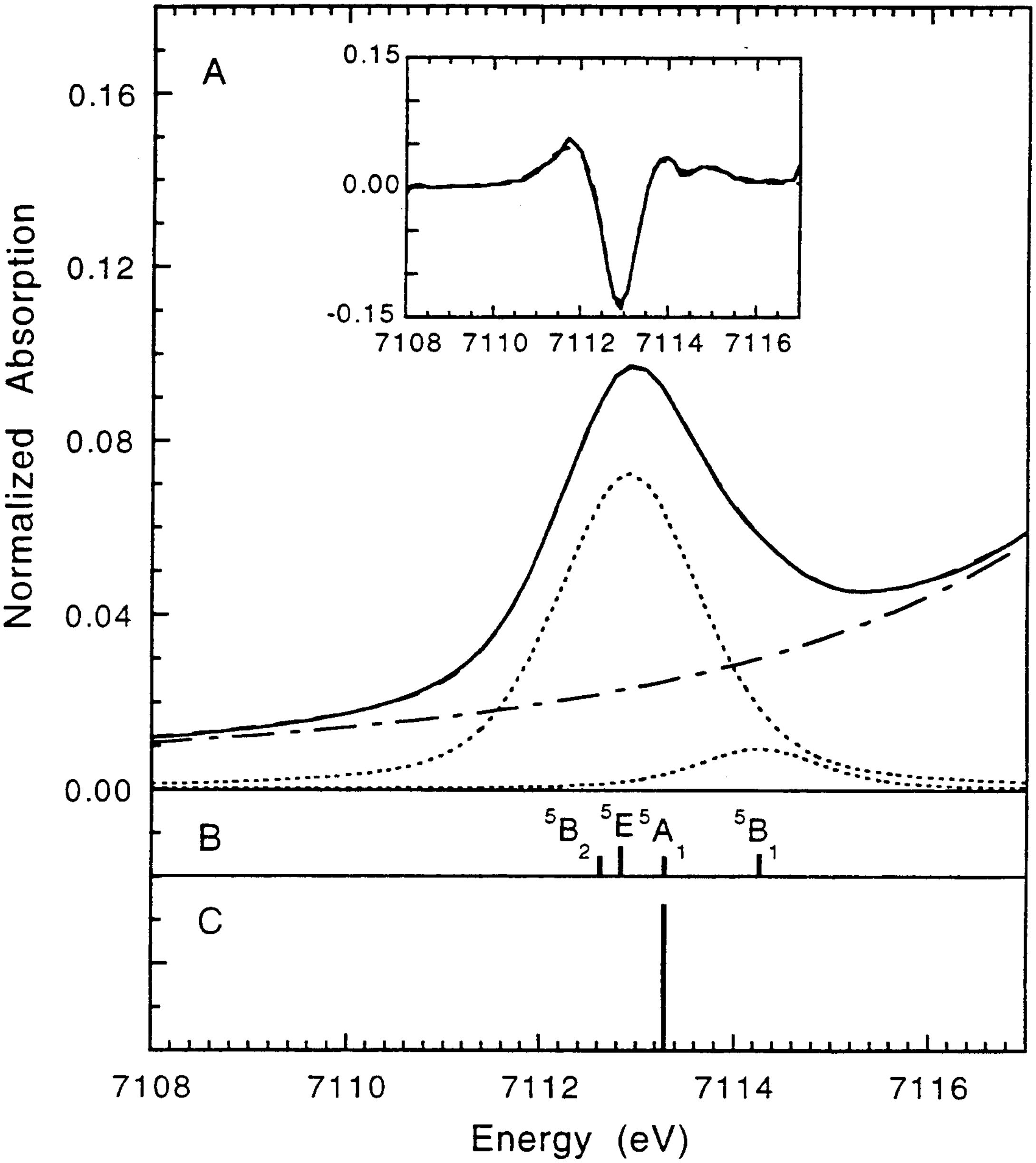

Figure 4.13. A) Fit to the Fe K-edge XAS pre-edge region of Fe(salen)Cl, where the solid line is the data, the dashed line is the fit to the data, the dashed-dot line is the background function, and the dotted lines are the individual pre-edge peaks. The inset is the second derivative of the data (—) and the second derivative of the fit to the data (---). B) The energy splitting and the quadrupole intensity distribution of the $^5B_2$, ^5E, $^5A_1$, and $^5B_1$ states. C) The energy splitting and the dipole intensity distribution (allowed by 4p mixing into the 3d states) of the $^5B_2$, ^5E, $^5A_1$, and $^5B_1$ states.

4.3.3. Binuclear Complexes

Fe K-edge data were also collected for a series of binuclear iron model complexes with varying oxidation states, geometries, and bridging ligation. The complexes studied are listed in Table 4.2. Figures 4.14, 4.15, and 4.16 display XAS spectra of representative complexes with the insets containing an expanded view of the 1s—>3d pre-edge region. Figure 4.14 shows a comparison of spectra of six- and five-coordinate diferrous complexes, $(Et_4N)_2[Fe_2(salmp)_2]\cdot 2DMF$ and $[Fe_2(OBz)(et\text{-}HPTB)](BF_4)_2$ to those of six- and five-coordinate monomeric complexes. $(Et_4N)_2[Fe_2(salmp)_2]\cdot 2DMF$ has a low intensity pre-edge feature that is split by ~2 eV, very similar to the monomeric six-coordinate complex. $[Fe_2(OBz)(et\text{-}HPTB)](BF_4)_2$ also has a split feature; however, the lower energy feature is much more intense, similar to the monomeric five-coordinate complex. In Figure 4.15 is shown an analogous comparison of six- and four-coordinate diferric complexes, $[Fe_2OH(OAc)_2(HB(pz)_3)_2](ClO_4)$ and $(BzPHMe_2N)_2[Fe_2OCl_6]$, with those of the corresponding six- and four-coordinate monomeric complexes. $[Fe_2OH(OAc)_2(HB(pz)_3)_2](ClO_4)$ has a low intensity pre-edge feature that is split, similar to the monomeric ferric complex. $(BzPHMe_2N)_2[Fe_2OCl_6]$ has a single very intense pre-edge feature, similar to the monomeric tetrahedral complex.

Spectra of $[Fe_2OH(OAc)_2(HB(pz)_3)_2](ClO_4)$, $[Fe_2O(OAc)_2(HB(pz)_3)_2]$, $[Fe_2(TPA)_2O(OAc)](ClO_4)_2$, and $(enH_2)[Fe_2O(HEDTA)_2]\cdot 6H_2O$ are shown in Figure 4.16. All four of these complexes are diferric with various bridging ligands. $[Fe_2OH(OAc)_2(HB(pz)_3)_2](ClO_4)$ and $[Fe_2O(OAc)_2(HB(pz)_3)_2]$ have the same ligand set with the exception of the former having a hydroxide bridge, while the latter has a μ-oxo bridge. $[Fe_2OH(OAc)_2(HB(pz)_3)_2](ClO_4)$ and $[Fe_2O(OAc)_2(HB(pz)_3)_2]$ display very different pre-edge features with the hydroxide bridged complex having a weak, split pre-edge feature and the μ-oxo bridged complex having a much more intense higher energy feature with a lower energy shoulder. $[Fe_2(TPA)_2O(OAc)](ClO_4)_2$ and $(enH_2)[Fe_2O(HEDTA)_2]\cdot 6H_2O$ also contain a μ-oxo bridge with $[Fe_2(TPA)_2O(OAc)](ClO_4)_2$ having an additional acetate bridge. Both of these complexes show a pre-edge feature similar to $[Fe_2O(OAc)_2(HB(pz)_3)_2]$. In fact, ***all*** the dimer complexes studied that contained a μ-oxo bridge had a distinctive pre-edge feature in their spectra with this higher energy intense feature and a lower energy shoulder (Table 4.2).

The first part to be addressed is the applicability of using the atomic multiplet analysis that was developed above for monomeric systems on dimeric iron systems. To resolve this question the pre-edge features of diferrous and diferric complexes were

Table 4.2. XAS Pre-Edge Energies and Areas for Binuclear Iron Model Complexes.

compound	oxidation state	ligation[a]	beamline, temperature	pre-edge peak energy[b]	pre-edge peak area[b,c]	total pre-edge peak area[c]	peak energy differences[d]	peak area ratio[e]	reference
$[Fe_2O(OAc)_2\{[OP(OEt)_2]_3\text{-}Co(C_2H_5)\}_2]$	diferric	6 O	NSLS X19A,	7112.81 (0.13)	3.3 (1.0)	13.9 (1.0)	1.4	0.24	68
		O, (OAc)$_2$	10K	7114.25 (0.06)	10.6 (1.9)				
$[Fe_2O(O_2CH)_4(BIPhMe_2)]\text{-}(CH_3OH)$	diferric	4 O, 2 N	SSRL 4-3,	7112.92 (0.08)	4.0 (0.7)	14.9 (0.7)	1.7	0.27	69
		O, (O$_2$*CH)*$_2$	10 K	7114.64 (0.02)	10.9 (1.3)				
$[Fe_2O(OAc)_2(HB(pz)_3)_2]$	diferric	3 O, 3 N	SSRL 7-3,	7112.68 (0.05)	4.1 (0.5)	16.6 (0.7)	1.7	0.25	70
		O, (OAc)$_2$	300 K	7114.35 (0.01)	12.5 (1.1)				
$[Fe_2OH(OAc)_2(HB(pz)_3)_2)](ClO_4)$	diferric	3 O, 3 N	SSRL 7-3,	7112.68 (<0.01)	3.2 (0.2)	5.5 (0.4)	1.7	0.57	51
		OH, (OAc)$_2$	300 K	7114.35 (0.01)	2.3 (0.2)				
$[FeOH(H_2O)Chel]_2(H_2O)_4$	diferric	5 O, 1 N	SSRL 7-3,	7112.88 (0.02)	5.8 (0.4)	8.5 (0.3)	1.4	0.68	71
		(OH)$_2$	300 K	7114.28 (0.03)	2.7 (0.4)				
$[FeOH(H_2O)Dipic]_2$	diferric	5 O, 1 N	SSRL 4-2,	7112.89 (0.02)	5.1 (0.6)	7.4 (0.6)	1.4	0.69	71
		(OH)$_2$	10 K	7114.30 (0.04)	2.3 (0.2)				
$[Fe_2(salmp)_2]\cdot 2DMF$	diferric	4 O, 2 N	SSRL 7-3,	7112.51 (0.01)	3.6 (0.2)	7.4 (0.2)	1.6	0.49	49
		(OPh)$_2$	10 K	7114.06 (0.02)	3.8 (0.2)				
$(Et_4N)[Fe_2(salmp)_2]\cdot 2DMF$	semimet	4 O, 2 N	SSRL 7-3,	7111.37 (0.12)	0.9 (0.5)	6.4 (0.3)	2.7	0.85	49
		(OPh)$_2$	10 K	7112.54 (0.04)	4.45 (0.7)				
				7114.03 (0.02)	1.0 (0.2)				
$(Et_4N)_2[Fe_2(salmp)_2]\cdot 2DMF$	diferrous	4 O, 2 N	SSRL 7-3,	7111.44 (0.04)	2.7 (0.2)	5.0 (0.3)	2.1	0.71	49
		(OPh)$_2$	10 K	7112.35 (0.07)	0.8 (0.3)				
				7113.57 (0.04)	1.4 (0.1)				
$[Fe_2(TPA)_2O(OAc)](ClO_4)_2$	diferric	2 O, 4 N	SSRL 7-3,	7112.51 (0.08)	3.4 (0.4)	14.9 (1.7)	1.7	0.22	72
		O, OAc	300 K	7114.21 (0.01)	11.6 (2.1)				
$[Fe_2(TPA)_2O(CO_3)](ClO_4)_2$	diferric	2 O, 4 N	SSRL 7-3,	7112.55 (0.06)	3.1 (0.3)	14.6 (1.8)	1.6	0.21	73
		O, CO$_3$	300 K	7114.11 (0.01)	11.5 (2.0)				
$[Fe_2(TPA)_2O(phthalate)](ClO_4)_2$	diferric	2 O, 4 N	SSRL 7-3,	7112.44 (0.06)	3.5 (0.3)	15.0 (1.9)	1.7	0.23	73
		O, OPht	300 K	7114.18 (0.02)	11.5 (2.1)				
$[Fe_2O(Phen)_4(H_2O)_2](ClO_4)$	diferric	2 O, 4 N	SSRL 4-2,	7112.58 (0.03)	3.0 (0.3)	13.2 (0.8)	1.8	0.23	74
		O	10 K	7114.37 (0.02)	10.2 (0.6)				
$(enH_2)[Fe_2O(HEDTA)_2]\cdot 6H_2O$	diferric	4 O, 2 N	SSRL 7-3,	7112.76 (0.04)	2.9 (0.5)	10.5 (0.6)	1.5	0.28	75
		O	10 K	7114.29 (0.02)	7.6 (0.5)				

$[Fe_2(OBz)(et\text{-}HPTB)](BF_4)_2$	diferrous	2 O, 3 N *alkoxo, OBz*	SSRL 7-3, 10 K	7111.68 (0.01) 7113.41 (0.01)	10.9 (0.2) 2.2 (0.1)	13.0 (0.3)	1.7	0.83	50
$(BzPhMe_2N)_2[Fe_2OCl_6]$	diferric	1 O, 3 Cl *O*	SSRL 2-3, 10 K	7113.37 (0.01)	27.1 (1.2)	27.1 (1.2)	---	---	52

[a] Bridging ligands are denoted by italics. [b] Pre-edge energies and intensities were determined by fits to the data (see the Experimental Section for details on the fitting procedure). [c] The values reported for the pre-edge areas were multiplied by 100. [d] Peak energy differences are the energy differences between the lowest energy and the highest energy pre-edge feature. [e] Peak area ratios are the area of the first pre-edge feature divided by the total pre-edge area.

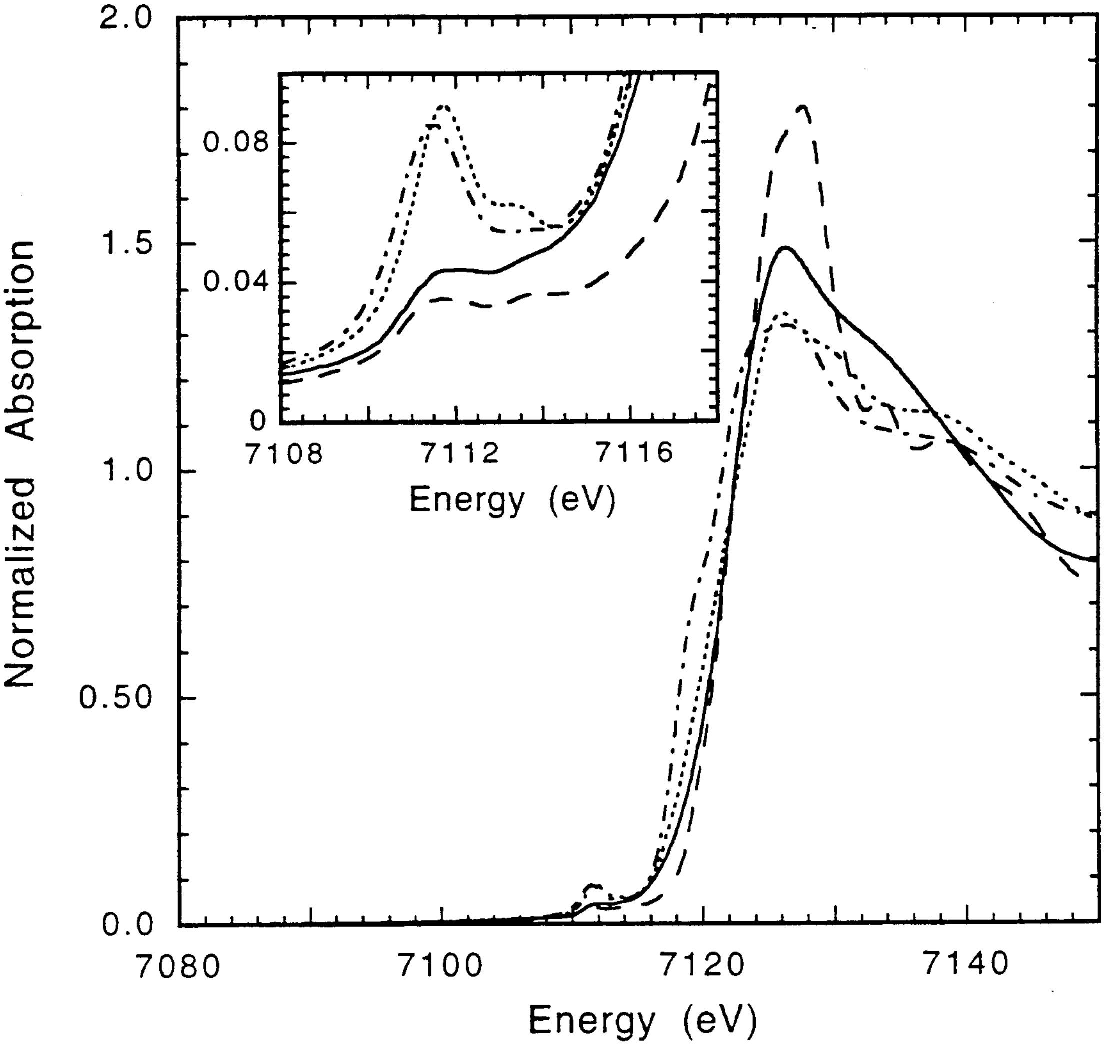

Figure 4.14. Fe K-edge XAS spectra of $(Et_4N)_2[Fe_2(salmp)_2]\cdot 2DMF$ (—), $FeSiF_6\cdot 6H_2O$ (---), $Fe_2(OBz)(et\text{-}HPTB)](BF_4)_2$ (·····), and $(BF_4)[Fe(TMC)Cl]$ (— -), where the inset is an expansion of the 1s—>3d pre-edge region.

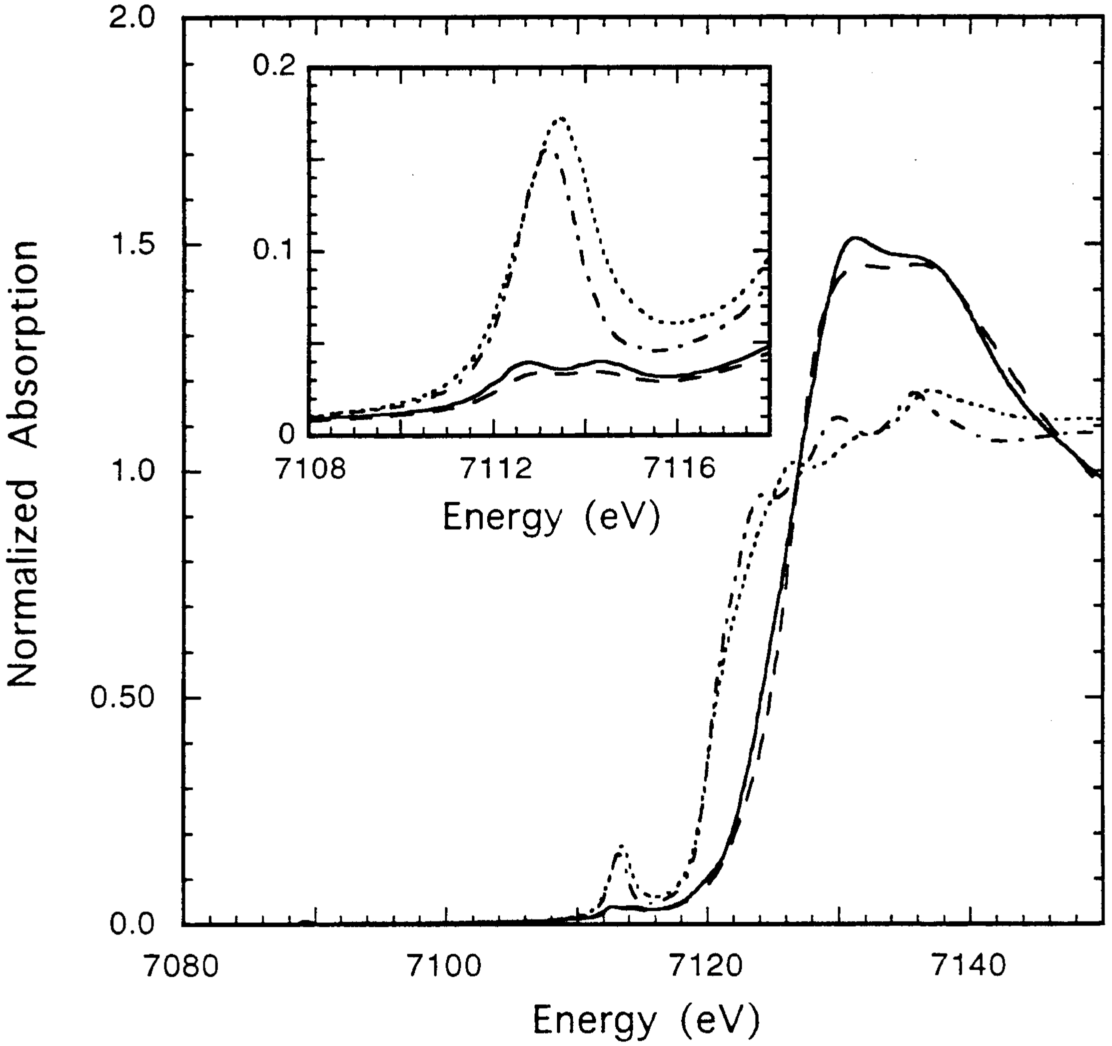

Figure 4.15. Fe K-edge XAS spectra of $[Fe_2OH(OAc)_2(HB(pz)_3)_2](ClO_4)$ (—), $Fe(acac)_3$ (---), $(BzPHMe_2N)_2[Fe_2OCl_6]$ (·····), and $(Et_4N)[FeCl_4]$ (— -), where the inset is an expansion of the 1s—>3d pre-edge region.

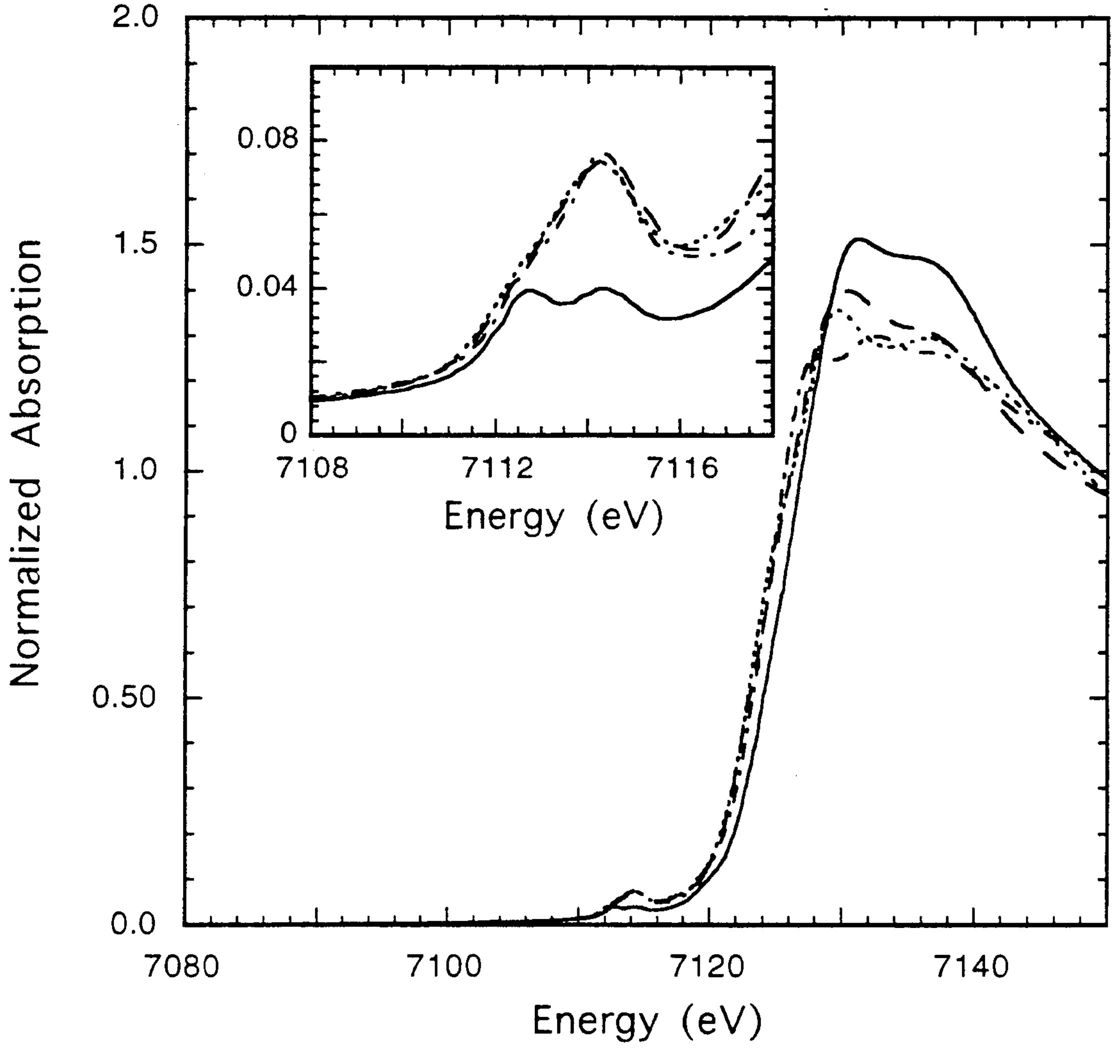

Figure 4.16. Fe K-edge XAS spectra of [$Fe_2OH(OAc)_2(HB(pz)_3)_2$]($ClO_4$) (—), [$Fe_2O(OAc)_2(HB(pz)_3)_2$] (---), [$Fe_2(TPA)_2$O(OAc)]($ClO_4$)$_2$ (·····), and (enH_2)[Fe_2O(HEDTA)$_2$]•$6H_2O$ (— -), where the inset is an expansion of the 1s—>3d pre-edge region.

compared to those of monomer complexes with similar ligation and geometry. $(Et_4N)_2[Fe_2(salmp)_2]$•2DMF has two six-coordinate iron centers with O and N ligation.[49] The pre-edge of this complex (Figure 4.14) is very similar to the pre-edges of monomeric octahedral complexes with O and N ligation (Figure 4.2). The fits to the $(Et_4N)_2[Fe_2(salmp)_2]$•2DMF data give pre-edge peak energies that are within 0.1 eV of the monomeric octahedral complexes with O and N ligation, with very similar areas of the three fitted peaks (Table 4.1 and 4.2). $Fe_2(OBz)(et\text{-}HPTB)](BF_4)_2$ has two five-coordinate iron sites[50] and has a pre-edge feature that is very similar to the square pyramidal high spin ferrous monomers (Figure 4.14; Tables 4.1 and 4.2). $[Fe_2OH(OAc)_2(HB(pz)_3)_2](ClO_4)$ has two six-coordinate iron sites that are very nearly octahedral.[51] The pre-edge feature of this complex is very similar to the pre-edge features of octahedral high spin ferric monomeric complexes with O and N ligation with a low intensity split pre-edge feature (Figures 4.15; Tables 4.1 and 4.2). $(BzPHMe_2N)_2[Fe_2OCl_6]$ contains iron sites with 3 Cl^- ligands and a μ-oxo bridge in a ~T_d geometry[52] and has a very intense single pre-edge feature that is very similar to that of $(Et_4N)[FeCl_4]$ (Figure 4.15; Tables 4.1 and 4.2). The pre-edge feature of $(BzPHMe_2N)_2[Fe_2OCl_6]$ is more intense since the iron site is more distorted due to the shorter μ-oxo bridge.

From the above similarities, in pre-edge features between monomeric and dimeric complexes of similar oxidation state, ligation and geometry, we can conclude that the pre-edge splittings and intensities predicted from atomic multiplet theory can be used to explain dimeric as well as monomeric iron complexes.

Dimeric iron complexes that contain a μ-oxo bridge all have a very similar and very distinctive pre-edge feature (Figure 4.16). The μ-oxo bridge seems to have a dominant effect on the pre-edge features, as mono-, di-, and tri-bridged complexes that contain a μ-oxo bridge all have very similar pre-edge features (Figure 4.16 and Table 4.2). There is also a striking difference in the pre-edge feature of hydroxide *vs.* μ-oxo bridged complexes, as can be seen in the pre-edge features of $[Fe_2OH(OAc)_2(HB(pz)_3)_2](ClO_4)$ and $[Fe_2O(OAc)_2(HB(pz)_3)_2]$ (Figure 4.16). The six-coordinate μ-oxo bridged dimers can be viewed as having an iron site with C_{4v} symmetry in which an axial ligand (the O of the μ-oxo bridge) has moved closer to the iron site. This shortening of the axial bond strongly perturbs the iron site allowing for 4p mixing into the 3d orbitals. As discussed previously, in the high spin ferric C_{4v} case, the 4p orbitals transform as e and a_1 and if the main distortion is along the z axis, the dominant effect will be that of the $4p_z$ orbital (of a_1 symmetry) mixing with the d_{z^2} orbital of a_1 symmetry. In this scenario, the transition to the $^5A_1$ state that contains the

$e^2b_2b_1$ component (Scheme 6) should be the most intense. Due to the increased ligand repulsion along the z-axis, the d_{xz}, d_{yz} and the $d_{z}2$ orbitals will increase in energy with respect to the d_{xy} and $d_{x^2-y^2}$ orbitals. This effect increases the energy of the $^5A_1$ state so that it is the state highest in energy. Thus, the higher energy pre-edge feature should be the most intense since $4p_z$ mixing into the $3d_{z^2}$ orbital will increase the intensity of the $^5A_1$ state. This explains the distinctive shape of all the μ-oxo bridged complexes (Figure 4.16 and Table 4.2).

The amount of $4p_z$ mixing can be quantitated. The total pre-edge peak intensities for all the octahedral dimer complexes with μ-oxo bridges ranges from 10.5 to 16.6 (Table 4.2) with the average total peak intensity being 14.2. A dipole intensity of 9.5 is calculated by subtracting the total quadrupole intensity of 4.7 (the value obtained from the octahedral ferric complexes). The amount of $4p_z$ mixing into the d_{z^2} orbital is 9.5/1.43, or 6.6%. As in the high spin ferric square pyramidal case, there is only one state that gains intensity from the $4p_z$ mixing into the d_{z^2} orbital; thus, the axial interaction will be reflected in the intensity and position of the most intense pre-edge feature.

4.3.4. Low Spin Iron Complexes

4.3.4.1. Ferrous Complexes. Fe K-edge XAS data were obtained for the low spin ferrous complexes $Fe(HB(pz)_3)_2$, $Fe(prpep)_2$ and $K_4Fe(CN)_6$. XAS spectra for these three complexes are shown in Figure 4.17 with the inset showing an expanded view of the 1s—>3d pre-edge region. All three complexes have a weak, single pre-edge feature with the feature of $Fe(HB(pz)_3)_2$ being the lowest in energy and that of $K_4Fe(CN)_6$ being highest in energy (Table 4.3).

All three of these low spin ferrous complexes have an octahedral iron site and, therefore, the only intensity mechanism for the 1s—>3d pre-edge feature is the allowed quadrupole transition. The ground state of these low spin ferrous complexes has an electronic hole configuration of e^4 with e^3 being the only excited state configuration (Scheme 7). Coupling of the three e holes produces a ^2E excited many-electron state.

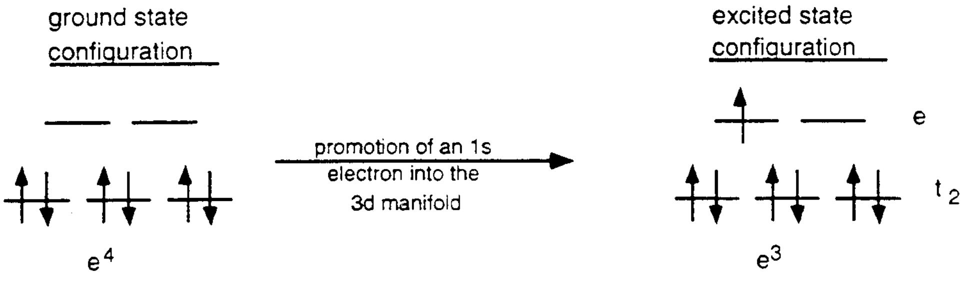

Scheme 7

Table 4.3. XAS Pre-Edge Energies and Areas for Low Spin Iron Model Complexes.

compound	oxidation state	ligation	beamline, temperature	pre-edge peak energy[a]	pre-edge peak area[a,b]	total pre-edge peak area[b]	peak energy differences[c]	peak area ratio[d]	reference
$Fe(HB(pz)_3)_2$	ferrous	6 N	NSLS X19A, 10 K	7111.70 (0.03)	4.2 (0.2)	4.2 (0.2)	---	---	76,77
$Fe(prpep)_2$	ferrous	6 N	SSRL 7-3, 10 K	7112.12 (0.01)	5.3 (0.2)	5.3 (0.2)	---	---	78
$K_4Fe(CN)_6$	ferrous	6 C	SSRL 7-3, 10 K	7112.85 (0.01)	4.2 (0.4)	4.2 (0.4)	---	---	67
$[Fe(prpep)_2](ClO_4)$	ferric	6 N	SSRL 7-3, 10 K	7110.96 (0.03) 7112.68 (0.02) 7114.44 (0.35)	0.7 (0.1) 4.5 (0.2) 1.2 (0.9)	6.4 (0.9)	1.7	0.14	78
$[Fe(HB(pz)_3)_2](ClO_4)$	ferric	6 N	NSLS X19A, 10 K	7110.95 (0.04) 7112.70 (0.01)	0.5 (0.1) 4.0 (0.6)	4.5 (0.7)	1.8	0.11	79
$K_3Fe(CN)_6$	ferric	6 C	SSRL 7-3, 10 K	7110.09 (0.01) 7113.30 (0.01)	1.0 (0.4) 4.1 (0.2)	5.2 (0.2)	3.2	0.20	80

[a] Pre-edge energies and intensities were determined by fits to the data (see the Experimental Section for details on the fitting procedure). [b] The values reported for the pre-edge areas were multiplied by 100. [c] Peak energy differences are the energy differences between the first and second pre-edge feature. [d] Peak area ratios are the area of the first pre-edge feature divided by the total pre-edge area.

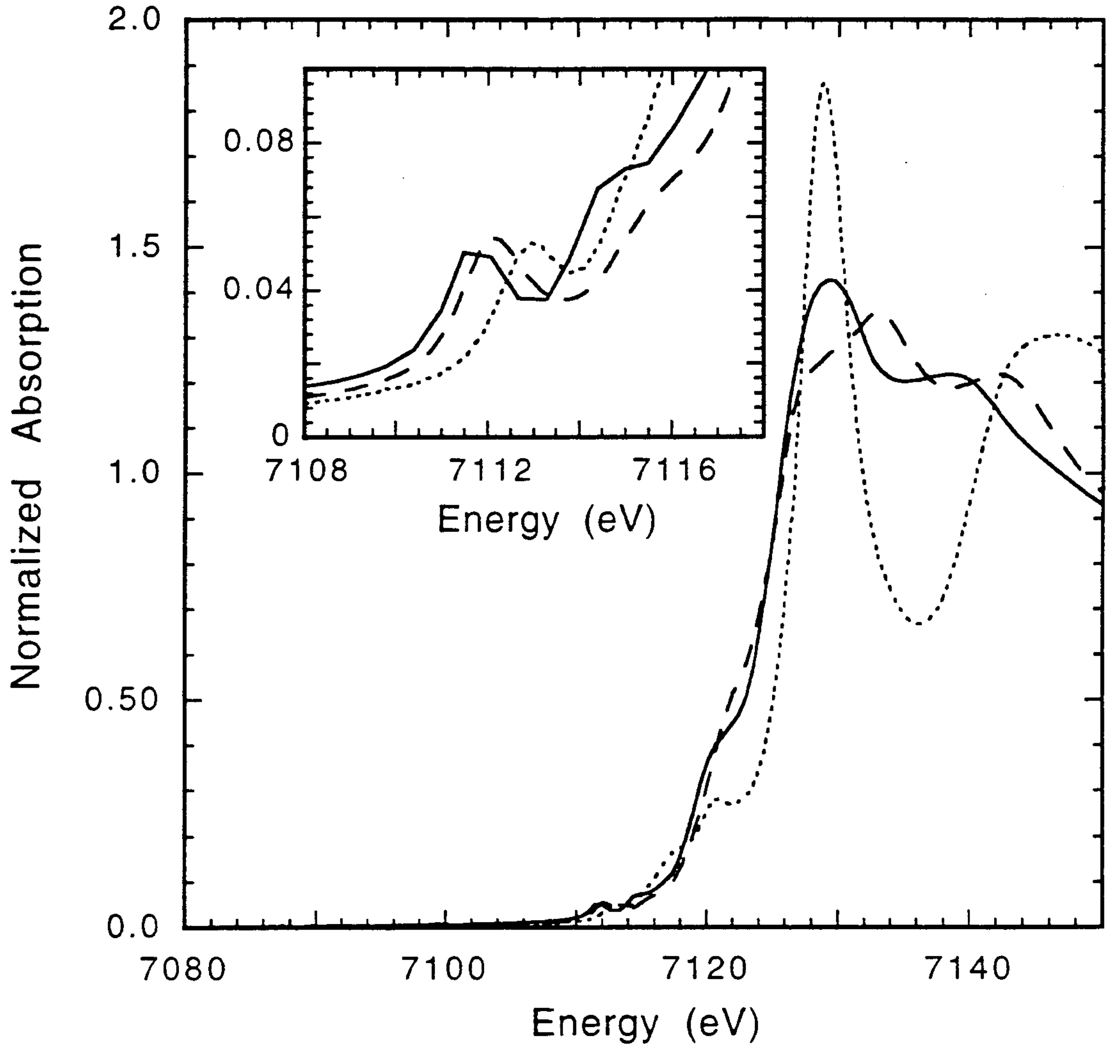

Figure 4.17. Fe K-edge XAS spectra of $Fe(HB(pz)_3)_2$ (—), $Fe(prpep)_2$ (---), and $K_4Fe(CN)_6$ (·····), where the inset is an expansion of the 1s—>3d pre-edge region.

A transition into the ^{2}E state gives rise to a single pre-edge feature (Figure 4.17 and Table 4.3). The average total pre-edge areas for these low spin complexes is 4.6, which is similar to that of the high spin ferrous complexes.

4.3.4.2. Ferric Complexes. Fe K-edge XAS data were obtained for the low spin ferric complexes [Fe(HB(pz)$_3$)$_2$](ClO$_4$), [Fe(prpep)$_2$](ClO$_4$), and K$_3$Fe(CN)$_6$. XAS spectra for these three complexes are shown in Figure 4.18 with an expanded view of the 1s—>3d pre-edge region shown in the inset. All three of these complexes have a weak pre-edge feature with a lower energy shoulder. The splitting between the lower energy shoulder and the higher energy feature is the greatest in K$_3$Fe(CN)$_6$ (Table 4.3).

These low spin ferric complexes all have an octahedral iron site and therefore the 1s—>3d pre-edge feature only gains intensity through an allowed quadrupole transition. The ground state of an octahedral low spin ferric complex has a t$_2$e^4 configuration, with two excited state configurations of e^4 and t$_2$e^3 (Scheme 8).

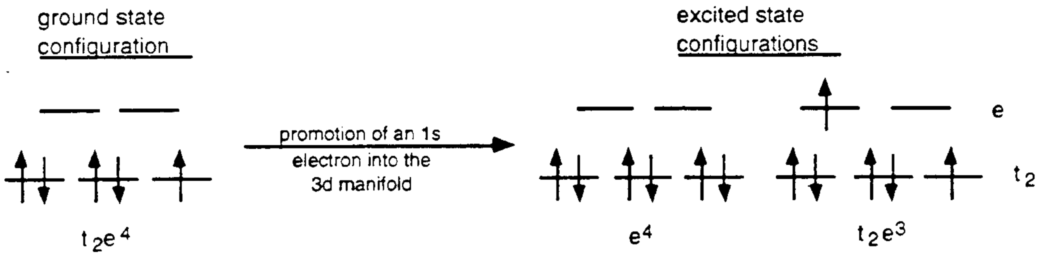

Scheme 8

Coupling of the four e holes produces a ^{1}A$_1$ state, while coupling of the holes in the t$_2$e^3 configuration produces ^{1}T$_1$, ^{3}T$_1$, ^{1}T$_2$, and ^{3}T$_2$ states. Using a 10Dq value of 20,000 cm^{-1}, a B value of 1058 cm^{-1}, and a C value of 4500 cm^{-1}, energy splittings of the five states were calculated. The lowest energy state is the ^{1}A$_1$ with the ^{3}T$_1$ state being 0.9 eV higher in energy, the ^{3}T$_2$ state being 0.8 eV above the ^{3}T$_1$ state, the ^{1}T$_1$ state being 0.5 eV above the ^{3}T$_2$ state, and the ^{1}T$_2$ being 1.4 eV above the ^{1}T$_1$ state (Figure 4.19). Comparison of these calculated energies to the fit of the [Fe(prpep)$_2$](ClO$_4$) pre-edge region, it appears that the lower energy feature originates from a transition to the ^{1}A$_1$ d$^{(n+1)}$ final state, while the higher energy feature gains intensity from the ^{3}T$_1$, ^{3}T$_2$, and ^{1}T$_1$ states. The ^{1}T$_2$ state is highest in energy and difficult to resolve due to the onset of the edge features (Figure 4.19).

Assuming that the feature at ~7112.7 eV contains the intensity from transitions in the ^{3}T$_1$, ^{3}T$_2$, and ^{1}T$_1$ states, the theoretical intensity ratio of the three pre-edge features should be 1:9:3. The fits to the [Fe(prpep)$_2$](ClO$_4$) pre-edge region give an intensity ratio of 1:6.4:1.7. The discrepancy between the theoretical intensity and that which is

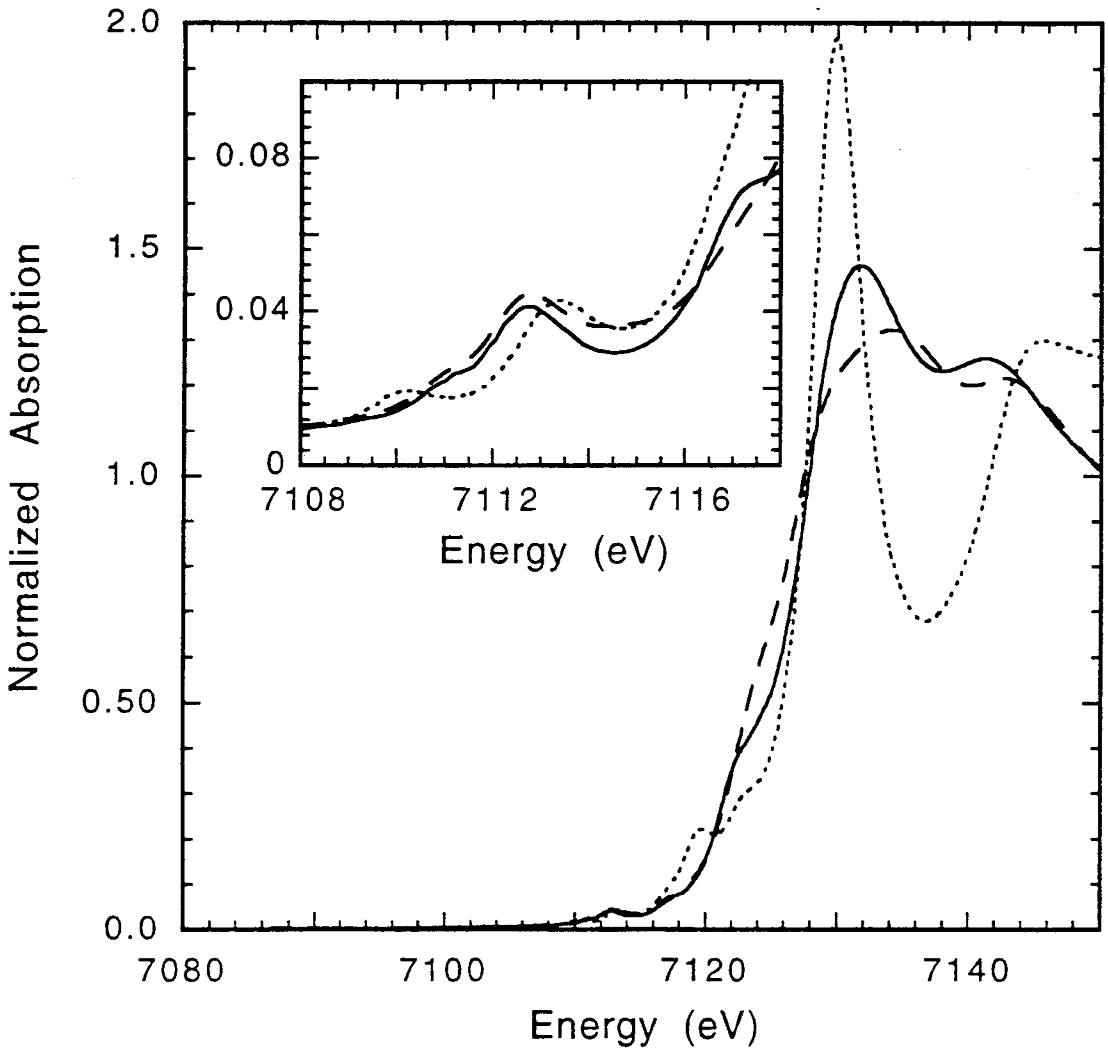

Figure 4.18. Fe K-edge XAS spectra of [Fe(HB(pz)$_3$)$_2$](ClO$_4$) (—), [Fe(prpep)$_2$](ClO$_4$) (---), and K$_3$Fe(CN)$_6$ (·····), where the inset is an expansion of the 1s—>3d pre-edge region.

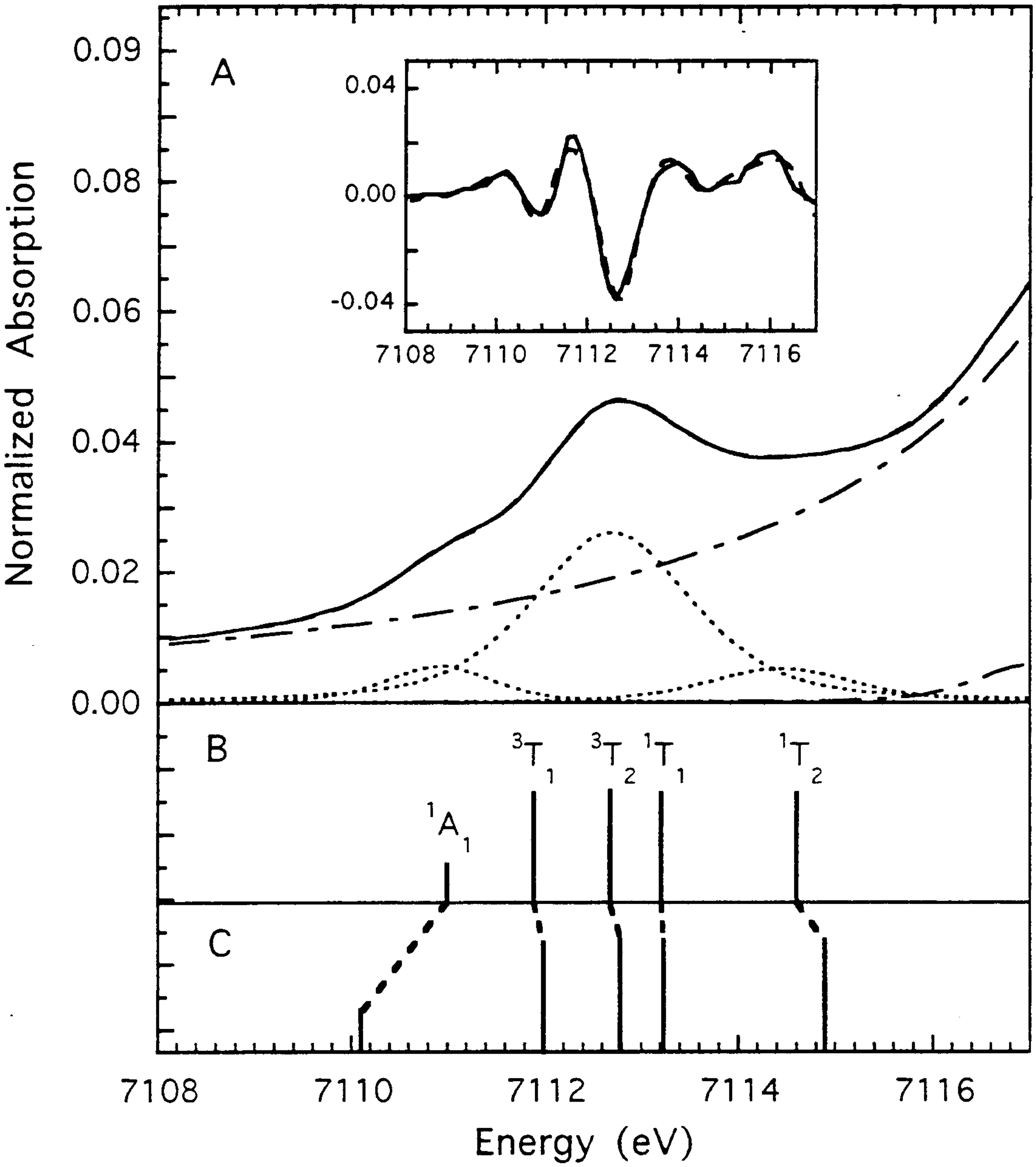

Figure 4.19. A) Fit to the Fe K-edge XAS pre-edge region of $K_3Fe(CN)_6$, where the solid line is the data, the dashed line is the fit to the data, the dashed-dot line is the background function, and the dotted lines are the individual pre-edge peaks. The inset is the second derivative of the data (—) and the second derivative of the fit to the data (---). B) The energy splitting and the quadrupole intensity distribution of the $^1A_1$, $^3T_1$, $^3T_2$, $^1T_1$, and $^1T_2$ states. C) The effect of increased 10Dq on the energy splitting of the $^1A_1$, $^3T_1$, $^3T_2$, $^1T_1$, and $^1T_2$ states.

observed can be explained by covalency effects. The e set of orbitals is more covalent than the t_2 set due to σ bonding interactions with the ligands; therefore, the transition to the $^1A_1$ state (the state containing the e^4 component) should have more relative intensity than transitions to the T states which is seen in the data. The energies of the four states were recalculated using a larger 10Dq value of 28,000 cm^{-1} (80% of the ground state 10Dq for $K_3Fe(CN)_6$)[41] (see Figure 4.19C). Again, the lower energy feature appears to originate from a transition to the $^1A_1$ state, while the higher energy feature gains intensity from transitions to the $^3T_1$, $^3T_2$, and $^1T_1$ states. The transition to the $^1T_2$ state is difficult to resolve from the edge features. In fact, a third higher energy pre-edge feature at ~7115 eV could be included in the fits to the $[Fe(HB(pz)_3)_2](ClO_4)$ and $K_3Fe(CN)_6$ data. However, the data could be fit well with only two pre-edge features (Table 4.3), while a third pre-edge feature was necessary to fit the data of $[Fe(prpep)_2](ClO_4)$ (Figure 4.19).

4.4. Discussion

The 1s—>3d pre-edge feature in the iron complexes studied was shown to be sensitive to the electronic and geometric structure of the iron site. For an iron atom in a symmetric six-coordinate environment, the number of features and the energy positions of those features differ with oxidation and spin state of the iron atom due to the differing many-electron excited states. In particular, upon promoting a 1s electron into the 3d manifold, i) a high spin ferrous atom in an O_h ligand field has three many-electron excited states, $^4T_1$, $^4T_2$, and $^4T_1$. The lowest energy $^4T_1$ state is barely resolvable from the $^4T_2$ state at the Fe K-edge with the higher energy $^4T_1$ state being ~2 eV above the other two states. Hence, a high spin ferrous atom in an octahedral environment has a pre-edge feature at ~7111.5 eV from transitions into the $^4T_1$ and $^4T_2$ states and a feature at ~7113.5 eV from a transition into the higher energy $^4T_1$ state. Splitting of the lower energy feature may be observable if the energy difference between the $^4T_1$ and $^4T_2$ is greater than the experimental energy resolution at the Fe K-edge. ii) A high spin ferric atom in an O_h ligand field typically has two 1s—>3d pre-edge features at approximately 7113.0 and 7114.5 eV split by 10Dq due to transitions into the $^5T_2$ and ^5E excited states. A direct measurement of the excited state 10Dq value is obtainable from the magnitude of the pre-edge splitting and, thus, trends in ligand field strength are observable. iii) A low spin ferrous atom only has one excited state and, thus, only a single pre-edge feature is observed at ~7112 eV for complexes with nitrogen ligation. iv) A low spin ferric complex in an O_h environment has five allowed excited states with the lowest in energy being a $^1A_1$ state and the $^3T_1$, $^3T_2$, $^1T_1$, and $^1T_2$ states at higher energy. Consequently, the 1—>3d pre-edge feature of a low spin ferric complex will have a low energy feature below 7111.0 eV due to the transition into the $^1A_1$ state with more intense features at higher energy due to transitions into the $^3T_1$, $^3T_2$, $^1T_1$, and $^1T_2$ states. In each of the cases mentioned above where the iron atom is in a symmetric site, the pre-edge features are very weak since the intensity originates from only from quadrupole transitions. The average total pre-edge intensity for the ferrous complexes is close to 4, while that of the ferric complexes is closer to 5. The increase in intensity on going from ferrous to ferric sites is due to the fact that a ferrous iron atom has four holes in the ground state 3d manifold, while in the ferric oxidation state there are five holes in the 3d manifold.

The 1s—>3d pre-edge feature is also sensitive to the geometry of the iron site as noncentrosymmetric distortions allow for 4p-3d mixing, thereby, increasing the intensity of the pre-edge feature. Dipole transitions are two orders of magnitude more intense than quadrupole transitions, so even a few percent of 4p mixing into the 3d orbitals will be visible in the intensity of the 1s—>3d pre-edge feature. The trend of increasing total intensity with decreasing coordination number has been observed previously.[1,20] However, a more detailed analysis of the intensity distribution over the pre-edge features allows for more accuracy in determining the coordination number of the iron atom. For example, $(BF_4)[Fe(TMC)Cl]$, a five-coordinate ferrous complex, and $(Et_4N)_2[FeCl_4]$, a four-coordinate ferrous complex, have the same total pre-edge intensity of 12.9. However, the pre-edge features of these complexes look very different. $(BF_4)[Fe(TMC)Cl]$ has an intense pre-edge feature at 7111.4 eV with an extremely weak feature at 7113.4 eV (Figure 4.7), while $(Et_4N)_2[FeCl_4]$ has two intense peaks at 7111.6 and 7113.1 eV (Figure 4.5). In the T_d case, the dipole intensity (from 4p mixing into the 3d orbitals of t_2 symmetry) is distributed over both pre-edge features (Figure 4.5), while in the C_{4v} case, where one axial ligand is removed, the dipole intensity from $4p_z$ mixing into the d_z2 orbital is located ***only*** in the lowest energy pre-edge feature (Figure 4.7). The effect is not quite as dramatic for ferric complexes (Figure 4.12), as there is no splitting of the pre-edge feature for ferric complexes in T_d ligand fields (10Dq is lower than the experimental energy resolution at the Fe K-edge). There are two pre-edge features in the spectrum of the ferric C_{4v} complex Fe(salen)Cl with the lower energy feature being much more intense than the higher energy feature (Figure 4.14). The increase in intensity of the lower energy feature is due to $4p_z$ mixing into d_z2 where removing an axial ligand decreases the energy of d_z2. The amount of 4p mixing into the 3d orbitals can be quantitated since the total pre-edge intensity is a sum of the quadrupole and dipole intensity and the quadrupole intensity can be estimated from the intensity of the pre-edge features of iron in symmetric environments. The values obtained for the amount of 4p mixing into the 3d orbitals for the iron model complexes in this study agree very well with theoretical estimates of the mixing from density functional calculations.

Analysis of the 1s—>3d transitions in high spin ferric complexes is simplified by the fact that there is only one many-electron state for each excited state configuration, which is not the true for the high spin ferrous case. Thus, when a ferric atom is in a distorted site, the 1s—>3d pre-edge feature can be used as a direct probe of the distortion. For example, when a ferric atom is in a C_{4v} site, the pre-edge feature is sensitive to the strength of the axial interaction. Since the $4p_z$ orbital only mixes into the d_z2 orbital, only the transition into the $d_z{}^2$ orbital (corresponding to a transition into the ${}^5A_1$ state) will gain dipole intensity. Hence, the energy of the most intense pre-edge feature reflects the energy of the d_z2 orbital and the intensity of this feature is affected by the strength of the axial interaction. When an axial ligand is removed, as is the case in a five-coordinate C_{4v} complex, the d_z2 orbital decreases in energy resulting in an intense lower energy (~7112.9 eV) feature in the pre-edge region (Figure 4.13). When there is a strong axial interaction, as is the case in a μ–oxo bridged binuclear complex, the d_z2 orbital increases in energy resulting in an intense higher energy (~7114.2 eV) feature in the pre-edge region (Figure 4.16). This intense higher energy feature can be used as a diagnostic tool for determining whether or not there is a μ–oxo bridge in binuclear proteins and model complexes.

Using both the edge and EXAFS region of the XAS spectrum, one can obtain a very detailed description of the iron active site in non-heme iron enzymes. An EXAFS analysis provides information on the type of ligating atoms and gives very accurate iron-ligand distances. This study demonstrates that an analysis of the energy splitting and intensity distribution of the 1s—>3d pre-edge feature can aid in elucidating the coordination number and geometry of the iron active site. In addition, the multiplet structure of the pre-edge feature is specific for a given oxidation and spin state of an iron atom. The results presented in this chapter should further aid in the interpretation of the 1s—>3d pre-edge region for non-heme iron enzymes as the energy splitting and intensity pattern of the pre-edge features are directly related to the oxidation state, spin state and geometry of the iron site.

4.5. Acknowledgments

Professors Nobu Kitajima, Stephen Lippard, Richard Holm, Pradip Mascharak, and the Smithsonian Institute should be thanked for providing some of the model complexes in this study. Lawrence Roe should be thanked for measuring the data on the

$(BF_4)[Fe(TMC)X]$ series and Jane DeWitt for measuring the data on the majority of the dimer complexes. Pierre Kennepohl performed the density functional calculations alluded to in the text. Susan Shadle and Cecelia Campochiaro should be thanked for their helpful discussions on the intricacies of many-electron wave functions and ligand field theory. This research is supported by grants from the NIH (GM40392, E.I.S.) and NSF (CHE-9121576, K.O.H.). The data were collected at the Stanford Synchrotron Radiation Laboratory and the National Synchrotron Light Source, Brookhaven National Laboratory, which are supported by the U.S. Department of Energy, Office of Basic Energy Science, Divisions of Chemical and Materials Sciences. SSRL is also supported in part by the National Institutes of Health, Biomedical Research Technology Program (RR-01209) and the U.S. Department of Energy, Office of Health and Environmental Research.

4.6. References and Notes

(1) Roe, A. L.; Schneider, D. J.; Mayer, R. L.; Pyrz, J. W.; Widom, J.; Que, L., Jr. *J. Am. Chem. Soc.* **1984**, *106*, 1676.

(2) Kauzlarich, S. M.; Teo, B. K.; Zirino, T.; Burman, S.; Davis, J. C.; Averill, B. A. *Inorg. Chem.* **1986**, *25*, 2781.

(3) Hedman, B.; Co, M. S.; Armstrong, W. H.; Hodgson, K. O.; Lippard, S. J. *Inorg. Chem.* **1986**, *25*, 3708.

(4) Bunker, G.; Petersson, L.; Sjöberg, B.-M.; Sahlin, M.; Chance, M.; Chance, B.; Ehrenberg, A. *Biochemistry* **1987**, *26*, 4708.

(5) Scarrow, R. C.; Maroney, M. J.; Palmer, S. M.; Que, L., Jr.; Roe, A. L.; Salowe, S. P.; Stubbe, J. *J. Am. Chem. Soc.* **1987**, *109*, 7857.

(6) Zhang, K.; Stern, E. A.; Ellis, F.; Sanders-Loehr, J.; Shiemke, A. K. *Biochemistry* **1988**, *27*, 7470.

(7) Tsang, H.-T.; Batie, C. J.; Ballou, D. P.; Penner-Hahn, J. E. *Biochemistry* **1989**, *28*, 7233.

(8) True, A. E.; Orville, A. M.; Pearce, L. L.; Lipscomb, J. D.; Que, L., Jr. *Biochemistry* **1990**, *29*, 10847.

(9) DeWitt, J. G.; Bentsen, J. G.; Rosenzweig, A. C.; Hedman, B.; Green, J.; Pilkington, S.; Papaefthymiou, C. G.; Dalton, H.; Hodgson, K. O.; Lippard, S. J. *J. Am. Chem. Soc.* **1991**, *113*, 9219.

(10) Van der Heijdt, L. M.; Feiters, M. C.; Navaratnam, S.; Nolting, H.-F.; Hermes, C.; Veldink, G. A.; Vliegenthart, J. F. G. *Eur. J. Biochem.* **1992**, *207*, 793.

(11) True, A. E.; Scarrow, R. C.; Randall, C. R.; Holz, R. C.; Que, L., Jr. *J. Am. Chem. Soc.* **1993**, *115*, 4246.

(12) Randall, C. R.; Zang, Y.; True, A. E.; Que, L., Jr.; Charnock, J. M.; Garner, C. D. *Biochemistry* **1993**, *32*, 6664.

(13) Scarrow, R. C.; Trimitsis, M. G.; Buck, C. P.; Grove, G. N.; Cowling, R. A.; Nelson, M. J. *Biochemistry* **1994**, *33*, 15023.

(14) Bertini, I.; Briganti, F.; Mangani, S.; Nolting, H. F.; Scozzafava, A. *Biochemistry* **1994**, *33*, 10777.

(15) Loeb, K. E.; Zaleski, J. M.; Westre, T. E.; Guajardo, R. J.; Mascharak, P. K.; Hedman, B.; Hodgson, K. O.; Solomon, E. I. *J. Am. Chem. Soc.* **1995**, *117*, 4545.

(16) Pavlosky, M. A.; Zhang, Y.; Westre, T. E.; Gan, Q.-F.; Pavel, E. G.; Campochiaro, C.; Hedman, B.; Hodgson, K. O.; Solomon, E. I. *J. Am. Chem. Soc.* **1995**, *117*, 4316.

(17) Westre, T. E.; Loeb, K. E.; Zaleski, J. M.; Hedman, B.; Hodgson, K. O.; Solomon, E. I. *J. Am. Chem. Soc.* **1995**, *117*, 1309.

(18) DeWitt, J. G.; Rosenzweig, A. C.; Salifoglou, A.; Hedman, B.; Lippard, S. J.; Hodgson, K. O. *Inorg. Chem.* **1995**, *34*, 2505.

(19) Shulman, R. G.; Yafet, Y.; Eisenberger, P.; Blumberg, W. E. *Proc. Natl. Acad. Sci. USA* **1976**, *73*, 1384.

(20) Randall, C. R.; Shu, L.; Chiou, Y.-M.; Hagen, K. S.; Ito, M.; Kitajima, N.; Lachicotte, R. J.; Zang, Y.; Que, L., Jr. *Inorg. Chem.* **1995**, *34*, 1036.

(21) DeWitt, J. G., Ph.D. Thesis, Stanford University, 1994.

(22) Blair, R. A.; Goddard, W. A. *Phys. Rev. B* **1980**, *22*, 2767.

(23) Brouder, C. *J. Phys.: Condens. Matter* **1990**, *2*, 701.

(24) Hahn, J. E.; Scott, R. A.; Hodgson, K. O.; Doniach, S.; Desjardins, S. R.; Solomon, E. I. *Chem. Phys. Let.* **1982**, *88*, 595.

(25) Wong, J.; Lytle, F. W.; Messmer, R. P.; Maylotte, D. H. *Phys. Rev. B* **1984**, *30*, 5596.

(26) Kau, L.-S.; Spira-Solomon, D. J.; Penner-Hahn, J. E.; Hodgson, K. O.; Solomon, E. I. *J. Am. Chem. Soc.* **1987**, *109*, 6433.

(27) Colpas, G. J.; Maroney, M. J.; Bagyinka, C.; Kumar, M.; Willis, W. S.; Suib, S. L.; Baidya, N.; Mascharak, P. K. *Inorg. Chem.* **1991**, *30*, 920.

(28) Sano, M.; Komorita, S.; Yamatera, H. *Inorg. Chem.* **1992**, *31*, 459.

(29) Abbreviations used: acac = acetylacetonate; BIPhMe$_2$ = 2,2'-bis(1-methylimidazolyl)phenylmethoxymethane; BzPhMe$_2$N = benzyldimethylphenylammonium; Chel = 4-hydroxo-2,6-pyridinedicarboxylate; Dipic = 2,6-

pyridinedicarboxylate; EDTA = ethylenediaminetetraacetic acid; HB(pz)$_3$ = [tri-1-pyrazolylborate]$^{1-}$; HB(3,5-*i*Pr$_2$pz)$_3$ = hydrotris(3,5-diisopropyl-1-pyrazolyl)borate; HPTB = [*N*,*N*,*N'*,*N'*-tetrakis(2-benzimidazoylmethyl)-2-hydroxy-1,3-diaminopropane]$^-$; PrpepH = *N*-(2-(4-imidazole)ethyl)pyrimidine-4-carboxamide; salmp = [2-bis(salicylideneamino)methylphenolate]$^{3-}$; TMC = 1,4,8,11-tetramethyl-1,4,8,11-tetraazacyclotetradecane; TPA = tris(2-pyridylmethyl)amine; *OAc* = acetate bridge; *OPh* = phenolate bridge; *OPht* = phthalate bridge; *OBz* = benzoate bridge.

(30) Scott, R. A.; Hahn, J. E.; Doniach, S.; Freeman, H. C.; Hodgson, K. O. *J. Am. Chem. Soc.* **1982**, *104*, 5364.

(31) Lytle, F. W. In *Applications of Synchrotron Radiation*; Winick, H.; Xiam, D.; Ye, M.-H.; Huang, T., Eds.; Gordon and Breach Science Publishers: New York, 1989; p 135.

(32) Argonne National Laboratory; B.S. Garbow, K.E. Hillstrom, J.J. More.

(33) Agarwal, B. K. *X-ray Spectroscopy*; Springer-Verlag: Berlin, 1979, p 276.

(34) Lytle, F. W.; Greegor, R. B.; Sandstrom, D. R.; Marques, E. C.; Wong, J.; Spiro, C. L.; Huffman, G. P.; Huggins, F. E. *Nucl. Instrum. Methods* **1984**, *226*, 542.

(35) Tyson, T. A.; Roe, A. L.; Frank, P.; Hodgson, K. O.; Hedman, B. *Phy. Rev. B* **1989**, *39*, 6305.

(36) Griffith, J. S. *The Theory of Transition Metal Ions*; Cambridge University Press: Cambridge, 1961.

(37) de Groot, F. M. F. *J. Electron Spectrosc. Relat. Phenom.* **1994**, *67*, 529.

(38) Sugano, S.; Tanabe, Y.; Kamimura, H. *Multiplets of Transition-Metal Ions in Crystals*; Academic Press: New York, 1970.

(39) Stout, J. W.; Reed, S. A. *J. Am. Chem. Soc.* **1954**, *76*, 5279.

(40) Karshipin, T. B.; Gebhard, M. S.; Solomon, E. I.; Raymond, K. N. *J. Am. Chem. Soc.* **1991**, *113*, 2977.

(41) Lever, A. B. P. *Inorganic Electronic Spectroscopy;* 2 ed.; Elsevier: Amsterdam, 1984.

(42) Gewirth, A. A.; Cohen, S. L.; Schugar, H. J.; Solomon, E. I. *Inorg. Chem.* **1987**, *26*, 1133.

(43) Shadle, S. E.; Penner-Hahn, J. E.; Schugar, H. J.; Hedman, B.; Hodgson, K. O.; Solomon, E. I. *J. Am. Chem. Soc.* **1993**, *115*, 767.

(44) Karplus, M.; Porter, R. N. *Atoms and Molecules*; W. A. Benjamin, Inc.: London, 1970, p 228.

(45) Furlane, E.; Cervone, E.; Valent, V. *J. Nucl. Chem.* **1963**, *25*, 159.

(46) Cotton, F. A. *Chemical Applications of Group Theory*; Interscience Publishers: New York, 1963.

(47) Westre, T. E.; Kennepohl, P.; DeWitt, J. G.; Hedman, B.; Hodgson, K. O.; Solomon, E. I. to be published.

(48) Deaton, J. C.; Gebhard, M. S.; Solomon, E. I. **1989**, *88*, 877.

(49) Bertrand, J. A.; Breece, J. L.; Eller, P. G. *Inorg. Chem.* **1974**, *13*, 125.

(50) Dong, Y.; Menage, S.; Brennan, B. A.; Elgren, T. E.; Jang, H. G.; Pearce, L. L.; Que, L., Jr. *J. Am. Chem. Soc.* **1993**, *115*, 1851.

(51) Armstrong, W. H.; Lippard, S. J. *J. Am. Chem. Soc.* **1984**, *106*, 4632.

(52) Neuse, E. W.; Kahn, F. B. D.; Berhalter, K.; Thewalt, U. *J. Cryst. Spectr. Res.* **1986**, *16*, 483.

(53) Lauher, J. W.; Ibers, J. A. *Inorg. Chem.* **1975**, *14*, 348.

(54) Briat, B.; Canit, J. C. *Molec. Phys.* **1983**, *48*, 33.

(55) Kitajima, N. **1994**, private communication.

(56) Pabst, A. *Am. Mineralogist* **1943**, *28*, 372.

(57) Pabst, A. *Acta Crystallogr.* **1959**, *12*, 733.

(58) Hodges, K. D.; Wollmann, R. G.; Barfield, E. K.; Hendrickson, D. N. *Inorg. Chem.* **1977**, *16*, 2746.

(59) Ferrari, A.; Braibanti, A.; Bigliardi, G. *Acta Crystallogr.* **1963**, *16*, 846.

(60) Gregory, N. W. *J. Phys. Chem* **1963**, *67*, 927.

(61) Hatfield, W. E.; Fay, R. C.; Pfluger, C. E.; Piper, T. S. *J. Am. Chem. Soc.* **1963**, *85*, 265.

(62) Beattie, J. K.; Moore, C. J. *Inorg. Chem.* **1982**, *21*, 1291.

(63) Iball, J.; Morgan, C. H. *Acta Crystallogr.* **1967**, *23*, 339.

(64) Holt, S.; Dingle, R. *Acta Chem. Scand.* **1968**, *22*, 1091.

(65) Jaeger, F. M.; Mees, R. T. A. *Proc. Acad. Sci. Amsterdam* **1918**, *20*, 283.

(66) Clark, H. C.; Curtis, N. F.; Odell, A. L. *J. Chem. Soc.* **1954**, 63.

(67) Wyckoff, R. W. G. *Crystal Structures;* 2 ed.; Robert E. Krieger Publishing Company: Malabar, Florida, 1982; Vol. 3, p 875,898.

(68) Feng, X.; Bott, S. G.; Lippard, S. J. *J. Am. Chem. Soc.* **1989**, *111*, 8046.

(69) Tolman, W. B.; Bino, A.; Lippard, S. J. *J. Am. Chem. Soc.* **1989**, *111*, 8522.

(70) Armstrong, W. H.; Spool, A.; Papaefthymiou, G. C.; Frankel, R. B.; Lippard, S. J. *J. Am. Chem. Soc.* **1984**, *106*, 3653.

(71) Thich, J. A.; Ou, C. C.; Powers, D.; Vasiliou, B.; Mastropaolo, D.; Potenza, J. A.; Schugar, H. J. *J. Am. Chem. Soc.* **1976**, *98*, 1425.

(72) Norman, R. E.; Yan, S.; Que, L., Jr.; Backes, G.; Ling, J.; Sanders-Loehr, J.; Zhang, J. H.; O'Connor, C. J. *J. Am. Chem. Soc.* **1990**, *112*, 1554.

(73) Norman, R. E.; Holz, R. C.; Ménage, S.; O'Connor, C. J.; Zhang, J. H.; Que, L., Jr. *Inorg. Chem.* **1990**, *29*, 4629.

(74) Gaines, A.; Hammett, L. P.; Walden, G. H. *J. Am. Chem. Soc.* **1963**, *58*, 1668.

(75) Lippard, S. J.; Schugar, H.; Walling, C. *Inorg. Chem.* **1967**, *6*, 1825.

(76) Trofimenko, S. *J. Am. Chem. Soc.* **1967**, *89*, 3170.

(77) Oliver, J. D.; Mullica, D. F.; Hutchinson, B. B.; Milligan, W. O. *Inorg. Chem.* **1980**, *19*, 165.

(78) Brown, S. J.; Olmstead, M. M.; Mascharak, P. K. *Inorg. Chem.* **1990**, *29*, 3229.

(79) Rosenzweig, A. C.; Lippard, S. J. **1992**, private communication.

(80) Figgis, B. N.; Skelton, B. W.; White, A. H. **1978**, *31*, 1195.